BEHAVIOUR AND ANALYSIS OF CONFINED CONCRETE

By

Esneyder Montoya

A Thesis submitted in conformity with the requirements
for the Degree of Doctor of Philosophy,
Graduate Department of Civil Engineering, in the
University of Toronto

Your file Votre référence
ISBN: 0-612-84680-6
Our file Notre référence
ISBN: 0-612-84680-6

BEHAVIOUR AND ANALYSIS OF CONFINED CONCRETE
Doctor of Philosophy, 2003.
Esneyder Montoya
Department of Civil Engineering, University of Toronto.

ABSTRACT

It is widely recognized that concrete strength and post-peak ductility depend upon the level of confinement. Brittle or ductile behaviour is a function of triaxial compression, unconfined concrete strength, volumetric expansion, and softening.

A comprehensive study of confined concrete is carried out. The effects known to have influence on its behaviour are studied through analyses of an extensive experimental database. A stress-strain curve for concrete in compression is proposed that accounts for three-dimensional effects. The pre-peak response is predicted utilizing the formulation proposed by Hoshikuma et al. (1996). The load carrying capacity of confined concrete is predicted utilizing the Ottosen surface with newly developed coefficients that account for a wide range of confinement levels (lateral pressures up to 100% of the unconfined concrete strength). Unconfined concrete strengths from 20 MPa to 130 MPa are considered. Concrete dilatation is modeled as a function of the lateral pressure ratio (lateral pressure to unconfined concrete strength) and concrete strength, beyond the incompressible limit (Poisson's ratio of 0.5). The strains at peak strength and at 80% of peak strength in the post-peak regime are also proposed as functions of the stress state. A new post-peak curve that accounts for brittle or ductile behaviour is also proposed.

The proposed models were corroborated at the material level with experimental results of concrete subjected to active or passive confinement, yielding accurate agreements regardless of the load paths. The models were implemented in two of the VecTor series of programs developed at the University of Toronto; VecTor3 for three-dimensional analysis of reinforced concrete solids, and a new program, developed for this work, VecTor6, for analysis of axisymmetric solids.

Analyses of confined concrete at the structural level were performed using compression field modeling of confined concrete (Montoya, Vecchio, and Sheikh 2001), a methodology for nonlinear elastic analysis that combines models from the modified compression field theory (Vecchio and Collins 1986) and models derived empirically and from plasticity approaches. Columns confined with FRP composites or steel were analyzed. The ability of the proposed constitutive models to accurately determine the peak strength, concrete dilatation, pre- and post- peak regimes is verified.

Acknowledgements

My sincere thanks go first to Professors F.J. Vecchio and S.A. Sheikh for their incredible support and advice in the course of my research. Not only have I learnt extraordinary academic thinking but you have taught me small things to carry on in my professional life.

Chats over a coffee or a beer, joking or talking research, those were the moments you have shared with me over these years. Your unconditional friendship is very much appreciated, Mukhtar Homam and Dan Palermo.

"Whatever path you take, be true to yourself". I always have found that support in you, encouraging me in difficult moments, relieving me from anxiety, staying by my side in silence. I never stop learning from you, Ana Maria. This is especially dedicated to you, mi Alma.

There is no distance that keeps my heart and feelings away from you, your white candles and prayers, your eternal vigil is always accompanying me, thanks to my family.

I would like to thank Professor Alaa Elwi from the University of Alberta for his comments and suggestions as external appraiser. The financial support of the Natural Sciences and Engineering Research Council, The University of Toronto and the Government of Ontario is gratefully appreciated.

Table of Contents

ABSTRACT ii

Acknowledgements iii

Table of Contents iv

List of Tables viii

List of Figures xii

Chapter 1: Introduction 1

1.1 Confined Concrete 1

1.2 Background 5

1.3 Contributions of this Thesis 6

1.4 Thesis Outline 8

Chapter 2: Literature Review 9

2.1 Introduction 9

2.2 Column Behaviour-Empirical Models 10
2.2.1 Steel-Confined Columns 10
2.2.1.1 Cleason (1999) 10
2.2.1.2 Vintzileou and Malliri (1999) 14
2.2.2 FRP-Confined Columns 19
2.2.2.1 Purba and Mufti (1999) 19
2.2.2.2 Demers and Neale (1999) 21
2.2.2.3 Xiao and Wu (2000) 23
2.2.2.4 Spoelstra and Monti (1999) 25
2.2.2.5 Lam and Teng (2002) 28
2.2.2.6 Karabinis and Rousakis (2002) 30
2.2.2.7 Rochette and Labossiere (2000) 33

2.3 Computational Models 37
2.3.1 Failure Surfaces for Concrete 37
2.3.1.1 Sfer, Carol, Gettu, and Etse (2002) 37
2.3.1.2 Pivonka, Lackner, and Mang (2000) 42
2.3.1.3 Sankarasubramanian and Rajasekaran (1996) 46
2.3.1.4 Barros (2001) 48
2.3.1.5 Mirmiran, Kenneth, and Yuan (2000) 52
2.3.2 Confinement Models 55

2.3.2.1 Yip (1998) 55
2.3.2.2 Li and Ansari (1999) 58
2.3.2.3 Liu and Foster (2000) 61
2.3.2.4 Ghazi, Attard, and Foster (2002) 65
2.3.2.5 Kwon and Spacone (2002) 69
2.3.2.6 Assa, Nishiyama, and Watanabe (2001a) 74
2.3.2.7 Assa, Nishiyama, and Watanabe (2001b) 78

2.4 Concrete Dilatation 81
2.4.1 Candappa, Setunge, and Sanjayan (1999) 81
2.4.2 Candappa, Sanjayan, and Setunge (2001) 83
2.4.3 Lee, Willam, and Kang (1997) 86

2.5 Conclusion 90
2.5.1 Summary 90
2.5.2 Limitations 92
2.5.3 Remarks 94

Chapter 3. Confined Concrete **99**

3.1 Introduction. 99

3.2 Concrete Dilatation. 100
3.2.1 Imran and Pantazopoulou Tests 100
3.2.2 Proposed Model 106
3.2.3 Comparison with Other Models 111
3.2.3.1 Imran and Pantazopoulou Model 111
3.2.3.2 Spoelstra and Monti Model 112
3.2.3.3 Vecchio Model 113
3.2.3.4 Kwon and Spacone Model 113
3.2.4 Analytical and Experimental Comparison of Lateral Strain at Peak Stress 114

3.3 Concrete Behaviour under Triaxial Compression 118
3.3.1 Column Behaviour at Peak Strength 118
3.3.2 Cylinder Behaviour at Peak Strength 123
3.3.3 Low and High Confinement, Normal and High Strength Concrete 125
3.3.3.1 Definitions of Concrete Strength and Confinement Levels 126
3.3.3.2 Ottosen Criterion 128
3.3.3.5 Comparison with Column and Cylinder Tests 131
3.3.3.6 Sensitivity of Parameter a 135
3.3.4 Strain at Peak Stress of Confined Concrete, ε_{cc}. 137

3.4 Stress-Strain Curve for Confined Concrete. 141
3.4.1 Pre-Peak Stress-Strain Curve. 141
3.4.2 Proposed Post-Peak Stress-Strain Curve. 142
3.4.2.1 The Witch of Agnesi. 142
3.4.2.2 Strain at 80% of Peak Stress, ε_{c80}. 143
3.4.2.3 Shape Factor K_d. 147

3.4.2.4 Analytical Expression for the Post-Peak Stress-Strain Curve. 149

Chapter 4. Solids of Revolution: VecTor6 **150**

4.1 General Description 150

4.2 Compression Field Modelling of Confined Concrete 151
4.2.1 Concrete in Compression 152
4.2.2 Concrete in Tension 153
4.2.3 Concrete Dilatation 153
4.2.5 Compression Softening 154
4.2.4 Strength Enhancement, Strain at Peak Stress, and Strain at 80% of Peak Stress 154
4.2.4.1 Strength Enhancement 154
4.2.4.1 Strain at Peak Stress 156
4.2.4.2 Strain at 80% of Peak Stress 156
4.2.6 Cracking Criterion 157
4.2.7 Steel and FRP Composites 157
4.2.7.1 Steel 157
4.2.7.2 FRP Composites 158

4.3 Element Library 158

4.4 Finite Element Analysis and Flow Chart 162

Chapter 5: Confined Concrete Behaviour and Analysis **166**

5.1 Analytical Comparison of Stress-Strain Curves of Triaxial Tests. 166
5.1.1 Candappa, Sanjayan, and Setunge (1999) 166
5.1.2 Xie, Elwi, and MacGregor (1995) 169
5.1.3 Attard and Setunge (1996) 172
5.1.4 Imran and Pantazopoulou (1996) 175
5.1.4 Karabinis and Rousakis (2002) 180

5.2 Analytical Comparison of Stress-Strain Curves of Column Tests. 184
5.2.1 Demers and Neale (1999) 184
5.2.2 Sheikh and Toklucu (1993) 189
5.2.3 Montgomery and Sheikh (1996) 198
5.2.4 Sheikh and Uzumeri (1980) 201

5.3 Applications 210
5.3.1 FRP shell-confined columns subjected to axial compression 210
5.3.2 FRP confined column subjected to lateral cyclic loading and axial load. 215

5.4 Summary. 220

Chapter 6: Conclusions and Recommendations **223**

6.1 Conclusions 223

6.2 Recommendations for Future Work 226

References **230**

Appendix A: Column Behaviour at Peak Strength **237**
A.1 Column Details 237
A.2 Analytical and Experimental Strengths for Column Database 244

Appendix B: Cylinder Behaviour at Peak Strength **249**
B.1 Cylinder Details 249
B.2 Analytical and Experimental Strengths for Cylinder Database 254

Appendix C: Determination of Parameter *a* for Ottosen Model **259**
C.1 Reinforced Concrete Columns 259
C.2 Concrete Cylinders 265
C.3 Final values for Parameter a 269
C.4 Analytical to Experimental Strength for Columns with Proposed Model 271
C.5 Analytical to Experimental Strength for Cylinders with Proposed Model 276

Appendix D: Determination of Strain at Peak Stress, ε_{cc}. **280**
D.1 Experimental Data 280
D.2 Normalized Strain at Peak Stress versus Confinement Level 282

Appendix E: Determination of Strain at 80% of Peak Stress, ε_{c80}. **284**
E.1 Experimental Data 284
E.2 Normalized Strain at 80% of Peak Stress versus Confinement Level 286

Appendix F: Stiffness Matrices for Torus Elements **288**
F.1 Four-node Torus Element 288
F.2 Three-node Torus Element 291
F.3 Ring Bar 294

Appendix G: Notation. **295**

List of Tables

Table 1. Properties of Cleason columns 11

Table 2. Synopsis of literature review. 96

Table 3. Regression parameter α and concrete properties for Imran-Pantazopoulou.107

Table 4. Comparison of experimental-to-calculated lateral strain ratios at peak stress 115

Table 5. Description of sets of columns per researcher (s). 119

Table 6. Failure surface models. 120

Table 7. Calculated to measured strength ratios, columns. 122

Table 8. Description of sets of cylinders per researcher (s). 124

Table 9. Calculated to measured strength ratios, cylinders. 124

Table 10. Proposed values for parameter a 130

Table 11. Calculated-to-experimental strength ratios, columns, proposed model. 132

Table 12. Calculated-to-experimental strength ratios, cylinders, proposed model. 133

Table 13. Experimental data used in the formulation of strain at peak stress, ε_{cc}. 137

Table 14. Values for coefficient k to determine ε_{cc}. 138

Table 15. Statistical values of predicted-to-experimental ratios for strain at peak stress. 140

Table 16. Experimental data used in the formulation of strain at 80 % peak stress, ε_{c80}. 144

Table 17. Values coefficient k_1 to determine ε_{c80}. 145

Table 18. Statistical values of analytical-to-experimental ratios for ε_{c80}. 147

Table 19. Proposed values for parameter a 155

Table 20. Experimental and analytical curve parameters of Candappa et al. curves. 168

Table 21. Experimental and analytical curve parameters of Xie et al. curves. 171

Table 22. Experimental and analytical curve parameters of Attard-Setunge curves. 174

Table 23. Experimental and analytical curve parameters of Imran-Pantazopoulou curves. 176

Table 24. Material properties of Karabinis et al. cylinders. 180

Table 25. Comparison of experimental and analytical results, Karabinis et al. tests. 183

Table 26. Column properties, Demers and Neale tests. 185

Table 27. Analytical and experimental results, Demers and Neale columns. 189

Table 28. Column properties, Sheikh and Toklucu tests. 190

Table 29. Analytical and experimental results, Sheikh and Toklucu columns. 196

Table 30. Column properties, Montgomery and Sheikh tests. 198

Table 31. Analytical and experimental results, Montgomery and Sheikh columns. 200

Table 32. Column properties, Sheikh and Uzumeri tests. 202

Table 33. Finite element mesh properties, Sheikh and Uzumeri columns. 205

Table 34. Analytical and experimental results, Sheikh and Uzumeri columns. 208

Table 35. Material properties of Cairns and Jaffry and Sheikh Columns 211

Table 36. Analytical and experimental results of Cairns and Jaffry and Sheikh columns. 213

Table 37. Material properties of column ST-2NT. 216

Table 38. Sheikh and Uzumeri columns (square). 238

Table 39. Sheikh and Toklucu columns (circular). 239

Table 40. Montgomery and Sheikh columns (circular). 240

Table 41. Pessiki et al. (circular). 240

Table 42. Razvi and Saatcioglu (circular). 241

Table 43. Razvi and Saatcioglu (square). 241

Table 44. Nagashima et al. (1992) (square). 242

Table 45. Nagashima et al. (1993) (square). 242

Table 46. Li (circular). 243

Table 47. Hurlbut specimens. 249

Table 48. Gardner specimens. 249

Table 49. Li and Ansari specimens. 250

Table 50. Richart et al. Specimens. 250

Table 51. Attard and Setunge specimens. 251

Table 52. Imran and Pantazopoulou specimens. 252

Table 53. Xie, Elwi and McGregor specimens. 253

Table 54. Values for parameter *a* from column specimens. 260

Table 55. Low confinement, normal strength concrete (LN). 261

Table 56. Low confinement, high strength concrete (LH). 262

Table 57. High confinement, high strength concrete (HH). 264

Table 58. Low confinement, normal strength concrete (LN). 265

Table 59. High confinement, normal strength concrete (HN). 265

Table 60. Low confinement, high strength concrete (LH). 266

Table 61. High confinement, high strength concrete (HH). 268

Table 62. Values for parameter *a* from cylinder specimens. 268

Table 63. Number of specimens per confinement category. 269

Table 64. Final proposed values for parameter *a*. 269

Table 65. Parameter *a* for various formulations of tensile strength f'_{ct} 270

Table 66. Li and Ansari tests. 280

Table 67. Imran and Pantazopoulou tests. 280

Table 68. Attard and Setunge tests. 281

Table 69. Li and Ansari tests. 284

Table 70. Attard and Setunge tests. 284

Table 71. Candappa et al. tests. 285

Table 72. Xie et al. tests. 285

List of Figures

Figure 1. (a) Crack propagation on confined concrete at low, and (b) High lateral pressures (Sfer et al. 2002). 1

Figure 2. (a) Pores at the beginning of loading, and (b) Pore collapse after a high lateral pressure is applied (Sfer et al. 2002). 2

Figure 3. Axial stress-strain curve for cylinders tested by Sfer et al.(2002). 2

Figure 4. (a) Anchor system (DYWIDAG), and (b) Strut-and-tie model. 3

Figure 5. Bolt-concrete interaction (The University of Stuttgart website). 3

Figure 6. Hoover dam (US Dept. of the Interior, CO.). 4

Figure 7. (a) FRP-confined column tested by Jaffry (2001), (b) Sheikh and Uzumeri column. 5

Figure 8. Cross sections of columns (Cleason 1999). 11

Figure 9. Stress-crack width relationship (Cleason 1999) 12

Figure 10. Beam element in ABAQUS with integration points (Cleason 1999). 13

Figure 11. Comparison of results for column 1 (Cleason 1999). 13

Figure 12. Experimental/predicted column strengths using MC90 model (Vintzileou and Malliri 1999). 16

Figure 13. Experimental/predicted ε_{co}^{*} using MC90 model (Vintzileou and Malliri 1999) 16

Figure 14. Experimental/predicted column strengths using proposed formulae (Vintzileou and Malliri 1999). 17

Figure 15. Experimental/predicted ε_{co}^{*} using proposed formulae (Vintzileou and Malliri 1999) 18

Figure 16. Experimental results of columns (Purba and Mufti 1999). 20

Figure 17. Comparison of experimental results with modified Mander et al. model (Purba and Mufti 1999). 20

Figure 18. Experimental results of columns (Demers and Neale 1999). 22

Figure 19. (a) Experimental results of Xiao and Wu tests, (b) Prediction of Hosotani et al. tests. (Xiao and Wu 2000). 24

Figure 20. Comparison of results of tests by Mirmiran and Shahawy. 26

Figure 21. Prediction of ultimate strength (Spoelstra and Monti 1999). 27

Figure 22. Prediction of ultimate strain (Spoelstra and Monti 1999). 27

Figure 23. Response of CFRP-confined concrete specimens with 2 layers of carbon Fibres (Karabinis and Rousakis 2002). 31

Figure 24. Analytical and experimental response of specimen C11 (Karabinis and Rousakis 2002). 33

Figure 25. Tensile stress-strain curves for (a) carbon fibre, and (b) aramid fibre (Rochette and Labossiere 2000). 35

Figure 26. Column dimensions (Rochette and Labossiere 2000). 36

Figure 27. Stress-strain curves for aramid-wrapped square columns (R = 25 mm) (Rochette and Labossiere 2000). 36

Figure 28. Effect of round corner in the response, square CFRP columns wrapped with 3 plies (Rochette and Labossiere 2000). 37

Figure 29. Typical lateral strain measured at corners and faces (Rochette and Labossiere 2000). 37

Figure 30. Axial stress-axial strain curves (Sfer et al. 2002). 38

Figure 31. (a) Axial stress-lateral strain curves, (b) Close-up of axial stress-axial strain curves (Sfer et al. 2002). 39

Figure 32. Axial stress-volumetric strain curves (Sfer et al. 2002). 40

Figure 33. Loading surface with cap (Sfer et al. 2002) 41

Figure 34. Failure surface and plastic strains in I1, √J2 space (Sfer et al. 2002). 41

Figure 35. Extended Leon model, hardening law (Pivonka et al. 2000). 43

Figure 36. Comparison of Hurlbut and Smith tests with ELM (Pivonka et al. 2000). 45

Figure 37. Comparison of Hurlbut and Smith tests with Rankine-DP results (associative rule) (Pivonka et al. 2000). 45

Figure 38. Comparison of Hurlbut and Smith tests with Rankine-DP results (non-associative rule) (Pivonka et al. 2000). 46

Figure 39. Stress-strain curve for concrete cylinder under a lateral pressure of 55 MPa. 48

Figure 40. Axial load-axial strain for cylinder C2 tested by Iyengar et al. 51

Figure 41. Analytical and experimental results of Mirmiran et al. tests (Mirmiran et al 2000). 53

Figure 42. Volumetric strain and concrete dilatation (Mirmiran et al 2000) 54

Figure 43. Analytical and experimental results of Mirmiran et al. square Columns (Mirmiran et al 2000). 54

Figure 44. Comparison of experimental and analytical results of 6 ksi Ansari-Li tests (Li and Ansari 1999). 60

Figure 45. Axial load-axial strain, Sheikh and Uzumeri column 2A5 (Liu and Foster 2000). 64

Figure 46. Comparison of simulation using microplane model M4 and Attard and Setunge formulae for cylinders subjected to uniaxial compression (Ghazi et al. 2002). 66

Figure 47. Uniaxial compression tests with modified microplane model M4 (Ghazi et al. 2002). 67

Figure 48. Microplane model M4 and Attard and Setunge analytical results for 120 MPa cylinders (Ghazi et al. 2002). 67

Figure 49. Modified microplane model M4 and Attard and Setunge analytical results for 120 MPa cylinders (Ghazi et al. 2002). 68

Figure 50. Stress-strain curve for the 3D model. 70

Figure 51. Experimental and analytical results of Hurlbut test at 0.5 ksi lateral pressure. 72

Figure 52. Experimental and analytical results of Xiao et al. column R3. 73

Figure 53. Axial stress-axial strain of cylinder reinforced with spirals (Assa et al. 2001a). 74

Figure 54. Axial strain-lateral strain of cylinder reinforced with spirals (Assa et al. 2001a). 75

Figure 55. Lateral expansion compatibility (Assa et al. 2001a). 76

Figure 56. Analytical and experimental results (Assa et al. 2001a). 77

Figure 57. Model of concrete struts (Assa et al. 2001b). 78

Figure 58. Deformation compatibility of a typical concrete strut (Assa et al. 2001b). 79

Figure 59. Axial stress-axial strain of column unit-6 tested by Scott et al. 80

Figure 60. Axial stress-axial strain for 100 MPa cylinders (Candappa et al. 1999). 82

Figure 61. Axial stress-lateral strain for 100 MPa cylinders (Candappa et al. 1999). 82

Figure 62. Axial stress-axial strain and axial stress-lateral strain for 40 MPa cylinders (Candappa et al. 2001). 85

Figure 63. Non-linearity index β versus secant Poisson ratio ν^a (Candappa et al. 2001). 85

Figure 64. Nominal stress-axial strain, and nominal stress-lateral strain results of uniaxial compression tests (Lee et al. 1997). 87

Figure 65. Nominal stress-axial deformation, nominal stress-lateral deformation (Lee et al. 1997). 88

Figure 66. Stiffness degradation versus (a) Normalized strength, and (b) Fracture energy (Lee et al. 1997). 89

Figure 67. Stiffness degradation versus normalized plastic deformation (Lee et al. 1997). 89

Figure 68. Loading types on Imran and Pantazopoulou tests. 101

Figure 69. Triaxial cell. 101

Figure 70. Axial stress-lateral, -axial strain curves for 28.6 MPa tests. 102

Figure 71. Axial stress -lateral, -axial strain curves for 47.4 MPa tests. 102

Figure 72. Axial stress-lateral, -axial strain curves for 73.4 MPa tests. 103

Figure 73. Lateral strain-axial strain ratio curves for 28.6 MPa tests. 103

Figure 74. Lateral strain-axial strain ratio curves for 47.4 MPa tests. 104

Figure 75. Lateral strain-axial strain ratio curves for 73.4 MPa tests. 104

Figure 76. Imran and Pantazopoulou sample tests: (a) cyclic loading, (b) stepwise loading. 106

Figure 79. Value of α versus f_{cl}/f'_c for all Imran-Pantazopoulou tests. 109

Figure 80. Sketch of the secant Poisson's ratio with variable and constant lateral pressure. 110

Figure 81. Plots of analytical to experimental lateral strains at peak stress. 116

Figure 82. Level of confinement and concrete strength for columns. 126

Figure 83. Level of confinement and concrete strength for cylinders. 126

Figure 84. Comparison of column strengths obtained with proposed model and the models by Vecchio, Ottosen (Chen 1982), Hsieh et al., and Mander et al. 132

Figure 85. Comparison of cylinder strengths obtained with proposed model and the models by Vecchio, and Ottosen (Chen 1982). 134

Figure 86. Comparison of cylinder strengths obtained with proposed model and the models by Mander et al., and Hsieh et al. 134

Figure 87. Sensitivity of parameter a 135

Figure 88. Determination of coefficient k from test data. 139

Figure 89. Analytical versus experimental strains at peak stress. 139

Figure 90. The witch of Agnesi. 143

Figure 91. Determination of coefficient k_1 from test data. 146

Figure 92. Analytical versus experimental strains at 80% of peak stress. 146

Figure 93. (a) The witch of Agnesi with axis of symmetry at $x=x_o$, (b) Typical proposed stress-strain curve. 148

Figure 94. Stress-strain curve for steel. 157

Figure 95. Stress-strain curve for FRP composites. 158

Figure 96. Cylindrical coordinate system. 159

Figure 97. Four-node torus element. 161

Figure 98. Three-node torus element. 162

Figure 99. Ring Bar. 162

Figure 100. Secant stiffness. 164

Figure 101. Flow chart for VecTor6. 165

Figure 102. Axial stress–axial strain, and axial stress- lateral strain curves, 60 MPa cylinders, Candappa et al. 167

Figure 103. Axial stress–axial strain, and axial stress- lateral strain curves, 75 MPa cylinders, Candappa et al. 167

Figure 104. Axial stress–axial strain, and axial stress- lateral strain curves, 100 MPa cylinders, Candappa et al. 168

Figure 105. Axial stress–axial strain curves, 60.2 MPa cylinders, Xie et al. 170

Figure 106. Axial stress–axial strain curves, 92.2 MPa cylinders, Xie et al. 171

Figure 107. Axial stress–axial strain curves, 110 MPa cylinders, Attard and Setunge. 173

Figure 108. Axial stress–axial strain curves, 118 MPa cylinders, Attard and Setunge. 173

Figure 109. Axial stress–axial strain curves, 120 MPa cylinders, Attard and Setunge. 174

Figure 110. Axial stress–axial strain, and axial stress-lateral strain curves, 73.4 MPa cylinders, Imran and Pantazopoulou. 177

Figure 111. Axial stress–axial strain, and axial stress-lateral strain curves, 47.4 MPa cylinders, Imran and Pantazopoulou. 178

Figure 112. Axial stress–axial strain, and axial stress-lateral strain curves, 28.6 MPa cylinders, Imran and Pantazopoulou. 179

Figure 113. VecTor6 model of Karabinis et al. cylinders 181

Figure 114. Experimental and analytical stress-strain curves, Type A, Karabinis et al. tests. 182

Figure 115. Experimental and analytical stress-strain curves, Type B, Karabinis et al. tests. 182

Figure 116. Mesh Details for Demers and Neale Columns. 186

Figure 117. Axial stress–axial strain curve, column U25-1, Demers and Neale. 187

Figure 118. Axial stress–axial strain curve, column U25-2, Demers and Neale. 187

Figure 119. Axial stress–axial strain curve, column U25-3, Demers and Neale. 188

Figure 120. Axial stress–axial strain curve, column U25-4, Demers and Neale. 188

Figure 121. Mesh details for Sheikh and Toklucu column D14-H10M-P3.0. 191

Figure 122. Axial load–axial strain, - spiral strain curves, column D14-S10M-P4.4 192

Figure 123. Axial load–axial strain curve, -spiral strain curves, column D14-H10M-P3.0 193

Figure 124. Axial load–axial strain, -spiral strain curves, column D10-S8M-P4.3 193

Figure 125. Axial load–axial strain curve, -spiral strain curves, column D10-SD4-P1.6 194

Figure 126. Axial load–axial strain, -spiral strain curves, column D8-SD5-P3.4 194

Figure 127. Axial load–axial strain, -spiral strain curves, column D8-SD5-P1.7 195

Figure 128. Axial load–axial strain curve, column D8-S3/16-P1.7 195

Figure 129. (a) Sketch of confined and unconfined zones, and (b) Deformed shape of column. 197

Figure 130. Axial load–axial strain curve, Montgomery and Sheikh column H-D25-S11.3-P109. 199

Figure 131. Axial load–axial strain curve, Montgomery and Sheikh column H-D25-S8-P79. 199

Figure 132. Axial load–axial strain curve, Montgomery and Sheikh column H-D20-S6.4-P43. 200

Figure 133. Typical Sheikh and Uzumeri column. 202

Figure 134. Type Sheikh and Uzumeri tie and longitudinal steel arrangements. 203

Figure 135. Mesh details for Sheikh and Uzumeri columns. 204

Figure 136. Behaviour of specimen 2C4-12. 205

Figure 137. Behaviour of specimen 4B3-19. 206

Figure 138. Behaviour of specimen 4B4-20 206

Figure 139. Behaviour of specimen 4D3-22. 207

Figure 140. Behaviour of specimen 4D6-24. 207

Figure 141. Typical distribution of analytical axial compressive stresses for a type-D column. 209

Figure 142. Analytical and experimental stress-strain curves for Cairns columns. 212

Figure 143. Analytical and experimental stress-strain curves for Jaffry and Sheikh columns. 213

Figure 144. Sketch of column ST-2NT. 217

Figure 145. Analytical response of column ST-2NT in monotonic compression. 218

Figure 146. Analytical axial stress-axial strain curve of column ST-2NT 218

Figure 147. Analytical and experimental moment-curvature responses of column ST-2NT. 219

Figure 148. Analytical responses of column ST-2NT with and without GFRP wraps. 220

Figure 149. Analytical to experimental strength, Tresca model. 244

Figure 150. Analytical to experimental strength, Von Mises model. 244

Figure 151. Analytical to experimental strength, Mohr-Coulomb model. 245

Figure 152. Analytical to experimental strength, Drucker-Prager model. 245

Figure 153. Analytical to experimental strength, Hsieh et al. model. 246

Figure 154. Analytical to experimental strength, Barros model. 246

Figure 155. Analytical to experimental strength, Ottosen model. 247

Figure 156. Analytical to experimental strength, Richart et al. model. 247

Figure 157. Analytical to experimental strength, Vecchio model. 248

Figure 158. Analytical to experimental strength, Mander model. 248

Figure 159. Analytical to experimental strength, Tresca and Von Mises model. 254

Figure 160. Analytical to experimental strength, Drucker-Prager and Mohr-Coulomb models. 255

Figure 161. Analytical to experimental strength, Hsieh et al. model. 255

Figure 162. Analytical to experimental strength, Barros model. 256

Figure 163. Analytical to experimental strength, Ottosen model. 256

Figure 164. Analytical to experimental strength, Richart et al. model. 257

Figure 165. Analytical to experimental Strength, Vecchio model. 257

Figure 166. Analytical to experimental Strength, Mander model. 258

Figure 167. Analytical to experimental results, Sheikh and Uzumeri columns, proposed model. 271

Figure 168. Analytical to experimental results, Montgomery and Sheikh columns, proposed model. 271

Figure 169. Analytical to experimental results, Sheikh and Toklucu columns, proposed model. 272

Figure 170. Analytical to experimental results, Pessiki et al. columns, proposed model. 272

Figure 171. Analytical to experimental results, Razvi and Saatcioglu circular columns, proposed model. 273

Figure 172. Analytical to experimental results, Razvi and Saatcioglu square columns, proposed model. 273

Figure 173. Analytical to experimental results, Nagashima et al. (1992) columns, proposed model. 274

Figure 174. Analytical to experimental results, Nagashima et al. (1993) columns, proposed model. 274

Figure 175. Analytical to experimental results, Li columns, proposed model. 275

Figure 176. Analytical to experimental results, Hurlbut cylinders, proposed model. 276

Figure 177. Analytical to experimental results, Gardner cylinders, proposed model. 276

Figure 178. Analytical to experimental results, Li and Ansari cylinders, proposed model. 277

Figure 179. Analytical to experimental results, Richart et al. cylinders, proposed model. 277

Figure 180. Analytical to experimental results, Attard and Setunge cylinders, proposed model. 278

Figure 181. Analytical to experimental results, Imran and Pantazopoulou cylinders, proposed model. 278

Figure 182. Analytical to experimental results Xie, Elwi and McGregor cylinders, proposed model. 279

Figure 183. Normalized strain at peak stress versus confinement level, Li and Ansari tests. 282

Figure 184. Normalized strain at peak stress versus confinement Level, Imran and Pantazopoulou tests. 282

Figure 185. Normalized strain at peak stress versus confinement level, Attard and Setunge tests. 283

Figure 186. Normalized strain at 80% peak stress versus confinement level, Li and Ansari tests. 286

Figure 187. Normalized strain at 80% peak stress versus confinement level, Attard and Setunge tests. 286

Figure 188. Normalized strain at 80% peak stress versus confinement level, Candappa et al. tests. 287

Figure 189. Normalized strain at 80% peak stress versus confinement level, Candappa et al. tests. 287

Figure 190. Four-node torus element, numbering. 290

Figure 191. Three-node torus element, numbering. 292

Figure 192. Ring bar, numbering. 294

Chapter 1: Introduction

1.1 Confined Concrete

When a concrete solid is subjected to compressive stresses in all (principal) directions, it is said to be confined. Triaxial compressive stresses delay expansion (i.e. crack growth) and damage propagation in concrete. As concrete compressive stresses become larger, the internal structure of paste, aggregates and pores change. Cracks develop, pores collapse, and the failure mode switches from brittle to ductile.

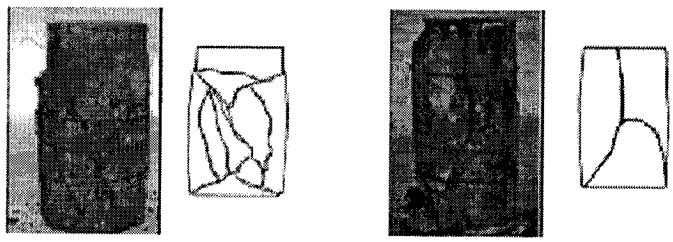

Figure 1. Crack propagation on confined concrete at (a) low, and (b) high lateral pressures (Sfer et al. 2002).

As an example of confined concrete behaviour, consider the principal stresses to be $0 \geq \sigma_1 \geq \sigma_2 \geq \sigma_3$. At low levels of confinement, at the time of failure, several cracks will surface on a concrete cylinder subjected to increasing axial compression and constant low levels of lateral pressure (i.e. $\sigma_1 = \sigma_2 \geq \sigma_3$), as shown in Figure 1a. As the lateral confinement increases, the mode of failure is characterized by fewer but larger cracks on the surface (see Figure 1b). The internal structure of the concrete mass will have changed, as can be seen in Figure 2, where the collapse of pores due to large confinement pressures is easily recognizable.

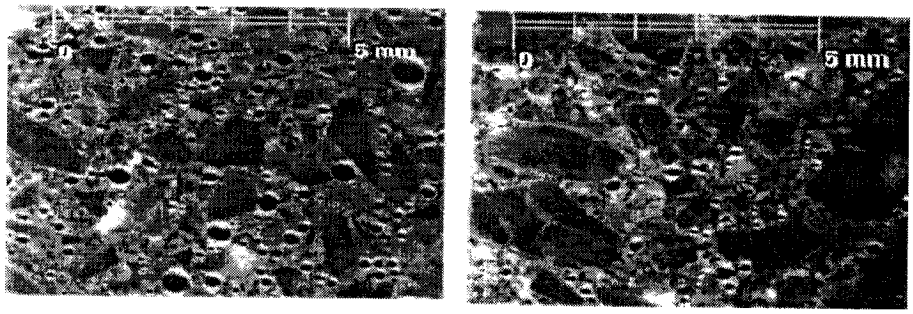

(a) (b)

Figure 2. (a) Pores at the beginning of loading, and (b) Pore collapse after a high lateral pressure is applied (Sfer et al. 2002).

It is also well known that confinement increases the capacity of concrete to sustain high loads at large deformations and delay the onset of damage. This can be seen in Figure 3 for the cylinders shown in Figure 1, where the axial stress-strain curves are shown. After peak strength, the low-confinement curve exhibits softening and decreasing capacity to sustain loads, whereas in the high-confinement curve it is difficult to identify the peak strength due to continuous hardening behaviour until failure.

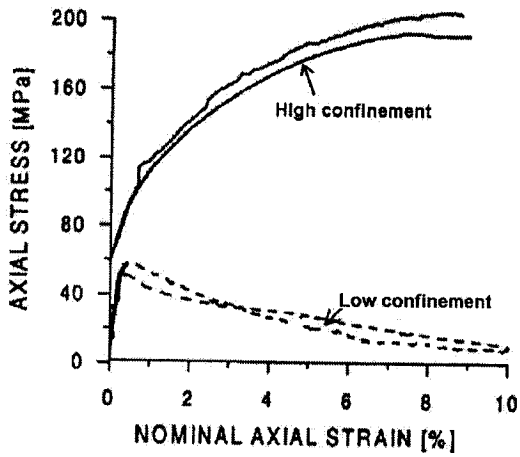

Figure 3. Axial stress-strain curve for cylinders tested by Sfer et al.(2002).

Concrete elements, subassemblies, and structures subjected to triaxial stresses can be found in many civil engineering applications. In prestressed structures, anchorage of

strands at the ends of members creates a disturbed zone (D zone) that requires the design of a set of stirrups around the anchorage cables to prevent the concrete from spalling out explosively. There is a complex triaxial stress distribution in the anchorage zone, as represented by the strut-and-tie lines in Figure 4.

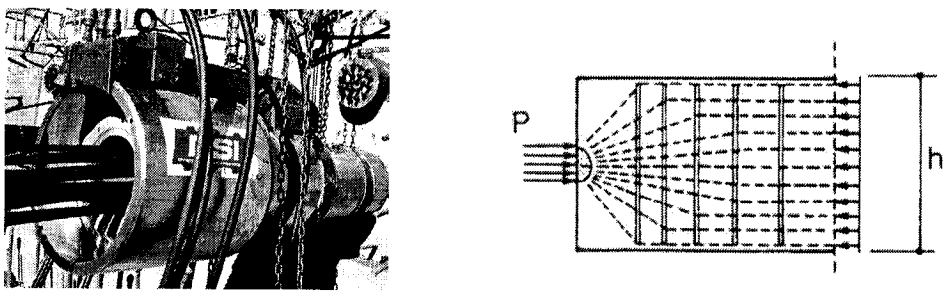

(a) (b)

Figure 4. (a) Anchor system (DYWIDAG), and (b) Strut-and-tie model.

Anchor fasteners embedded in concrete and subjected to tension produce high axisymmetric triaxial compressive stresses in the concrete, in the vicinity of the bolt head (Pivonka et al. 2000).The study of the behaviour of bolt-concrete interaction (see Figure 5) in structures subjected to dynamic excitations (e.g. earthquakes) is a new emerging field of investigation.

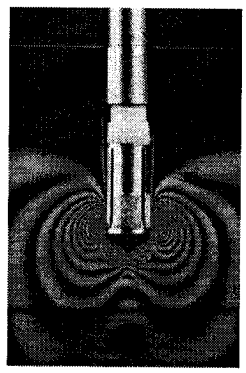

Figure 5. Bolt-concrete interaction (University of Stuttgart website).

Concrete in massive dams (see Figure 6) is subjected to triaxial compression due to its self-weight, and to restraints at its base and lateral supports. Water pressure and earthquake loading also contribute to increasing compressive (and tensile) stresses in concrete dams.

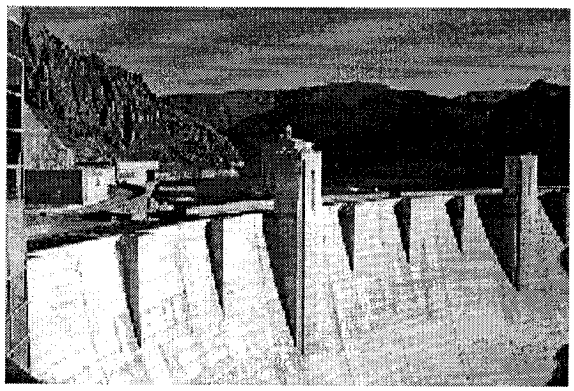

Figure 6. Hoover dam (US Dept. of the Interior, CO.).

Finally, the most common structural engineering application where an element is subjected to triaxial stresses is in reinforced concrete columns. The confining material may be steel, fibre reinforced polymer (FRP) fabric or a combination of both (see Figure 7). The behavioural enhancement of FRP composites for structural retrofitting has long been investigated. Many of the current models to predict the behaviour of confined concrete are based on FRP-confined column tests, responding to the need for strengthening old bridge and building structures.

The difficulties in obtaining experimental results (e.g. strains) in concrete specimens such as bolts subjected to pull-out tests, prestressed anchorages, and scaled models of concrete dams, just to mention some, have led to the formulation of material behaviour models based on simpler tests (e.g. cylinder specimens), and the extrapolation of those models to analyze more complex subassemblies. Finite element

techniques provide useful insight on material and structural behaviour. Well engineered models and numerical analyses contribute to the design of experimental tests, and the determination of simple formulations for design purposes based on realistic material and structural behaviour.

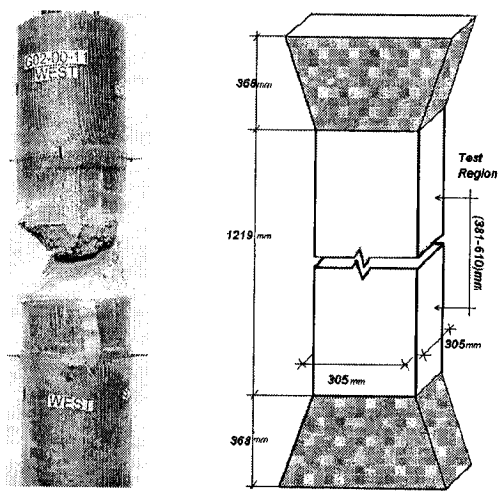

(a) (b)

Figure 7. (a) FRP-confined column tested by Jaffry (2001),(b) Sheikh and Uzumeri column.

1.2 Background

Confined concrete has been studied since the early 20th century, when Considére (See Pessiki et al. 2001) discovered that reinforcing concrete cylinders with spirals resulted in strength gain. Richart, Brandtzaeg and Brown (1928) published their famous studies on triaxial compression of concrete cylinders and proposed their simple formula for strength enhancement of reinforced concrete columns, which still remains part of 21st century codes since its implementation in the ACI-318 Code in 1933.

With the development of the basic sciences of engineering mechanics, and with increasing computational power, new constitutive material models for three-

dimensional analysis of concrete based on the theory of plasticity (Chen 1982), fracture mechanics, or combinations of both (Lee, Willam, and Kang 1997) have been developed. Continuum damage mechanics (CDM) models have also emerged for the interpretation of concrete softening (Li and Ansari 1999), and nonlinear elasticity models based on incremental tangent or secant stiffness approaches have been implemented in finite element programs (VecTor series).

Simplified formulations derived from experimental results on full-scale column tests have resulted in empirical models well suited for design purposes, yet not applicable to finite element programs for the analysis of other types of confined concrete elements. On the other hand, the more rational yet complex and laborious plasticity-, fracture mechanics-, and CDM- based models require the determination of numerous parameters from experimental tests that are applicable only under certain load path conditions or range of material properties. The nonlinear elastic approach can combine the rationality of elaborate plasticity-type models with the simplicity of basic three-dimensional stress-strain behaviour. The secant stiffness procedure is numerically stable and produces reliable responses, provided good engineering judgement is applied.

1.3 Contributions of this Thesis

The achievements of this thesis are two-fold. First, a complete model for confined concrete was developed. The model includes a stress-strain curve that accounts for three-dimensional effects: concrete dilatation, strength enhancement, post-peak softening and increased strain hardening. The range of concretes studied covers all types of commercially available concrete, from low strength (20 MPa) to very high

strength (130 MPa), and a large range of confining pressures, from zero confinement (i.e. uniaxial compression) up to a lateral pressure equal to 100% of the unconfined concrete strength. Simple relationships between the type of concrete and the confinement level were established in the development of the failure surface for strength enhancement. Concrete dilatation plays a key role in the behaviour of confined concrete; it was found to depend upon the exerted lateral pressure and the type of concrete. The relationship developed for concrete dilatation was not limited to a Poisson's ratio of 0.5.

All the developed relationships are given in terms of stresses and strains, which make them suitable for incremental nonlinear elastic analysis whereby the material models are combined and iterated until secant stiffness convergence is achieved at each load increment. The models are suitable for a wide range of applications and types of confinement (e.g. constant lateral pressure, steel- and FRP- confined concrete), regardless of loading history.

Second, a new program for nonlinear finite element analysis of reinforced concrete solids of revolution, VecTor6, was developed. The program allows for the analysis of solids having an axis of symmetry subjected to axisymmetric loading (e.g. circular columns, tanks, domes, circular slabs, pull-out tests) Three finite elements were implemented, a four- and a three-node torus, and a "ring" bar. The program was based on the formulations implemented for three-dimensional solids in program VecTor3 (Selby and Vecchio 1993, 1997) modified and adapted for solids with an axisymmetrical geometry. The confinement models developed in this thesis were

implemented in both programs and corroborated against the results of a series of concrete cylinders and columns.

1.4 Thesis Outline

This thesis is divided into five Chapters. Chapter 2 covers a literature review of published models and experimental research on confined concrete. A description is given for each of the investigations and their limitations are established.

Chapter 3 provides descriptions and formulations of the proposed models for concrete dilatation, strength enhancement, strain at peak stress, strain at 80% of peak stress in the post-peak regime, and the basic stress-strain curve for concrete in compression. The laboratory tests utilized in the development of the models are described and the prediction from the models for each behavioural mechanism is presented.

Chapter 4 describes program VecTor6, the element library, the compression field methodology behind the analysis of structural elements subjected to compression and confined by either lateral steel or FRP composites, and the limitations in the use of the program.

Chapter 5 presents comparisons of analytical and experimental results of a series of circular and square columns tested by various researchers. Conclusions and recommendations for future work are given in Chapter 6.

Chapter 2: Literature Review

2.1 Introduction

Several types of formulations have been used in the analysis of concrete columns confined by steel stirrups or spirals. They range from simple empirical models that utilize physical variables [such as distribution of lateral and longitudinal reinforcement, reinforcement ratios, overall section dimensions, and material properties (e.g. Kent and Park 1972; Sheikh and Uzumeri 1980; Mander 1988; Razvi and Saatciouglu 1999; Vintzileou and Malliri 1999)], to finite element analysis procedures (e.g. Liu and Foster 2000; Montoya, Vecchio and Sheikh 2001; Barros 2001) that implement advanced techniques and theories [such as nonlinear elasticity, plasticity, fracture mechanics, and continuum damage mechanics].

Several models for the calculation of complete stress-strain curves for unconfined concrete (e.g. Yip 1998; Lee and Willam 1999), and confined concrete (e.g. Xie, Elwi and McGregor 1995; Spoelstra and Monti 1999; Ansari and Li 1999; Xiao and Wu 2000; Pivonka, Lackner and Mang 2000; Lam and Teng 2002; Ghazi, Attard; and Foster 2002) have recently been proposed. The understanding of concrete dilatation effects on confinement and damage is becoming important in the definition of new confinement models, and some attempts have been made to establish a database of experimental tests that contains information on the lateral expansion of concrete when subjected to triaxial tests (e.g. Imran and Pantazopoulou 1996; Candappa, Setunge, and Sanjayan 1999; Candappa, Sanjayan, and Setunge 2001; Assa, Nishiyama, and Watanabe 2001). The difficulties in measuring lateral strains in confined concrete have

led to the creation of new systems of measurement (Li and Ansari 1999; Candappa, Setunge, and Sanjayan 2001). However, the database remains small to date.

In the following sections of this Chapter, a description of the work undertaken by other researchers, and some of their analytical and/or experimental results, are presented. Limitations on the application of the models and their findings are discussed at the end of each review. The Chapter is divided into three sections. The first section describes studies on columns and cylinders confined with steel or FRP composites. The second section reviews computational models for failure surfaces and complete confinement behaviour. The last section studies experimental and analytical models regarding concrete dilatation. A summary and conclusion is given at the end of the Chapter.

2.2 Column Behaviour-Empirical Models

2.2.1 Steel-Confined Columns

2.2.1.1 Cleason (1999)

Cleason carried out a testing program involving rectangular columns and implemented the Cousson and Paultre (1999) constitutive model for high strength concrete (HSC) columns into a commercial program to determine the accuracy of analytical results when compared to test results. A parametric study was then conducted using variables that most influenced column behaviour. The investigation ended with the determination of the volumetric ratio of transverse reinforcement required in the design of HSC columns to sustain at least the same ductility of that of normal strength concrete (NSC) columns.

Figure 8 and Table 1 show the cross sections and properties of the columns tested. The columns were subjected to concentric axial compression or eccentric compression. The slenderness effect was also taken into account for columns 4 and 5. In Table 1, s is the tie spacing, e is the eccentricity, and f'_c is the nominal concrete cylinder strength. No reference to the test apparatus or the stress-strain properties of the materials was given in the report.

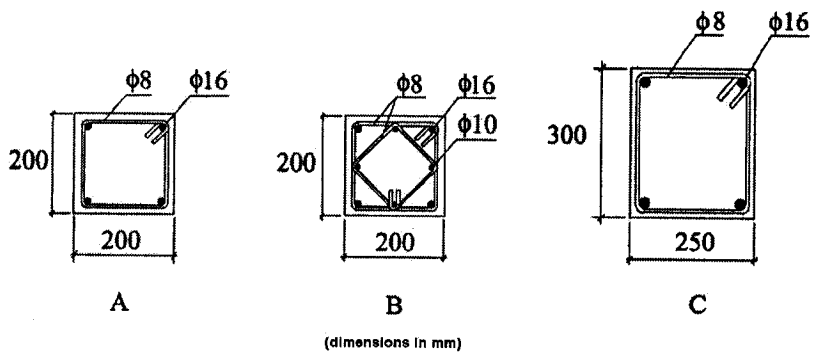

Figure 8. Cross sections of columns (Cleason 1999).

Table 1. Properties of Cleason columns

Column	Dimensions [mm]	Concrete	f'_c [MPa]	e [mm]	s [mm]	Reinforcement Configuration	Max. Load [kN]
1	200x200x800	HSC	91	0	130	A	3920
2	200x200x800	NSC	33	0	130	A	1650
3	250x300x900	HSC	112	90	50	C	3064
4	200x200x3000	HSC	91	20	130	B	2310
5	200x200x3000	NSC	33	20	130	B	990

Confined concrete was modelled using the model proposed by Cusson and Paultre (1999). Concrete in tension was modelled using a smeared crack approach with a bilinear stress-crack width (σ_{ct}-w) formulation, as shown in Figure 9, where f_{ct} is the tensile strength of concrete, G_f is the fracture energy, and w_u is the maximum crack width.

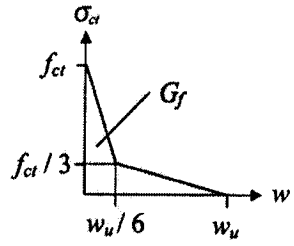

Figure 9. Stress-crack width relationship (Cleason 1999)

The ABAQUS program was used to implement the constitutive models. A three-dimensional two-node hybrid beam element was used. This element permitted the definition of different stress-strain curves at different integration points in the cross section. This allowed for the definition of unconfined concrete properties for cover concrete integration points and confined concrete properties for core concrete points, as shown in Figure 10.

The analytical study was carried out using a plain concrete strength of $0.85f_{co}$. In general, column strengths were slightly higher than the tests results for both HSC and NSC (only results for Column 1 in Figure 11 shown here), whereas for normal strength concrete, a stiffer response was obtained. For column 3, the decay in the post-peak branch of the load-deflection (at midheight) curve was steeper than the actual test.

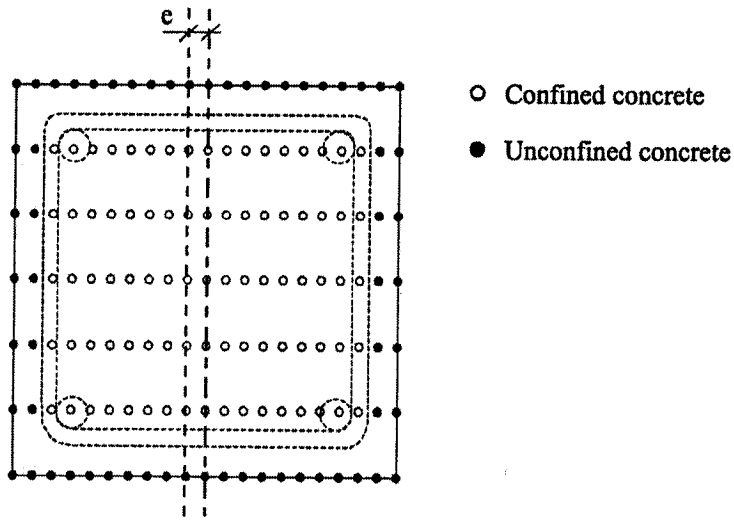

Figure 10. Beam element in ABAQUS with integration points (Cleason 1999).

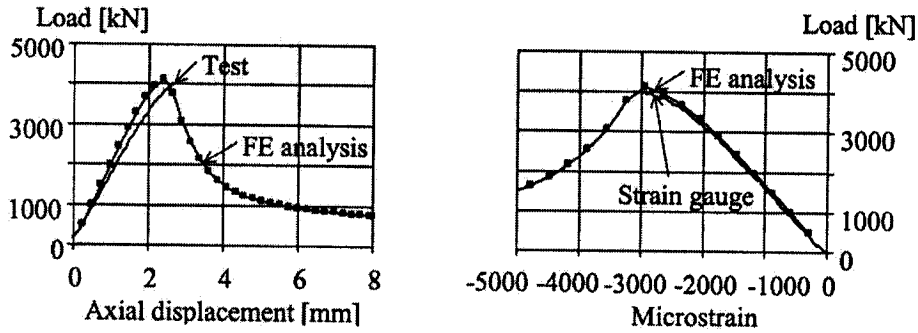

Figure 11. Comparison of results for column 1 (Cleason 1999).

In the parametric study, six variables were used: yield strengths of longitudinal steel and tie steel, tie spacing, load eccentricity, reinforcement configuration, and concrete compressive strength. It was found that the yield strength of longitudinal reinforcement had little effect on the post-peak behaviour. As the yield strength of transverse steel increased, the slope of the post-peak load-deformation curve slightly decreased. Also, a decrease in tie spacing greatly decreased the decay slope in the post-peak regime; this was more prevalent for concentric loading.

The report concluded with a comparison chart of the volumetric ratio of transverse reinforcement that was needed by a column to reach at least the same ductility as that of a NSC column having a concrete strength of 40 MPa subjected to the same loading conditions. It was shown that the volumetric ratio increased with the concrete strength and decreased with the eccentricity of the applied load.

Some observations can be made from this investigation. It was not possible to have a unique formulation for the behaviour of concrete in the finite element used without distinguishing between cover and core concrete. There were no references to the sequence of events in the loading of the columns, such as cover spalling, stress in the transverse reinforcement at peak axial stress, and failure mode. Concrete dilatation was limited to 0.5 in the material model, although it was recognized in the report that values higher than that have been published. The author used a well-known HSC model to predict the behaviour of both HSC and NSC, and proposed minimum volumetric ratios of lateral steel obtained from a parametric study whereby HSC column behaviour was compared against the results of a NSC column.

2.2.1.2 Vintzileou and Malliri (1999)

The empirical model for confined concrete in the CEB-FIP Model Code 90 (MC90) was evaluated using the experimental results of columns subjected to monotonic axial compression published in the literature. It was found that the model code predictions for strength, strain at peak stress, and strain at ultimate, did not match accurately the experimental results. Modified formulae for both strength and strains were proposed.

The formulae for confined concrete of MC90 are given below:

$$f_c^* = (1 + 2.5\alpha\omega_w) f_c \,, \quad \alpha\omega \le 0.10 \qquad \textbf{Eq. 1}$$

$$f_c^* = (1.125 + 1.25\alpha\omega_w) f_c \,, \quad \alpha\omega \ge 0.10 \qquad \textbf{Eq. 2}$$

$$\varepsilon_{co}{}^* = \left(\frac{f_c^*}{f_c}\right)^2 .\varepsilon_{co} \,, \quad \varepsilon_{co} = 0.002 \qquad \textbf{Eq. 3}$$

$$\varepsilon_{cu}{}^* = \varepsilon_{cu} + 0.1\alpha\omega_w \,, \quad \varepsilon_{cu} = 0.0035 \qquad \textbf{Eq. 4}$$

where f_c^* and f_c are the confined and unconfined concrete strengths, respectively, ε_{co}^* and ε_{cu}^*, ε_{co} and ε_{cu} are the strains at peak stress and at ultimate for confined concrete and unconfined concrete, respectively. The coefficients α and ω_w represent the confinement effectiveness and the volumetric mechanical ratio of the confining steel.

A series of column tests (approximately 300) published in the literature having concrete strengths ranging from 17 MPa to 124 MPa, confining steel yield strength ranging from 258 MPa to 1433 MPa, several steel configurations, circular and square shapes, and various sizes, were utilized to predict strengths and strains according to the formulae in Eqs. 1 to 4. The scatter in the predictions for concrete strength was more pronounced for HSC than for NSC. The MC90 model tended to overestimate f_c^* for HSC, as shown in Figure 12. The strain at peak stress, ε_{co}^*, was overly underestimated by the model, as can be seen in Figure 13. Also, a large scatter was found in the calculation of strain at ultimate (not shown.)

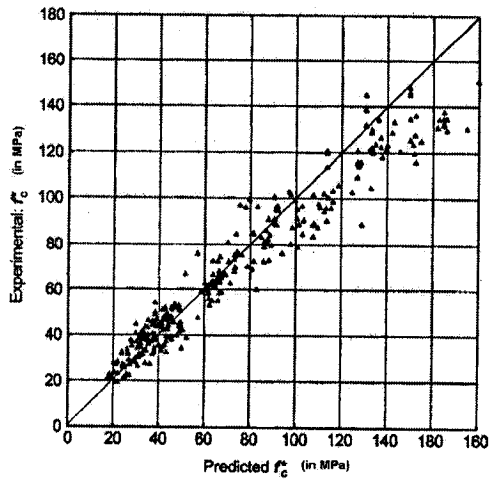

Figure 12. Experimental/predicted column strengths using MC90 model (Vintzileou and Malliri 1999).

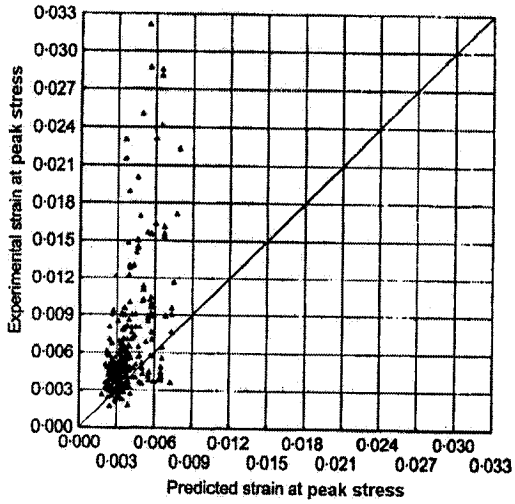

Figure 13. Experimental/predicted ε_{co}^* using MC90 model (Vintzileou and Malliri 1999)

The authors proposed new formulae that account for the variation of experimental values of the variables studied (f_c^*, ε_{co}^*, ε_{cu}^*) with respect to the concrete strength f_c and the effective confinement factor $\alpha\omega_w$, as shown below:

$$f_c^* = (1 + 1.85\alpha\omega_w)(1.15 - 0.0025 f_c) f_c \qquad \text{Eq. 5}$$

$$\varepsilon_{co}^{*} = (0.003 + 0.015\alpha\omega_w)(1.15 - 0.0025 f_c), \quad \alpha\omega_w \le 0.15 \qquad \textbf{Eq. 6}$$

$$\varepsilon_{co}^{*} = (0.0005 + 0.039\alpha\omega_w)(1.15 - 0.0025 f_c), \quad \alpha\omega_w \ge 0.15 \qquad \textbf{Eq. 7}$$

$$\varepsilon_{cu}^{*} = (0.002 + 0.085\alpha\omega_w)(1.60 - 0.007 f_c) \qquad \textbf{Eq. 8}$$

The predictions of f_c^{*} and ε_{co}^{*} using these formulae are shown in Figure 14 and Figure 15. The scatter in both graphs is smaller than that of the MC90 model. It should be noted that some tests were not included in the statistical fitting and development of the empirical Eqs 5 to 8, due to differences in methods of testing and measurement, elements size, unusual specimens, and assumptions made in the behaviour of concrete cover. It was also observed by the authors that the attainment of strength in HSC columns may occur without yielding of the confining steel, and that high yield strength confining steel and closer tie spacing might contribute to enhanced HSC behaviour.

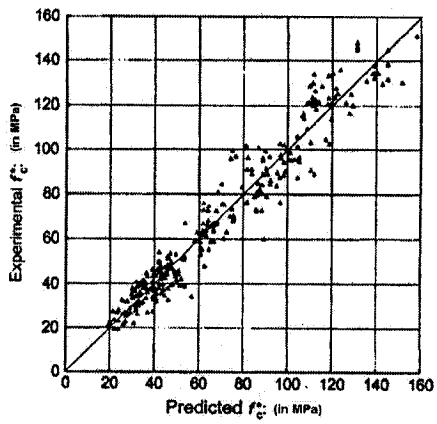

Figure 14. Experimental/predicted column strengths using proposed formulae (Vintzileou and Malliri 1999).

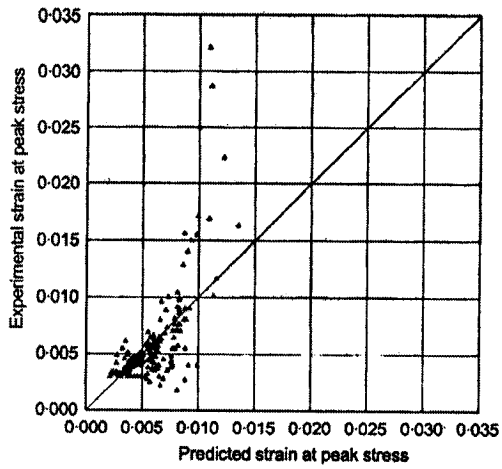

Figure 15. Experimental/predicted ε_{co}^* using proposed formulae (Vintzileou and Malliri 1999)

The authors concluded that the modified model can predict the experimental results with reasonable accuracy. There was, however, the inevitable scatter in calculating strains, due mainly to the testing procedure. It was recommended that strain-controlled tests be used, and that strains be measured in the concrete core and not on the surface. Finally, it was suggested that high yield strength steel may be beneficial in confining HSC.

The parameters in both the proposed empirical formulation and MC90 models for confined concrete are based on variables such as tie spacing, tie configuration, shape, and material properties. These variables are suitable for design calculations. However, they are not convenient to study confined concrete at the material level, and the formulae should be written in terms of strains and stresses for implementation in finite element codes.

2.2.2 FRP-Confined Columns

2.2.2.1 Purba and Mufti (1999)

A preliminary investigation on the use of CFRP jackets for confinement of concrete columns was presented. Two CFRP-confined columns and one control column were tested in uniaxial compression. The model of Mander et al.(1988) for confined concrete was modified to account for the behaviour of the FRP wraps and predictions were made on the stress-strain curves of the specimens.

Three circular columns having a diameter of 191 mm and height of 788 mm, with a target concrete strength of 30 MPa and without steel reinforcement, were tested in monotonic concentric compression. Two of the columns were reinforced with two layers of CFRP in the circumferential direction. The CFRP material had a stiffness of 230,500 MPa, and rupture stress and strain of 3480 MPa and 0.015, respectively. The thickness of the FRP ply was 0.11 mm. The axial load-axial strain and axial load–lateral strain results of the tests are shown in Figure 16. The wrapped columns exhibited larger strengths and ultimate strains than those of the control specimen, and large lateral strains due to concrete dilatation.

The results are compared to the stress-strain curve obtained from the modified Mander et al. model in Figure 17. The modified model accounts for the determination of the ultimate axial strain as a function of the rupture of the FRP jacket, by equating the stored energy in the fabric to the difference in the stored energy of the confined concrete and the unconfined concrete. The trend in the stress-strain curve was deemed acceptable.

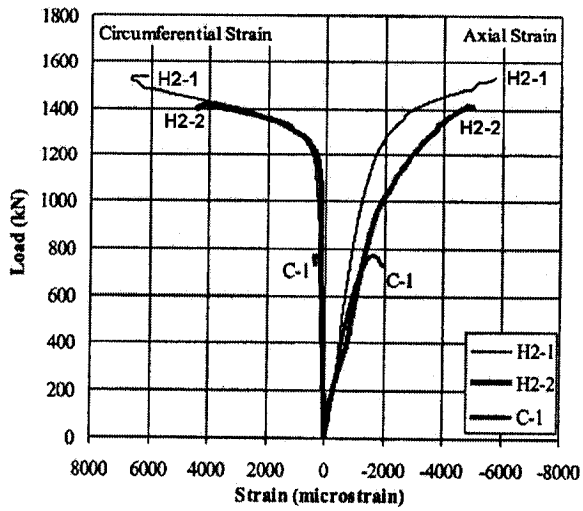

Figure 16. Experimental results of columns (Purba and Mufti 1999).

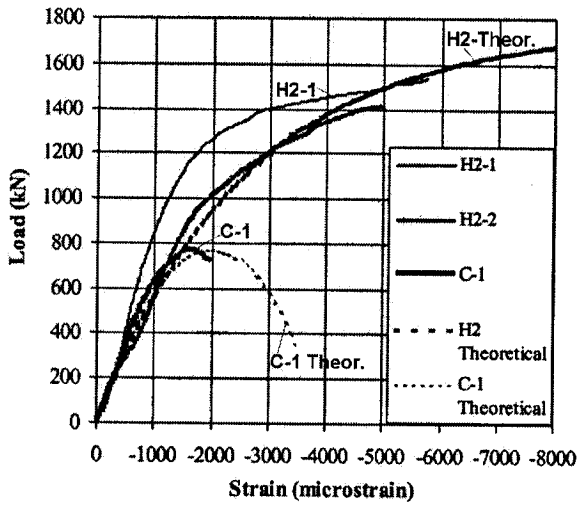

Figure 17. Comparison of experimental results with modified Mander et al. model (Purba and Mufti 1999).

In these tests the ratio of lateral strain to axial strain at ultimate was greater than 1.0 for both confined columns, corroborating once more the role of dilatation on the effectiveness of the confinement.

2.2.2.2 Demers and Neale (1999)

Sixteen columns, wrapped with carbon fibre subjected to concentric compression, were tested to evaluate their behaviour. The aim of the test program was to investigate the ability of FRP to restore the strength of damaged columns and to produce ductile behaviour. The variables studied included concrete strength, stirrups, longitudinal reinforcement, extent of corrosion, and damage.

The circular columns had a diameter of 300 mm and height of 1200 mm. The specimens were wrapped with three carbon layers in the circumferential direction. The target concrete strengths were 25 MPa and 40 MPa. For transverse steel 10M bars were utilized, and for longitudinal steel 15M or 25M bars were used. To model the effect of corrosion on the loss of steel section, the bar diameters were reduced by about 5 mm; i.e., 6.4 mm bars were used for stirrups, and 10M or 20M bars were used for longitudinal steel. The stirrup spacing was either 150 mm or 300 mm, and the longitudinal reinforcement ratio was kept to either 0.014 or 0.035. To simulate damage, half of the column specimens were first loaded without FRP confinement up to the peak strength, then unloaded and wrapped with FRP. The testing program was intended to reproduce the conditions of retrofitting of damage columns built 30 or more years ago.

Figure 18 shows the results for columns D25-1 and U25-1, where D stands for "damaged" and 'U" stands for "undamaged". All the remaining conditions were unchanged except for the stirrup spacing. The two top graphs in the figure show the capacity of the FRP to restore the damaged column to the original "undamaged" condition. The restored column gained strength and ductility. The dashed curve on the top left graph shows the initial loading of the "unconfined" column (i.e. with only steel

stirrups) up to peak strength and the corresponding unloading. The mark "X" represents FRP rupture, which occurred before buckling of the longitudinal steel. The two bottom graphs indicate the contributions to lateral pressure of the steel, the FRP fabric, and the sum of both. It can be seen that the stirrup contribution to lateral pressure was relatively small for both stirrup spacings. These results are typical for all specimens.

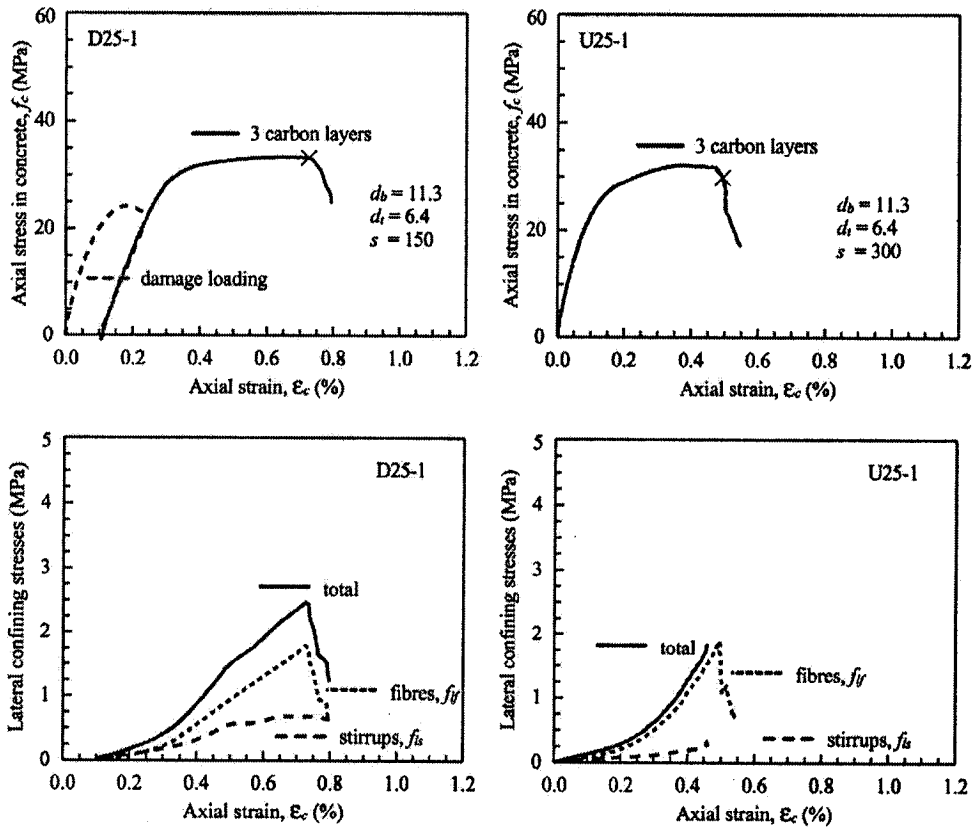

Figure 18. Experimental results of columns (Demers and Neale 1999)

It was concluded that longitudinal steel ratio, transverse steel spacing, and reduction of diameters to simulate corrosion, had no effect on the behaviour of concrete itself, for these specimens. FRP fabric wrapped on the columns resulted in strength and ductility enhancement without changing the elastic modulus of concrete.

2.2.2.3 Xiao and Wu (2000)

A total of 36 concrete cylinders were tested in uniaxial compression; 27 were confined with carbon fiber polymers. As expected, the results showed increasing strength and ductility with the number of plies utilized. A confinement modulus was defined and used to describe a simple bilinear model for the stress-strain curve.

Three values of concrete strength were used in the testing: 27.6 MPa, 37.9 MPa, and 48.2 MPa. The cylinders had a diameter of 152 mm and height of 305 mm. A total of 12 cylinders per concrete strength were tested. Three of the cylinders were tested without wrapping, and the remaining nine were wrapped in sets of three with one, two or three plies of carbon fibre. The FRP fabric had a thickness t_j of 0.381 mm per ply, with a strength f_{ju} of 1580 MPa, ultimate strain ε_{ju} of 0.015 and stiffness E_j of 105000 MPa. A confinement modulus C_j was defined as:

$$C_j = \frac{2t_j}{D} E_j \qquad \text{Eq. 9}$$

where D is the concrete cylinder diameter. From equilibrium, it was shown that the ultimate confinement strength, which is the confinement at rupture of the FRP, was:

$$f_{ru} = C_j \varepsilon_{j_u} \qquad \text{Eq. 10}$$

The axial strain ε_{cz} versus lateral strain ε_r response was approximated by a linear relationship obtained from statistical regression of the experimental results:

$$\varepsilon_r = \varepsilon_{ro}' - \nu'_c \varepsilon_{cz} \qquad \text{Eq. 11a}$$

$$\nu'_c = 7\left(\frac{f'_c}{C_j}\right)^{0.8} \qquad \text{Eq.11b}$$

where ε_{r0}', the intersection at zero axial strain, was found to be approximately -0.0005 (lateral strain negative), and ν_c' was the slope of the curve. The increase in strength due to confinement was also proposed as a linear relationship:

$$\frac{f_{cz}}{f'_c} = 1.10 + \left(4.1 - 0.75\left(\frac{f'^{\,2}_c}{C_j}\right)\right)\left(\frac{f_r}{f'_c}\right) \qquad \text{Eq. 12}$$

Two equations were proposed for the description of the stress f_{cz} versus strain ε_{cz} curve. The initial branch was derived from basic elasticity as:

$$f_{cz} = E_c\varepsilon_{cz} + 2\nu_c f_r \qquad \text{Eq. 13a}$$

$$\varepsilon_r = \frac{\nu_c}{1 + \frac{C_j}{E_c}\left(1 - \nu_c - 2\nu_c^{\,2}\right)} \qquad \text{Eq.13b}$$

$$f_r = C_j\varepsilon_r \qquad \text{Eq.13c}$$

The second branch (i.e. post-peak) was given by Eqs 11 and 12. Analytical results for Xiao and Wu tests (2000) are shown in Figure 19 (b).

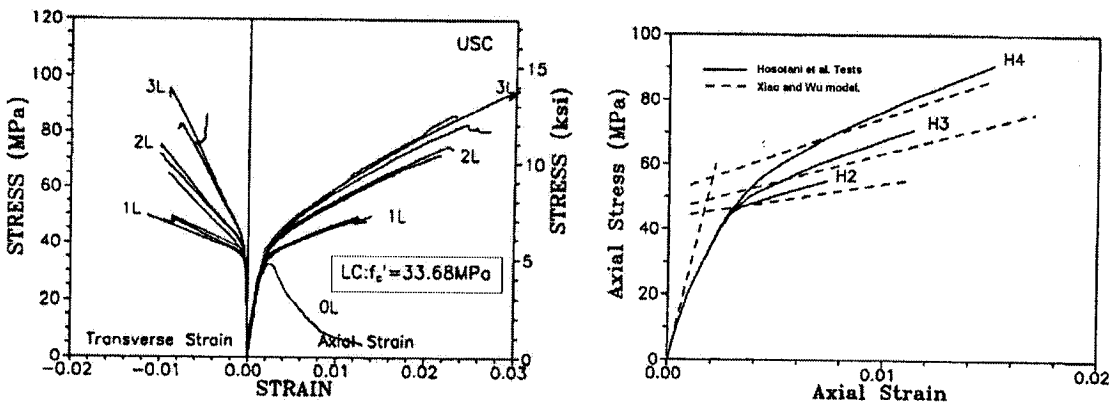

(a) (b)

Figure 19. (a) Experimental results of Xiao and Wu tests, (b) Prediction of Hosotani et al. tests. (Xiao and Wu 2000).

The experimental program showed that the behaviour of FRP-confined concrete was improved with an increase in the stiffness of the confining FRP composite. It also

showed that as concrete strength increased, concrete dilatation decreased, and that FRP wraps were not activated to the same extend in HSC specimens, as they were in lower strength concrete columns. Full activation of FRP confinement became noticeable after the cylinder reached the unconfined strength.

2.2.2.4 Spoelstra and Monti (1999)

An analytical model was developed for the determination of the behaviour of FRP-confined concrete based on formulations proposed by other researchers. The model was corroborated with experimental results. Predictions of the ultimate strength and strain utilizing the proposed model, and based on a parametric study, were also given.

Pantazopoulou and Mills (1995) reported a formula for calculating the secant stiffness E_{sec} of the stress-strain curve for concrete in compression, as a function of the area strain ε_A, which is calculated as two times the lateral strain in the cylinder:

$$E_{sec} = E_c \frac{1}{1+\beta\varepsilon_A} \qquad \textbf{Eq. 14}$$

where the parameter β was evaluated as a function of the water / cement ratio, and the volume fraction of paste. In this study β was modified and calculated as:

$$\beta = \frac{E_c / E_{sec,o} - 1}{2\varepsilon_{lo}} \qquad \textbf{Eq. 15a}$$

$$\varepsilon_{lo} = -\nu\varepsilon_{co} - (\frac{1}{2} - \nu)\alpha\varepsilon_{co}\left(\frac{\varepsilon_{lim} - \varepsilon_{co}}{\varepsilon_{lim} - \alpha\varepsilon_{co}}\right)^2 \qquad \textbf{Eq.15b}$$

where ν is the initial Poisson's ratio, $E_{sec,o}$ and ε_{co} are the secant stiffness at peak stress, and the unconfined peak strain, respectively, α=0.9-1.0, and ε_{lim}=-0.001.

An iterative procedure was implemented whereby the Mander et al. (1988) model was used to calculate the stress-strain curve for FRP-confined concrete. The equations for secant stiffness and lateral strain were modified for FRP-confined concrete. The secant stiffness and lateral strain were expressed as:

$$E_{\sec}(\varepsilon_c, f_l) = \frac{f_c}{\varepsilon_c} \qquad \text{Eq. 16a}$$

$$\varepsilon_l = \frac{E_c \varepsilon_c - f_c}{2\beta f_c} \qquad \text{Eq.16b}$$

where ε_c and f_c are the current axial strain and stress, respectively. At each iteration a new value for axial strain, ε_c, was entered, and the lateral pressure was calculated using Eq. 16 and the properties of the FRP fabric. The lateral pressure f_l was then used in the Mander et al. model to calculate f_c. The process was terminated when the fabric ruptured. Results of the proposed model are compared in Figure 20 with the tests of Mirmiran and Shahawy (1997).

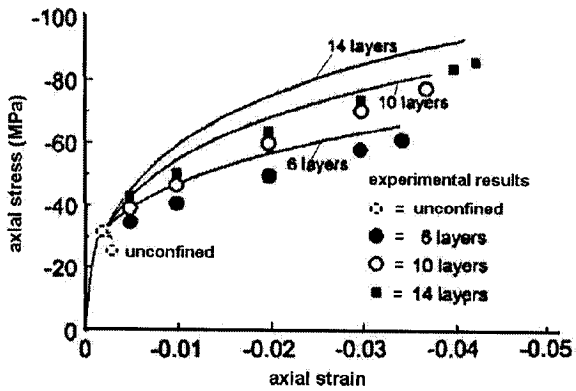

Figure 20. Comparison of results of tests by Mirmiran and Shahawy.

A parametric study was also conducted using closed-form expressions for the ultimate strain ε_{cu}, and the ultimate strength f_{cu}, obtained from the Mander et al. model, and the ultimate confining pressure f_{lu} produced by the FRP jacket. The variables

studied were the ultimate lateral confining pressure ratio (f_{lu} / f'_c), the ultimate jacket strain ε_{ju}, and the relation E_c / f'_c, where E_c is the initial stiffness of concrete. Two regression equations were obtained from the parametric study:

$$f_{cu} = f'_c(0.2+3\sqrt{f_{lu}/f'_c}) \qquad \textbf{Eq. 17a}$$

$$\varepsilon_{cu} = \varepsilon_{co}\left(2+1.25\left(\frac{E_c}{f'_c}\right)\varepsilon_{ju}\sqrt{f_{lu}/f'_c}\right) \qquad \textbf{Eq. 17b}$$

The predictions of the ultimate stress and strain using these equations are shown in Figure 21 and Figure 22; respectively.

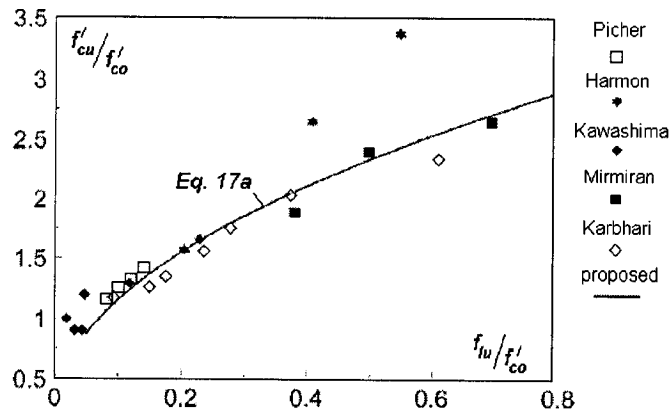

Figure 21. Prediction of ultimate strength (Spoelstra and Monti 1999).

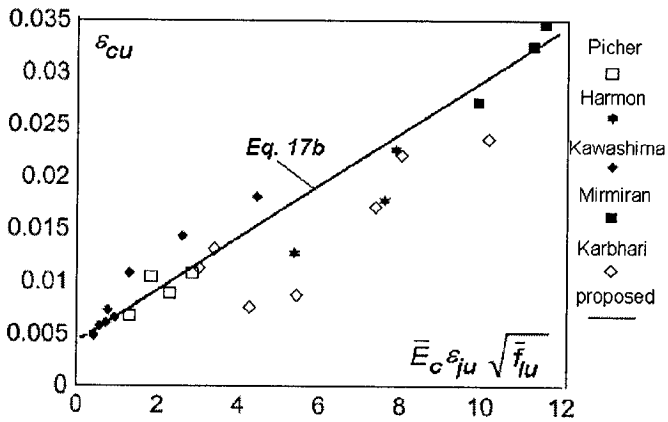

Figure 22. Prediction of ultimate strain (Spoelstra and Monti 1999).

The simple model developed showed reasonable correlation with experimental results for specimens wrapped with FRP fabric. The iteration procedure was based on the assumption of a confinement effectiveness of 100% (i.e. uniform distribution of lateral pressure). However, this assumption is not valid for rectangular sections wrapped with FRP, or for columns reinforced with steel ties or spirals in addition to FRP. The application of the model may be limited to circular columns.

2.2.2.5 Lam and Teng (2002)

The authors reviewed an extensive database of FRP-confined cylinder tests and formulations for FRP-confined concrete strength. A simple model to predict the strength of FRP-confined concrete cylinders was proposed.

The database (not shown for brevity) reported about 200 tests on concrete cylinders confined with FRP. The variables in the study comprised the unconfined concrete strength, specimen size, length-to-diameter ratio, and tensile strength of the FRP. The FRP fabrics used included: carbon, glass, aramid, S-glass sheets, E-glass and glass filaments, glass and E-glass strands, and aramid tape. The specimen database was divided into three categories based upon the method used by the researchers to obtain the tensile strength of the FRP. The first set of tests was that in which the tensile strength of the fabric was obtained from coupons subjected to direct tension. The second was that which used ring splitting tests. The last category included the results from those tests that relied on the manufacturers' specification for the tensile strength of the fabric.

The generic formula used extensively for calculating the gain in strength was written as:

$$\frac{f'_{cc}}{f'_{co}} = a + k_1 \frac{f_l}{f'_{co}} \qquad \text{Eq. 18}$$

where f'_{cc} is the strength of confined concrete, f'_{co} is the unconfined concrete strength, k_1 is the confinement effectiveness coefficient, and f_l is the lateral pressure applied to the cylinder. By fitting this equation to the database, it was found that a and k_1 vary in the ranges of 0.95 to 1.24, and 2.04 to 2.62, respectively.

The database was divided again into two categories: tests involving wrapped concrete cylinders, and tests involving FRP tubes filled with concrete. The values obtained for a and k_1 in each category of were: 1.09 and 1.05; and 2.37 and 2.43, respectively.

A simple model for design purposes was proposed for the determination of FRP-confined concrete strength. In this model, the FRP tensile strength must be obtained from direct tensile or ring splitting tests, and the confinement effectiveness should be less than 1.0, if the latter test is used.

$$\frac{f'_{cc}}{f'_{co}} = 1 + 2\frac{f_l}{f'_{co}} \qquad \text{Eq. 19}$$

It was also found that FRP-confined concrete strength did not depend on f'_{co}, size or length-to-diameter ratio.

The proposed formula for concrete strength was based on the analysis of an extensive database of experimental results. It followed the trend of several models

proposed up to date. From Eq. 19, it is seen that models such as that proposed by Richart et al. (1928), with a coefficient k_1 of 4.1, are not suitable for FRP confined concrete. The authors stated that FRP-confined concrete strength did not depend on f'_{co}. A closer look at the database reveals that only 21% of the tests had unconfined concrete strengths greater than 40 MPa. The maximum unconfined strength was 64 MPa for just one cylinder. It is not possible to deduct from the database the influence of f'_{co} due to the narrow range of concrete types studied.

2.2.2.6 Karabinis and Rousakis (2002)

A series of 18 concrete specimens reinforced with carbon FRP were tested in axial compression. The results showed an increase in axial strength and ductility with an increase in the stiffness of the CFRP. A plasticity model was applied to represent the behaviour of concrete confined with FRP.

In addition to 18 specimens reinforced with CFRP, four specimens without confinement were also tested. The concrete cylinders were divided into two sets of 11 specimens each, with concrete strengths of 38.5 MPa and 35.7 MPa, respectively. Groups of three cylinders of each set were wrapped with one, two, and three layers, respectively. The cylinders had a diameter of 200 mm and height of 320 mm. Details of the tests are given in Chapter 5. The test results for both sets of concrete cylinders wrapped with two layers of FRP are shown in Figure 23. Cylinders of concrete type A C7, C8 and C9 were wrapped with two layers of FRP, as well as cylinders C10, C11, and C12 of concrete type B. The unconfined test results (A2 of concrete type A, and B2 of concrete type B) are also shown.

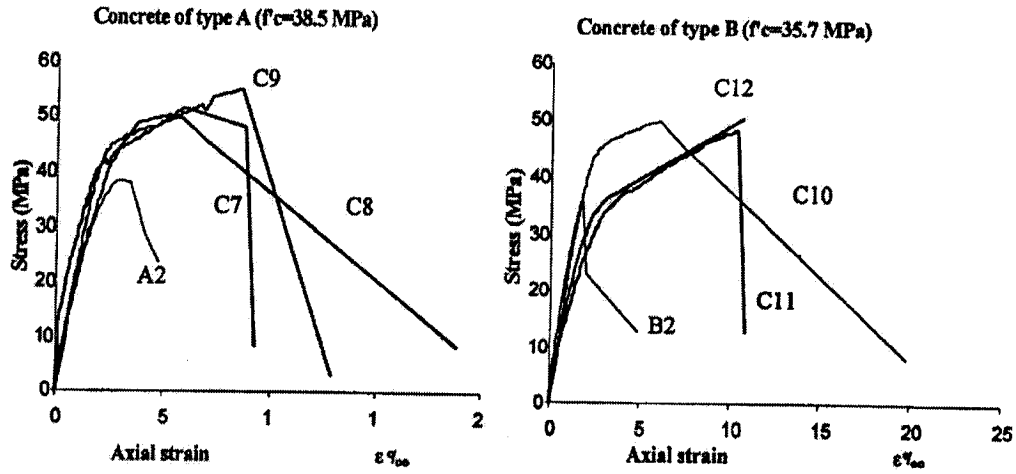

Figure 23. Response of CFRP-confined concrete specimens with 2 layers of carbon fibres (Karabinis and Rousakis 2002).

In general, the results showed an increase in ductility and strength with an increase in the number of FRP layers used. The recorded stress-strain curves of confined concrete were bilinear with two well-defined stiffnesses.

A Drucker-Prager criterion was utilized to model the hardening-softening response of FRP-confined concrete. The model included a loading function *F*, a hardening function κ, and a nonassociative flow law *G*.

$$F = \sqrt{J_{2D}} + \theta J_1 - \kappa = 0 \qquad \text{Eq. 20}$$

$$\kappa = \left(\frac{1}{\sqrt{3}} - \theta\right)\left(\frac{\tilde{\varepsilon}}{1/K_1 + \tilde{\varepsilon}/f'_u - f'_y} - R(\sigma_3)K_2\tilde{\varepsilon} + f'_y\right) \qquad \text{Eq. 21}$$

$$G = \sqrt{I_{2D}} + \beta J_1 \qquad \text{Eq. 22}$$

where J_1, J_{2D} , and I_{2D} are stress invariants, θ is a frictional parameter for pressure sensitivity, $\tilde{\varepsilon}$ is a function of the plastic strain and concrete dilatation, K_1 and K_2 are the initial plastic modulus and the slope of the unconfined post-peak curve, respectively. $R(\sigma_3)$ is a damage function that controls the steepness of the post-peak curve (i.e.

confinement effectiveness). The variable β is a function of the concrete dilatation, which is given by the slope of the (I_1^P - $\sqrt{J_2^P}$) diagram, where I_1^P and J_2^P are invariants of plastic strains. And f'_y and f'_u are the elastic limit of the concrete stress, and the ultimate strength of concrete, respectively. (Details of the model implementation were described in the paper.)

A total of 14 parameters must be calibrated (not all shown here) to reproduce the behaviour of FRP-confined concrete. The authors calibrated the parameters using a set of 8 specimens. Five of those specimens were tested by other researchers, and the remaining three were tested by the authors. For these specimens, the concrete strength varied between 32 MPa and 39 MPa, the stiffness of the FRP material was in the range of 37000 MPa to 240000 MPa, and the ultimate strength of FRP was in the range of 520 MPa to 3720 MPa.

The plasticity model responses were compared with experimental results of concrete confined by tubes, jackets and sheets. Figure 24 shows the experimental results of specimen C11 tested by the authors, along with the analytical results obtained from the proposed model and models by other researchers. It was concluded that the corroborated results produced acceptable accuracy.

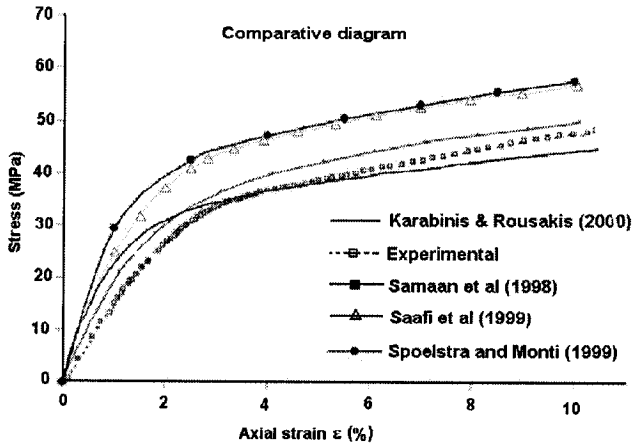

Figure 24. Analytical and experimental response of specimen C11 (Karabinis and Rousakis 2002).

Plasticity models generally involve the calibration of a large number of parameters. In this case, only 8 tests were used to calibrate 14 parameters. This model might be considered preliminary due to the limited range of concrete strengths used in its calibration. It is also known that the Drucker-Prager loading criterion does not reproduce realistic concrete dilatations.

2.2.2.7 Rochette and Labossiere (2000)

A series of tests on small-scale rectangular, square, and circular specimens wrapped with FRP composites was presented. It was found that the load capacity and ductility of the confined specimens increased with confinement.

Plain concrete specimens having unconfined strengths ranging from 35 MPa to 44 MPa were subjected to monotonic axial compression. From these specimens, 19 were wrapped with carbon FRP, and 14 with aramid FRP. Five additional specimens were tested without confining composites. Coupons of the composites were tested in uniaxial tension. Their stress-strain curves are shown in Figure 25. The dimensions of the

concrete columns are given in Figure 26. The columns were wrapped with fabric perpendicular to the longitudinal axis. However, the aramid composite had fibres in both directions whereas the carbon composite had fibres only in one direction. Two to five plies of carbon composite, and three, six, nine, and 12 plies of aramid were applied in each of the series, respectively.

Strain gauges were glued to the concrete and fabric surfaces, at a section close to mid-height. The gauges were glued on the middle of opposite faces, and on diagonally opposed corners of the section. This distribution of gauges gave an approximation of the magnitude of concrete dilatation at different points on the concrete section. The corners of the square and rectangular columns were rounded off at different values of radius to cross-section dimension ratios.

Some of the stress-strain results for the aramid fabric are shown in Figure 27. It was observed that an increase in the number of plies produced an increase in both the load capacity and ductility. In this figure, ρ is the volumetric ratio of the composite. A similar trend was observed for the carbon fibre tests. The effect of the rounded corner is shown in Figure 28, where the D/R ratio is the section dimension (D) to the corner radius (R). It is seen that the higher this value became, the less effective was the confinement, even for columns with the same dimensions and number of plies of the same composite (see Figure 28).

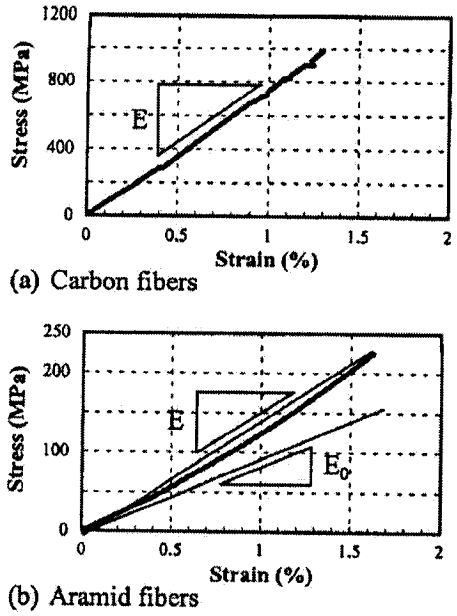

Figure 25. Tensile stress-strain curves for (a) carbon fibre, and (b) aramid fibre (Rochette and Labossiere 2000).

Concrete expansion in square or rectangular columns subjected to axial load is not distributed homogeneously as in circular columns; this was also verified for composite-wrapped columns. The gauge readings on the concrete on diagonally opposite section corners yielded smaller strains than those gauges located on the face centres, as shown in Figure 29, indicating lower confinement in the centre of the faces than that at the corners. Finally, the failure of all of the specimens was due to the rupture of the fibres, initiating at the corners at about the column midheight, and expanding along the column length. Fibre punching occurred before the ultimate strain in CFRP columns, and twisting and warping of the aramid FRP produced a more extended and diffuse failure zone in the aramid FRP wrapped columns.

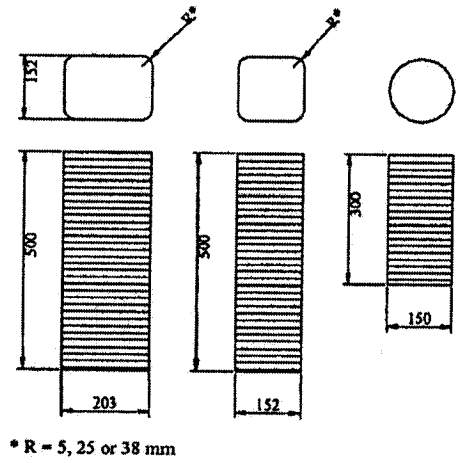

Figure 26. Column dimensions (Rochette and Labossiere 2000).

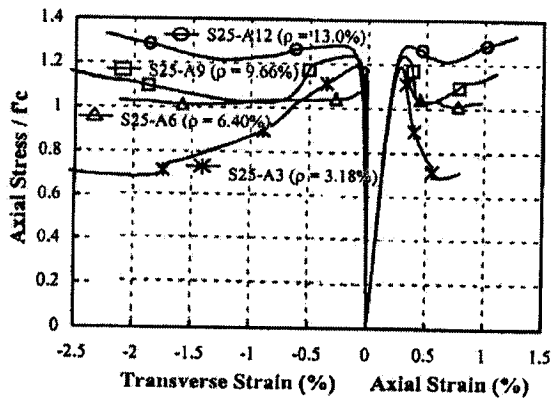

Figure 27. Stress-strain curves for aramid-wrapped square columns (R = 25 mm) (Rochette and Labossiere 2000).

These set of experiments provided additional data on the behaviour of confined concrete. Although there were some differences in the stress-strain curves for both types of composites, three typical behaviours were described by the author: a response with a well-defined peak stress followed by softening, an almost elasto-plastic behaviour with a defined plateau, and a continuously increasing stress-strain curve with two well-defined stiffnesses.

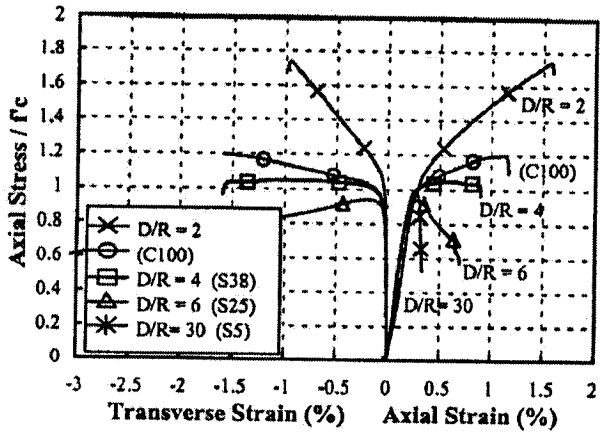

Figure 28. Effect of round corner in the response, square CFRP columns wrapped with 3 plies (Rochette and Labossiere 2000).

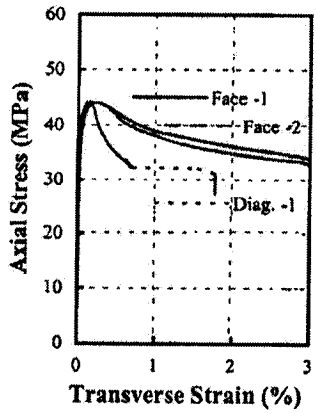

Figure 29. Typical lateral strain measured at corners and faces (Rochette and Labossiere 2000).

2.3 Computational Models

2.3.1 Failure Surfaces for Concrete

2.3.1.1 Sfer, Carol, Gettu, and Etse (2002)

Experimental tests of concrete cylinders with strength of 30 MPa, subjected to confining pressures of up to $2f'_c$, were conducted. The tests parameters included the longitudinal and transversal strains, the axial stress, and the mode of failure. A

transition from brittle to ductile failure mode with increasing confinement agreed well with published results. The theory of elastoplasticity was used to interpret the results.

Plain concrete cylinders of NSC (30 MPa) were tested in a triaxial cell at confining pressures of 0, 1.5, 4.5, 9.0, 30.0, and 60 MPa. Two cylinders were tested at each confining level. The lateral pressure was applied first using an oil pump, and then the axial stress was applied in a strain-controlled mode. Figure 30 and Figure 31(a) show the axial stress-axial strain, and axial stress-lateral strain curves obtained from the experiments, respectively.

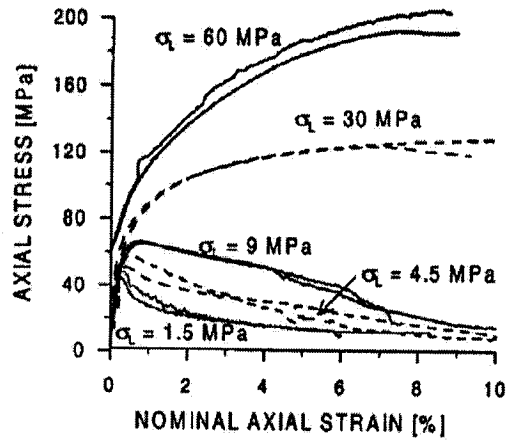

Figure 30. Axial stress-axial strain curves (Sfer et al. 2002).

At low confinement (up to 4.5 MPa of lateral pressure), the peak stress was followed by a softened response. The post-peak curve decay was steep for low confinement and flattened with increasing lateral pressure. After testing, the cylinders exhibited distributed microcracks on the surface.

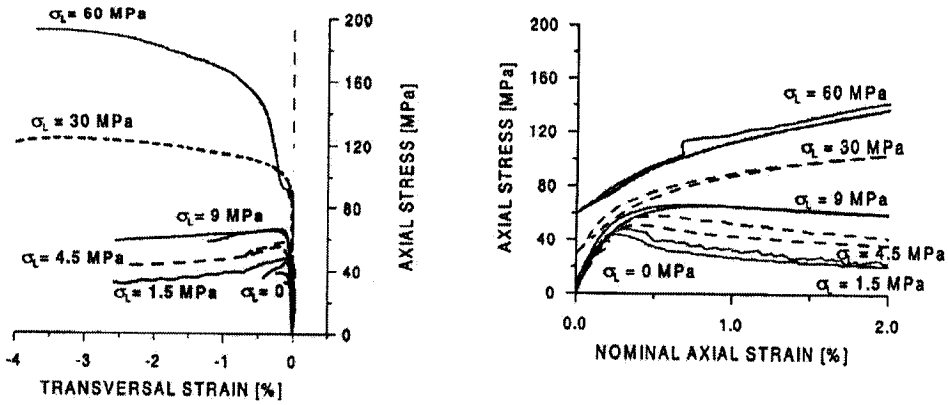

(a) (b)

Figure 31. (a) Axial stress-lateral strain curves, (b) Close-up of axial stress-axial strain curves (Sfer et al. 2002).

For high confining pressures (≥ 9.0 MPa), the axial load capacity and the ductility of the cylinders increased considerably. The axial strain-axial stress curves tended to form a plateau without a well-defined peak stress. Photographs of the fractured cylinders after testing showed a maximum of three macrocracks on the surface. The cylinders broke into two or three pieces. The tests were terminated at axial strains of 10%, or when the load decreased to 10% of the peak load.

In very-high confined tests (30 and 60 MPa of lateral pressure), the initial ascending stiffness decreased with an increase in lateral pressure (See Figure 31b). Pore collapse and extensive microcracking of the aggregates were observed. The volumetric strain versus the axial stress measured is plotted in Figure 32, where positive volumetric strains represent volume contraction and negative values of volumetric strains represent expansion. It is seen in the figure that just below the peak stress, a

reversal trend from contraction to expansion occurred at low confinements. The same occurred at high confinements at earlier stresses.

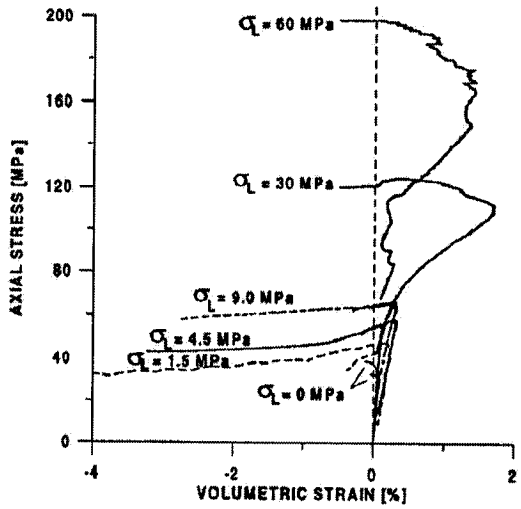

Figure 32. Axial stress-volumetric strain curves (Sfer et al. 2002).

The authors explained their results in the light of the theory of elastoplasticity. The decrease in the initial stiffness after the application of high confining pressure was explained by adding a "cap" to the loading surface, as shown in Figure 33 in the stress space (σ_1, σ_2, σ_3). An increase in the lateral pressure "takes the stress state to the cap of the loading surface", and plastic strains develop immediately after the application of lateral pressure. Also, the test results were plotted in the I_1-$\sqrt{J_2}$ coordinate system as shown in Figure 34, where I_1 and J_2 are invariants of the stress tensor. The loading path for each cylinder was described by a horizontal line on the hydrostatic axis (I_1), representing the application of the confining pressure, followed by an inclined line up to the point representing the peak stress on the loading surface. The line joining the peak values is the experimental failure surface. Along the inclined loading paths are lines that represent the flow of plastic strains developed throughout each test. The horizontal

projection of the plastic strains represents the changes in the volumetric expansion (left of the stress path), or contraction (right). The cylinders tended to expand close to the peak stresses. Also noted was that the plastic strains at peak stresses were not perpendicular to the loading surface, confirming the nonassociative nature of the plastic flow in confined concrete.

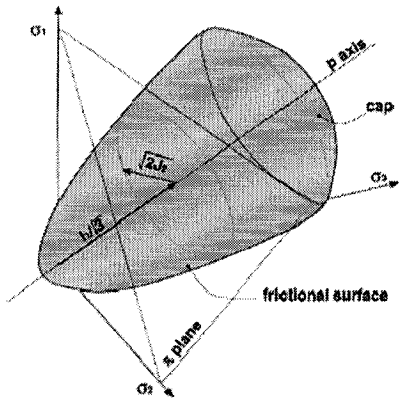

Figure 33. Loading surface with cap (Sfer et al. 2002)

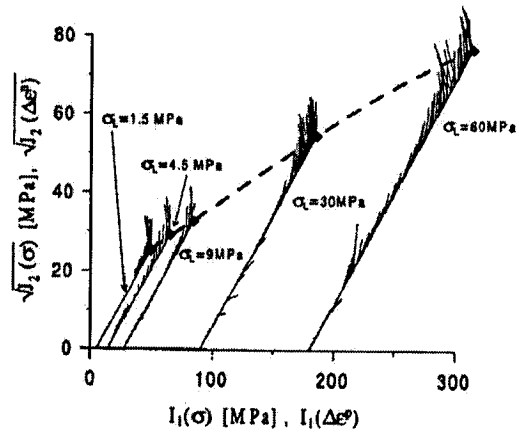

Figure 34. Failure surface and plastic strains in I1, √J2 space (Sfer et al. 2002).

2.3.1.2 Pivonka, Lackner, and Mang (2000)

Two plasticity models were modified to account for the confinement and ductility of concrete subjected to triaxial loading. The first model was the Extended Leon model, proposed by Etse (1996). The second was a multisurface model comprised of three Rankine surfaces for concrete in tension and a Drucker-Prager model for concrete in compression. The characteristics of confinement were developed as a function of the major principal stress. The experimental results of Hurlbut (1985) and Smith (1989) were used to corroborate both models.

Detailed descriptions of the models are not given here for brevity. However, a general description of the two models is given below.

The Extended Leon Model (ELM) comprised two surfaces, one for loading, and one for softening. The loading surface is a function of the hydrostatic pressure p, the Lode angle θ, two internal stress variables q_h^* and q_s^*, the elastic concrete limit f_{cy}, the tensile strength f_{tu}, and the deviatoric radius r.

$$f\left(p,r,\theta,q_h^*,q_s^*\right)=0 \qquad \textbf{Eq. 23a}$$

$$q_h^* = f_{cy} - q_h \qquad \textbf{Eq. 23b}$$

$$q_s^* = f_{tu} - q_s \qquad \textbf{Eq. 23c}$$

where q_h and q_s are stress-like internal variables defined for the hardening and softening ranges, respectively. The shape of the deviatoric surface for the loading part is elliptical and is a function of the Lode angle θ and the eccentricity parameter $e = r_t / r_c$. Figure 35 shows a sketch of the ELM loading surface in the meridian and deviatoric planes. The softening behaviour was characterized by the initiation of macro-cracks

and the decreasing of tensile strength (i.e. similar to tension softening). The ELM used a non-associative flow rule to calculate the plastic strains. The flow rule was similar to the yield function modified to calculate the volumetric strains without affecting the deviatoric components.

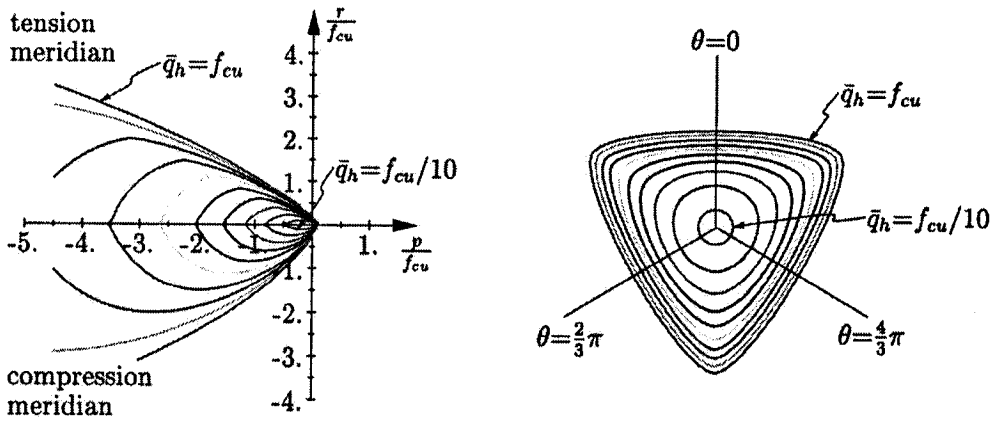

Figure 35. Extended Leon model, hardening law (Pivonka et al. 2000).

The loading-softening process was assumed isotropic. In the loading process, plastic strains did not develop before reaching the loading surface corresponding to the elastic limit f_{cy}. Beyond this limit and up to the maximum strength f_{cu}, a nonlinear isotropic hardening law was defined as a function of the plastic strains and a ductility parameter which is a function of the level of confinement (p / f_{cu}). To calculate the ductility parameter, two quadratic equations with three parameters each were formulated for low and high confinement, respectively. A similar law for softening was also described in the paper. Calibration of the ELM followed a fracture energy approach, whereby the ductility parameter in the softening law was calculated as a function of the fracture energy release for Mode I (tensile test), and Mode II (mixed mode of cracking). The fracture energy for Mode II was a function of the hydrostatic pressure p in triaxial compression.

The second model was a combination of three Rankine-type surfaces for concrete in tension and a Drucker-Prager (DP) type model for concrete in compression. The two parameters of the DP model were obtained from uniaxial and biaxial strength tests. Details of the hardening and softening laws for both types of models (Rankine and DP) are given in the article. To account for confinement, the peak stress f_{cu} was determined as a function of the major principal stress σ_1 ($\sigma_1 > \sigma_2 > \sigma_3$). A regression equation obtained from the experimental results of Hurlbut (1985) and Smith (1989) showed a linear variation of the peak stress with the lateral pressure ratio ($\sigma_1 / f_{cu,o}$), where $f_{cu,o}$ is the unconfined concrete strength. Similar relationships were obtained for the residual stress, and the peak strain in the softening regime (i.e. post-peak residual stress). The ultimate DP surface for f_{cu} was then rewritten as a function of the major principal stress σ_1. It was found from the tests that a transition point from brittle to ductile behaviour (i.e. from softening to continuous hardening) occurred at a lateral pressure ratio of about 0.28. An additional DP surface was proposed to calculate the residual stress based on the constraint of the transition point.

The experimental tests of Hurlbut and Smith were compared with both models. The results are shown in Figures 36 to 38. Figure 36 shows the results obtained from the ELM, and Figures 37 and 38 show the results obtained from the Rankine-DP model for both associative (Figure 37) and non-associative (Figure 38) flow rules.

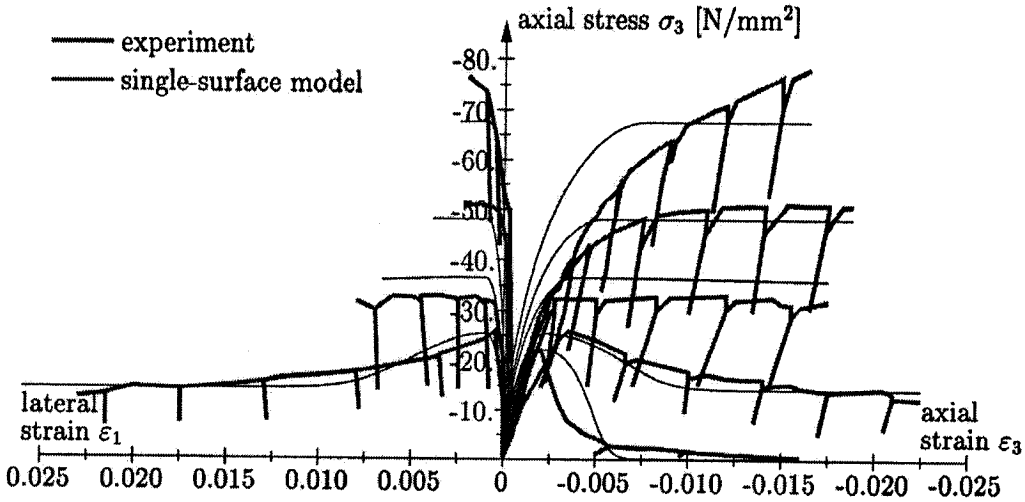

Figure 36. Comparison of Hurlbut and Smith tests with ELM (Pivonka et al. 2000).

It was concluded that there was good agreement with the experimental results when using both models. The lateral deformation was modelled well only for medium levels of confinement using the Rankine-DP model. A good agreement was obtained for lateral deformations at all levels of confinement when using the ELM.

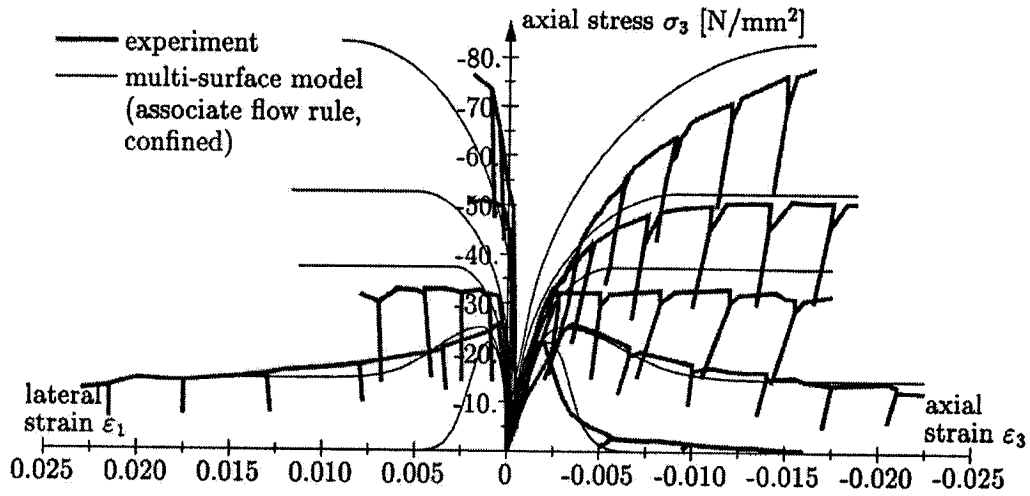

Figure 37. Comparison of Hurlbut and Smith tests with Rankine-DP results (associative rule) (Pivonka et al. 2000).

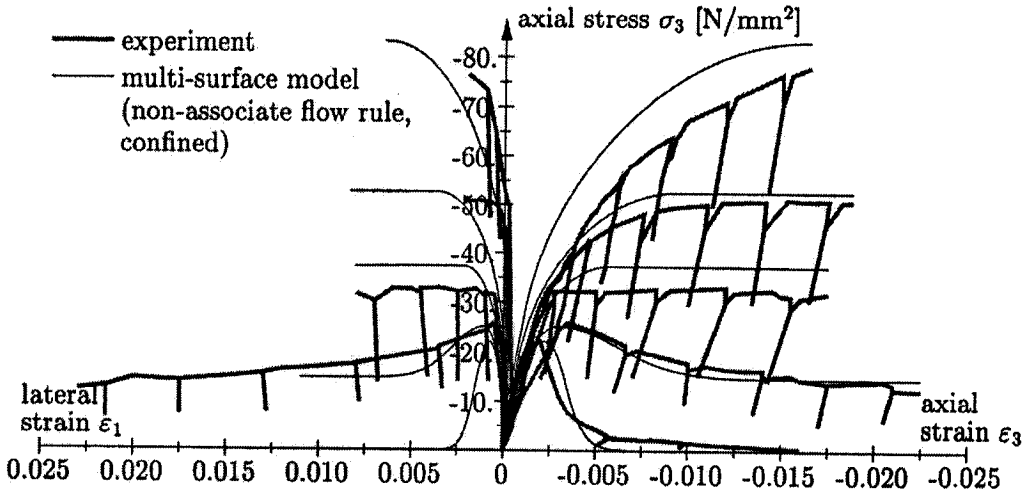

Figure 38. Comparison of Hurlbut and Smith tests with Rankine-DP results (non-associative rule) (Pivonka et al. 2000).

The ELM required the calibration of 13 parameters, and the Rankine-DP required 6. The ELM model produced stiffer axial stress-axial strain curves than the experimental results, and a lower prediction of strength. It was suggested by the authors that the yield surface for the Rankine-DP model needed modifications to account for proper predictions of lateral deformations. The applicability of the model is limited to NSC, as the parameters were calibrated from normal strength concrete tests.

2.3.1.3 Sankarasubramanian and Rajasekaran (1996)

The equivalent uniaxial stress-uniaxial strain formulation proposed by Darwin and Pecknold was implemented in a model for the analysis of axisymmetric and plane reinforced concrete structures. The model utilized a modified version of the Willam and Warnke (1975) failure surface, and the stress-strain curve proposed by Alexander (1965).

An incremental stress-strain formulation based on the uniaxial stress-uniaxial strain model that allowed for orthotropic description of concrete behaviour was proposed. The stress-strain curve of Alexander (1965) was used to express the uniaxial stress in terms of the equivalent strain.

$$\sigma_i = \sigma_{ci}\left[\frac{a_o\left(\frac{\varepsilon_{ui}}{\varepsilon_{ci}}\right)}{\left\{\left(\frac{\varepsilon_{ui}}{\varepsilon_{ci}}\right)^2 + 2b_o\left(\frac{\varepsilon_{ui}}{\varepsilon_{ci}}\right) + \varepsilon_o{}^2\right\}} - h\left(\frac{\varepsilon_{ui}}{\varepsilon_{ci}}\right)\right] \qquad \textbf{Eq. 24}$$

where σ_i and ε_{ui} are the uniaxial stress and strain, σ_{ci} and ε_{ci} are the peak stress and peak uniaxial strain, respectively. The other parameters are constants. Similar curves were used for the shear stress-shear strain, and for concrete in tension. The ultimate stress surface was a modified version of the surface proposed by Willam and Warnke (1975). The shape of this surface in the deviatoric plane was represented by the equation:

$$r = r_c e^{-\rho\theta} \qquad \textbf{Eq. 25a}$$

$$\rho = \left(3/\pi\right)\ln\left(r_c/r_t\right) \qquad \textbf{Eq. 25b}$$

where θ is the polar angle in the deviatoric plane, and r_c and r_t are the radii of the compressive and tensile meridians, respectively. The values for r_c and r_t were obtained from a neural network analysis using back propagation. The network was trained with experimental values of hydrostatic stress σ_m, r_c and r_t. The network was then used to obtain analytical values for r_c and r_t from an input value for σ_m, to generate the failure surface. The model of Elwi and Murray (1979) for concrete dilatation was adopted. The results of a cylinder subjected to a constant lateral pressure of 55 MPa and axial

compression, tested by Palaniswamy and Shah (1974), is shown in Figure 39. The results were also compared with those obtained using Elwi and Murray model.

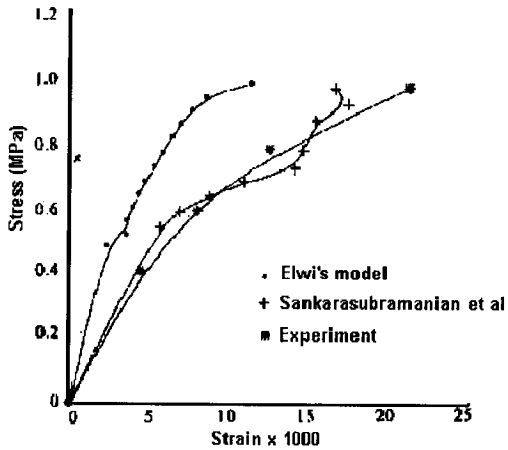

Figure 39. Stress-strain curve for concrete cylinder under a lateral pressure of 55 MPa (Sankarasubramanian et al. 1996).

The authors reported comparisons of their model to different types of tests, including: uniaxial compression of cylinders, panels in biaxial compression, a deep beam, panels, and a nuclear vessel (not included here). In general, the analytical model was unable to reach the peak stress for the uniaxial and biaxial tests reported. It showed stiffer stress-strain curves than the experimental specimens. Also, the analytical models of the tests failed at very low deflection (or strain). No description was given of the neural network, and compression softening was not captured well.

2.3.1.4 Barros (2001)

A stress-strain model based on the theory of elastoplasticity was developed for concrete in compression. The yield surfaces of Drucker-Prager and Ottosen were used to determine the three-dimensional behaviour of concrete. The unconfined stress-strain model proposed in the model code MC90 (CEB-FIP) was used to model the hardening and softening responses of concrete. Analyses of concrete cylinders tested by Iyengar,

Desaiy, and Reddy (1970) showed reasonable agreement with the experimental results.

The proposed elasto-plastic model was derived from the additive postulate, which was given in terms of infinitesimal deformations. Thus

$$d\varepsilon = d\varepsilon^e + d\varepsilon^p \qquad \textbf{Eq. 26}$$

where the total strain increment $d\varepsilon$ is the sum of the elastic and plastic strains, $d\varepsilon^e$ and $d\varepsilon^p$, respectively. Following a series of transformations, the constitutive relationship between stress $d\sigma$ and strain $d\varepsilon$ was given by:

$$d\sigma = D_{ep} d\varepsilon \qquad \textbf{Eq. 27}$$

where D_{ep} is the elastoplastic material matrix:

$$D_{ep} = D - \frac{Dba^T D}{a^T Db + H} \qquad \textbf{Eq. 28}$$

Here, D is the elastic material matrix, the coefficients a^T (transpose of a) and b are the gradients of the yield and potential surfaces F and G, and H is a hardening parameter.

$$a = \frac{dF}{d\sigma} \qquad \textbf{Eq. 29a}$$

$$b = \frac{dG}{d\sigma} \qquad \textbf{Eq. 29b}$$

The yield and potential surfaces F and G were different if a non-associative flow rule was used to calculate plastic strains. The hardening parameter H is a function of the yield surface, which could be either the Drucker-Prager surface or the Ottosen surface.

The model code MC90 equation for uniaxial stress-strain was used to simulate the hardening and softening behaviour. It was described by the following equation:

$$\sigma_c = -\left[\frac{\left(\frac{E_{ci}.\varepsilon_c}{E_{c1}.\varepsilon_{c1}} - \left(\frac{\varepsilon_c}{\varepsilon_{c1}}\right)^2\right)}{\left(1+\left(\frac{E_{ci}}{E_{c1}}-2\right)\frac{\varepsilon_c}{\varepsilon_{c1}}\right)}\right] f_c \qquad \text{Eq. 30}$$

where E_{ci} is the initial tangential modulus, ε_{c1}=-0.0022, E_{c1} is the secant stiffness at peak stress f_c, and ε_c is the total strain.

The confinement effect was modelled by multiplying the slope of the softening portion of the strain-stress curve, represented by the tangential stiffness E^T, by a factor R (Eq. 31) that was a function of the intermediate principal stress σ_2 (χ taken as 0.867):

$$R = e^{\chi\sigma_2} \qquad \text{Eq. 31}$$

The model was used to analyze concrete cylinders of 150 mm diameter by 300 mm height, with concrete strengths of 25 MPa to 34 MPa, and reinforced with spirals, tested by Iyengar et al. The results for cylinder C2 are shown in Figure 40. The figure shows the experimental axial load-axial strain curve along with the predictions using the MC90 model, and the model proposed by Barros. The yield surface used was that of Drucker-Prager, with an associative flow law. It was concluded that the proposed model approximated the experimental strengths of the cylinders, as well as the softening behaviour.

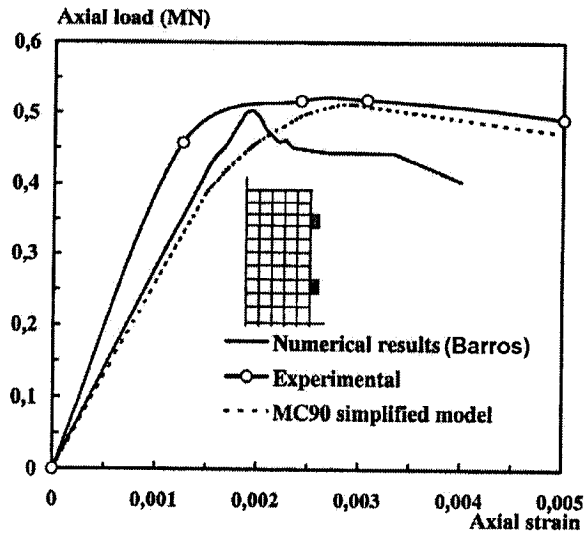

Figure 40. Axial load-axial strain for cylinder C2 tested by Iyengar et al. (Barros 2001)

As can be seen from the results, the numerical model predicts the strength of the cylinders with reasonable accuracy, but the pre- and post-peak behaviour poorly resembled that of the experiments. The author stated that a non-associative flow rule should be used to represent the plastic behaviour of concrete. However, an associative flow rule was used for numerical convenience. In this case, the author used the Drucker-Prager model for both the yield and potential surfaces. The conical surface of this model produced constant increments of plastic volumetric strains, which did not correspond well to the observed behaviour of concrete dilatation. It was also mentioned that the elasto-plastic matrix, D_{ep}, produced an unsymmetrical system of equations when the tangential stiffness method was used along with non-associative flow rules. This further complicates the numerical evaluation of the analytical response.

2.3.1.5 Mirmiran, Kenneth, and Yuan (2000)

An elasto-plastic Drucker-Prager type model was utilized in the analysis of FRP-confined concrete. Uniaxial compression tests on circular and square specimens wrapped with 6, 10, and 14 plies of E-glass fiber were used to corroborate the analytical model. The analytical axial stress-axial strain results compared well with the experimental results. However, concrete dilatancy of FRP-columns was not captured well.

The Drucker-Prager type formulation had the following form:

$$\sigma_e = 3\beta\sigma_m + \left[\frac{1}{2}\{s\}^T[M]\{s\}\right]^{1/2} \qquad \textbf{Eq. 32}$$

where M is a function of a 3 x 3 unit matrix. The material constant β, and the yield parameter σ_y were expressed as:

$$\beta = \frac{2\sin\phi}{\sqrt{3}(3-\sin\phi)} \qquad \textbf{Eq. 33a}$$

$$\sigma_y = \frac{6c\sin\phi}{\sqrt{3}(3-\sin\phi)} \qquad \textbf{Eq. 33b}$$

where ϕ and c are the internal angle of friction, and the cohesion, respectively. The hydrostatic and deviatoric stresses are σ_m and s, respectively. The flow rule was a function of an angle of dilatancy. If this angle was smaller than the friction angle ϕ, the flow rule was nonassociative, and it produced smaller volumetric expansion than an associative rule. If the angle was null, there was no volumetric expansion.

The parameters for the model, ϕ and c, were determined as functions of the uniaxial concrete strength and the confinement effectiveness factor, f'_c and k_1, respectively. The

confinement factor was calculated using the formulae proposed by one of the following models: Richart et al (1929), Mander et al. (1988), Samaan et al. (1998), or Rochette et al. (1996). The user of the finite element model may select the angle of dilatancy (i.e. the type of flow rule) to calculate the plastic strains.

The authors tested 30 cylinders with a diameter of 153 mm and height of 305 mm, and 12 square prisms with a 152 x 152 mm cross section and 305 mm height. The specimens were wrapped with 6, 10, and 14 E-glass plies. The average stiffness of the FRP fabric was in the range of 37000 to 41000 MPa, and the ultimate stress was in the range of 520 to 640 MPa. Axial stress-axial strain and axial stress-lateral strain curves for two of the tests are shown in Figure 41, along with the analytical response using the proposed model with all the alternatives for calculating the factor k_1 given above, and using a null dilatancy angle

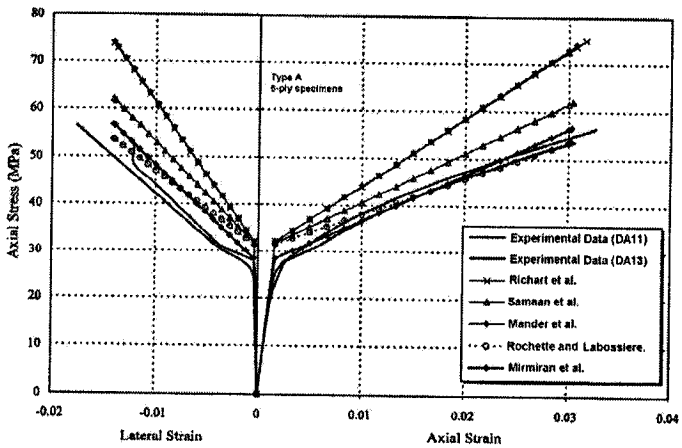

Figure 41. Analytical and experimental results of Mirmiran et al. tests (Mirmiran et al 2000).

The best analytical results were obtained when using the model of Rochette et al.(1996) in the calculation of the parameters ϕ and c. The volumetric and dilatation responses with respect to the normalized axial stress (f_c/f'_c) are given in Figure 42. As

can be seen, the Drucker-Prager type model was not able to reproduce the volumetric strain and dilatation of the FRP-confined specimens.

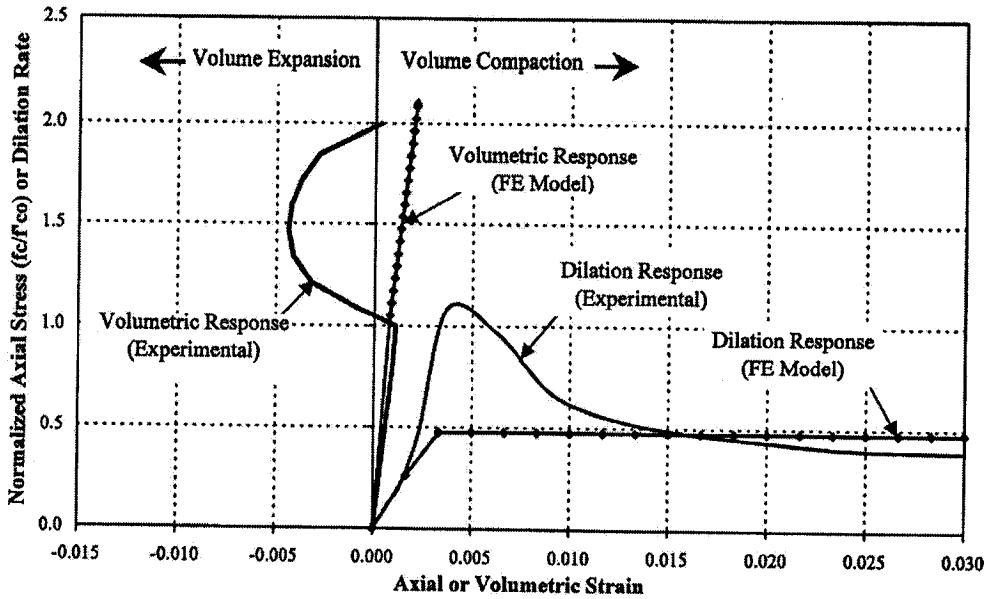

Figure 42. Volumetric strain and concrete dilatation (Mirmiran et al 2000)

Figure 43 shows the comparison of analytical and the experimental results for some of the rectangular tests. It can be seen that neither the compression softening nor the concrete strength were captured well by the finite element model.

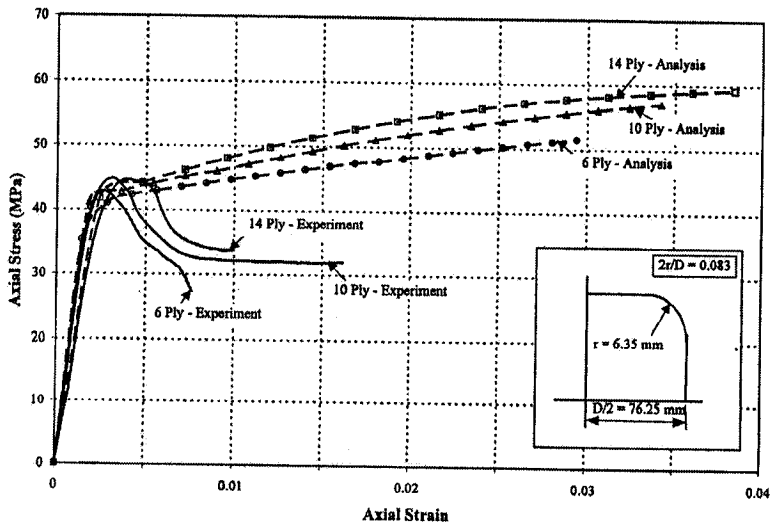

Figure 43. Analytical and experimental results of Mirmiran et al. square Columns (Mirmiran et al 2000)

The Drucker-Prager type model is not suitable for modeling the response of FRP-confined columns. The volumetric compaction increases linearly with the axial stress due to the conical shape of the model along the surface meridians in the I_1-$\sqrt{J_2}$ space; moreover, this is true even when nonassociative flow rules are used, as demonstrated by the analytical results. The dilatation behaviour followed an elasto-plastic curve that remained at a constant value close to 0.5 (incompressible limit) for large axial strains; which did not reflect the decreasing dilatancy of the FRP-confined concrete columns tested. The assumption of a null angle of dilatancy to match the axial stress-axial strain curves resulted in an unrealistic prediction of the volumetric changes seen in the tests just after the attainment of the unconfined concrete strength. Finally, the post-peak regime was grossly overestimated for the square columns.

2.3.2 Confinement Models

2.3.2.1 Yip (1998)

Several of the published strain-stress relations for concrete in uniaxial compression were reviewed. It was found that they evolved from a general equation proposed by Yip. A series of tests of plain concrete specimens having different strengths were conducted to determine the suitability of each of the studied formulations to reproduce the ascending part of the stress-strain curve.

It was stated that concrete behaviour is elastic up to a 30% of its unconfined strength f'_c, and nonlinear behaviour commences just after reaching a stress of $0.3f'_c$. The stress-strain curve bends quickly and flattens at peak stress. The understanding of the internal phenomena in concrete materials had led to formulations of stress-strain curves that depended on the loading path, and involved several empirical parameters.

The author anticipated that a single stress-strain equation would not consider all the behavioural aspects of concrete.

The general formula for the stress-strain curve for concrete in compression developed by the author is shown below:

$$\frac{f_c}{f'_c} = \frac{\varepsilon_c}{\varepsilon_{co}} . e^{\left[1-\frac{\varepsilon_c}{\varepsilon_{co}}\right]} \qquad \textbf{Eq. 34}$$

where ε_{co} is the peak strain, f_c is the stress at a strain ε_c, and f'_c is the peak stress. Eq. 34 can be transformed using exponential series to:

$$f_c = \frac{2.7182 . E_{\sec} . \varepsilon_c}{1 + \left(\frac{\varepsilon_c}{\varepsilon_{co}}\right) + \frac{1}{2}\left(\frac{\varepsilon_c}{\varepsilon_{co}}\right)^2 + \frac{1}{6}\left(\frac{\varepsilon_c}{\varepsilon_{co}}\right)^3} \qquad \textbf{Eq. 35}$$

where E_{sec} is the secant stiffness at peak stress.

Equation 35 was compared with several of the stress-strain curves proposed by other researchers, given below:

$$f_c = \frac{2 . E_{\sec} . \varepsilon_c}{1 + \left(\frac{\varepsilon_c}{\varepsilon_{co}}\right)^2} \qquad \textbf{Eq. 36}$$

$$f_c = \frac{E_o . \varepsilon_c}{1 + \left(\frac{E_o}{E_{\sec}} - 2\right)\left(\frac{\varepsilon_c}{\varepsilon_{co}}\right) + \left(\frac{\varepsilon_c}{\varepsilon_{co}}\right)^2} \qquad \textbf{Eq. 37}$$

$$f_c = \frac{3 . E_{\sec} . \varepsilon_c}{2 + \left(\frac{\varepsilon_c}{\varepsilon_{co}}\right)^3} \qquad \textbf{Eq. 38}$$

$$f_c = \frac{n . E_{\sec} . \varepsilon_c}{n - 1 + \left(\frac{\varepsilon_c}{\varepsilon_{co}}\right)^n} \qquad \textbf{Eq. 39}$$

where E_o is the initial tangent stiffness, and n is calculated from:

$$\frac{E_o}{E_{sec}} = \frac{n}{n-1} \qquad \text{Eq. 40}$$

Equations 36 to 39 were the models developed by: Desayi and Krishnan, Todeschini et al., Tulin and Gerstle, and Popovics, respectively. (details are given in the paper). Depending on the values of E_o and n, Eqs.36 to 39 resembled Eq.35. Also, Eqs. 36 and 38 yielded softer ascending branches than that of Eq.34. It was also noted that the smaller the coefficient accompanying the factor $E_{sec}.\varepsilon_c$, the better was the fit of the ascending stress-strain curve for high strength concrete, as it approached a straight line.

An experimental program that comprised 9 sets of concrete mixes having strengths ranging from 27 MPa to 49 MPa was conducted. The specimens with section dimensions of 100 x 100 mm and height of 250 mm were tested in stress-controlled monotonic axial compression. The experimental pre-peak stress-strain curves were compared to the analytical Eqs. 34, 35, and 38. It was found that Eq.34 fitted the curves of concrete specimens with strengths less than or equal to 30 MPa, Eq.35 fitted the results of specimens with strengths between 35 MPa and 40 MPa, and Eq.38 fitted those of stronger concrete. It was mentioned that strain-controlled tests may be used in determining the post-peak behaviour of concrete. The formulation of post-peak models required the determination of parameters to fit experimental data.

The experiments described in the article were stress-controlled; it was difficult to obtain information about the post-peak behaviour of concrete. The shape of the specimens did not match the standard cylinder test in uniaxial compression. Therefore,

making comparisons of basic stress-strain formulations that were based on different test settings may not be accurate. The range of concrete strengths used in the experimental program was narrow. The highest concrete strength (49 MPa) may now be considered slightly greater than normal strength concrete (up to about 40 MPa). The initial tangential and the ascending secant stiffness should vary according to the concrete type (NSC, HSC), the generic equation (Eq.34) proposed by Yip produced an initial tangential stiffness E_o that was about three times larger than the secant stiffness E_{sec} at peak. The model may reproduce the behaviour of low concrete strength, but its application to current available concretes higher than 30 MPa is not practical.

2.3.2.2 Li and Ansari (1999)

Concepts of continuum damage mechanics (CDM) were used to develop a constitutive relationship for confined HSC, where the ultimate surface in the stress space was the bounding surface and the loading surfaces were defined as a function of the damage in the concrete. Results from an experimental program conducted by the authors were compared to the analytical model.

The formulation of the continuum damage model was based on the failure surface by Ottosen (1977), modified to account for the damage in the concrete:

$$F(\sigma_{ij},\bar{D}) = A\frac{J_2}{f'^{\,2}_c} + \lambda\frac{\sqrt{J_2}}{f'_c} + B\frac{I_1}{f'_c} - g(\bar{D}) = 0 \qquad \textbf{Eq. 41}$$

where I_1 and J_2 are stress invariants and $g(\bar{D})$ is a function of damage. The evolution of damage was described with the help of loading surfaces, starting at an initial damage surface, that was considered as the elastic limit. No damage is inflicted in the concrete if the stress state lies on or within this surface. Increasing loading (i.e.

initiation of damage) after passing the initial damage surface, was represented by loading surfaces with similar shapes as that of the bounding surface. The increase in damage and the evolution of the loading surface were accounted for by Eq.41, modified by a shape factor K obtained from experimental data:

$$f(\sigma_{ij},\overline{D}) = A\frac{J_2}{f'^{\,2}_c} + K\lambda\frac{\sqrt{J_2}}{f'_c} + K^2B\frac{I_1}{f'_c} - K^2 g(\overline{D}) = 0 \qquad \textbf{Eq. 42}$$

Damage surfaces were proposed for tensile and compressive cracking separately. The stress tensor was divided into a tensile stress tensor and a compressive stress tensor, and the function of damage $g(\overline{D})$ was defined accordingly as:

$$g_t(\overline{D}) = 1 + \overline{D}_t \qquad \textbf{Eq. 43}$$

$$g_c(\overline{D}) = 1 + \frac{\overline{D}_c}{20} \qquad \textbf{Eq. 44}$$

where the subscripts *t* and *c* stand for tension and compression, respectively, and the damage parameter $\overline{D}$ is the Euclidian length of the principal values of the damage tensor. The flow rule of damage was defined as:

$$\dot{\overline{D}}_{ij} = \dot{L}\frac{\partial f}{\partial \sigma_{ij}} \qquad \textbf{Eq. 45a}$$

$$\dot{L} = \frac{1}{h}\frac{\partial f}{\partial \sigma_{mn}}\dot{\sigma}_{mn} \qquad \textbf{Eq.45b}$$

where the parameter $\dot{L}$ is the normal projection of the rate of the stress tensor, and *h* is a damage modulus which is a function of the stress invariant I_1 and the distance of the actual stress tensor to the initial damage surface in the deviatoric plane. The further apart the current stress state is from the initial surface, the more is the damage caused to the concrete. Softening was modelled by considering only damage; it was expressed as a function of the damage modulus *h* when the stress state moves along the bounding surface (i.e. after peak)

The stress strain relationship was defined in terms of the stress invariant I_1, the deviatoric stress tensor s_{ij}, and the damage tensor D_{ij}:

$$d\varepsilon_{ij} = \frac{\partial \varepsilon_{ij}}{\partial I_1} dI_1 + \frac{\partial \varepsilon_{ij}}{\partial s_{kl}} ds_{kl} + \frac{\partial \varepsilon_{ij}}{\partial D_{kl}} dD_{kl} \qquad \text{Eq. 46}$$

The model was compared to the experimental results of a series of tests carried out by the authors. The experimental work (See Chapter 3) consisted of HSC cylinders having a diameter of 101 mm and height of 202 mm, with concrete strengths of 42 MPa, 69 MPa, and 103 MPa, subjected to confining pressure ratios of up to 92% of the unconfined concrete strength f'_c.

The results for the 42 MPa (6 ksi) cylinders are shown in Figure 44. It was concluded that the constitutive model was able to reproduce the damage mechanism in high strength concrete.

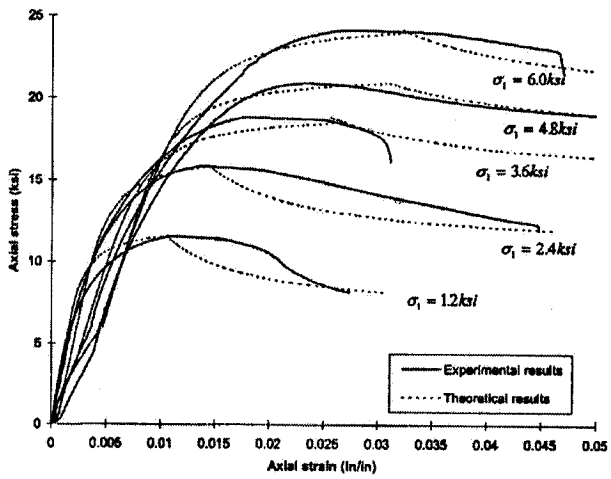

Figure 44. Comparison of experimental and analytical results of 6 Ksi Ansari-Li tests (Li and Ansari 1999).

The experimental program undertaken by the authors added to the yet small database of tests on HSC subjected to high levels of confinement. More tests are needed to implement a reliable constitutive model that takes into account a large

spectrum of concrete strengths and levels of confinement. The Ottosen model provides a suitable failure surface for concrete in triaxial compression. It was also noted from the predictions that in the post-peak range, some of the stress-strain curves concave upwards and had a discontinuity at peak stress with respect to the pre-peak regime, regardless of the lateral pressure applied, and therefore softener behaviour was obtained. The behaviour of HSC at high levels of confinement seemed to not follow this trend, where it was difficult to determine the peak strength. The determination of the softening behaviour using the model should be revised in order to account for this effect.

2.3.2.3 Liu and Foster (2000)

The microplane model developed by Carol, Prat, and Bažant (1992) was calibrated using the results of concrete cylinders subjected to triaxial compression. The model was then implemented in a finite element program and used to analyze two reinforced concrete columns published in the literature.

In the microplane model, normal and shear microstrains for any plane at any point within a concrete solid are calculated as the components of a microstrain tensor ε_{ij}. These strain components were then used in micromaterial laws to calculate the volumetric, deviatoric and tangential microstresses, as follows:

Volumetric Law, for concrete in compression is given by Eq.47 and in tension by Eq.48

$$\sigma_v = E_v^{\,o}.\varepsilon_v\left[\left(1+\left|\varepsilon_v\right|/a\right)^{-p}+\left(\left|\varepsilon_v\right|/b\right)^{q}\right] \qquad \textbf{Eq. 47}$$

$$\sigma_v = E_v^{\,o}.\varepsilon_v.e^{-\left(\left|\varepsilon_v\right|/a_1\right)^{p_1}} \qquad \textbf{Eq. 48}$$

Deviatoric law, in compression (Eq.49) and in tension (Eq.50)

$$\sigma_D = E_D{}^o.\varepsilon_D.e^{-\left(|\varepsilon_D|/a_2\right)^{p2}} \quad \textbf{Eq. 49}$$

$$\sigma_D = E_D{}^o.\varepsilon_D.e^{-\left(|\varepsilon_D|/a_1\right)^{p1}} \quad \textbf{Eq. 50}$$

Tangential law:

$$\sigma_T = \tau.\varepsilon_T / \nu \quad \textbf{Eq. 51}$$

$$\tau = E_T{}^o.\nu.e^{-\left(\nu/a_3\right)^{p3}} \quad \textbf{Eq. 52}$$

The microstresses σ were related to the microstrains ε through the initial Moduli of Elasticity E^o. In this model, ν is the length of the tangential strain vector, and *V*, *D* and *T* refer to the volumetric, deviatoric, and tangential directions, respectively.

The numerical solution of the stress tensor at the macrolevel was obtained by equating the virtual work at the micro-level to that at the macro-level. The integration scheme used a unit sphere at each Gauss point within each three-dimensional finite element. Only 28 planes on the surface of the sphere were used to calculate the stress tensor.

One of the drawbacks of the microplane model was that when it was used for concrete in tension, the stress-strain curve was reliable but the volumetric strains were spurious. However, results of analyses in uni-, bi-, and tri- axial compression were satisfactory. To calibrate the 10 empirical parameters of the model (shown in Eqs. 47 to 52), the authors fixed five of them for all concrete strengths, and made a series of trial-and-error back analyses, whereby the remaining parameters were modified by

comparing and fitting the analytical results to those of concrete cylinders tested in the laboratory. As a result, parameters a_1, a_2, a_3, p_2 and p_3 were statistically fitted to a cubic spline as a function of the ratio of the maximum to minimum principal stresses (σ_1/σ_3). A finite element model of a plain concrete cylinder subjected to uniaxial compression and to $0.025f'_c$ of confining pressure was analyzed by inducing two types of failure modes, conical shear failure and band shear failure. Similar stress-strain curves were obtained for each failure mode.

Two columns, one HSC tested by Razvi and Saatcioglu (1996) and one NSC tested by Sheikh and Uzumeri (1980), were analyzed using the finite element program with the microplane model. The columns were modelled using 20-node brick elements for concrete, and truss bars for the steel. The material model for the steel was elasto-perfect plastic for both longitudinal and transverse steel. To simulate cover spalling, the authors set a low stiffness in the cover elements once the tensile strain reached a value of 0.75×10^{-3}. The experimental axial load-axial strain curve for the Sheikh and Uzumeri (1980) column is shown in Figure 45. Analyses with and without cover spalling made by the authors, as well as one analysis made by Selby and Vecchio (1993), are also graphed in Figure 45.

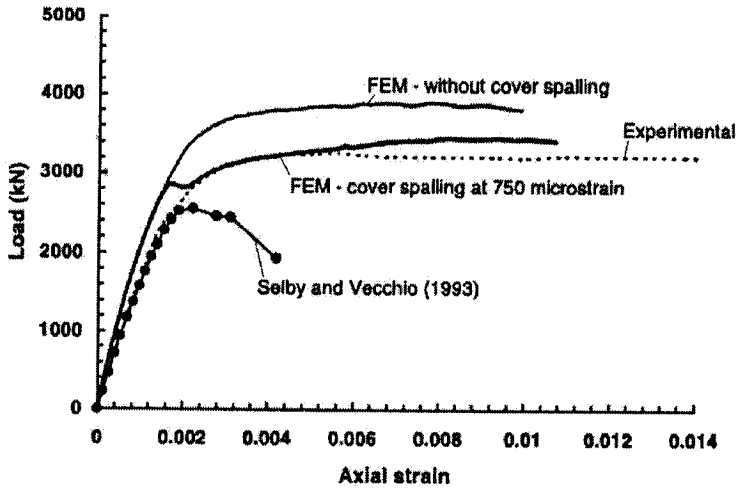

Figure 45. Axial load-axial strain, Sheikh and Uzumeri column 2A5 (Liu and Foster 2000).

As mentioned in the paper, there was no set of parameters in the microplane model that was adaptable to every state of stress in the analysis of a structure. These parameters were highly dependent on the experimental tests and the load path. The definition of cubic spline coefficients were based on reverse engineering of confined concrete tests only, and no trial-and-error analyses were described on tensile tests to calculate the microplane parameters. This might give an explanation for the very different analytical results between the columns without cover spalling and those with induced spalling. Another deficiency was the spurious volumetric strains mentioned by the authors when dealing with elements subjected to tension. Volumetric strains are directly related to concrete dilatation and compaction, and therefore to internal damage (i.e. microcracking). Usage of the model in combined and alternated tensile-compressive states of stresses (cyclic loading, earthquake loading) could be inaccurate.

2.3.2.4 Ghazi, Attard, and Foster (2002)

The microplane model M4 developed by Bažant et al. (2000) was used to model the behaviour of concrete in uniaxial and triaxial compression. Large deformations were accounted for using a complete Lagrangian finite element formulation. The microplane model was modified to account for the steepness of the post-peak regime and the increase in peak stress of confined concrete.

As mentioned in the paper by Liu and Foster (2000) and described previously in this chapter, the microplane model related the microstrains and microstresses to macrostrain and macrostress tensors. Constitutive laws for volumetric, deviatoric, and tangential strains on each microplane were derived. The macrostress tensor was calculated by integrating the microstresses over a unit sphere. The formulations for model M4, and the methodology to calculate the strain and stress tensors, are given in the paper.

The microplane model M4 had a total of 21 parameters; 17 of them were fixed and calibrated using basic concrete tests. Those coefficients, called C_1 to C_{17} by Bažant et al.(2000) were kept the same in this paper. The other four coefficients, K_1 to K_4, were adjusted. The latter coefficients controlled the values for uniaxial concrete strength, the strain at uniaxial peak stress, the volumetric boundary, and the plastic limit under high confinement.

The microplane model M4 was compared to the empirical stress-strain curves obtained using the formulae of Attard and Setunge (1996) for uniaxial compression. The results are shown in Figure 46 for different concrete strengths.

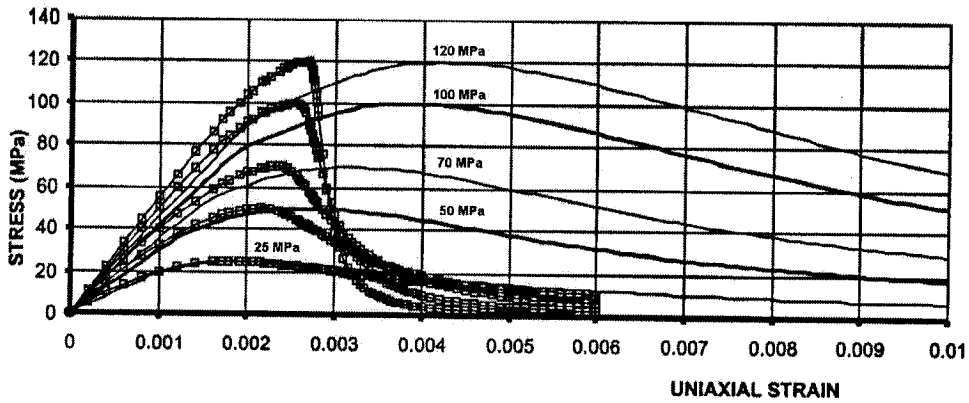

Figure 46. Comparison of simulation using microplane model M4 and Attard and Setunge formulae for cylinders subjected to uniaxial compression (Ghazi et al. 2002).

In Figure 46, the solid lines correspond to the results using M4. The difference in the post-peak behaviour was noticeable. The authors gave three reasons for these inconsistencies.

First, the parameter controlling the softening behaviour of concrete (C_7) was constant and did not vary with the concrete strength. Second, spurious deviatoric microstresses were found to occur in some of the microplanes used in the integration scheme over the unit sphere. This was resolved by neglecting the participation of the microplanes with insignificant deviatoric microstrains, in the distribution of deviatoric stresses, as opposed to the even distribution of the original model. And finally, the shear boundary in the model M4 was a Mohr-Coulomb-type criterion. The coefficient that represented the cohesion on the shear boundary (i.e. C_{10}) was modified to account for post-peak softening. It was given as a function of the volumetric strain ε_V as:

$$C_{10}^{\ softened} = \frac{C_{10}}{1+\langle a\varepsilon_V \rangle^2} \qquad \text{Eq. 53}$$

where the values for the parameter a are in the range of 0-10000, and the parentheses <> are the McCauley brackets. The results obtained from the model with these modifications are shown in Figure 47 for analytical uniaxial compression curves.

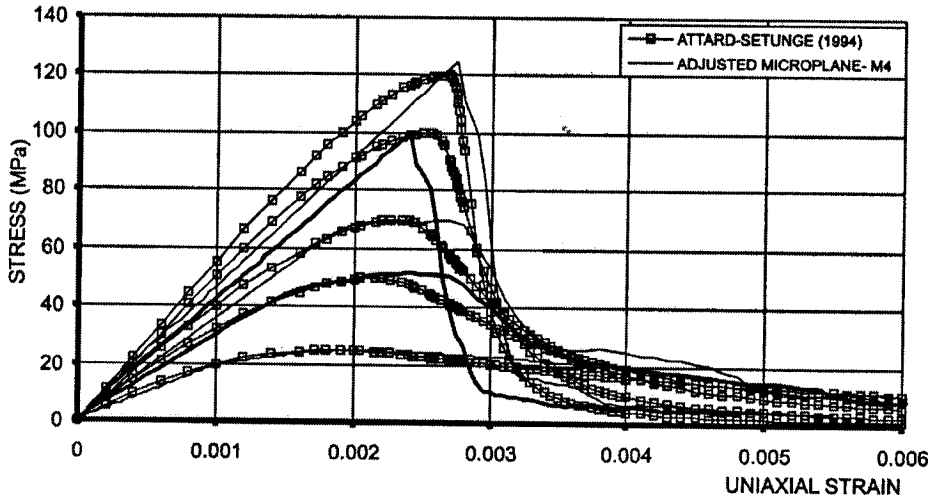

Figure 47. Uniaxial compression tests with modified microplane model M4 (Ghazi et al. 2002).

For confined concrete, the Microplane Model M4 without modifications was compared against analytical curves by Attard and Setunge (1994). Models of standard concrete cylinders subjected to confinement ratios (lateral pressure to unconfined concrete strength ratio) between 0 and 25% were analyzed. Figure 48 shows the results for HSC cylinders with strength (f'_c) of 120 MPa.

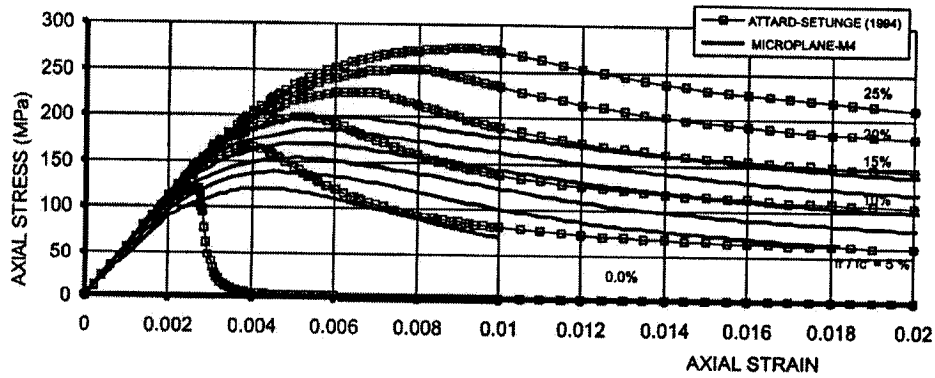

Figure 48. Microplane model M4 and Attard and Setunge analytical results for 120 MPa cylinders (Ghazi et al. 2002).

In general, the peak stresses obtained from the model M4 were smaller for all confinement ratios and concrete strengths studied (25, 50, 70, 100, and 120 MPa). Also, the post-peak responses decayed faster than the empirical curves obtained from the Attard and Setunge model, producing residual stresses smaller than the empirical stresses at the same axial strains.

As for the case of uniaxial compression, modifications to the softening coefficients C_7 and C_{10}, and the parameter K_1 (used to adjust the concrete strength) were proposed. A numerical study was conducted on a concrete cylinder modelled with 360 8-node Lagrangian bricks, subjected to confining ratios of 0, 5, 10, 15, 20, and 25%, and having concrete strengths of 25, 50, 70, 100, and 120 MPa. The best fit for each parameter was found. Sets of three equations for each parameter at different confinement ratios were proposed. The parameter C_{10} was proposed as a function of the volumetric strain and the confinement ratio, and the parameters C_7 and K_1 were proposed as a function of the concrete strength. The modified model results are shown in Figure 49 for the 120 MPa cylinders analyzed with the Attard and Setunge model (1994).

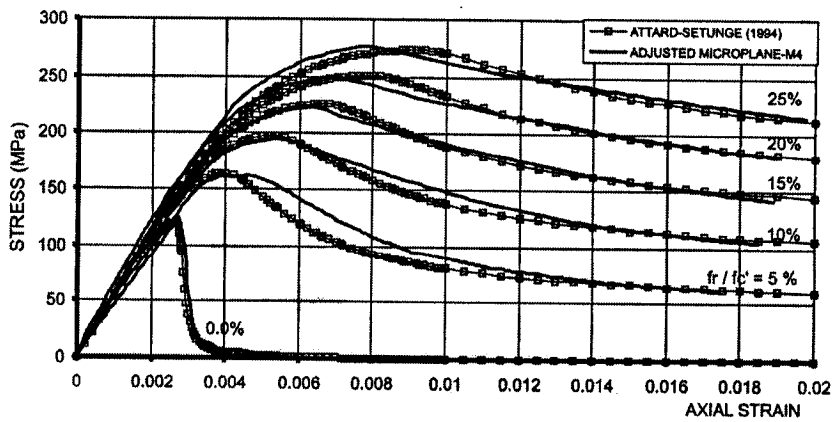

Figure 49. Modified microplane model M4 and Attard and Setunge analytical results for 120 MPa cylinders (Ghazi et al. 2002).

The arrangement of the parameters of the Microplane Model M4 makes impossible to change one of them without affecting others (as mentioned in the article). The selection of variables that affect a particular behaviour of concrete may not be useful for another type of behaviour. This was the case for the arrangements made for unconfined and confined concrete, where different sets of modified parameters were proposed. It might be inferred that there is lack of uniqueness in the proposed model. The nature of the microplane formulation makes the determination of spurious behaviour in some of the microplanes a cumbersome task, even for a single Gaussian point within a finite element. Additionally, only low confinement was investigated.

2.3.2.5 Kwon and Spacone (2002)

A recently proposed 3D model for the analysis of reinforced concrete was modified and used to model concrete reinforced with steel or FRP. Three columns tested at the University of California at San Diego were modelled to corroborate the computer model.

The model was based on an incremental approach whereby:

$$d\sigma = C_o d\varepsilon \qquad \textbf{Eq. 54}$$

The increment in stress $d\sigma$ was calculated using the increment in strain $d\varepsilon$. The matrix C_o is the material matrix. The stress-strain model for concrete was based on a uniaxial stress-uniaxial strain formulation. Uniaxial stresses were calculated in each principal direction. Principal stress directions were not coaxial with principal strain directions. The stress-strain curve in compression for each direction was calculated using the Popovics curve for pre-peak and the Saenz curve for post-peak, as shown in Figure 50.

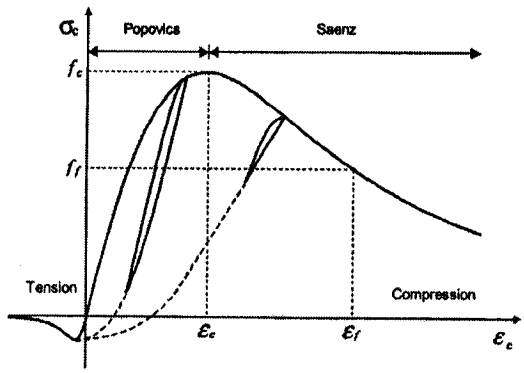

Figure 50. Stress-strain curve for the 3D model

The tensile behaviour was also calculated using the same curve shapes as those used in compression, with the peak values for stress and strain being those corresponding to the tensile strength f_t, and the corresponding strain ε_t, respectively. The tensile curve was cut off in the descending branch at the point ($3\varepsilon_t$, $0.25f_t$). To calculate the ultimate stresses and their corresponding strains for a particular combination of given principal stresses, two ultimate surfaces were proposed separately for the stress space and the strain space. A modified version of the Willam-Warnke failure surface was used where the coefficient for the roundness e of the surface in the deviatoric projection was proposed as a function of the brittleness α:

$$e = \frac{2+\alpha}{4-\alpha} \qquad \textbf{Eq. 55}$$

where the brittleness α is f_t / f'_c, and f'_c is the unconfined concrete strength.

To maintain the symmetry of the material matrix, the following form of the transverse strain ratio v_{ij} was given:

$$v_{ij} = \sqrt{v_{ui} \cdot v_{uj} \cdot \frac{E_i}{E_j}} \qquad \textbf{Eq. 56}$$

where ν_{ij} is the transverse strain ratio for the strain in j-direction, caused by strain in i-direction, ν_{ui} is the uniaxial transverse ratio in i-direction, and E_i is the material modulus in the i-direction. The formula for ν_{ui} was:

$$\nu_{ui} = \nu_o \left[1 + \frac{1}{K_\nu} \left\{ A_i \left(\frac{\varepsilon_{ui}}{\varepsilon_{ci}} \right) + B_i \left(\frac{\varepsilon_{ui}}{\varepsilon_{ci}} \right)^2 + C_i \left(\frac{\varepsilon_{ui}}{\varepsilon_{ci}} \right)^3 \right\} \right] \quad \text{Eq. 57}$$

where ν_o is the initial Poisson's ratio and A, B, C, and K_ν are defined as:

$$K = \frac{1}{2\nu_o} \quad \text{Eq.57a}$$

$$K_\varepsilon = \frac{\varepsilon_f}{\varepsilon_c} \quad \text{Eq.57b}$$

$$K_\sigma = \frac{f_c}{f_f} \quad \text{Eq.57c}$$

$$K_\nu = E_o \frac{\varepsilon_c}{f_c} \quad \text{Eq.57d}$$

$$A = C + K - 2 \quad \text{Eq.57e}$$

$$B = 1 - 2C \quad \text{Eq.57f}$$

$$C = K \frac{K_\sigma - 1}{(K_\varepsilon - 1)^2} - \frac{1}{K_\varepsilon} \quad \text{Eq.57g}$$

The strains ε_c and ε_f, and the stresses f_c and f_f, are depicted in Figure 50. A rotating crack approach was assumed, and the steel constitutive model was a simple bilinear elasto-plastic curve with strain hardening.

As the initial model proposed by the authors did not account for volumetric changes when an element is subjected to shear, a modification to the volumetric stress (and strain) was proposed in the new revised model. A term containing the octahedral shear stress (strain) was added to the definition of volumetric stress σ_v:

$$\sigma_v = \frac{\sigma_1 + \sigma_2 + \sigma_3}{3} - 1.4142\beta\tau_{oe} \qquad \text{Eq. 58}$$

where $\beta = \tau_o/\tau_{oc}$, $\tau_{oe}=2G_o\gamma_o$, τ_o and τ_{oc} are the current octahedral and ultimate octahedral stresses, respectively. G_o and γ_o are the initial shear modulus and the linear elastic octahedral strain, respectively. Loading and unloading followed the cyclic behaviour model proposed by Lee et al.(1997).

The model was corroborated using the tests of Hurlbut (1985). The results of one of the specimens subjected to a lateral pressure of 0.5 ksi (3.5 MPa) are shown in Figure 51.

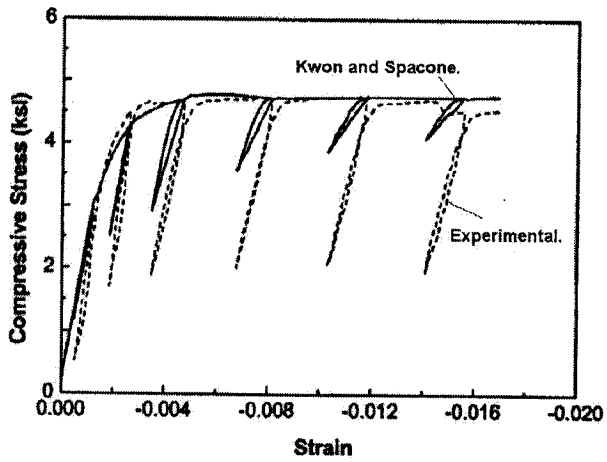

Figure 51. Experimental and analytical results of Hurlbut test at 0.5 ksi Lateral Pressure. (Kwon and Spacone 2002)

Three test specimens of bridge columns subjected to cyclic loading, tested by Xiao et al. (1993) at the University of California at San Diego, were modelled. The results for column R3 are shown in Figure 52. The analytical results showed concrete crushing (point A) followed by shear failure (point B). This was the only column that exhibited

yielding of hoops in the analytical results, whereas in the other two the hoops did not yield, although yielding of hoops was reported in all the specimens.

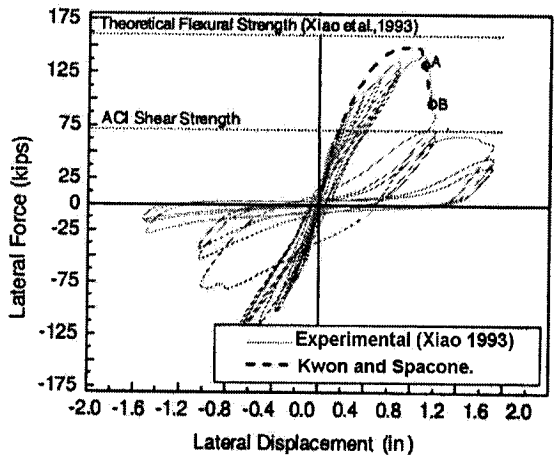

Figure 52. Experimental and analytical results of Xiao et al. column R3. (Kwon and Spacone 2002).

Although not shown here, numerical instability was reported in the corroboration of FRP-confined tests when the Poisson's ratio reached the incompressible value (i.e. 0.5).

The model proposed used a combination of nonlinear elasticity with failure surfaces to calculate the behaviour of concrete subjected to different loading paths. A dilatation model for concrete that is a function of the three-dimensional response was also proposed. Numerical instability of the solution makes the dilatation model useful up to the limit of 0.5 for some types of tests. It was also found that in modelling structural elements, the modelled lateral expansion did not make the lateral steel yield. Finally, due to the uncoupled behaviour, the volumetric stress and strain had to be modified by a correction factor to account for volumetric changes.

2.3.2.6 Assa, Nishiyama, and Watanabe (2001a)

The interaction between concrete and spiral steel was studied. Reinforced concrete cylinders were tested to track the axial compression and lateral expansion of confined concrete. The relationship between the spiral steel deformation and the concrete expansion was determined analytically. The stress-strain curve for confined concrete was formulated based on the lateral stress and lateral strain calculated at peak axial stress.

The lateral stress f_r in a reinforced concrete cylinder with spiral reinforcing was calculated using equilibrium of forces:

$$f_r = \frac{2A_s f_s}{D_c s} \qquad \text{Eq. 59}$$

where A_s is the steel section area, f_s is the stress in the steel, D_c is the cylinder diameter, and s is the spiral spacing. If the stress-strain curve for the spiral steel is known, Eq. 59 could be used to calculate the confining stress in the concrete.

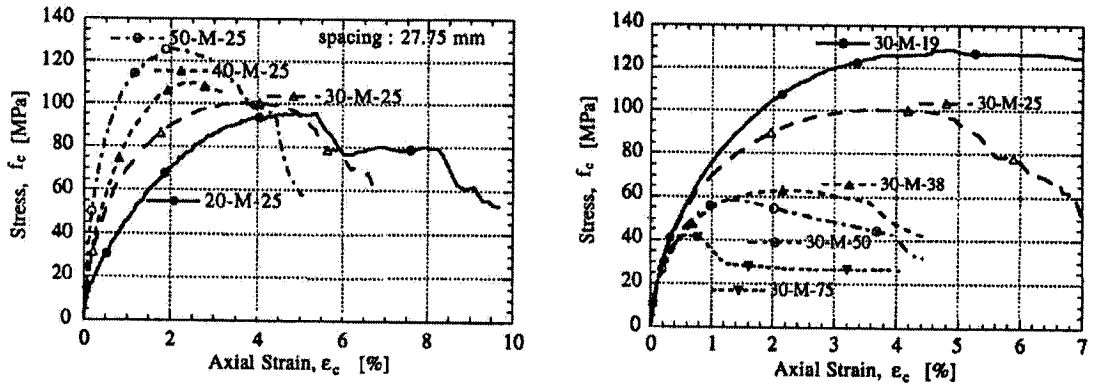

Figure 53. Axial stress-axial strain of cylinder reinforced with spirals (Assa et al. 2001a).

A series of 24 cylinders were tested in axial compression, with concrete strengths varying between 20 MPa and 90 MPa, and the yield strength of steel either 910 MPa or 1300 MPa. Spiral spacing varied between 19 mm and 75 mm. Figure 53 shows the influence of concrete strength, (a), and spacing and amount of lateral pressure (spiral steel), (b), on the axial stress-axial strain response. As expected, the loading capacity and ductility improved with smaller spacing and amount of lateral pressure. It was also noted that axial strains at peak stress decreased with an increase in the unconfined concrete strength.

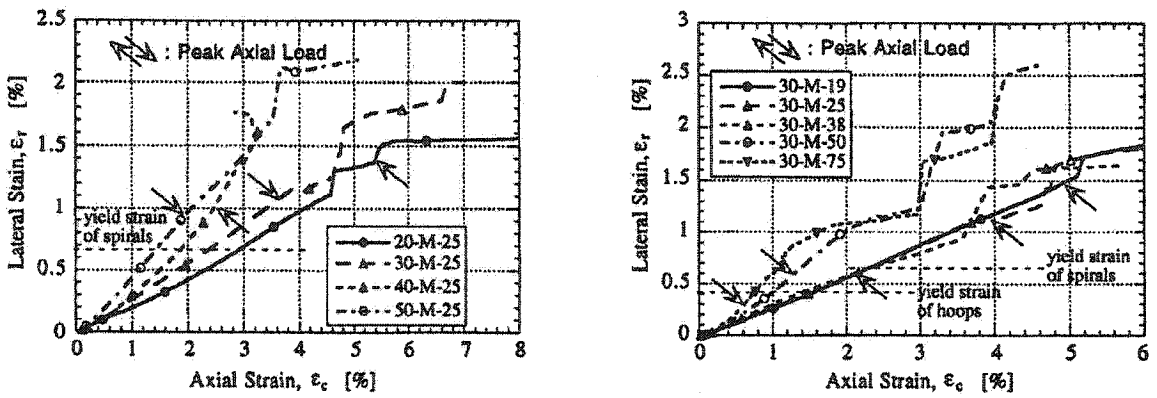

(a) (b)

Figure 54. Axial strain-lateral strain of cylinder reinforced with spirals (Assa et al. 2001a).

The lateral strains in concrete ε_r increased with an increase in spiral spacing, as seen in Figure 54b. Apparently, high concrete strength cylinders exhibited larger lateral strains than those of normal strength concrete (see Figure 54a). However, the attainment of peak stresses in HSC occurred at lower lateral strains than in NSC, indicating less lateral expansion. Moreover, in only one of the HSC concrete cylinders did the spiral steel yield, which was not the case for well-confined NSC cylinders.

The following equations were proposed:

$$\frac{f_{cc}}{f_{cu}} = 1 + 3.36\frac{f_{rp}}{f_{cu}} \quad \text{Eq. 60}$$

$$\frac{\varepsilon_{cc}}{\varepsilon_{cu}} = 1 + 21.5\frac{f_{rp}}{f_{cu}} \quad \text{Eq. 61}$$

$$\frac{\varepsilon_{80}}{\varepsilon_{cu}} = 2.74 + 32.84\frac{f_{rp}}{f_{cu}} \quad \text{Eq. 62}$$

$$\varepsilon_{rp} = 0.0021 + 0.0160\frac{f_{rp}}{f_{cu}} \quad \text{Eq. 63}$$

where ε_{cu} is the strain at peak unconfined stress f_{cu}, ε_{80} is the strain at a stress of 80% of the strength on the descending branch, ε_{cc} and f_{cc} are the peak strain and peak stress, respectively, and ε_{rp} and f_{rp} are the lateral strain and lateral pressure at peak stress, respectively. The compatibility of deformations between the lateral expansion of confined concrete, and the imposed lateral compression by the confining steel, is represented in Figure 55, where a circular segment of concrete in a cross section is modelled as a linear strut element subjected to a lateral force F_r. If the concrete segment were allowed to expand freely (i.e. not confined) the total lateral deformation would be Δ_{cr} (say, at crushing). The presence of confining steel reduces the free expansion by Δ_{ro} resulting in a net expansion Δd_r, delaying the failure of concrete. The compatibility formulation states that:

$$\Delta d_r = \Delta_{cr} - \Delta r_o \quad \text{Eq. 64}$$

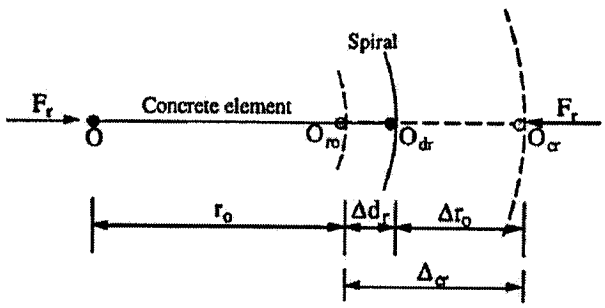

Figure 55. Lateral expansion compatibility (Assa et al. 2001a).

The lateral expansion of confined concrete Δd_r was equal to the expansion of the spiral, $\varepsilon_r.r_o$, where r_o is the radius of the concrete cylinder. To determine the stress-strain curve for confined concrete, the lateral stress-lateral strain f_r-ε_r curve was first calculated using Eq. 59, then by combining Eq. 63 and the f_r-ε_r curve, the value of f_{rp} / f_{cu} at peak stress was obtained. Finally, using Equations 60 to 62, the parameters for the complete stress-strain curve were calculated. (The stress-strain curve formulation is not shown here). Figure 56 shows analytical and experimental stress-strain curves for two of the cylinders, along with the results from the model proposed by Mander et al. (1988). It was concluded that the analytical model followed the experimental curves well.

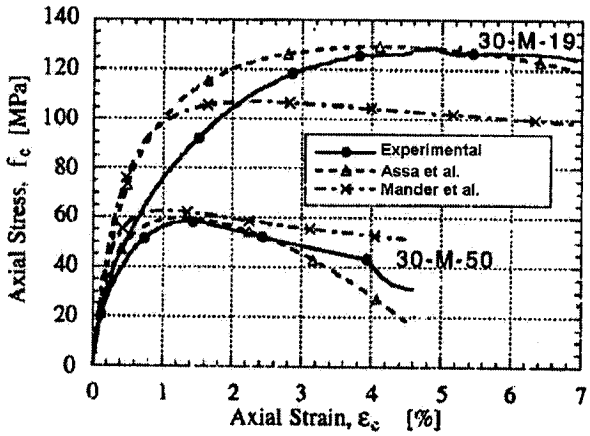

Figure 56. Analytical and experimental results (Assa et al. 2001a).

The article presents a rationale for understanding the mechanics of confinement of concrete. The major objective was to find realistic values of lateral stresses at peak stress according to the compatibility of lateral deformations. The method is suitable for hand calculations of the behaviour of circular columns without concrete cover. However, the assumption of uniform lateral pressure along the spiral spacing seems not reasonable for large spacings, and the methodology is only applicable to circular columns.

2.3.2.7 Assa, Nishiyama, and Watanabe (2001b)

This paper extended the analytical model derived in the previous paper, to the analysis of rectangular columns.

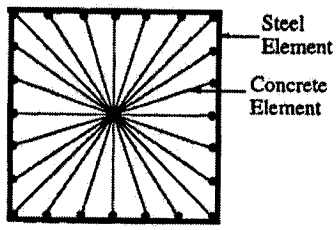

Figure 57. Model of concrete struts (Assa et al. 2001b).

The rectangular section was idealized as shown in Figure 57, where each of the concrete segments were treated as struts having only axial stiffness, and the steel was modelled as beam-column elements. It was assumed that the struts were subjected to uniform stress f_r and strain ε_r:

$$f_r(r) = \frac{F_r}{L_e s} \qquad \text{Eq. 65}$$

$$\varepsilon_r(r) = \frac{F_r}{E_{cr} L_e s} \qquad \text{Eq. 66}$$

where F_r is the compressive force in the strut, L_e is the width of the segment at the intersection with the steel, s is the spiral spacing, and E_{cr} is the concrete stiffness in the lateral direction. The axial stiffness of the strut was given by:

$$kc = \frac{F_r}{\Delta_{ro}} = \frac{E_{cr} L_e s}{r_o} \qquad \text{Eq. 67}$$

where r_o is the initial length of the strut and Δ_{ro} is the total axial deformation. The tangential stiffness at each load step could be calculated if the Poisson's ratio were known:

$$E_{cr} = \frac{f_r(1-\nu)}{(\nu\varepsilon_c - \varepsilon_r)}$$ **Eq. 68**

The authors calculated the f_r - ε_r curve by imposing lateral expansion increments to all struts, thus pushing the steel outwards as shown in Figure 58. The compatibility equation deduced by Assa et al. (2001a), was applied to each strut in the directions *j-1*, *j*, and *j+1* at each node that connects the concrete strut with the steel elements. The force on the concrete struts at each intersecting node *i* was given by:

$$\Delta F_r = k_c . \Delta_{ro}$$ **Eq. 69**

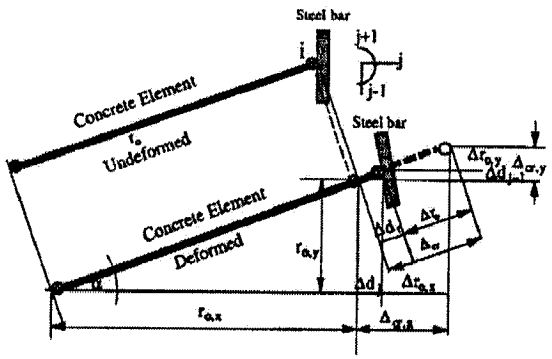

Figure 58. Deformation compatibility of a typical concrete strut (Assa et al. 2001b).

These forces should be in equilibrium at the node with those produced by the steel. Additionally, the rotational equilibrium at each degree of freedom *j+1* yielded null moments. The resulting system of equations for all connecting nodes was then solved for each lateral deformation increment. The empirical equations for the key parameters for the stress-strain curve for confined concrete (f_{cc}, ε_{cc}, ε_{80}, ε_{rp}, f_{rp}), deduced for circular columns, could not be applied directly to rectangular columns, due to the difference in lateral expansion along the sides of the rectangular section. Thus, by equating the energy stored in the confining steel to the work done in compressing the concrete, an "equivalent" circular column was deduced from the dimensions and properties of the rectangular column. To obtain the axial stress-axial strain response, a procedure

similar to that described in the previous paper was utilized to calculate the lateral displacements, and the transformation of the equivalent stress $f_{r,eq}$ of the "equivalent" circular column into the stress f_{rp} for the rectangular column. This methodology was applied to a series of rectangular columns tested by several researchers. One of the columns tested by Scott et al.(1982) is shown in Figure 59. In general, mean errors of 9% and 0.3% in the strength were obtained for NSC and HSC columns (coefficients of variation not given in the paper), respectively, from a total of 34 NSC and 31 HSC columns analyzed.

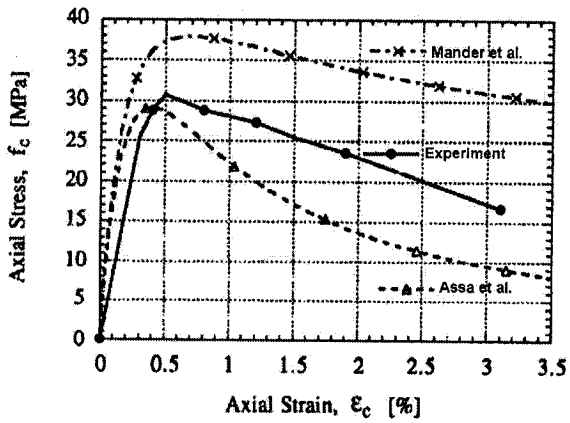

Figure 59. Axial stress-axial strain of column unit-6 tested by Scott et al. (Assa et al. 2001b).

Several simplifications were made in the analysis of the strut-confining steel system. The value of E_{cr} was taken constant throughout the analysis. This assumption omitted the progressive microcracking damage of concrete in the lateral direction, and a reduced stiffness should be expected with increasing lateral deformations. The total deformation on the struts was based on a prismatic section; this assumption did not consider the variability of confinement from the centre of the column section towards the sides along each strut. Finally, the method is only applicable to confined columns when an analogy can be found between the actual column and a circular column.

2.4 Concrete Dilatation

2.4.1 Candappa, Setunge, and Sanjayan (1999)

A series of tests were performed to measure the axial stress, axial strain, and lateral strain of concrete cylinders subjected to triaxial stresses. The cylinders were 98 x 200 mm (diameter x height), and had concrete strengths of 60 MPa and 100 MPa. Lateral pressures of 0, 4, 8, and 12 MPa were applied using oil pressure in a triaxial cell. The experimental results showed a 20% lower lateral expansion of the 100 MPa concrete cylinders, with respect to that of the 60 MPa concrete cylinders.

A total of 16 cylinders were tested in a triaxial cell, using a loading path in which the total lateral pressure was applied first followed by monotonic axial compression. The lateral strains were measured using a gauge designed by the authors. The gauge measured the overall lateral strain at mid-height of the cylinder. The objective of this investigation was to gather experimental data on the behaviour of HSC subjected to triaxial stresses, and to measure the lateral expansion at different levels of confinement. The axial stress-axial strain and axial stress-lateral strain curves for the 100 MPa tests are shown in Figure 60 and Figure 61, respectively.

The authors concluded that at low confinement the lateral strain at peak stress for both types of concrete were similar, and for high confinement the lateral strain of the 100 MPa concrete was 80% of that of the 60 MPa concrete. It was also suggested that the confinement produced by lateral reinforcement in HSC columns subjected to high confinement would be less effective than that for lower strength columns.

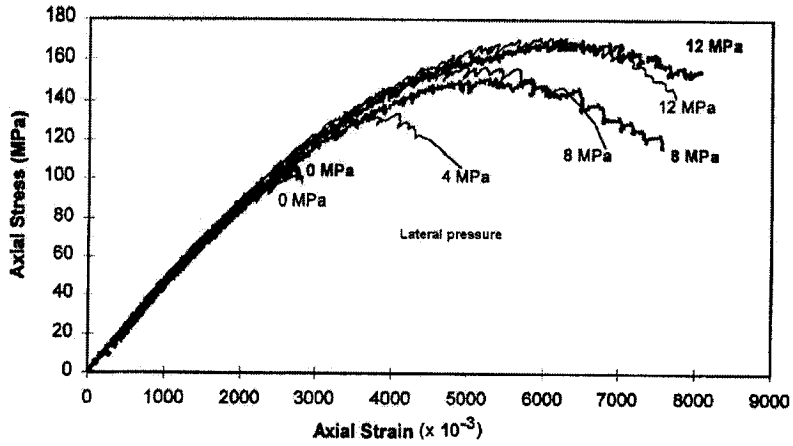

Figure 60. Axial stress-axial strain for 100 MPa cylinders (Candappa et al. 1999).

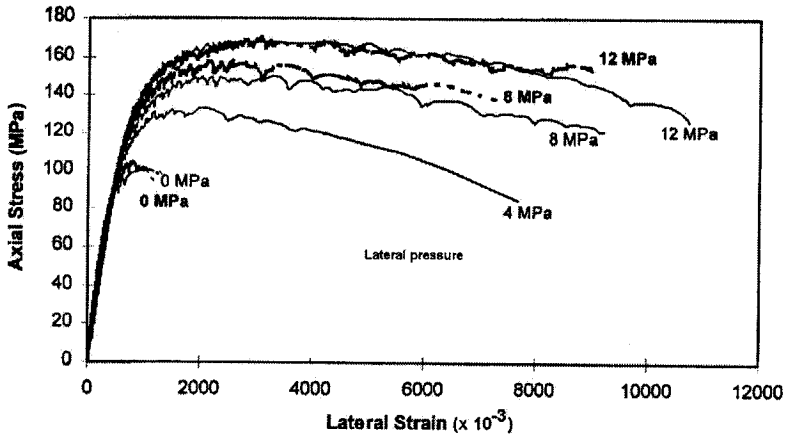

Figure 61. Axial stress-lateral strain for 100 MPa cylinders (Candappa et al. 1999).

Although the number of tests was small, they gave an idea of the confinement behavior of HSC. The lateral pressure to concrete cylinder strength ratios were in the range of 6% to 20% for the 60 MPa cylinders, and in the range of 4% to 12% for the 100 MPa cylinders. It should be said that these confinement ratios were limited to the range of lateral pressures on concrete columns due to tie or hoop reinforcement. They represent only a portion of the spectrum of confinement pressures that may occur in reinforced concrete solids. The lateral strain to axial strain ratio at ultimate was more than 1.0 for most of the specimens.

2.4.2 Candappa, Sanjayan, and Setunge (2001)

A series of tests were performed to measure the axial stress, axial strain and lateral strain of concrete cylinders subjected to triaxial stresses. The cylinders were 98 x 200 mm (diameter x height), and had concrete strengths of 42 MPa, 61 MPa, 73 MPa, and 103 MPa. Lateral pressures of 4 MPa, 8 MPa, and 12 MPa were applied using oil pressure in a triaxial cell. The Mohr-Coulomb criterion was modified to account for high strength concrete at low confining ratios. The nonlinear elastic model of Ottosen implemented in the model code MC90, for the variation of secant Poisson's ratio, was modified. A linear equation to calculate the peak strain was established.

This paper described the work of the authors that began with the paper discussed previously. The tests were extended to cover concrete strengths of 40 and 75 MPa (target values). The database of results of HSC subjected to triaxial compression was further expanded with these new results. Figure 62 shows the axial stress-axial strain, and axial stress-lateral strain curves for 40 MPa.

The failure criterion of Mohr-Coulomb gave the peak stress σ_{1P} as a function of the uniaxial concrete strength f'_c, and the lateral confinement σ_3 as:

$$\sigma_{1P} = f'_c + k.\sigma_3 \qquad \textbf{Eq. 70}$$

The authors assumed that a common value for k was 4.0. However, from the results, it was found that a better fit for k was 5.3 for low confinement ratios (i.e. $\sigma_3 / f'_c < 0.20$). This value tended to decrease with high levels of confinement. The peak strain, ε^{μ}_1, was found to have a linear relationship with the confinement ratio σ_3 / f'_c, as shown in the equation below:

$$\frac{\varepsilon^u_1}{\varepsilon^u_c} = 1 + 20\left(\frac{\sigma_3}{f'_c}\right) \qquad \text{Eq. 71}$$

where ε^u_c is the peak unconfined strain. The peak confined strain did not depend on the unconfined concrete strength.

The Ottosen model for the secant Poisson's ratio model was also investigated. This nonlinear elastic model was adopted by the Model Code 90 (MC90) of the CEB-FIP. It related the axial stress ratio $\beta = \sigma_1 / \sigma_{1P}$, called the non-linearity index, to the secant Poisson's ratio ν^a as follows:

$$\nu^a = \nu^a_i, \quad \beta \le \beta_1 \qquad \text{Eq. 72}$$

$$\nu^a = \nu^a_f - \left(\nu^a_f - \nu^a_i\right)\sqrt{1-\left(\frac{\beta-\beta_1}{1-\beta_1}\right)^2}, \quad \beta \ge \beta_1 \qquad \text{Eq. 73}$$

Here, ν^a_i and ν^a_f are the initial and final values for the Poisson's ratio; the latter was calculated at peak stress. β_1 is the value taken by β when the Poisson's ratio starts to increase. It was taken as 0.8 in the Ottosen model, which agreed well with the values found in the tests. At peak stress (β = 1.0), the secant Poisson's ratio was close to 0.5, instead of 0.36 suggested in the original model. The descending branch of the β-ν^a curve after the peak stress, β_D, and the initial Poisson's ratio ν^a_i, were fitted to the experimental results.

$$\nu^a_i = 8x10^{-6}\left(f'_c\right)^2 + 0.0002 f'_c + 0.138 \qquad \text{Eq. 74}$$

$$\beta_D = -0.5\left(\nu^a\right)^2 + 0.45\nu^a + 0.9 \qquad \text{Eq. 75}$$

The modified model is plotted along with experimental results in Figure 63 for the 40 MPa test series.

It was concluded that the value of k in the Mohr-Coulomb criterion should be at least 5.0 for the case of HSC at low confining levels. The peak strain varied linearly with respect to the confinement ratio, and finally, modified equations for the Ottosen model were proposed. It was also found that the descending branch of the β-ν^a curve did not depend on the confining level.

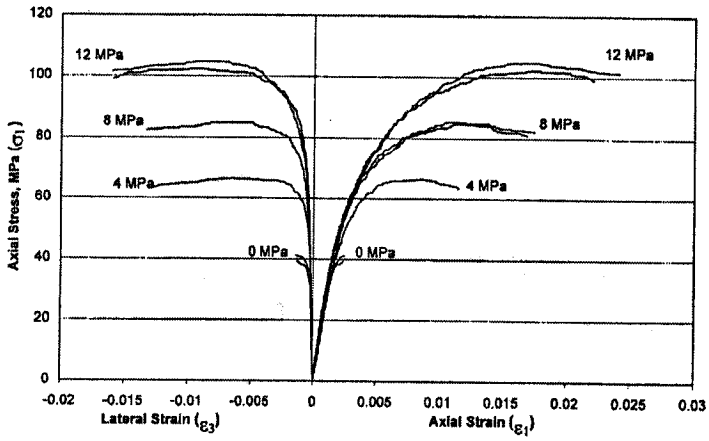

Figure 62. Axial stress-axial strain and axial stress-lateral strain for 40 MPa cylinders (Candappa et al. 2001).

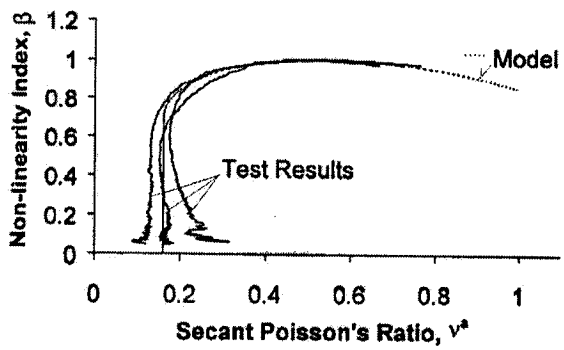

Figure 63. Non-linearity index β versus secant Poisson ratio ν^a (Candappa et al. 2001).

The authors expanded the database of tests results of HSC subjected to lateral pressure. It can be stated that these tests confirmed that the secant Poisson ratio can reach values greater than 0.5. Moreover, values close to 1.0 were reported. These tests suggested independency of the concrete dilatation on the level of lateral pressure in the post-peak regime, which contradicts other articles reviewed in this Chapter.

2.4.3 Lee, Willam, and Kang (1997)

Observations on the pre- and post-peak response of concrete cylinders of different height were described. Degradation of strength and stiffness during axial loading and reloading were also investigated. It was found that axial splitting was the predominant mode of failure of concrete in uniaxial compression.

Three NSC specimens of 3-in (75 mm) diameter, and heights of 5.4 in, 3.6 in, and 1.8 in (135 mm, 90 mm, and 45 mm), were subjected to uniaxial compression. The shortest specimen was attached to two HSC cylinders of 1.8 in height at the top and bottom of the testing machine. This set-up eliminated boundary problems, as the HSC has elastic properties not drastically different than the NSC specimen. As for the other cylinders, their surfaces were covered with "grease" to reduce friction with the machine platens. The uniaxial concrete strength was found to be 4.65 ksi (32.0 MPa) for the shortest cylinder and 4.45 ksi (30.7 MPa) for the others, showing a negligible variation of strength between them.

From the experimental observations, it was found that the extensive lateral deformation in the post-peak behaviour produced axial splitting. The observed phenomenon was similar to Mode I failure in tensile cracking in the uniaxial tension tests, except for the presence of axial compression. The axial stress-axial strain and axial stress-lateral strain curves for the specimens are shown in Figure 64. As the fracture energy release G_f in uniaxial tension is constant, an attempt was made to determine if it remained constant for the uniaxial compression tests regardless of the specimen height. This energy was calculated using the axial stress-axial deformation

curves, which are shown in Figure 65. It can be seen that the axial stress-axial deformation curves for the three specimens were similar, demonstrating that the fracture energy release (area under the curve) in the uniaxial compression tests remained constant, and did not depend on the specimen height. It was also observed that the ratio of lateral deformation to axial deformation was constant, reaching values of about 12.

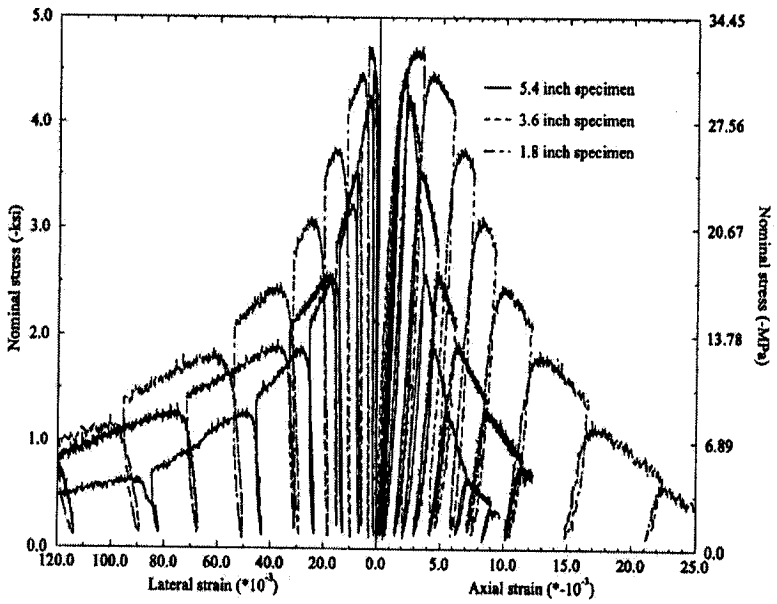

Figure 64. Nominal stress-axial strain, and nominal stress-lateral strain results of uniaxial compression tests (Lee et al. 1997).

The beginning of a constant ratio of lateral deformation to axial deformation coincided with the inflection point in the post-peak range of the axial stress-axial strain curve. At this point, the lateral expansion of cracks resembled the failure mode in tensile tests.

With respect to the stiffness, in the pre-peak range, the unloading stiffness did not change, whereas the reloading stiffness was reduced to about 76% of the initial stiffness, triggering the initiation of microcracking.

In the post-peak regime, the degradation of the stiffness was described as a function of the degradation of strength, fracture energy release, and plastic deformation. The degradation of stiffness E_d with respect to the axial stress, and to the progressive release of fracture energy (G_f / G_f^{max}), showed a linear variation. (See Figure 66 a and b).

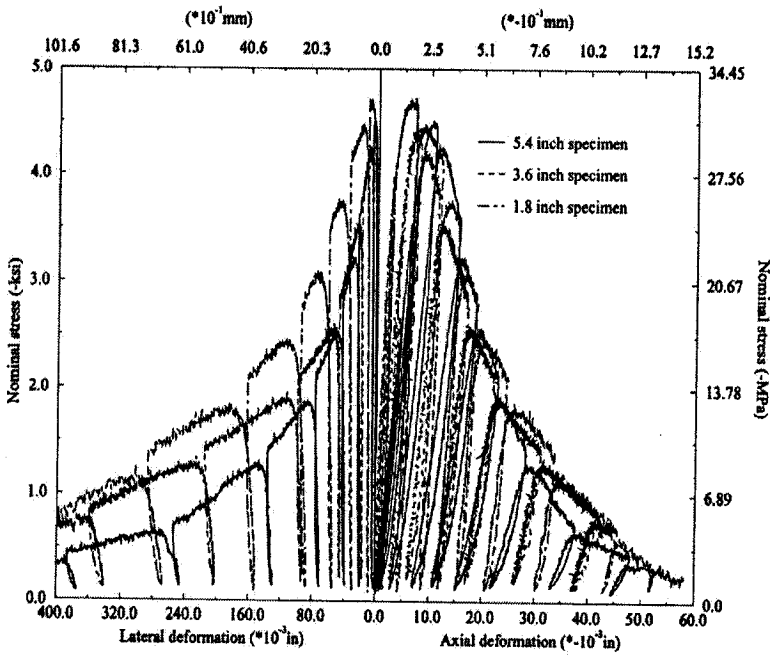

Figure 65. Nominal stress-axial deformation, nominal stress-lateral deformation (Lee et al. 1997).

The stiffness degradation versus plastic deformation after peak stress (zeroed at peak) had a hyperbolic shape, which was similar for all three heights (Figure 67). The plots were normalized with respect to the initial stiffness E_o at peak, and with respect to

the maximum values for strength f'_c, fracture energy G_f^{max}, and total plastic deformation u_p^{total}.

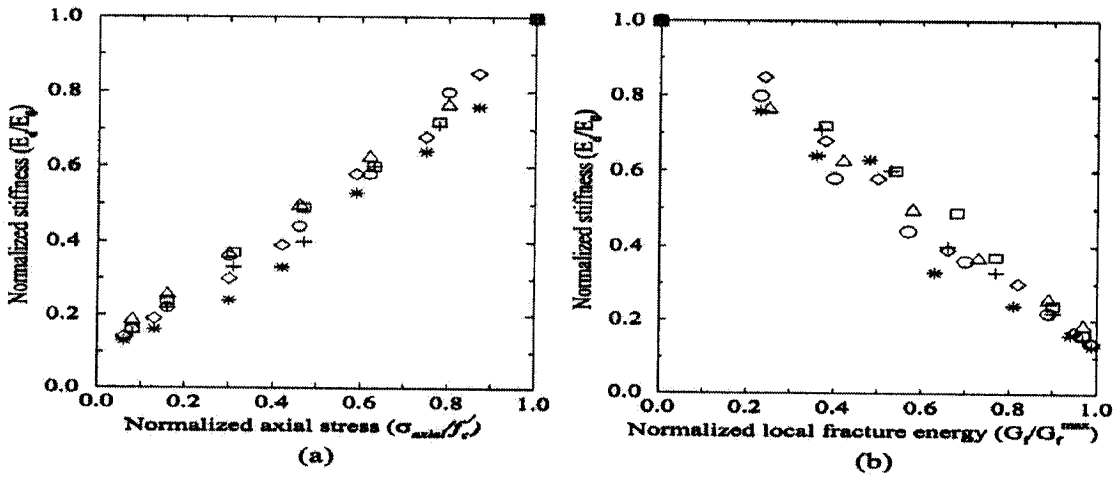

Figure 66. Stiffness degradation versus (a) Normalized strength, and (b) Fracture energy (Lee et al. 1997).

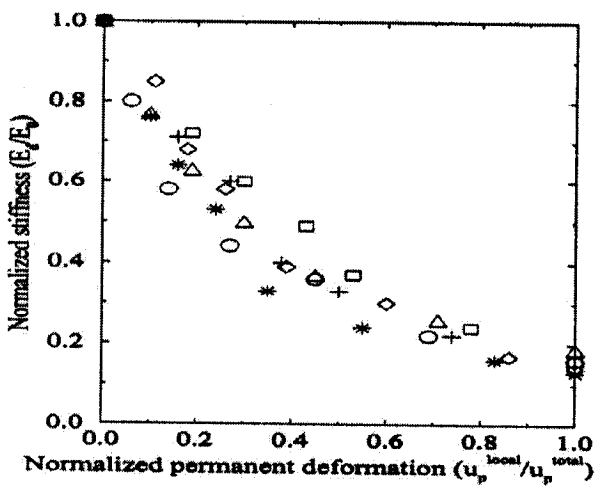

Figure 67. Stiffness degradation versus normalized plastic deformation (Lee et al. 1997).

In summary, three concrete cylindrical specimens of different length were tested in uniaxial compression. The investigation concentrated on the effects of fracture in

compression softening. It was found that the fracture energy release was similar for all specimens, irrespective of their length, and that the predominant failure mode (compression failure with axial splitting) was similar to that of uniaxial tensile tests. Stiffness degradation varied linearly with the fracture energy and strength degradation, and was not a function of the specimen length.

Uniaxial compression can be seen as a special case of confined concrete compression without lateral pressure. The experimental results showed the large concrete dilatations that can be reached due to the effect of lateral expansion of axial cracks. Lateral strains greater than six times the axial strain can be deduced from Figure 64.

2.5 Conclusion

2.5.1 Summary

A series of experimental and analytical investigations on confined concrete were studied and discussed. The experimental works of several researchers contribute to an understanding of the behaviour of confined concrete, and add to the database of experimental data. It has generally agreed that confinement increases the capacity of the concrete to sustain greater load and larger deformations.

The behaviour of FRP-confined concrete was independent of the type of fabric used in the tests. Circumferential confinement had little effect on the axial stiffness of the concrete cylinders and columns. However, the more plies of fabric applied to the specimens, the larger was the increase in strength and ductility. Concrete cylinders

subjected to active constant confinement also increased their strength and ductility with increased pressure. Formulae for the strength of concrete confined with FRP were also proposed.

Measured lateral and axial strains at ultimate, on concrete cylinder specimens, showed ratios of lateral to axial strain greater than 1.0 for most of the tests of confined concrete studied. Ratios of about 6 in some uniaxial compression tests were also reported. It was also observed that concrete dilatation depends on the level of lateral pressure.

Experimental work on concrete dilatation was done by Candappa et al. (1999) on low confined cylinders (i.e. confinement ratios less than 20%). They also proposed a modified Ottosen formula for the Poisson's ratio. Lee et al. (1997) examined the mode of failure of cylinder specimens subjected to uniaxial compression, and found extensive lateral deformation after peak. Kwon and Spacone (2002) proposed a polynomial for calculating the Poisson's ratio based on confinement parameters of their stress-strain curve for confined concrete.

Several computational models for confined concrete have been proposed. The theory of plasticity was used in the majority of the cases to propose models to account for concrete strength increase due to confinement, concrete dilatation, and ductility. The extended Leon model and a combination of Rankine and Drucker-Prager models were used by Pivonka et al. (2000). The Willam and Warnke model and a neural network were used by Sankarasubramanian et al. (1996). Barros (2001) used model code MC90 equations and a Drucker-Prager surface to model cylinder confined with

spirals. Mirmiran et al. (2000) also used a Drucker-Prager surface to model concrete confined with FRP.

Other computational models included a formulation for a general stress-strain curve for concrete subjected to uniaxial compression (Yip (1998)). A continuum damage mechanic model was suggested to simulate high strength concrete subjected to high confinement ratios (Li and Ansari 1999). Models based on the microplane model (Liu and Foster 2000, Ghazi et al. 2002), and a strut-and-tie model combined with phenomenological equations to reproduce concrete confinement in square and circular columns (Assa et al. 2001), have also been proposed.

2.5.2 Limitations

The following is a brief summary of the limitations of the current state-of-the-art of confined concrete.

- The finite element analysis of HSC columns by Cleason (1999) did not have a unique formulation for the behaviour of cover concrete and core concrete. The model of Cusson and Paultre was used to analyze the behaviour of HSC and NSC.

- The modified equations of the model code MC90 given by Vintzileou and Malliri (1999) were based on variables suitable for design calculations, which are not convenient for finite element analysis.

- Some of the analytical models were specifically developed for predicting the behaviour of FRP-confined concrete. These models can only be applied to specific

cases, such as circular columns (Spoelstra and Monti 1999), or to small ranges of concrete strength (Lam and Teng 2002). One of the models was developed based on too few number of tests (eight) (Karabinis and Rousakis 2002) and should be considered preliminary. The model by Mirmiran et al. (2000) did not reflect the volumetric expansion and post-peak behaviour of the specimens analyzed.

- Some of the proposed failure and loading surfaces of plasticity type models used Drucker-Prager models, which did not reproduce accurately the volumetric strain behaviour. They require a large number of parameters to be calibrated (e.g. Pivonka et al. 2000), and the parameters applied to certain types of analyses had to be re-determined for another type of loading paths (Liu and Foster 2000). These parameters, generally based on experimental results, were unique for the type of concrete (e.g. normal strength concrete, or high strength concrete), and could only be applied according to their constraints. Some of the analytical curves did not reach the peak stress, and failed to track the post-peak behaviour of the strain-stress curve, or the post-peak behaviour did not resemble the experiments (e.g. Sankarasubramanian et al.1996, Mirmiran et al. 2000).

- Models based on compatibility of deformations and simple formulations for concrete strength, made several assumptions that limited their usefulness to reproduce the general behaviour of structural elements with certain types of cross sections (e.g. circular sections), but gave no insight on the distribution of confinement between ties, or within the cross sections of the columns (e.g. Assa et al 2001a, 2001b).

- It was also found that some of the computational models showed numerical instabilities when the value for the Poisson's ratio was over 0.5, or when the equations for the model produced unsymmetrical stiffness matrices (e.g. Barros 2001).

2.5.3 Remarks

The experimental programs and computational models reviewed address specific problems on confinement of concrete, such as confinement of high strength concrete and normal strength concrete columns reinforced with lateral steel or FRP fabric, normal strength concrete cylinders subjected to low confinement ratios, or high strength concrete subjected to high confinement ratios. The analytical models are limited by the range of unconfined concrete strengths of the specimens used for their formulation (e.g. FRP or steel). Limitations are also found in the variables included in the models that are not suitable for finite element analysis.

This thesis addresses the deficiencies of the current confinement models for concrete by proposing formulations for strength enhancement, concrete dilatation, and a stress-strain curve based on a wide range of unconfined concrete strengths (from 20 MPa to 130 MPa) and confinement levels (from 0 to 100% of the unconfined concrete strength). The proposed formulations for confinement and formulations from the modified compression field theory (Vecchio and Collins 1986) are combined and are readily adaptable for implementation in finite element programs that consider three-dimensional states of stresses, as they are given in terms of strains and stresses, and can be used for the analysis of confined concrete by FRP, steel, or lateral pressure exerted by means of applied stresses on the surfaces of the elements.

A finite element program for reinforced concrete solids of revolution was also developed and the proposed and the proposed models were implemented in the program. The capabilities of the program were tested by corroborating the experimental results of circular specimens subjected to axial compression and lateral pressure.

The models were also implemented in a general three-dimensional nonlinear finite element analysis program to determine the capabilities of the models by corroborating experimental results of square columns subjected to axial compression and passive lateral pressure.

A synopsis of the literature review, specifically of the several models proposed, their analytical approach, the parameters analyzed, the experiments on which they were based or corroborated against, and a summary of remarks and limitations found, is given in Table 2.

Model	Approach	Parameters analyzed	Experiments	Remarks and Limitations
Cleason (1999)	Used NLFEA program (ABAQUS), and Cusson and Paultre model for HSC to determine post-peak behaviour of steel-reinforced columns	steel yield strength lateral steel spacing cross-section configuration load eccentricity	five columns tested from 33MPa to 112MPa Cross sections of 200x200 or 250x200 mm Lengths 800, 900, 2000 mm	. No unique formulation for unconfined and confined behaviour in the NLFEA. . Used HSC model to analyze NSC. . Examined only low confined elements.
Vintzileou and Malliri (1999)	Empirical model for columns confined with hoops or spirals, based on MC90.	strength strain at peak stress strain at ultimate	300 tests on axially compressed columns from 17 researchers	. Based on physical parameters of common column sections. . Suitable for design calculations and not for finite element analysis.
Purba and Mufti (1999)	Used Mander model (1988) to analyzed CFRP-confined columns	stress-strain curve of axially compressed columns	three circular columns with two layers of CFRP	. Should be considered a preliminary set of tests. . Mander model not appropriate to model columns where rupture of CFRP is the source of failure.
Xiao and Wu (2000)	Bilinear stress-strain model for CFRP-confined cylinders based on compatibility of deformations and empirical relation between axial and lateral strains	Ultimate (maximum) confinement pressure confinement modulus	27 cylinders wrapped with CFRP 9 cylinders tested unconfined	. Only applicable to cylinders wrapped with CFRP. . Ascending curve is linear elastic, independent of the concrete strength.
Spoelstra and Monti (1999)	Empirical model to determine the stress-strain response of FRP-confined cylinders Used Mander (1988) and Pantazopoulou and Mills models (1995)	ultimate strength ultimate strain secant stiffness lateral strain	tests of Mirmiran and Shahawy	. Model limited to circular columns wrapped with FRP.
Lam and Teng (2002)	Empirical model for strength of FRP-wrapped circular specimens	strength	200 tests from several researchers	. Limited to calculating the strength. . Applicable only to circular elements . 79% of specimens in database with concrete strengths below 40 MPa.
Karabinis and Rousakis (2002)	Plasticity model based on Drucker-Prager criterion	pressure sensitivity plastic strains slope of post-peak curve plastic modulus concrete dilatation	18 cylinder wrapped with one, two, or three layers of CFRP	. 14 parameters to be calibrated. . Calibration from eight tests. . Limited to FRP confinement.
Pivonka, Lackner, and Mang (2000)	Plasticity models based on the Extended Leon Model, and Multisurface model (Rankine, Drucker-Prager)	stress-strain behaviour of confined concrete	test on NSC cylinders from the University of Colorado, Boulder. (Hurlbut, Smith)	. Large number of parameters calibrated. . Parameters based on cylinders of low concrete strength (22 MPa, 27 MPa).
Sankarasubramanian and Rajasekaran (1996)	Combination of a plasticity failure surface (Willam and Warnke), neural networks, and a empirical formula for stress-strain of concrete (Alexander)	concrete subjected to any state of stress	cylinder subjected to lateral pressure of 55 MPa. panels in biaxial compression cylinders in uniaxial compression beams, and a nuclear vessel.	. Model unable to capture peak stresses. . Shows stiffer responses than experiments. . Post-peak response not captured. . Neural network and calibration of the model not described.

Table 2. Synopsis of literature review.

Model	Approach	Parameters analyzed	Experiments	Remarks and Limitations
Barros (2001)	Plasticity model based on a Drucker-Prager criterion and MC90 formulations	stress-strain behaviour of confined concrete	cylinders confined with steel	. Associative flow rule used not appropriate. . Drucker-Prager criterion does not reproduce reliable volumetric strains. . Unsymmetrical elasto-plastic matrix when non-associative rule used. . Poor analytical stress-strain responses.
Mirmiran, Kenneth, and Yuan (2000)	Plasticity model based on a Drucker-Prager Criterion.	stress-strain behaviour of FRP-confined concrete internal friction angle cohesion concrete strength	30 cylinders and 12 square prisms wrapped with E-glass fibre	. Drucker-Prager criterion does not reproduce reliable volumetric strains. . Post-peak behaviour grossly overestimated. . Dilatation of concrete did not follow experiments . FRP specimens not prepared appropriately.
Li and Ansari (1999)	Continuous damage mechanics model based on Ottosen failure criterion	behaviour of HSC subjected to a wide range of confinement pressures	tests on cylinders subjected to pressures from 0 to 100% of f'c	. Expanded database of experiments. . Descending post-peak behaviour shows discontinuity in the stress-strain curve.
Liu and Foster (2000)	Calibration of a Microplane model (Carol et al. 1992)	behaviour of columns confined with steel	tests of Sheikh and Uzumeri (1980), and Razvi and Saatciouglu (1996)	. No set of parameters of the model adaptable to every state of stress. . Highly dependent on the load history. . Spurious volumetric strains reported for elements in tension.
Ghazi, Attard, and Foster (2002)	Calibration of a Microplane model M4 (Bažant et al. 2000)	stress-strain curve of cylinders subjected to low confinement	analytical curves obtained from the model by Attard and Setunge	. Change of one parameter affect s the others. . Selection of parameters for one behaviour not usable for another type (e.g. unconfined and confined tests). . Determination of spurious strain behaviour difficult.
Kwon and Spacone (2002)	Combination of empirical formulations for stress-strain, concrete dilatation, and a plasticity criterion	concrete confined with steel or FRP	tests of Hurlbut (1985) on cylinders tests of Xiao et al. (1993) on columns subjected to cyclic loading	. Presented numerical instability if Poisson's ratio larger than 0.5. . Uncoupled behaviour of volumetric strains and deviatoric strains, corrected empirically. . Lateral expansion underpredicted strain in lateral steel of columns.
Assa, Nishiyama, and Watanabe (2001a, 2001b)	Combination of strain compatibility, strut and tie model, and empirical formulations	stress-strain behaviour of circular and square columns confined with steel	24 cylinders confined with spirals 34 NSC columns 31 HSC columns	. Suitable for hand calculations of circular columns. . Assumed uniform lateral pressure for circular cylinders, independent of spiral spacing. . Lateral stiffness of concrete assumed constant. . Struts based on prismatic sections, cover not considered. . Not suitable for analyzing the behaviour of different zones of confinement in the column.

Table 2. Continued.

Model	Approach	Parameters analyzed	Experiments	Remarks and Limitations
Candappa, Sanjayan, and Setunge (1999, 2001)	Modification of the nonlinear elastic model of Ottosen for secant Poisson's ratio	stress-axial strain and stress-lateral strain behaviour of cylinders subjected to low confinement	tests on cylinders from 42 MPa to 103 MPa subjected to lateral pressures of 4, 8, and 12 MPa	. Expanded database of tests. . Secant Poisson's ratios measured larger than 0.5 and close to 1.0.
Lee, Willam, and Kang (1997)	Study of stress-strain response of unconfined concrete		tests on three cylinders with different lengths	. Energy release after peak stress similar for all tests. . Predominant mode of failure was compression with axial splitting. . Stiffness degradation varied linearly with fracture energy and strength degradation. .Large dilatations occur for unconfined specimens.

Table 2. Continued.

Chapter 3. Confined Concrete

3.1 Introduction.

A set of constitutive models for confined concrete is proposed. The models consider the three-dimensional effects of concrete when it is subjected to triaxial compressive stresses. A model for concrete dilatation, a failure surface for strength enhancement, and a stress-strain curve are developed based on a large database of tests on cylinders subjected to constant lateral pressure and axial compression, and reinforced concrete columns subjected to monotonic axial compression. These models can be applied to a wide range of commercially available concretes, with strengths from 20 MPa to 130 MPa, subjected to confinement levels from 0% (unconfined) to 100% of the concrete strength.

The proposed models are combined with models from the modified compression field theory (Vecchio and Collins 1986) and then implemented in two finite element programs, one of which was developed in this work to analyze reinforced concrete solids of revolution. The programs use a nonlinear elasticity approach. The compression field modelling approach is then used to corroborate results from cylinders and columns with steel or fibre reinforced polymers (FRP).

The model for concrete dilatation is first explained in this Chapter, followed by the description of the failure surface for strength enhancement and the stress-strain curve. The post-peak behaviour of confined concrete is described by a formulation that accounts for the decay in the post-peak regime as a function of the maximum stress, the strain at peak stress, and the strain at 80% of the peak stress.

3.2 Concrete Dilatation.

This section describes the experimental program on concrete cylinders subjected to triaxial compressive stresses, carried out by Imran and Pantazopoulou (1996). The results were used in the formulation of a simple model for concrete dilatation presented herein. The model is then compared to other models from the literature using the experimental results of Imran and Pantazopoulou. Complete lateral strain-axial strain behaviour from experimental results of other researchers is given in Chapter 5.

3.2.1 Imran and Pantazopoulou Tests

A total of 130 concrete cylinders were tested under triaxial compressive stresses in a triaxial cell. The main objective of the testing program was to enhance the database on lateral deformations of confined concrete. The variables studied were: the water/cement (w/c) ratio, the level of confinement, and the load history.

The cylinders had a diameter of 54 mm and height of 108 mm. The target unconfined concrete strengths (f'_c) were: 65, 43, and 21 MPa. The w/c ratios utilized were: 0.40, 0.55, and 0.75. The cylinders were subjected to seven levels of confinement (i.e. ratio of lateral pressure to unconfined concrete strength, f_{cl} / f'_c), 0, 0.05, 0.10, 0.20, 0.40, 0.70, and 1.00, and four different load histories, as shown in Figure 68. At the time of testing, the unconfined strengths were 73.4, 47.4, and 28.6 MPa, respectively.

The axial strain was measured with Linear Voltage Displacement Transducers (LVDT's), and the lateral strain ε_{cl} was measured with 60 mm strain gauges with high

strain capacity (from 10 to 20%) located at the mid-height of the cylinder. The length of the lateral strain gauge was about one-third the perimeter of the cylinder, thus yielding average measurements of lateral strains instead of local effects. The cylinder was embedded in a rubber jacket to avoid penetration of pressurized oil during testing. A sketch of the triaxial cell is shown in Figure 69. The axial load was applied using a servo-controlled loading frame in displacement control. The lateral pressure capacity of the cell was 70 MPa; this limited the applied lateral pressure to $0.80f'_c$ on specimens with water/cement content of 0.40.

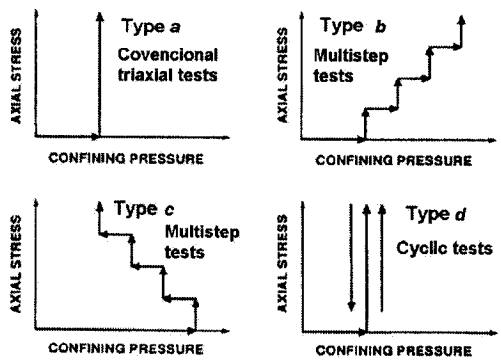

Figure 68. Loading types on Imran and Pantazopoulou tests.

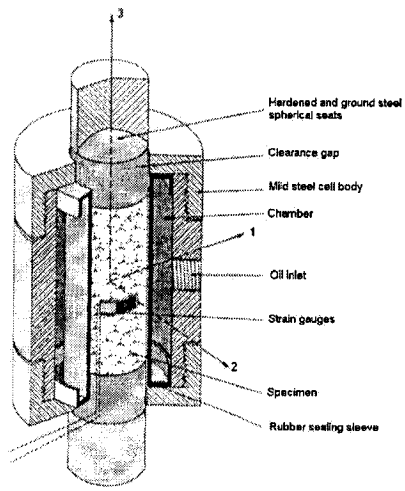

Figure 69. Triaxial cell.

The results for Type-a loading are shown here[1]. The axial stress versus axial and lateral strain curves (lateral strain shown negative, axial strain shown positive), and the lateral strain (ε_{cl}) versus axial strain ratio (ε_c / ε_{cc}) curves (axial and lateral strains positive), for the three types of concrete are shown in Figures 70 to 72, and Figures 73 to 75, respectively. The labels in Figures 70 to 72 show the lateral pressure exerted in each test.

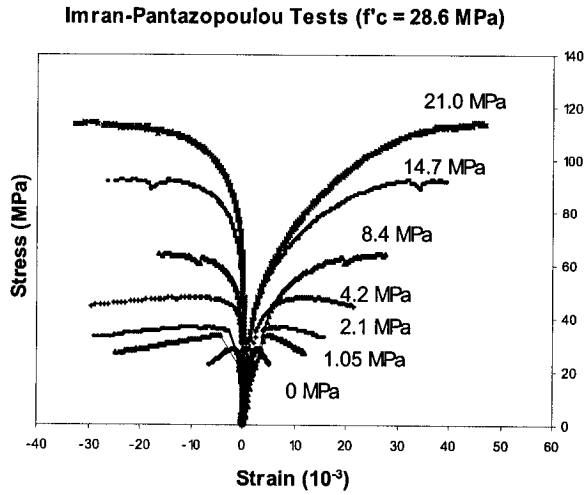

Figure 70. Axial stress-lateral, -axial strain curves for 28.6 MPa tests.

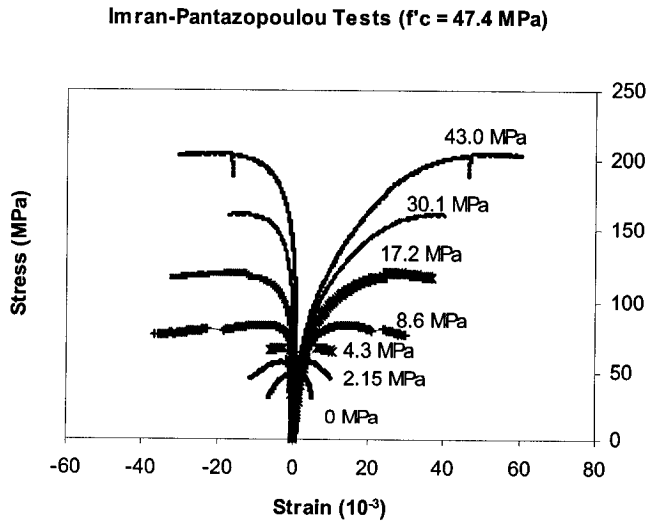

Figure 71. Axial stress -lateral, -axial strain curves for 47.4 MPa tests.

[1] "Dry" conditions at the time of testing, cylinders dried at 60°C for 72 hours before testing.

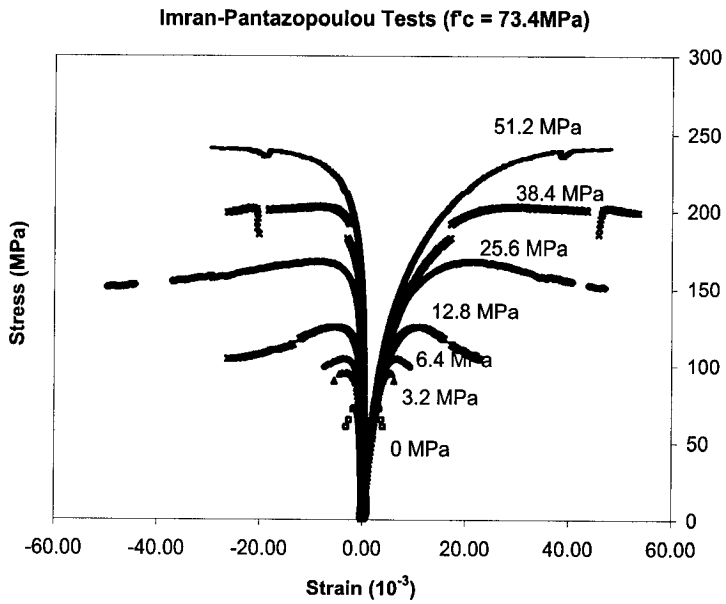

Figure 72. Axial stress-lateral, -axial strain curves for 73.4 MPa tests.

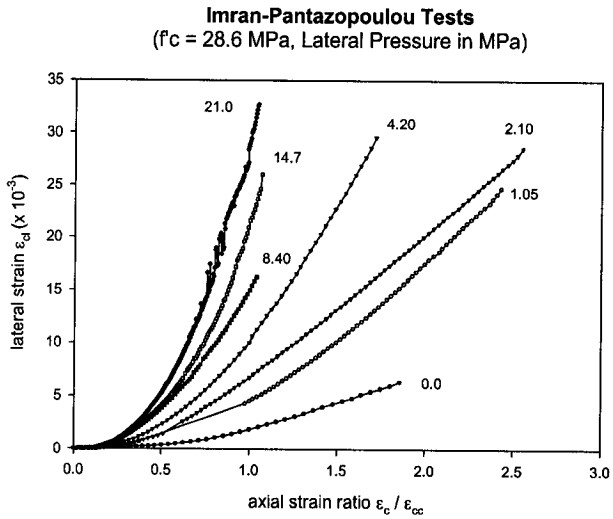

Figure 73. Lateral strain-axial strain ratio curves for 28.6 MPa tests.

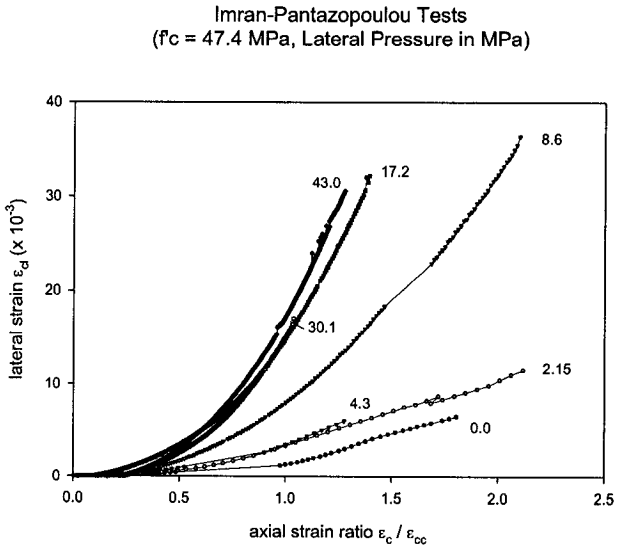

Figure 74. Lateral strain-axial strain ratio curves for 47.4 MPa tests.

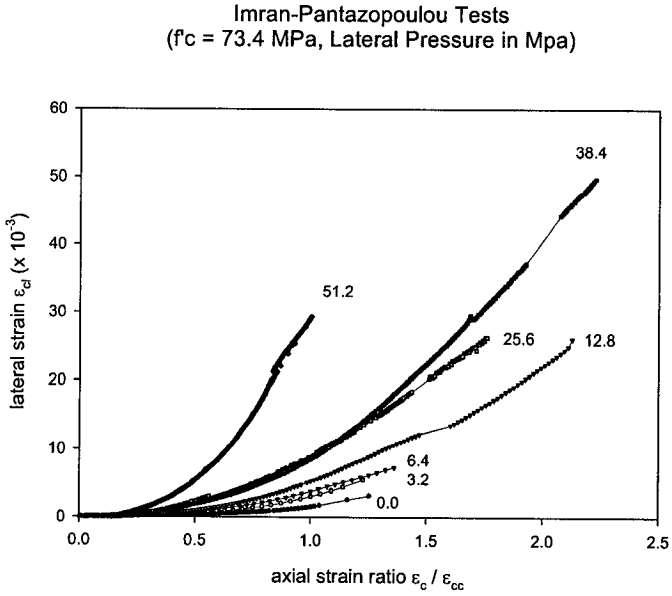

Figure 75. Lateral strain-axial strain ratio curves for 73.4 MPa tests.

The strain ε_{cc} is the strain at peak stress for each of the curves, and ε_c is the axial strain. It can be seen from Figures 73 to 75 show that for a constant axial strain ratio, the lateral strain increases with an increase in the lateral pressure on the cylinder. However, for a constant lateral strain, the axial strain ratio decreases with an increase in lateral pressure, from about 2.0 at ultimate for moderate or low confinements, to 1.0 for high confinements. This trend of lateral deformation is consistent with the results from other researchers (Hurlbut 1985, Li and Ansari 1999, Candappa et al. 2001) where the same loading type was utilized; that is, the total lateral pressure was applied first followed by incremental axial load.

Imran and Pantazopoulou found that the concrete strengths obtained in all the tests were independent with respect to the loading history. Although there were some differences in the volumetric behaviour of cylinders subjected to a monotonic load relative to the other load types (cyclic, stepwise), the axial stress-axial strain curve obtained from the monotonic load was the envelope for all other tests, and the trend from volumetric contraction to expansion was maintained. This can be seen in Figure 76 for a specimen subjected to cyclic loading, and a specimen subjected to stepwise loading (for the series of tests published in Imran et al.1996).

The deduction of a simple model for concrete dilatation based on the previous tests is presented in the next section.

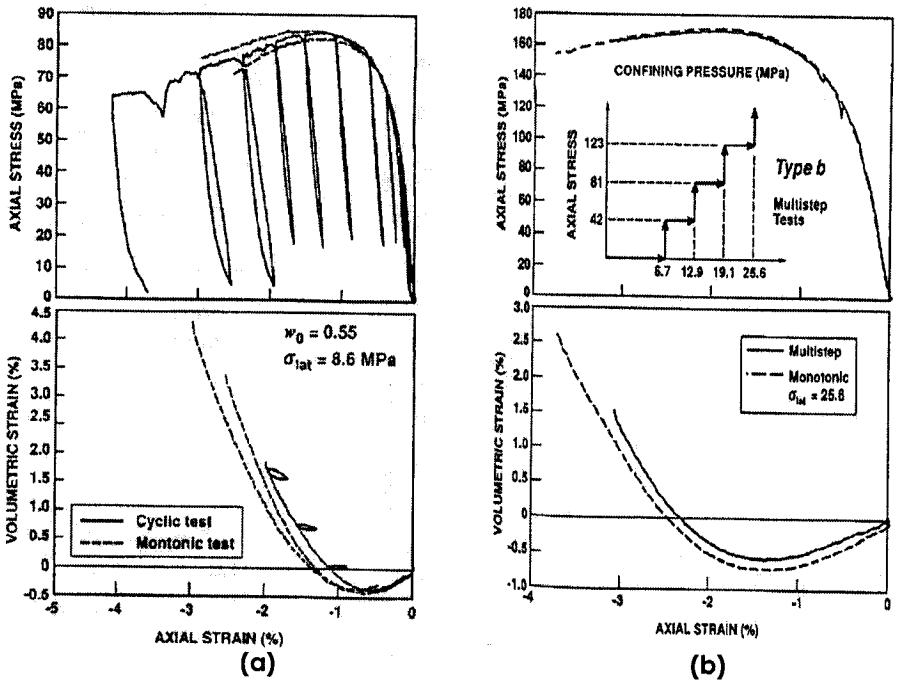

Figure 76. Imran and Pantazopoulou sample tests: (a) cyclic loading, (b) stepwise loading.

3.2.2 Proposed Model

The lateral strain (ε_{cl}) versus axial strain ratio (ε_c / ε_{cc}) curves from Figure 73 to Figure 75 were fitted to a parabola in this project:

$$\varepsilon_{cl} = \alpha \left(\frac{\varepsilon_c}{\varepsilon_{cc}} \right)^2 \qquad \text{Eq. 76}$$

The values for the parameter α, which is a function of the lateral pressure ratio f_{cl} / f'_c, are given in Table 3. It should be noted that f_{cl} is in turn a function of ε_c / ε_{cc} (and the properties of lateral reinforcement in columns). Typical regression and experimental curves for two tests are shown in Figure 77.

Table 3. Regression parameter α and concrete properties for Imran-Pantazopoulou.

f'_c [MPa]	α	f_{cl} [MPa]	f_{cl} / f'_c	ε_{cc} [%]
28.6*	1.8985	0	0.00	0.2778
	4.3352	1.05	0.037	0.4983
	4.9043	2.10	0.073	0.6325
	10.2148	4.20	0.147	1.2541
	15.1241	8.40	0.294	2.6489
	20.0389	14.7	0.514	3.7148
	27.5234	21.0	0.734	4.4927
47.4*	1.9283	0.0	0.00	0.2898
	2.7851	2.15	0.045	0.4759
	3.5487	4.30	0.09	0.7055
	8.1453	8.60	0.18	1.4225
	13.7797	30.10	0.635	3.9090
	17.5211	43.0	0.907	4.7276
73.4*	1.5829	0.00	0.00	0.3145
	3.1191	3.20	0.044	0.5011
	3.8827	6.40	0.87	0.6817
	5.4994	12.80	0.174	1.0793
	9.9812	25.60	0.348	2.1177

*actual concrete strength.

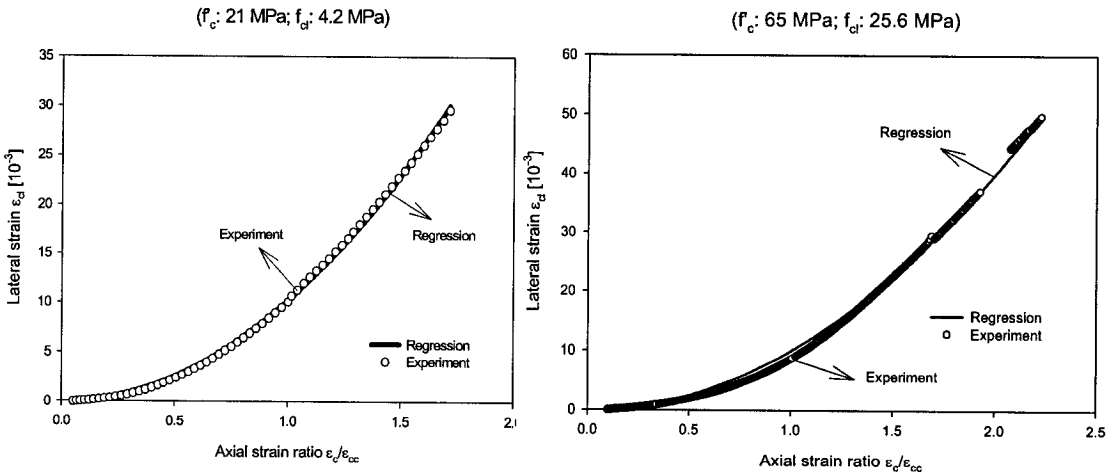

Figure 77. Lateral strain-axial strain curves for Imran-Pantazopoulou tests (target strengths 21 and 65 MPa).

The values for α were plotted against the lateral pressure ratio f_{cl} / f'_c, for each concrete type. The plots are shown in Figure 78, along with the trend line for each plot and its correlation.

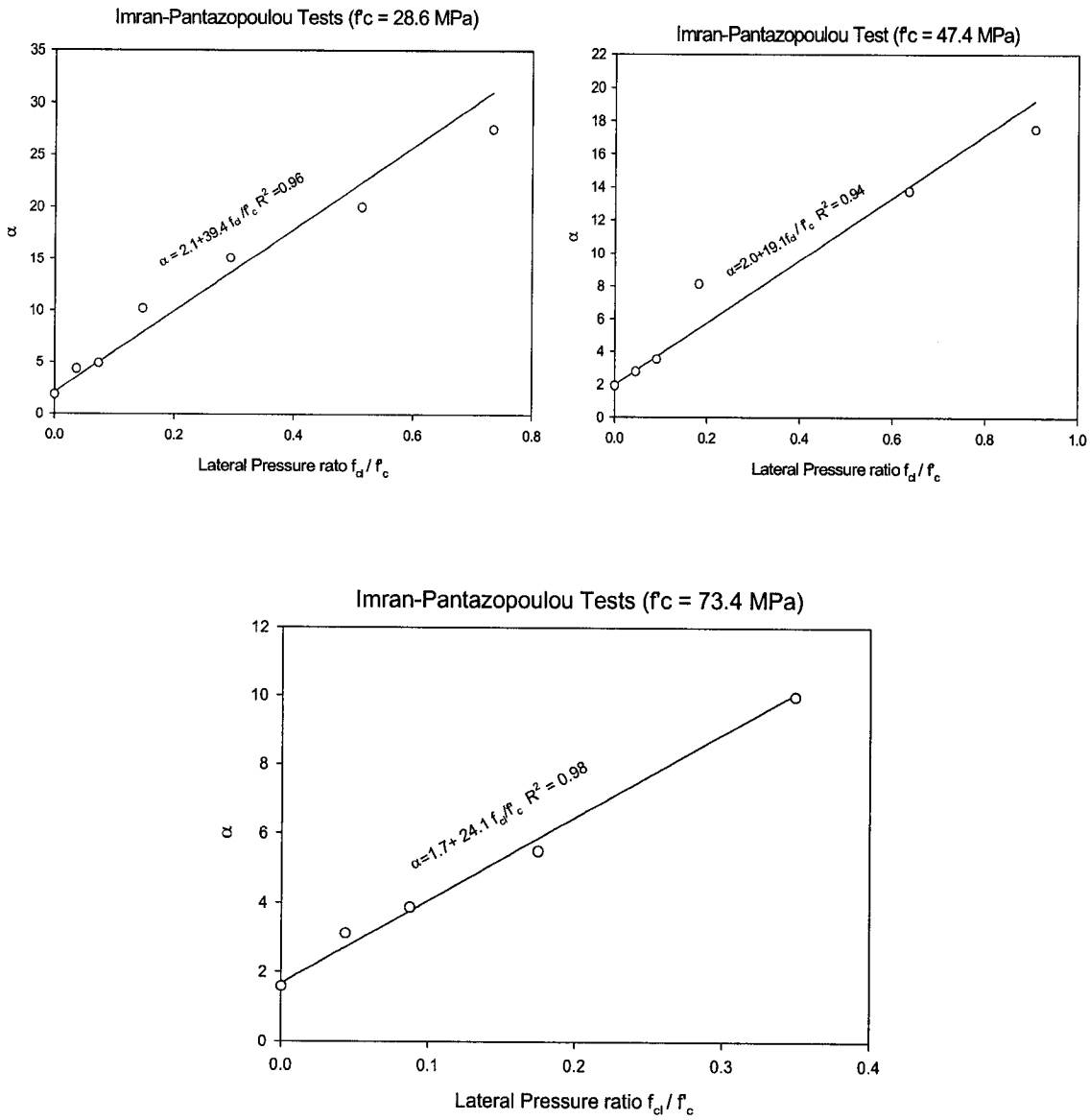

Figure 78. Curves for α versus lateral pressure ratio f_{cl} / f'_c.

The data used in the regression excluded three data points that seemed not to follow the general trend showed by the experiments. One corresponded to the 47.4 MPa concrete and two to the 73.4 MPa concrete. Good correlations were found for the three types of concrete, with R^2 values of 0.96, 0.94, and 0.98 for the 28.6 MPa, 47.4 MPa, and 73.4 MPa concretes, respectively. To evaluate the variability of α with respect to the lateral pressure ratio f_{cl} / f'_c for all concrete types, and obtain a general expression for all the series of concrete strength used in the experiments, all the plots were grouped in one graph as shown in Figure 79 with the associated linear trend.

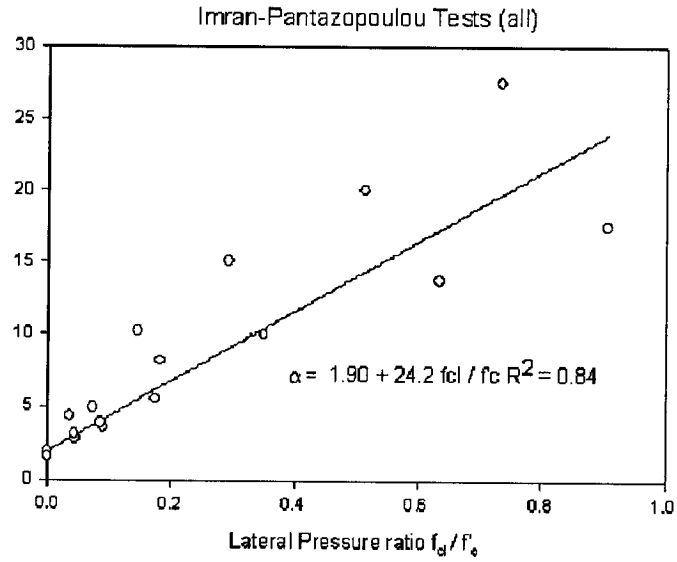

Figure 79. Value of α versus f_{cl}/f'_c for all Imran-Pantazopoulou tests.

The value of α increases with an increase in the lateral pressure ratio or confinement level. At low confinement levels ($f_{cl} / f'_c \leq 0.20$) the values for α are closer to the general trend line, and the scatter increases for larger confinement levels. However, a good correlation was obtained. The equation for lateral strain given above can be expressed in terms of the confinement level as:

$$\varepsilon_{cl} = \left(1.9 + 24.2\frac{f_{cl}}{f'_c}\right)\left(\frac{\varepsilon_c}{\varepsilon_{cc}}\right)^2 \qquad \text{Eq. 77}$$

The proposed "secant Poisson's ratio" ν, is defined as the ratio between the lateral strain and the concrete axial strain, considering the initial Poisson's ratio ν_o:

$$\nu = \left(1.9 + 24.2\frac{f_{cl}}{f'_c}\right)\frac{\varepsilon_c}{\varepsilon_{cc}^{\,2}}.10^{-3} + \nu_o \qquad \text{Eq. 78}$$

Although this relationship is based on tests on cylinders subjected to constant lateral pressure throughout the loading process, it may be used in incremental calculations with varying lateral pressure f_{cl} and strain at peak stress ε_{cc}, as can be seen in Figure 80, where the relationship becomes nonlinear. If the lateral pressure and the peak strain are kept constant, the formulation results in a straight line, which means the lateral strain increases proportional to the axial strain. This trend was also observed by Lee et al. (1997) in their experiments.

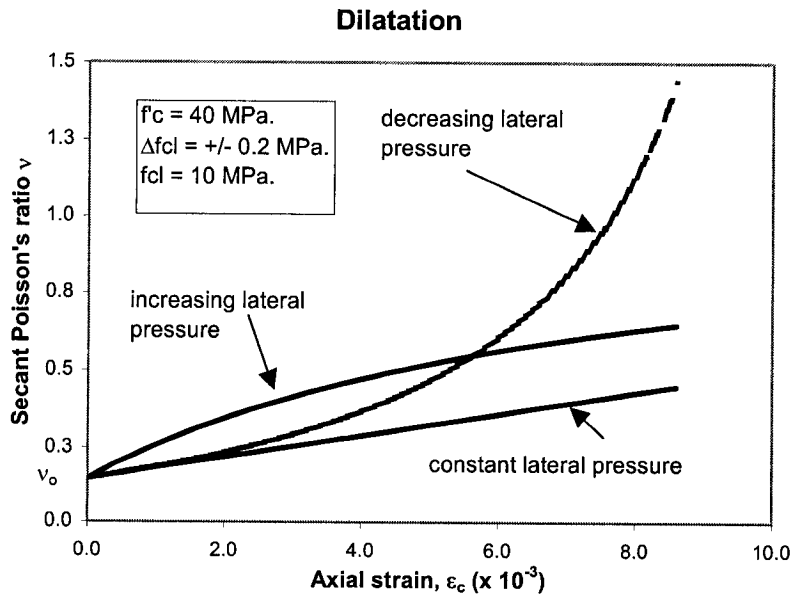

Figure 80. Sketch of the secant Poisson's ratio with variable and constant lateral pressure.

The model for concrete dilatation captures the behaviour of confined concrete in a simple manner. It is a function of the confinement represented by the lateral pressure f_{cl}, the strain at peak stress ε_{cc}, and the unconfined concrete strength f'_c. There is no upper boundary for the maximum value of the secant Poisson's ratio and may only be limited in finite element applications by the type of elements utilized and their deformation capabilities. It follows the behavioural tendency of volumetric changes in concrete independent of the loading history.

3.2.3 Comparison with Other Models

The experimental results of Imran and Pantazopoulou were also used in the comparison of analytical results obtained from the proposed model and those from the models by Imran and Pantazopoulou (1996), Spoelstra and Monti (1999), Vecchio (1992), and Kwon and Spacone (2002). A brief description of each model is given next and comparisons of lateral strain at peak stress obtained from the models and the experimental results follow afterwards. Complete axial stress versus axial strain, and axial stress-lateral strain curves of specimens tested by other researchers are given in Chapter 5.

3.2.3.1 Imran and Pantazopoulou Model

The volumetric strain ε_v is given by the equation:

$$\varepsilon_v = (1-2\nu_o)\left[\frac{2f'_{cl}}{E} + \varepsilon_c{}^o\left(\frac{\varepsilon_c}{\varepsilon_c{}^o} - \left[\frac{\langle \varepsilon_c{}^{\lim} - \varepsilon_c \rangle}{\varepsilon_c{}^o - \varepsilon_c{}^{\lim}}\right]^2\right)\right] \qquad \text{Eq. 79}$$

Here ε_c^o is the axial strain (negative) at which the volumetric strain becomes null. It is taken equal to the strain at peak stress ε_{cc}. ε_c^{lim} is the axial strain at which the concrete cracks in the lateral direction:

$$\varepsilon_c^{\lim} = \frac{1-\nu_o}{\nu_o E} f'_{cl} - \frac{\varepsilon_{cr}}{\nu_o} \qquad \text{Eq. 80}$$

where ε_{cr} is the cracking strain, E is the material stiffness, and f'_{cl} is the "effective" lateral pressure:

$$f'_{cl} = f_{cl} - p\nu_{void} \qquad \text{Eq. 81}$$

where the "effective porosity" is ν_{void}, and p is the pore pressure. The McCauley brackets < > are calculated as: <x> = 0.5[x + abs(x)]. Due to the lack of information about the pore pressure and porosity, the "effective" lateral pressure is taken equal to the applied lateral pressure (i.e. $f'_{cl} = f_{cl}$) in the calculation of the lateral strain at peak.

3.2.3.2 Spoelstra and Monti Model

The stress-strain formulation proposed by Spoelstra and Monti (1999) for FRP-confined concrete was discussed in the literature review (Chapter 2). The model for lateral strain in concrete, ε_{cl}, can also be applied to cylinders with constant lateral pressure. The lateral strain in concrete is calculated as follows:

$$\varepsilon_{cl} = \frac{E_c\varepsilon_c - f_c}{2\beta.f_c}, \qquad \text{Eq. 82}$$

$$\beta = \frac{E_c}{f'_c} - \frac{1}{\varepsilon_{co}} \qquad \text{Eq. 83}$$

where f_c is the axial stress in the concrete cylinder, ε_c is the axial strain, E_c the initial stiffness and ε_{co} is the unconfined peak strain.

3.2.3.3 Vecchio Model

This model established a relationship for the Poisson's ratio as a function of the axial strain:

If $\varepsilon_c < 0.5\ \varepsilon_{co}$, $\nu = \nu_o$.

If $\varepsilon_c > 0.5\ \varepsilon_{co}$:

$$\nu = \nu_o\left[1+1.5\left(2\frac{\varepsilon_c}{\varepsilon_{co}}-1\right)^2\right] \le 0.5 \qquad \text{Eq. 84}$$

3.2.3.4 Kwon and Spacone Model

The uniaxial transverse strain ratio ν_{ui}, in any i-direction of a concrete solid subjected to triaxial stresses was expressed as:

$$\nu_{ui} = \nu_o\left[1+\frac{1}{K_\nu}\left\{A_i\left(\frac{\varepsilon_{ui}}{\varepsilon_{cci}}\right)+B_i\left(\frac{\varepsilon_{ui}}{\varepsilon_{cci}}\right)^2+C_i\left(\frac{\varepsilon_{ui}}{\varepsilon_{cci}}\right)^3\right\}\right] \qquad \text{Eq. 85}$$

where ε_{ui} is the uniaxial strain. The coefficients were defined as:

$$K = \frac{1}{2\nu_o} \qquad \text{Eq.86a}$$

$$K_\varepsilon = \frac{\varepsilon_f}{\varepsilon_{cc}} \qquad \text{Eq.86b}$$

$$K_\sigma = \frac{f_{cc}}{f_f} \qquad \text{Eq.86c}$$

$$K_\nu = E_o\frac{\varepsilon_{cc}}{f_{cc}} \qquad \text{Eq.86d}$$

$$A = C + K - 2 \qquad \text{Eq.86e}$$

$$B = 1 - 2C \qquad \text{Eq.86f}$$

$$C = K\frac{K_\sigma - 1}{(K_\varepsilon - 1)^2} - \frac{1}{K_\varepsilon} \qquad \text{Eq. 86f}$$

and

$$f_f = \frac{f_{cc} f'_c}{(5f'_c - f_{cc})} \leq 1.4$$ **Eq. 87**

The strain ε_f corresponding to f_f is obtained from the post-peak branch of the Saenz stress-strain curve (see Chapter 2):

$$f_c = f_{cc} \frac{K_v \left(\frac{\varepsilon_{ui}}{\varepsilon_{cci}} \right)}{1 + (K_v - 1) \left(\frac{\varepsilon_{ui}}{\varepsilon_{cci}} \right)^{K_v / K_v - 1}}$$ **Eq. 88**

3.2.4 Analytical and Experimental Comparison of Lateral Strain at Peak Stress

The four models described in the previous sections, along with the proposed model, were used to calculate the lateral strain at peak stress of the Imran and Pantazopoulou tests described in Section 3.2.1. The experimental-to-calculated lateral strain ratios are shown in Table 4, and are also graphed in Figure 81.

Table 4. Comparison of experimental-to-calculated lateral strain ratios at peak stress

f'c	ε_{co}* [%]	E* [MPa]	f_{cl}	ε_{cl} (peak)* [10-3]	ε_{cl}(exp) / ε_{cl}(calc.) Imran Pant.	Vecchio	Spoelstra Monti	Kwon Spacone	Proposed Model
28.6	0.2778	19700	0.00	1.87	1.35	1.80	1.35	2.03	0.81
			1.05	4.53	1.85	1.82	1.58	3.36	1.28
			2.10	6.73	2.18	2.13	1.83	4.23	1.45
			4.20	10.06	1.64	1.60	1.61	3.68	1.37
			8.40	14.96	1.16	1.13	1.39	2.93	1.15
			14.70	21.56	1.19	1.16	2.06	2.99	1.08
			21.00	29.21	1.35	1.30	2.88	-----	1.10
47.4	0.2898	22300	0.00	1.24	0.86	1.14	0.86	1.04	0.53
			2.15	3.24	1.40	1.36	0.89	2.01	0.88
			4.30	3.40	1.00	0.96	0.59	1.61	0.66
			8.60	7.96	1.16	1.12	0.67	2.31	0.95
			17.20	14.89	1.17	1.12	0.89	2.53	1.03
			30.10	15.12	0.81	0.77	0.80	1.80	0.66
			43.00	17.21	0.77	0.73	0.97	-----	0.56
73.4	0.3145	29700	0.00	1.54	0.98	1.30	0.98	1.16	0.65
			3.20	3.05	1.26	1.22	0.98	1.62	0.82
			6.40	3.78	1.16	1.11	0.72	1.67	0.75
			12.80	5.28	1.04	0.98	0.61	1.70	0.68
			25.60	8.62	0.86	0.81	0.56	1.67	0.64
			38.40	8.84	0.62	0.58	0.46	1.27	0.46
			51.20	29.33	1.30	1.23	1.08	2.94	1.13
* From Exp. Results				**Ave**	1.20	1.21	1.13	2.24	0.89
				Dev	0.37	0.38	0.59	0.90	0.29
				CV [%]	30.7	31.4	52.5	40.0	32.3

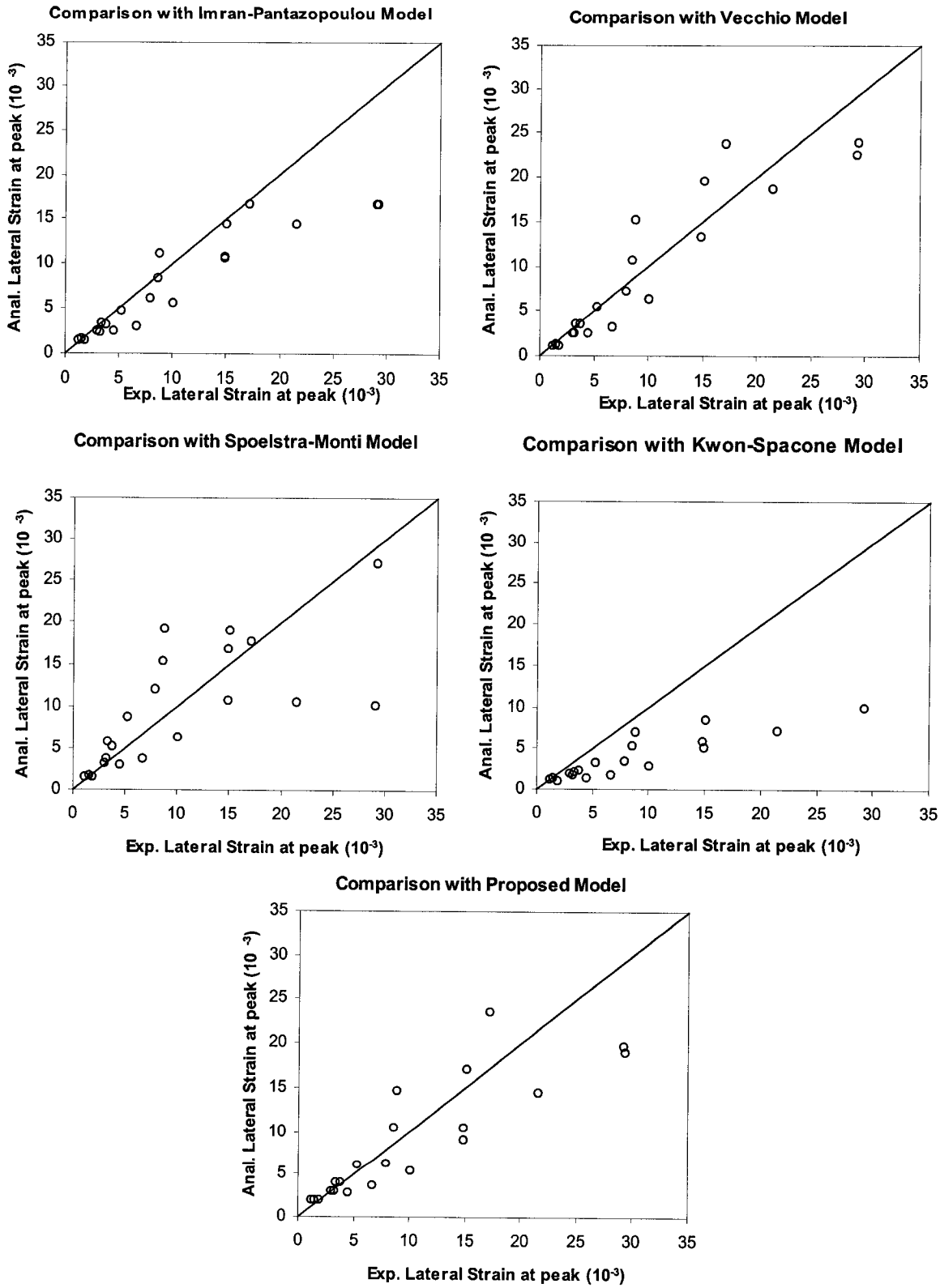

Figure 81. Plots of analytical to experimental lateral strains at peak stress.

By measuring the scatter as a function of the coefficient of variation (CV), large scatter is obtained from the models by Spoelstra and Monti, and Kwon and Spacone. The models of Vecchio, Imran and Pantazopoulou, and the proposed model produce similar scatter. In general, the proposed model overestimates by 11% the value of lateral strain at peak stress for this set of tests. The models of Vecchio and Imran and Pantazopoulou underestimate the lateral strain at peak stress by 21% and 20%, respectively. Note, however, that the predictions of all the models show large variance in the calculation of the lateral strain at peak stress.

Note that the model of Imran and Pantazopoulou relies on the computation of the pore pressure and porosity, which are not readily available in many of the tests carried out by other researchers. At the same time, the upper boundary of 0.5 for the Poisson's ratio imposed in the Vecchio model limits the possible expansion of the material beyond peak stress, which has been observed to be larger than 0.5 (see Chapter 2).

The model of Spoelstra and Monti is based on that of Imran and Pantazopoulou; it utilizes mechanical properties of the unconfined cylinder in the calculation of lateral strain, instead of the more elaborate tests to determine porosity and pore pressure. However, the scatter is larger than that for the Imran and Pantazopoulou model. Finally, the Kwon and Spacone model produces very low Poisson's ratios at peak stress, resulting in a gross underestimation of the lateral strain at peak. The phenomenological model proposed has the advantage of being simple, has no upper limit with respect to the maximum secant Poisson's ratio that can be reached, and is a function of the triaxial compressive state in the concrete.

3.3 Concrete Behaviour under Triaxial Compression

A study of the strength of concrete subjected to triaxial compressive stresses is presented. The capacity of available models to predict the strength of reinforced concrete columns and small confined concrete cylinders is discussed first. Then, the levels of confinement (i.e. lateral pressure to unconfined concrete strength ratio) and concrete types are divided into ranges according to the observed behaviour of concrete columns and cylinders subjected to constant lateral pressure.

The four-parameter failure surface of Ottosen (1977) is utilized in this thesis. By solving a system of equations based on the results of basic concrete tests, three of the failure surface parameters are expressed as a function of the chosen independent parameter. This parameter is then obtained from statistical analyses of experimental results, according to the categories of confinement levels and concrete types described earlier. Values for this parameter are proposed for each category to predict the strength of confined concrete, and comparisons are made with respect to the analytical results from previous models and the experimental results of columns and cylinders described above. A simple model for predicting the strain at peak stress of confined concrete is proposed based on triaxial compressive tests. The strain at peak stress is found to be a function of the unconfined concrete strength, the strain at peak unconfined concrete strength, and of the level of confinement.

3.3.1 Column Behaviour at Peak Strength

A total of 168 concrete columns tested by several researchers were used to investigate the ability of available models to predict strength. All the columns were tested in monotonic axial compression. The unconfined concrete strength varied from

31 to 105 MPa; half of the 168 columns were square and the other half were circular. The side of the square section ranged from 205 to 305 mm, and the diameter of circular columns ranged from 203 to 610 mm. Table 5 shows the number of columns per researcher(s), dimensions, unconfined concrete strength f'_c, and the range of confinement level (i.e. lateral pressure to unconfined concrete strength ratio, f_{cl} / f'_c) for each set of columns. The average maximum concrete lateral pressure was obtained by equilibrium of lateral forces in the concrete and the steel ties. The steel stress that produced the maximum lateral pressure was used to calculate the maximum concrete stress, and not the yield stress (if different) reported by the researchers. Complete details of all the columns are given in Appendix A, Section A.1.

Table 5. Description of sets of columns per researcher (s).

Researcher (s)	Tests	Section Size [mm]	f'_c [MPa] max	f'_c [MPa] min	f_{cl} / f'_c max	f_{cl} / f'_c min
Sheikh and Uzumeri (1978)	22	305 x 305 305 x 305 305 x 305	40.9	31.3	0.22	0.03
Sheikh and Toklucu (1993)	26	356 254 203	35.9	34.9	0.19	0.02
Montgomery and Sheikh (1996)	15	305 254	89.8	69.7	0.17	0.01
Pessiki (2001)	13	610 356	58.6	52.1	0.21	0.04
Razvi and Saatcioglu [Circular] (1996)	16	230	105.4	51.0	0.08	0.02
Razvi and Saatcioglu [Square] (1996)	24	230 x 230	105.4	51.0	0.13	0.03
Nagashima (1992)	24	205 x 205	100.4	51.3	0.11	0.04
Nagashima (1993)	14	220 x 220	96.2	92.4	0.16	0.04
Li (1994)	14	210	82.5	52.0	0.32	0.03
Total	*168*					

Ten models widely used in the literature to evaluate the analytical strength of confined concrete were used to calculate the loading capacity of the sets of columns in Table 5. The analytical formulations of the models are given in Table 6.

Model	Expression	Variables
Tresca (Chen 1982)	$\sqrt{J_2}.\sin\left(\theta+\frac{\pi}{3}\right)-\frac{f'_c}{2}=0$	$\theta=\frac{1}{3}\arccos\left[\sqrt{2}\frac{J_3}{\tau_{oct}^{\ 3}}\right]$ $\tau_{oct}=\sqrt{\frac{2}{3}J_2}$
Von Mises (VM) (Chen 1982)	$J_2-k^2=0$	$k=\frac{1}{\sqrt{3}}f'_c$
Mohr-Coulomb (MC) (Chen 1982)	$\frac{1}{3}I_1.\sin\phi+\sqrt{J_2}.\sin\left(\theta+\frac{\pi}{3}\right)+\frac{\sqrt{J_2}}{\sqrt{3}}\cos\left(\theta+\frac{\pi}{3}\right).\sin\phi-c.\cos\phi=0$	$\phi=37^0$ $c=f'_c\frac{1-\sin\phi}{2\cos\phi}$
Drucker-Prager (DP) (Chen 1982)	$\alpha_c I_1+\sqrt{J_2}-k_c=0$	$\alpha_c=\frac{2\sin\phi}{\sqrt{3}(3-\sin\phi)}$ $k_c=\frac{6c.\cos\phi}{\sqrt{3}(3-\sin\phi)}$
Hsieh et al. (Chen 1982)	$2.0108\ \frac{J_2}{f'^{\,2}_c}+0.9714\ \frac{\sqrt{J_2}}{f'_c}+9.1412\ \frac{f_{c1}}{f'_c}+0.2313\ \frac{I_1}{f'_c}-1=0$	

Table 6. Failure surface models.

Model	Expression	Variables
Barros (2001)	$\alpha\frac{J_2}{f'_c}+\lambda\sqrt{J_2}+\beta I_1=0$	$\lambda=c_1.\cos\left[\frac{1}{3}\arccos(c_2.\cos 3\theta)\right], \cos 3\theta \geq 0$ $\lambda=c_1.\cos\left[\frac{\pi}{3}-\frac{1}{3}\arccos(-c_2\cos 3\theta)\right], \cos 3\theta \leq 0$ $r=\frac{f'_c}{f_{ct}}, \alpha=\frac{1}{9r^{1.4}}, \beta=\frac{1}{3.7r^{1.1}}$ $c_1=\frac{1}{0.7r^{0.9}}, c_2=1.0-6.8(r-0.07)^2$ θ is the Lode angle, f'_{ct} is the tensile strength
Ottosen (Chen 1982)	$\alpha\frac{J_2}{f'_c}+\lambda\sqrt{J_2}+\beta I_1=0$	
Richart et al. (1928)	$f_{cc}=f'_c+4.1f_{cl}$	
Vecchio (1992)	$f_{cc}=f'_c\left[4.0\frac{f_{cb}}{f'_c}+\left(1+0.92\frac{f_{cn}}{f'_c}-0.76\left(\frac{f_{cn}}{f'_c}\right)^2\right)\right]$	$f_{cb}=-f_{c1}, f_{cn}=-(f_{c2}-f_{c1})$ $f_{cn}=-(f_{c2}-f_{c1})$
Mander et al. (1988)	$f_{cc}=f'_c\left(2.254\sqrt{1+7.94\frac{f_{cl}}{f'_c}}-2\frac{f_{cl}}{f'_c}-1.254\right)$	

Table 6. Cont'd.

In Table 6, I_1, J_2 and J_3 are stress invariants calculated from principal concrete stresses $f_{c1} \geq f_{c2} \geq f_{c3}$. The calculated to measured strength ratios are shown in Table 7 along with the average, standard deviation, and coefficient of variance, for each group of columns, and for the complete database. The model that best predicted the strength for each set of columns is highlighted in bold script.

Table 7. Calculated to measured strength ratios, columns.

Researcher	Failure Surface Models										
	Tresca	VM	MC	DP	Hsieh et al.	Barros	Ottosen	Richart et al.	Vecchio	Mander	
Sheikh and Uzumeri	**0.95**	**0.95**	1.08	1.08	1.37	1.27	1.45	1.22	1.21	1.35	**Ave.**
	0.068	**0.068**	0.111	0.111	0.134	0.127	0.155	0.102	0.100	0.119	**St.Dev.**
	7.10	**7.10**	10.28	10.28	9.72	10.03	10.73	8.34	8.19	8.85	**CV**
Montgomery and Sheikh	0.93	0.93	**1.00**	**1.00**	1.26	1.08	1.32	1.14	1.13	1.24	**Ave.**
	0.059	0.059	**0.100**	**0.100**	0.174	0.169	0.202	0.127	0.124	0.159	**St.Dev.**
	6.39	6.39	**10.06**	**10.06**	13.76	15.57	15.32	11.16	10.94	12.76	**CV**
Sheikh and Toklucu	0.83	0.83	0.89	0.89	1.12	1.03	1.17	1.01	**1.01**	1.11	**Ave.**
	0.056	0.056	0.095	0.095	0.160	0.152	0.186	0.120	**0.117**	0.145	**St.Dev.**
	6.78	6.78	10.68	10.68	14.27	14.70	15.89	11.83	**11.59**	13.08	**CV]**
Pessiki et al.	0.66	0.66	0.73	0.73	0.94	0.84	**0.99**	0.84	0.84	0.92	**Ave.**
	0.103	0.103	0.092	0.092	0.124	0.114	**0.139**	0.108	0.106	0.114	**St.Dev.**
	15.67	15.67	12.51	12.51	13.18	13.63	**14.06**	12.79	12.72	12.37	**CV**
Razvi and Saatcioglu (Circular)	0.85	0.85	0.85	0.85	1.04	0.87	1.07	**0.96**	0.95	**1.03**	**Ave.**
	0.039	0.039	0.032	0.032	0.051	0.059	0.059	**0.038**	0.037	**0.049**	**St.Dev.**
	4.57	4.57	3.76	3.76	4.96	6.74	5.56	**3.94**	3.89	**4.76**	**CV**
Razvi and Saatcioglu (Square)	0.87	0.87	0.93	0.93	1.18	1.01	1.24	1.07	**1.06**	1.17	**Ave.**
	0.065	0.065	0.051	0.051	0.086	0.097	0.101	0.062	**0.060**	0.080	**St.Dev.**
	7.49	7.49	5.43	5.43	7.26	9.59	8.18	5.78	**5.70**	6.80	**CV**
Nagashima* et al. (1992)	0.77	0.77	0.81	0.81	1.03	0.88	1.07	0.93	0.92	**1.02**	**Ave.**
	0.065	0.065	0.058	0.058	0.077	0.081	0.082	0.066	0.066	**0.074**	**St.Dev.**
	8.47	8.47	7.09	7.09	7.50	9.17	7.65	7.15	7.13	**7.30**	**CV**
Nagashima* et al. (1993)	0.83	0.83	0.90	0.90	1.15	0.97	1.20	1.03	**1.02**	1.13	**Ave.**
	0.053	0.053	0.039	0.039	0.072	0.074	0.089	0.051	**0.050**	0.062	**St.Dev.**
	6.44	6.44	4.38	4.38	6.30	7.60	7.38	4.98	**4.85**	5.50	**CV**
Li*	0.81	0.81	0.88	0.88	1.11	0.96	1.16	**1.00**	1.00	1.09	**Ave.**
	0.125	0.125	0.064	0.064	0.081	0.076	0.091	**0.069**	0.069	0.084	**St.Dev.**
	15.35	15.35	7.33	7.33	7.29	7.98	7.82	**6.85**	6.92	7.69	**CV**
All	0.84	0.84	0.90	0.90	1.14	1.00	1.19	**1.03**	**1.02**	1.13	**Ave.**
	0.104	0.104	0.120	0.120	0.167	0.169	0.186	**0.137**	**0.135**	0.157	**St.Dev.**
	12.42	12.42	13.34	13.34	14.61	16.83	15.58	**13.27**	**13.16**	13.97	**CV**

* See Razvi and Saatciouglu (1999)

Plots of the predicted versus experimental strengths are given in Appendix A, Section A.2. In general, the Vecchio and Richart et al. models reasonably predict the strength of these columns. It should be noted that the model by Vecchio slightly differs from that by Richart et al. For each set of specimens, some models produce better

results than others. The Tresca and Von Mises models predicted the same strength when the lateral stresses in all directions were considered equal (i.e. $f_{c1} = f_{c2}$). The Drucker-Prager model reduced to the Mohr-Coulomb model and yielded the same results when considering the predictions along the compressive meridian. These four models underestimated the strengths by as much as 34%. The models by Hsieh et al., Ottosen (as in Chen 1982), and Mander considerably overestimated most of the strengths (up to 45%). Although the average strength ratio for all the columns was equal to 1.0 when using the model by Barros, a careful examination shows that this model yielded the largest coefficient of variance, and that strength predictions of 70% of columns were better when using the Vecchio or Richart et al. models.

3.3.2 Cylinder Behaviour at Peak Strength

Small concrete cylinders subjected to triaxial compression are considered here. The confining pressure was applied uniformly around the cylinder using pressurized oil. These sets of experimental results allow for the examination of the effectiveness of each of the previous models to calculate the strength enhancement at the material level. The description of each group of specimens is given in Table 8. Details of all the specimens are given in Appendix B, Section B.1. Using the models described in Table 6, the overall average calculated-to- measured strength ratios, standard deviations, and coefficients of variance, are given in Table 9. Plots of analytical against experimental results for each set of specimens are shown in Appendix B, section B.2.

Table 8. Description of sets of cylinders per researcher (s).

Researcher	Tests	ϕ x h [mm]	f'_c [MPa] max	min	f_{cl} / f'_c max	min
Hurlbut (See Pivonka et al. 2000)	4		22.1	22.1	0.63	0.03
Gardner (1969)	3	75 x 150	27.6	27.6	0.94	0.31
Li-Ansari (1999)	14	100 x 200	103.0	42.0	0.93	0.18
Richart et al. (1928)	16*	100 x 200	25.2	7.2	3.90	0.07
Attard-Setunge (1996)	38	100 x 200	132.0	60.0	0.25	0.02
Imran-Pantazopoulou (1996)	18	54 x 108	64.7	21.2	1.00	0.05
Xie-Alwi-McGregor (1995)	26	55.5 x 110	119.0	60.2	0.50	0.01
Total:	***119***					

* Average of four tests

ϕ: Diameter

h: Height

Table 9. Calculated to measured strength ratios, cylinders.

Researcher(s)	Failure Surface Models								
	VM/ Tresca	DP/ MC	Hsieh et al.	Barros	Ottosen	Richart et al.	Vecchio	Mander	
Hurlbut	0.67	0.87	1.10	1.06	1.18	1.01	**1.00**	1.02	**Ave.**
	0.191	0.054	0.104	0.108	0.119	0.059	**0.058**	0.148	**St.Dev.**
	28.52	6.22	9.46	10.15	10.07	5.81	**5.76**	14.44	**CV [%]**
Gardner	0.42	0.72	0.90	0.83	**1.00**	0.87	0.86	0.75	**Ave.**
	0.073	0.031	0.061	0.065	**0.055**	0.045	0.043	0.124	**St.Dev.**
	17.44	4.27	6.74	7.87	**5.55**	5.14	5.01	16.55	**CV [%]**
Li and Ansari	0.66	1.27	1.38	1.17	1.39	1.31	1.29	**1.17**	**Ave.**
	0.047	0.239	0.107	0.108	0.131	0.176	0.169	**0.048**	**St.Dev.**
	7.16	18.91	7.75	9.29	9.41	13.42	13.13	**4.07**	**CV [%]**
Richart et al.	0.46	0.79	0.95	0.89	1.04	**0.96**	0.94	0.76	**Ave.**
	0.132	0.056	0.116	0.119	0.115	**0.075**	0.072	0.229	**St.Dev.**
	28.48	7.08	12.21	13.35	11.06	**7.83**	7.63	30.17	**CV [%]**
Attard and Setunge	0.73	0.79	**1.00**	0.83	1.04	0.90	0.90	0.98	**Ave.**
	0.102	0.052	**0.060**	0.064	0.071	0.055	0.055	0.058	**St.Dev.**
	13.94	6.63	**6.04**	7.68	6.78	6.10	6.18	5.87	**CV [%]**
Imran and Pantazopoulou	0.64	1.00	1.09	0.90	1.25	1.01	**1.00**	0.99	**Ave.**
	0.150	0.068	0.063	0.087	0.130	0.072	**0.067**	0.101	**St.Dev.**
	23.37	6.83	5.78	9.62	10.39	7.12	**6.74**	10.13	**CV [%]**
Xie, Elwi and McGregor	0.59	0.76	**0.98**	0.84	1.05	0.89	0.88	0.92	**Ave.**
	0.124	0.058	**0.060**	0.055	0.077	0.069	0.068	0.054	**St.Dev.**
	20.87	7.67	**6.08**	6.51	7.28	7.83	7.74	5.88	**CV [%]**
All	0.63	0.87	**1.05**	0.90	1.09	**0.97**	**0.96**	**0.96**	**Ave.**
	0.148	0.191	**0.151**	0.134	0.147	**0.156**	**0.151**	**0.153**	**St.Dev.**
	23.40	21.86	**14.45**	14.93	13.44	**16.01**	**15.69**	**15.95**	**CV [%]**

The strength of these cylinders, in general, best predicted with the Hsieh et al. model, followed closely by the predictions obtained with the Richart et al. and Vecchio models. The Tresca and Von Mises models predicted the same strengths, as did Mohr-Coulomb and Drucker-Prager models for the case of cylinders subjected to equal pressure around their circumference. Similar results from the two models are represented in Table 9.

Von Mises predictions grossly underestimated all of the experimental results by 37%, followed by those obtained with the Mohr-Coulomb (or Drucker-Prager) model which underestimated the strengths by 13 %. It should be said that the Mohr-Coulomb model is widely used in commercial finite element programs. As for columns, the Ottosen model (as in Chen 1982) overestimated the results by about 9%. The Barros and Mander models underestimated the results of about 70% of the total number of specimens. With all the models, as can be seen in the figures of Appendix B, Section B.2, the scatter increased with an increase in the experimental strength; the predictions were closer to the analytical values for strengths less than 75 MPa, except when the Tresca (and Von Mises) and Mohr-Coulomb (and Drucker-Prager) models were utilized.

3.3.3 Low and High Confinement, Normal and High Strength Concrete

According to the level of confinement attained in the experimental results of reinforced concrete columns and concrete cylinders, a set of definitions are presented to relate the type of concrete and the lateral pressure ratio.

3.3.3.1 Definitions of Concrete Strength and Confinement Levels

The total number of reinforced concrete column and cylinder specimens examined above was subdivided into ranges of confinement levels, f_{cl} / f'_c, and ranges of unconfined concrete strengths. Figure 82 shows the histograms for column specimens, and Figure 83 does so for concrete cylinders.

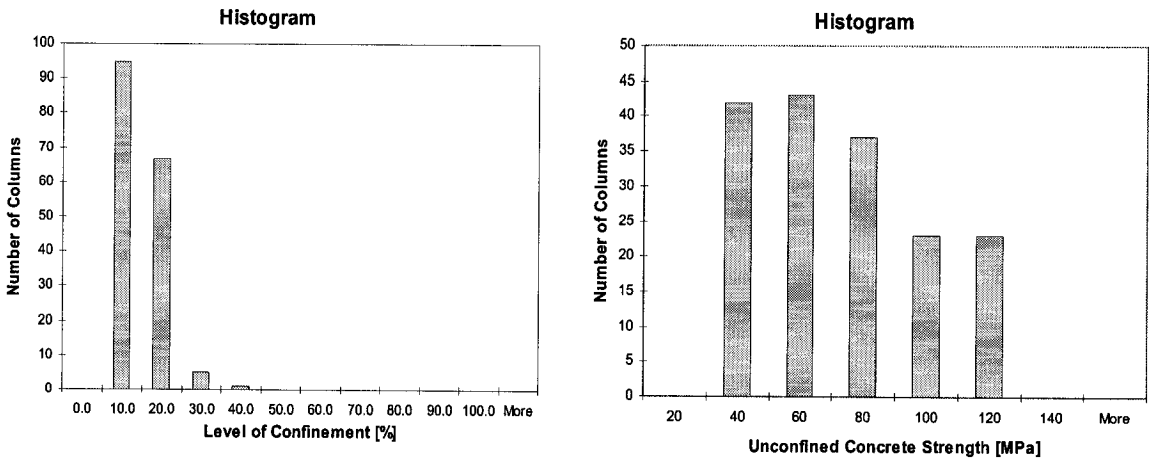

Figure 82. Level of confinement and concrete strength for columns.

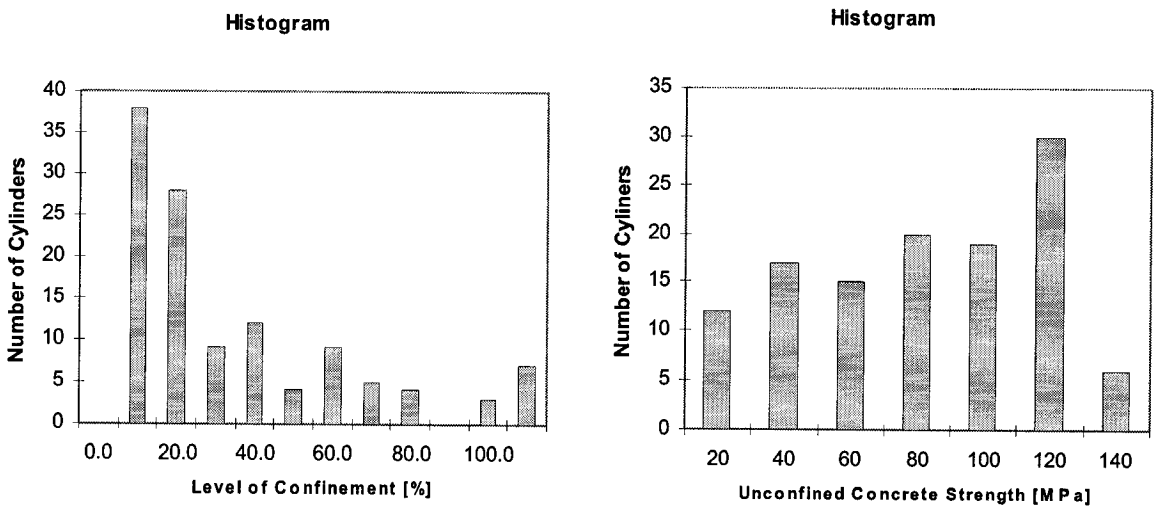

Figure 83. Level of confinement and concrete strength for cylinders.

About 96% of the total number of column specimens studied had a level of confinement between 0 and 20% (i.e. $f_{cl} / f'_c \leq 0.20$) for concrete strengths from 30 to 110 MPa. From the tables given in Appendix A, Section A.1, it was also found that the confinement level tended to decrease with an increase in the unconfined concrete strength, which may be expected due to the reduced lateral dilatation of high strength concrete (HSC), and the impractical amount of lateral reinforcement required. The average number of columns per concrete strength range was 24, with 86% of the total number of columns having unconfined strengths less than or equal to 100 MPa.

In the case of the concrete cylinders, about 63% of the cylinders were subjected to active pressure ratios less than or equal to 20%, 31 % of the cylinders to lateral pressure ratios between 20% and 100%, and the remaining 6% to pressure ratios over 100%. The average number of specimens per concrete strength range was 15, with 70% of the cylinders having f'_c less than or equal to 100 MPa.

From the observed data, the following definitions for confinement of triaxially compressed concrete elements are proposed in order to calibrate the parameters for the failure surface model:

- *Low confinement*: when a concrete element is subjected to an average lateral pressure ratio less than or equal to 0.20, in a plane normal to the major principal compressive stress (i.e. f_{c3}).
- *High confinement*: when a concrete element is subjected to an average lateral pressure ratio larger than 0.20 and less than 1.00, in a plane normal to the major principal compressive stress (i.e. f_{c3}).

The unconfined concrete strengths are divided into two simplified ranges:

- *Normal Strength Concrete (NSC)*: when a concrete element has an unconfined concrete strength f'_c less than or equal to 40 MPa.
- *High Strength Concrete (HSC)*: when a concrete element has an unconfined concrete strength f'_c larger than 40 MPa and less than 130 MPa

These definitions are solely based on the histograms obtained from the database of column and cylinder specimens. The range of possibilities for confined concrete elements fall into four categories:

- *LN*: Low-confined normal strength concrete.
- *HN*: High-confined normal strength concrete.
- *LH*: Low-confined high strength concrete; and,
- *HH*: High-confined high strength concrete.

These categories are used to calibrate the proposed failure surface model, presented next. Note that the ranges of values cover a wide spectrum of combinations.

3.3.3.2 Ottosen Criterion

The four-parameter Ottosen criterion in the stress space (f_{c1}, f_{c2}, f_{c3}), can be represented by the following set of equations (compression negative):

$$a\frac{J_2}{f'^{\,2}_c}+\lambda\frac{\sqrt{J_2}}{f'_c}+b\frac{I_1}{f'_c}-1=0\ ;\ (f'_c>0) \qquad \textbf{Eq. 89}$$

$$\lambda=k_1+k_2.\cos 3\theta \qquad \textbf{Eq. 90}$$

where the parameters are a, b, k_1, k_2, and where the stress invariants (I_1, J_2, J_3) are calculated as functions of the principal stresses.

$$\cos 3\theta=\frac{3\sqrt{3}}{2}\frac{J_3}{J_2^{3/2}} \qquad \textbf{Eq. 91}$$

$$J_2 = \frac{1}{2}\left(s_1^{\,2} + s_2^{\,2} + s_3^{\,2}\right)$$ **Eq. 92**

$$J_3 = \frac{1}{3}\left(s_1^{\,3} + s_2^{\,3} + s_3^{\,3}\right)$$ **Eq. 93**

$$s_i = f_{ci} - \frac{1}{3}I_1 \qquad i = 1,2,3$$ **Eq. 94**

$$I_1 = f_{c1} + f_{c2} + f_{c3}$$ **Eq. 95**

3.3.3.2.1 Proposed Ottosen Parameters

Four tests are needed to determine the parameters: the uniaxial compressive test and a triaxial test to define the compressive meridian, and the uniaxial tensile test and a biaxial test to define the tensile meridian. Three of the parameters, b, k_1, and k_2, are resolved in terms of the parameter a using the following boundary conditions:

Uniaxial test: $f_{c1} = f_{c2} = 0$; $f_{c3} = -f'_c$; $(0, 0, -f'_c)$

Tensile test: $f_{c1} = f'_{ct}$; $f_{c2} = f_{c3} = 0$; $(f'_{ct}, 0, 0)$

Biaxial test: $f_{c1} = 0$; $f_{c2} = f_{c3} = -f_{bc}$; $(0, -f_{bc}, -f_{bc})$

where f'_{ct} and f_{bc} are the concrete uniaxial tensile and biaxial compressive strengths, respectively. By solving the system of equations, the parameters b, k_1, and k_2 are:

$$b = \frac{1}{9}a\left[\frac{f_{bc} - f'_{ct}}{f'_c}\right] + \frac{1}{3}\left[\frac{f'_c}{f'_{ct}} - \frac{f'_c}{f_{bc}}\right]$$ **Eq. 96**

$$k_1 = \frac{\sqrt{3}}{2}\left\{1 + \frac{f'_c}{f'_{ct}} - \frac{1}{3}a\left[1 + \frac{f'_{ct}}{f'_c}\right]\right\}$$ **Eq. 97**

$$k_2 = \frac{\sqrt{3}}{2}\left\{\frac{f'_c}{f'_{ct}} - 1 - 2b - \frac{1}{3}a\left[\frac{f'_{ct}}{f'_c} - 1\right]\right\}$$ **Eq. 98**

The tensile and biaxial compressive strengths are calculated from the Eqs. 99 and 100:

$$f'_{ct} = 0.65 f'^{\,0.33}_c$$ **Eq. 99**

$$f_{bc} = 1.16 f'_c$$ **Eq. 100**

Although the tensile strength f'_{ct} is calculated using the formulation given by Yamamoto and Vecchio (2001), the following section gives the proposed values for the independent parameter a as a function of various available formulations for tensile strength. Equation 100 represents the strength enhancement of concrete elements subjected to biaxial compression, based on an approximation of the tests by Kupfer et al. (1969).

3.3.3.2.2 Determination of Ottosen Parameters

The Ottosen failure surface (with the proposed parameters given in the previous section) was fitted to the experimental results of reinforced concrete columns and concrete cylinders presented in Appendices A and B. The complete details of the calculations to obtain the parameter a are given in Appendix C. The proposed values for parameter a are reproduced in Table 10 for various formulations of tensile strength f'_{ct}.

Table 10. Proposed values for parameter a

f'_{ct}	LN	HN	LH	HH
$0.65f'^{0.33}_c$	17.10	2.41	17.45	15.06
$0.33f'^{0.5}_c$	18.72	2.94	10.62	13.91
$0.60f'^{0.5}_c$	8.07	1.10	4.63	6.67
$0.10f'_c$	8.14	1.59	1.98	3.57

This set of values for a, along with the corresponding values for b, k_1, and k_2 obtained in the previous section, are used to predict the concrete strength of the examined columns and cylinders.

The Ottosen criterion provides a failure surface that has proved (Chen 1982) to give accurate predictions of the strength of concrete in a three-dimensional state of stress,

especially when concrete is subjected to compressive stresses. The shape of the criterion in the meridian and deviatoric planes in the stress space simulates well the nature of the behaviour of concrete. Curved meridians show the variability of the response of concrete to deviatoric stress states and volumetric changes, and the shape in the deviatoric plane changes from a triangle when no hydrostatic stresses are applied to the concrete, up to a perfect circle at large hydrostatic stresses.

A limitation of the previous Ottosen-type criteria (e.g. see Chen 1982) is that they were generally applied to normal strength concrete. The criterion is then extended in this work to cover a large range of concretes and confinement levels, when compressive states of stress act in the concrete.

3.3.3.5 Comparison with Column and Cylinder Tests

Columns: the analytical concrete strength f_{cc} (i.e. $f_{cc} = f_{c3}$) for each column was obtained from the modified Ottosen model using the respective parameters, the unconfined concrete strength f'_c, and the lateral pressure f_{cl} from the experimental results (i.e. $f_{c1} = f_{c2} = -f_{cl}$; f_{cl} positive). Tables 52 to 54 in Appendix C, Section C.1, show the normalized Haigh-Westergaard coordinates (ξ / f'_c, ρ / f'_c, where $\xi = I_1/\sqrt{3}$, and $\rho = \sqrt{2J_2}$) obtained with the model, and Figures 159 to 167 in Section C.4 show the ratio of analytical-to-experiment strength against the lateral pressure f_{cl} for each group of columns described in Table 5, Section 3.3.1 of this Chapter. The average strength ratio, standard deviation, and coefficient of variance for the proposed model are given in Table 11. Comparisons with the models by Vecchio, Ottosen (Chen 1982), Hsieh et al., and Mander are shown in Figure 84.

Table 11. Calculated-to-experimental strength ratios, columns, proposed model.

	Sheikh Uzumeri	Mont. Sheikh	Sheikh. Tokl.	Pessiki et al.	Razvi & Saatc. (Circ.)	Razvi & Saatc. (Sq)	Nagash. et al. (92)	Nagash. et al. (93)	Li	All
Ave.	1.19	1.18	0.99	0.85	1.00	1.11	0.96	1.10	1.03	**1.05**
St.Dev.	0.083	0.136	0.098	0.106	0.048	0.074	0.076	0.053	0.083	**0.131**
CV [%]	7.00	11.53	9.94	12.55	4.81	6.68	7.87	4.84	8.10	**12.47**

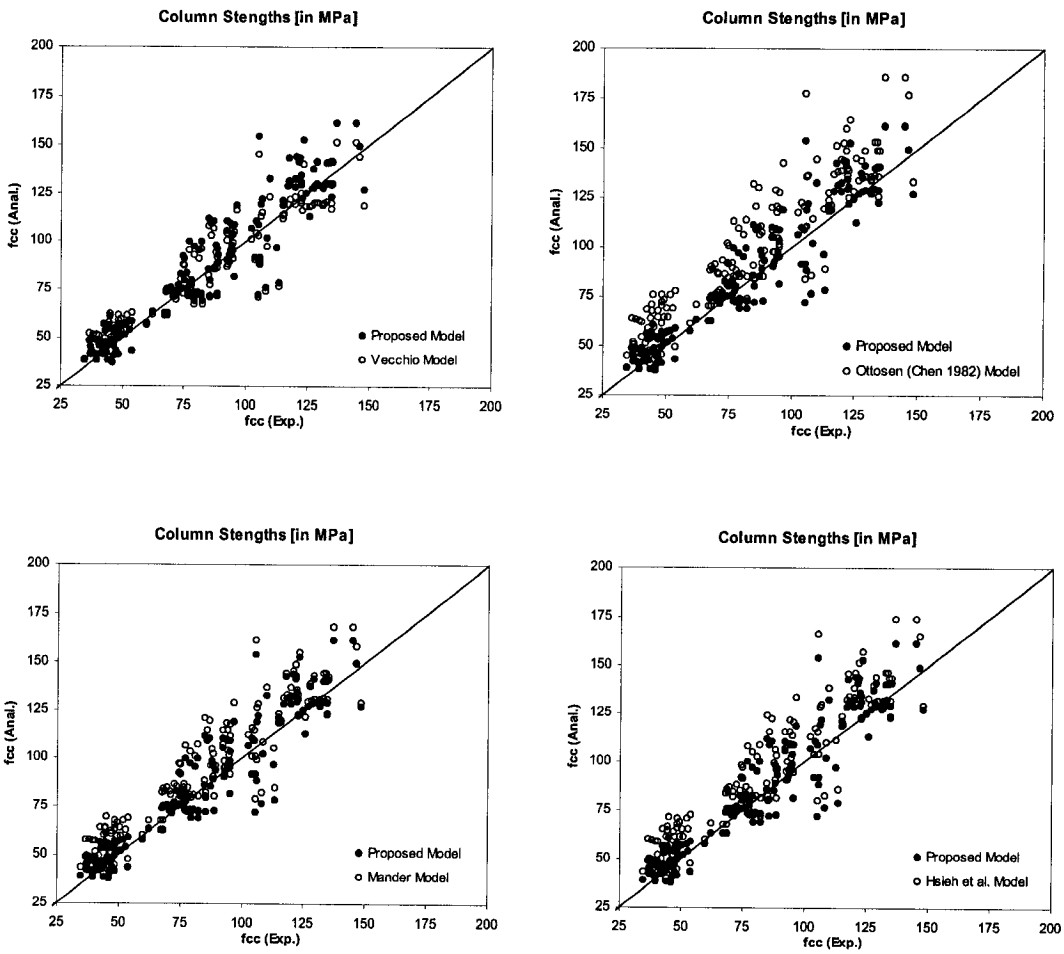

Figure 84. Comparison of column strengths obtained with proposed model and the models by Vecchio, Ottosen (Chen 1982), Hsieh et al., and Mander et al.

The proposed model yielded overall better results than those obtained from the Vecchio model, which produced the best results from the group of models discussed in Section 3.3.1. The average strength ratio was 5% larger than the experimental values, and the coefficient of variance was 12.5%. From Figure 84, it can be seen that the scatter slightly decreased with respect to that for the Vecchio (or Richart et al.) model, and was significantly reduced with respect to those obtained from the Mander, Hsieh et al., and Ottosen (Chen 1982) models. It should be noted that the modified Ottosen model evaluated with the new parameters is more accurate than the Ottosen model described in Chen (1982). However, the new model keeps the beneficial features (see Chen 1982) of the original one.

Cylinders: Tables 55 to 58 of Appendix C, Section C.2, shows the normalized Haigh-Westergaard coordinates (ξ / f'_c, ρ / f'_c) obtained from the proposed model, and Figures 168 to 174 in Section C.5 show the ratio of analytical-to-experiment strength against the lateral pressure f_{cl}, for each group of cylinders described in Table 8, Section 3.3.2 of this Chapter. The average strength ratio, standard deviation, and coefficient of variance for the proposed model are given in Table 12, and comparisons with the models by Vecchio, Ottosen (Chen 1982), Hsieh et al., and Mander are shown in Figures 85 and 86.

Table 12. Calculated-to-experimental strength ratios, cylinders, proposed model.

	Hurlbut	Gardner	Li and Ansari	Richart et al.	Attard and Setunge	Imran and Pantazopoulou	Xie, Elwi and McGregor	**All**
Ave.	1.04	1.00	1.17	0.99	0.97	0.98	0.91	0.98
St.Dev.	0.09	0.07	0.09	0.09	0.06	0.10	0.07	0.12
CV [%]	8.85	6.77	8.03	9.48	6.13	9.74	7.80	12.80

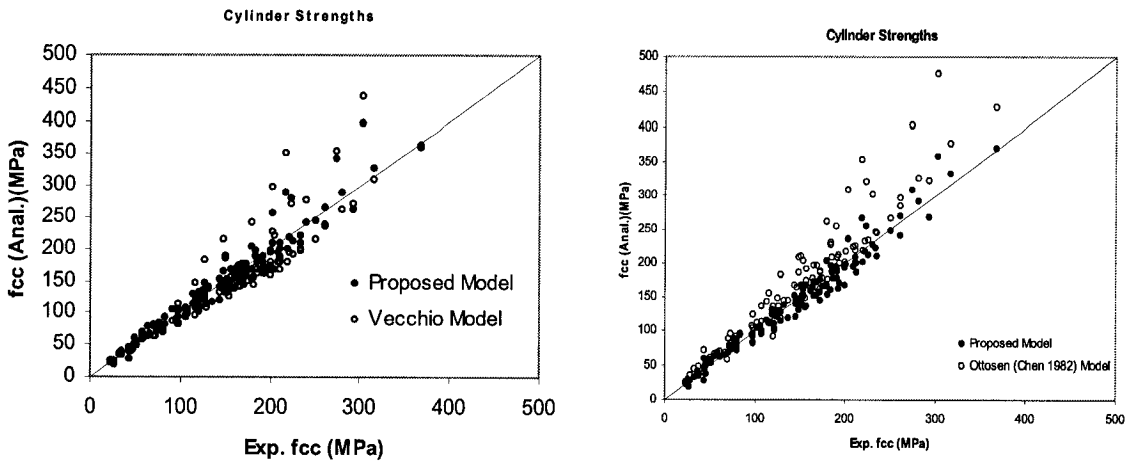

Figure 85. Comparison of cylinder strengths obtained with proposed model and the models by Vecchio, and Ottosen (Chen 1982).

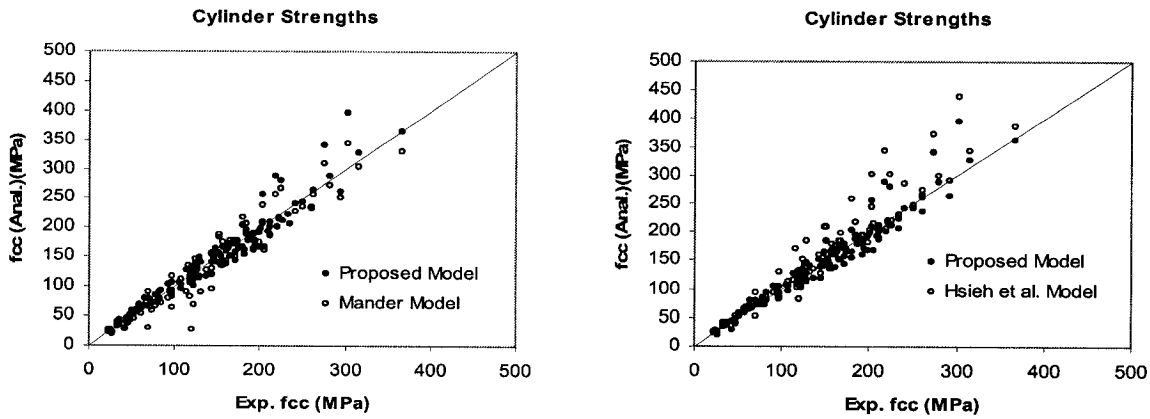

Figure 86. Comparison of cylinder strengths obtained with proposed model and the models by Mander et al., and Hsieh et al.

The proposed model predicted well the strength of the cylinder specimens. The average calculated strength was 2% smaller than the experimental values, and the coefficient of variance was 12.8%. The confined strength was better predicted than that obtained from the model by Hsieh et al., which produced the best predictions of all the models analyzed in Section 3.3.2. A large scatter remained for very high confining pressures and high concrete strengths, suggesting the need for more experimental data in that range.

3.3.3.6 Sensitivity of parameter a

In the previous Section the modified Ottosen criterion was used to calculate the analytical strengths of the columns and cylinders that were included in the database of experiments for determining the parameter *a*. As expected, the statistical fitting of the experimental values reproduced the strengths of the experiments. The value of parameter *a* has a strong influence on the calculation of the strength of confined elements, because all other parameters in the proposed criterion, depend on it.

Figure 87 shows the strength enhancement ratio (i.e. the ratio of strength f_{cc} to unconfined concrete strength f'_c) versus the confinement level (f_{cl} / f'_c) for two unconfined concrete strengths of 39.9 MPa and 40.1 MPa and confinement levels from 0% to 100%. These values represent the boundaries of the proposed regions.

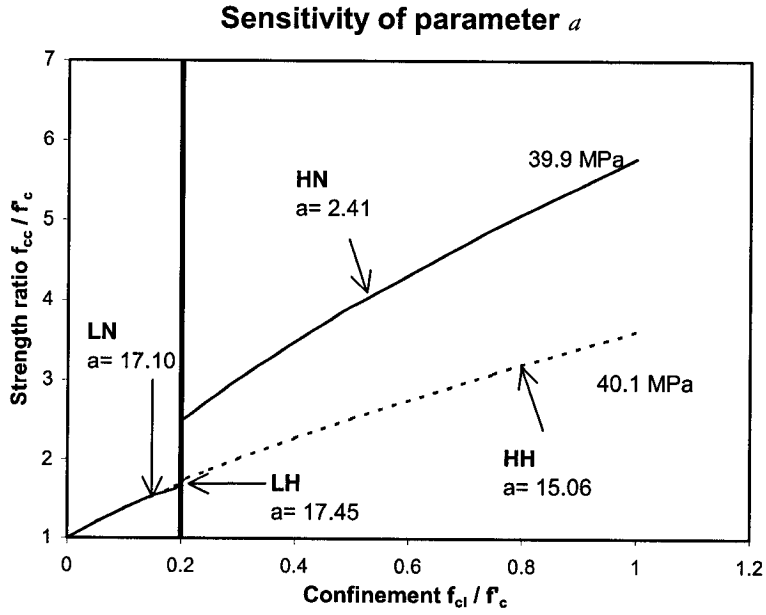

Figure 87. Sensitivity of parameter *a*

It can be seen from the figure that the statistical fitting of the parameter a shows a smooth transition between low confinement and high confinement levels for unconfined concrete strength larger than 40 MPa (i.e. ranges LH and HH). However, an abrupt jump in this transition is observed from the statistical fitting between low and high confinement of concrete strengths less than 40 MPa (i.e. LN and HN), which does not reflect the expected behaviour. This may be explained by the fact that in the determination of the value of parameter a for the range HN (i.e. high confined normal strength concrete), only a small number of specimens fell into this category (6% of the total database, see Appendix C, Section C.3). Additional experimentation and gathering of data in the range of normal concrete strength and high confinement levels is also necessary in future investigations.

In order to obtain a reasonable behaviour in the transition between low and high confinement of normal strength concrete, the value of parameter a for the HN range in the corroboration of experimental responses of structural elements given in Chapter 5 remained unchanged from that in the LN range.

The smoothness of the change between the LH and HH ranges and the closeness of the strength gain values between the ranges LH and LN, suggest the possibility of setting a uniform value for all ranges of confinement levels and strength ratios. In the case of a tensile strength of $0.65f'_c{}^{0.33}$, that value could be 16.5. The effects of this unified value on the mean and coefficient of variance of the different tests on the corroboration (Chapter 5) was not investigated.

3.3.4 Strain at Peak Stress of Confined Concrete, ε_{cc}.

The experimental data from the triaxial tests conducted by Li and Ansari (1999), Attard and Setunge (1996), and Imran and Pantazopoulou (1996), were used to propose a model to determine the strain at peak stress, ε_{cc}. Table 13 describes the different test series. The detailed list of the specimens is given in Appendix D, Section D.1.

Table 13. Experimental data used in the formulation of strain at peak stress, ε_{cc}.

Researcher	Tests	ϕ x h [mm]
Li-Ansari	14	100 x 200
Attard-Setunge	32	100 x 200
Imran-Pantazopoulou	18	54 x 108
Total:	***64***	
ϕ: Diameter h: Height		

Each series was subdivided according to the unconfined concrete strength. The normalized strain at peak stress, ε_{cc}, was plotted against the lateral pressure ratio (i.e. the confinement level). The strain ε_{cc} was normalized with respect to the experimental strain at peak stress, f'_c, of unconfined concrete, ε_{co}; i.e. $\varepsilon_{cc} / \varepsilon_{co}$. The plots are shown in Appendix D, Section D.2.

A linear relationship between the normalized strain at peak, $\varepsilon_{cc} / \varepsilon_{co}$, and the confinement level, f_{cl} / f'_c, is proposed to calculate the peak strain, based on the behaviour observed in the triaxial tests described in Table 13.

$$\frac{\varepsilon_{cc}}{\varepsilon_{co}} = 1.0 + k\frac{f_{cl}}{f'_c} \geq 1.0 \qquad \textbf{Eq. 101}$$

where k is a factor that depends on the unconfined concrete strength f'_c. The experimental data (Appendix D, Section D.2.) show that the slope of the trend lines, of the normalized strain versus the confinement level graphs, decrease with an increase in the unconfined concrete strength. To determine the factor k, the trend lines for each set of tests were computed; these lines intercept the ordinate (i.e. normalized strain) at an approximate value of 1.0 (unconfined tests). The slope (i.e. the value for k) of each trend line was then plotted in Figure 88, against the unconfined strength f'_c. Table 14 shows the calculated values for k, the unconfined strength, and the correlation for each trend line.

Table 14. Values for coefficient k to determine ε_{cc}.

Researcher	Number Tests	f'_c [MPa]	k	Correlation R2
Li-Ansari	5	47.8	16.7	0.75
	5	75.7	18.6	0.96
	4	106	13.5	0.89
Imran-Pantazopoulou	6	28.7	29.4	0.96
	6	47.4	21.0	0.96
	6	73.4	19.3	0.98
Attard-Setunge	4	60	15.1	1.00
	9	120	9.0	0.95
	6	110	8.3	0.85
	7	100	9.6	0.83
	3	132	10.9	0.94
	3	126	13.5	0.99

Also shown in Figure 88 is the linear regression obtained from the data set. From the experimental results, it was evident that for a particular confinement level, the normalized strain at peak decreased with an increase in the concrete strength. The proposed formulation to calculate the strain at peak is given below.

$$\frac{\varepsilon_{cc}}{\varepsilon_{co}} = 1.0 + \left(24.4 - 0.116 f'_c\right)\frac{f_{cl}}{f'_c} \geq 1.0 \qquad \textbf{Eq. 102}$$

Note that the data set covered a wide range of concrete strengths between 20 MPa and 130 MPa, and confinement levels (f_{cl} / f'_c) from 0 to 1.0.

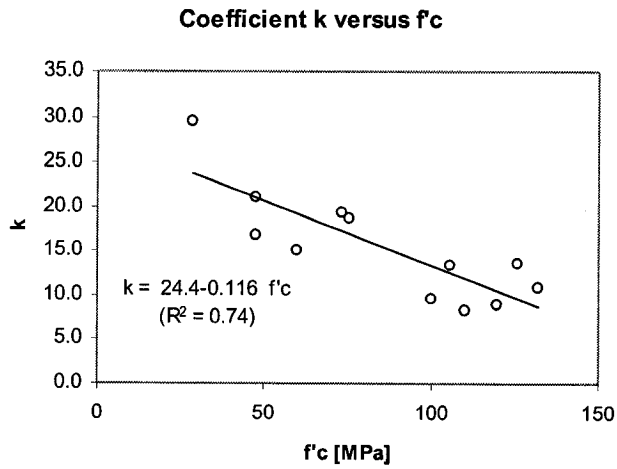

Figure 88. Determination of coefficient k from test data.

The analytical-to-experimental values for the strain at peak stress of the test data are plotted in Figure 89. The analytical values for each specimen are also given in Appendix D, Section D.1. The strains at peak were calculated using the experimental values for ε_{co}. The corresponding average, standard deviation, and coefficient of variance for the ratios of predicted to experimental strain are given in Table 15.

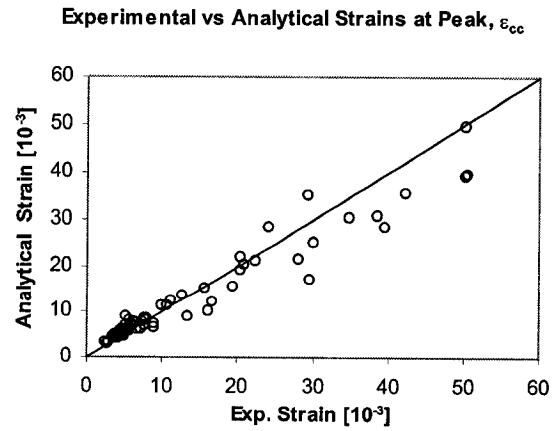

Figure 89. Analytical versus experimental strains at peak stress.

Table 15. Statistical values of predicted-to-experimental ratios for strain at peak stress.

	Li and Ansari	Imran and Pantazopoulou	Attard and Setunge	All
Ave.	1.09	1.14	0.92	1.01
St.Dev.	0.21	28.00	0.12	0.21
CV [%]	19.0	24.3	13.5	21.0

The strain at peak stress was reasonably well predicted using the proposed formulation. The scatter was small for values of the strain less than 0.010, and increased for larger values. The coefficient of variation of the predicted values with respect to the experimental ones was calculated between 13% and 24%.

3.4 Stress-Strain Curve for Confined Concrete.

A formulation for the complete stress-strain curve for concrete subjected to triaxial compressive stresses is presented. The curve has two branches defined by different mathematical formulations, an ascending portion up to the peak stress and a descending or softening branch after the peak stress. The definition for each branch is given, and their properties are stated. The origin of the proposed softening curve is also described. The complete confined concrete stress-strain curve is then used to corroborate a series of experimental results.

3.4.1 Pre-Peak Stress-Strain Curve.

The stress-strain curve by Hoshikuma et al. (1996) was adopted to model the ascending branch of the compressive behaviour of concrete. The stress f_c, is related to the strain ε_c, using the following formulae.

$$f_c = E_c \varepsilon_c \left[1 + \frac{1}{n} \left(\frac{\varepsilon_c}{\varepsilon_{cc}} \right)^{n-1} \right] \qquad \text{Eq. 103}$$

$$n = \frac{E_c . \varepsilon_{cc}}{E_c . \varepsilon_{cc} - f_{cc}} \qquad \text{Eq. 104}$$

where E_c is the initial stiffness, and ε_{cc} is the strain at peak stress f_{cc}. If the initial stiffness is not known from experimental observations, it is suggested here to be calculated using Eq.105a for NSC and Eq.105b for HSC:

$$E_c = 5000\sqrt{f'_c} \qquad \text{Eq. 105a}$$

$$E_c = 3320\sqrt{f'_c} + 6900 \qquad \text{Eq.105b}$$

The Hoshikuma et al. curve has the following features:

- The initial stiffness of the curve does not depend on the values for peak stress and strain at peak stress, $(\varepsilon_{cc}, f_{cc})$.

- The initial stiffness E_c is equal to the derivative of the stress-strain relationship

$$\left.\frac{\partial f_c}{\partial \varepsilon_c}\right|_{\varepsilon_c=0} = E_c$$

- At the strain, ε_{cc}, the tangent to the stress-strain curve is horizontal.
- At the strain, ε_{cc}, the stress is equal to the peak stress, $f_c = f_{cc}$.

This curve was derived taking into account only the boundaries discussed above, and not the type of concrete to which it can be applied (e.g. NSC or HSC).

3.4.2 Proposed Post-Peak Stress-Strain Curve.

This section presents a brief commentary on the origin of the proposed curve, and the factors considered in the definition of the post-peak behaviour, such as the strain at 80% of the peak stress, and a "shape factor" that depends on the confining conditions of concrete. The mathematical expression for the proposed curve is then presented.

3.4.2.1 The Witch of Agnesi.

Maria Gaetana Agnesi (1718-1799)[2] was an Italian mathematician from Milan, who published in 1748-49 the "*Instituzioni analitiche ad uso della gioventù italiana*" [In Italian, Analytical Institutions for the Use of Italian Youth], which was a two-volume mathematical treatise. In that work, she published an analytical expression for a curve, believed to be developed by Fermat[2], which she called *"la versiera"*, an Italian translation from the Latin word *"versoria"*, given by Grandi[2] . The word *"versiera"* means "rope that turns a sail". In an English translation of Agnesi's book, *"la versiera"*, was

[2] See http://www-groups.dcs.st-and.ac.uk/~history/Mathematicians/Agnesi.html

translated as *"l'aversiera"*, which means the "wife of the devil", or "witch". The "witch" of Agnesi can be expressed in the Cartesian coordinate (x,y) system as (Tuma 1997):

$$y = \frac{a^3}{x^2 + a^2} \qquad \textbf{Eq. 106}$$

Plots for a = 1, 2, and 3, are shown in Figure 90.

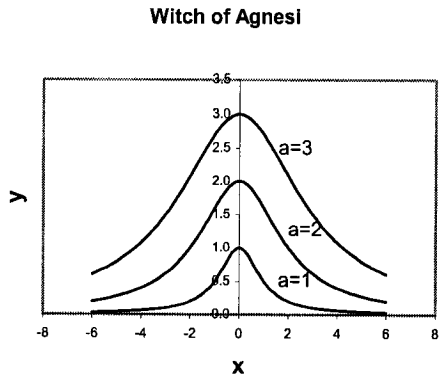

Figure 90. The witch of Agnesi.

The curve is symmetric with respect to the y-axis, reaches its maximum value when x = 0, y_{max} = a, and is asymptotic when x → +/- ∞. Also, the derivative of the function is null at (x= 0, y=y_{max}). This function is transformed in the next sections to account for the properties of confined concrete.

3.4.2.2 Strain at 80% of Peak Stress, ε_{c80}.

The experimental data from the triaxial tests conducted by Li and Ansari (1999), Attard and Setunge (1996), Candappa et al.(2001), and Xie et al. (1995), were used to propose a model to determine the strain ε_{c80} (Table 16). The detailed list of the specimens is given in Appendix E, Section E.1.

Table 16. Experimental data used in the formulation of strain at 80 % peak stress, ε_{c80}.

Researcher	Tests	ϕ x h [mm]
Li-Ansari	16	100 x 200
Attard-Setunge	9	100 x 200
Candappa et al.	15	100 x 200
Xie et al.	18	55 x 110
Total:	***58***	
ϕ: Diameter h: Height		

As previously done for the strain at peak stress, each group of tests was subdivided according to the unconfined concrete strength. The strain at 80% of peak stress, ε_{c80}, was normalized with respect to the strain at peak of unconfined concrete, ε_{co}, and plotted against the lateral pressure ratio (i.e. the confinement level). The plots are shown in Appendix E, Section E.2. When the post-peak range of the experimental curve did not decay enough to reach the stress value corresponding to 80% of f_{cc}, the curve was approximated to a polynomial and the strain value ε_{c80} was calculated using the fitted curve.

A linear relationship between the normalized strain, ε_{c80} / ε_{co}, and the confinement level, f_{cl} / f'_c, is also proposed to calculate the strain ε_{c80} on the post-peak curve, based on the behaviour observed in the triaxial tests described in Table 16.

$$\frac{\varepsilon_{c80}}{\varepsilon_{co}} = 1.5 + k_1 \frac{f_{cl}}{f'_c} \geq 1.5 \qquad \textbf{Eq. 107}$$

where k_1 is a factor that depends on the unconfined concrete strength f'_c. It can be seen from the experimental data (Appendix E, Section E.2) that the slope of the trend lines, of the normalized strain versus the confinement level graphs, decreased with an increase in unconfined concrete strength, as was the case for the strain at peak stress.

The factor k_1 was calculated using the same procedure described in Section 3.3.4. The slope (i.e. the value for k_1) of each trend line is plotted in Figure 91 against the unconfined strength f'_c. Table 17 shows the calculated values for k_1, the unconfined strength, and the correlation for each trend line.

Table 17. Values coefficient k_1 to determine ε_{c80}.

Researcher	Number Tests	f'_c [MPa]	k_1	Correlation R^2
Li-Ansari	6	47.8	42.4	0.97
	5	75.7	61.0	0.91
	5	106	30.7	0.97
Attard and Setunge	3	110	13.0	0.91
	3	120	9.3	0.87
	3	132	11.6	0.97
Candappa et al.	4	40	73.8	0.96
	3	60	51.8	0.91
	4	75	35.5	0.99
	4	100	23.6	0.87
Xie et al.	9	89	33.0	0.93
	9	120	28.7	0.88

Figure 91 also shows the linear regression obtained from the data set. Again, for a particular confinement level, the normalized strain at 80% of peak stress decreased with an increase in the concrete strength. The propose formulation for calculating the strain at 80% of peak stress is given as:

$$\frac{\varepsilon_{c80}}{\varepsilon_{co}} = 1.5 + (89.5 - 0.60 f'_c)\frac{f_{cl}}{f'_c} \geq 1.5 \qquad \textbf{Eq. 108}$$

Note that the data set covered concrete strengths between 40 MPa and 130 MPa, and confinement levels (f_{cl} / f'_c) from 0 to 1.0.

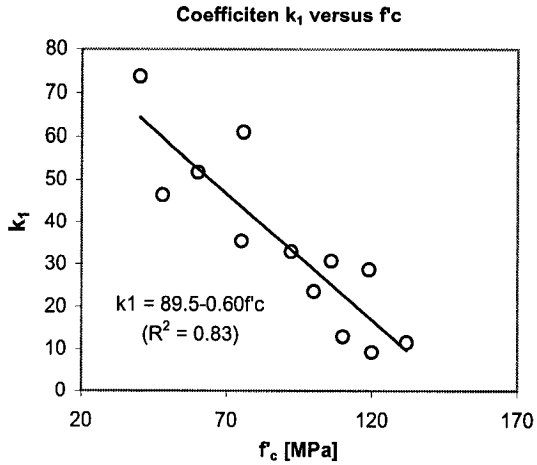

Figure 91. Determination of coefficient k_1 from test data.

The analytical-to-experimental values for the strain at 80% of peak stress of the test data are plotted in Figure 92. The analytical values for each specimen are given in Appendix E, Section E.1. The experimental values for ε_{co} were used in the estimation of ε_{c80}. The corresponding average, standard deviation, and coefficient of variance for the ratios of predicted to experimental strain, are given in Table 18.

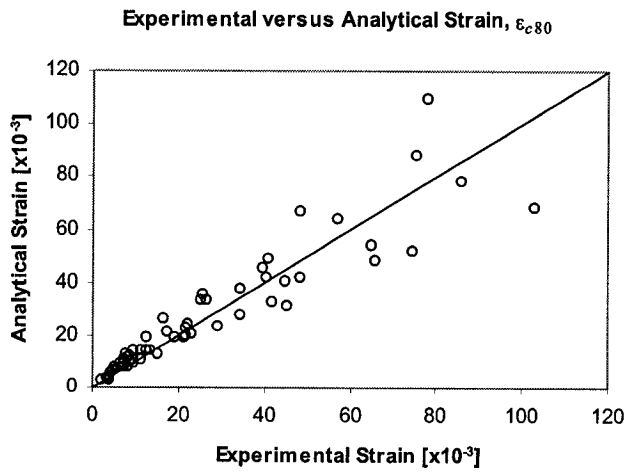

Figure 92. Analytical versus experimental strains at 80% of peak stress.

Table 18. Statistical values of analytical-to-experimental ratios for ε_{c80}.

	Li and Ansari	Attard and Setunge	Candappa et al.	Xie et al.	All
Average	1.04	1..26	1.08	1.11	1.11
St.Dev.	0.26	0.22	0.18	0.27	0.24
CV [%]	24.98	17.27	16.56	24.24	22.00

The analytical strains are close to the experimental values for strains smaller than 0.020. The scatter increases thereafter. However, specimens subjected to high confinement exhibited little or no softening after reaching the peak stress. Large dilatations (i.e. lateral strains approximately equal to or larger than axial peak strains were observed in tested cylinders; see Chapter 2) caused internal damage and failure of the specimens just after peak stress. The combining action of these effects was considered in the compression field modelling of structural elements in Chapter 5.

3.4.2.3 Shape Factor K_d.

If the axis of symmetry of the witch of Agnesi (Figure 90) is relocated to $x = x_0$ ($x_0 > 0$), and considering only the symmetrical right-side branch of the curve, the modified equation for the curve in the new position is:

$$y = \frac{a^3}{(x - x_o)^2 + a^2} \qquad \text{Eq. 109}$$

Figure 93a shows an sketch of the curve in the new position for values of $a = 1$, and $x_o = 0.75$.

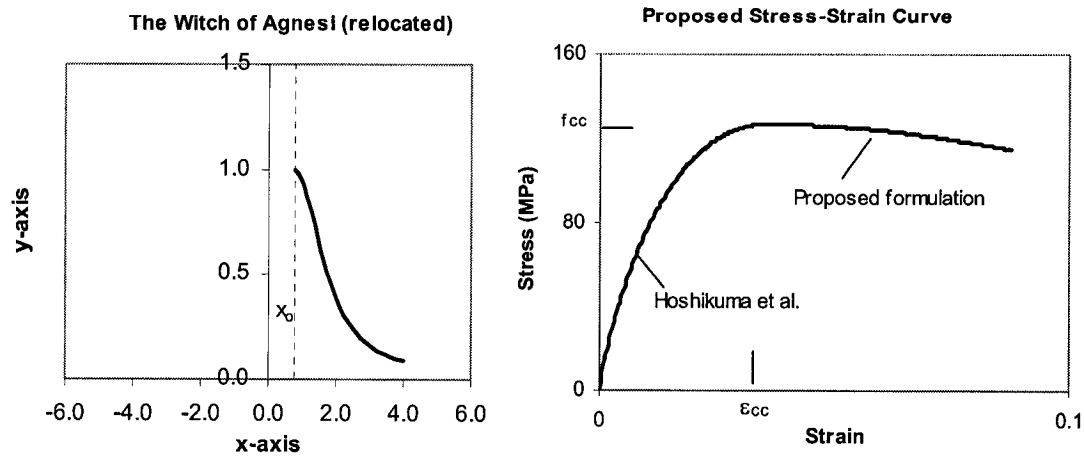

Figure 93. (a) The witch of Agnesi with axis of symmetry at $x=x_o$, (b) Typical proposed stress-strain curve.

Transformation of the witch of Agnesi is necessary to account for the characteristics seen in the behaviour and shape of the stress-strain curve for confined concrete. A shape factor, k_d, is proposed to force the relocated curve to pass through the stress-strain point corresponding to 80% of peak stress, 0.80 f_{cc}, in the post-peak segment of the concrete curve, i.e. (ε_{c80}, 0.80f_{cc}). The shape factor is an indicator of the steepness of the stress-strain curve beyond the peak strength. The transformation of Agnesi's curve in terms of stresses and strains results in the following equation for the post-peak region (i.e. ε_c greater or equal than ε_{cc}) of the stress versus strain curve for concrete:

$$f_c = \frac{f_{cc}^{\ 3}}{f_{cc}^{\ 2} + k_d\left(\varepsilon_c - \varepsilon_{cc}\right)^2} \qquad \text{Eq. 110}$$

where the peak strength f_{cc} replaced the value a, the variable y was replaced by the stress f_c, and the variables x and the new axis of symmetry x_o, were replaced by the strain ε_c, and the strain at peak ε_{cc}, modified by the proposed shape factor k_d. It should be noted that when the strain ε_c equals the strain at peak, $\varepsilon_c = \varepsilon_{cc}$, the stress f_c

becomes the peak strength f_{cc}. Replacing the point (ε_{c80}, $0.80f_{cc}$) in the latter equation gives the following formulation for the shape factor k_d:

$$k_d = \frac{1}{4}\left(\frac{f_{cc}}{\varepsilon_{c80} - \varepsilon_{cc}}\right)^2 \qquad \text{Eq. 111}$$

where the values for the strains ε_{c80} and ε_{cc} are calculated using the formulations developed in Sections 3.4.2.2 and 3.3.3, respectively. The stress at peak f_{cc} is obtained from the modified Ottosen criterion developed in Sections 3.3.3.2 to 3.3.3.4.

3.4.2.4 Analytical Expression for the Post-Peak Stress-Strain Curve.

The formulation for the stress-strain curve in the post-peak range (Eq. 110) is mathematically modified to produce the final expression given below.

$$f_c = \frac{f_{cc}}{A\left(\frac{\varepsilon_c}{f_{cc}}\right)^2 - B\left(\frac{\varepsilon_c}{f_{cc}}\right) + C + 1.0} \qquad \text{Eq. 112}$$

where:

$$A = k_d = \frac{1}{4}\left(\frac{f_{cc}}{\varepsilon_{c80} - \varepsilon_{cc}}\right) \qquad \text{Eq. 113}$$

$$B = 2\frac{A}{E_{sec}} \qquad \text{Eq. 114}$$

$$C = \frac{A}{E_{sec}^{\ 2}} \qquad \text{Eq. 115}$$

$$E_{sec} = \frac{f_{cc}}{\varepsilon_{cc}} \qquad \text{Eq. 116}$$

The slope of the stress-strain curve at the strain at peak strength is horizontal. A sketch of the proposed curve is given in Figure 93(b)

Chapter 4. Solids of Revolution: VecTor6

4.1 General Description

The program VecTor6 is a nonlinear finite element program for the analysis of reinforced concrete solids of revolution, developed in this work to implement the proposed models for confinement and to corroborate the response of reinforced concrete circular columns and cylinders. Its development was based on the program VecTor3 (Selby and Vecchio 1993, 1997), which is used for the analysis of general three-dimensional reinforced concrete solids. Both programs are part of the VecTor series of programs developed at The University of Toronto.

The main objective in developing VecTor6 was to model and interpret results from analyses of reinforced concrete elements or structures that have an axis of revolution. Although VecTor6 has the same capabilities as VecTor3, the latter has no pre-processor for meshing complex three-dimensional structures and hence model creation is time-consuming. Also, VecTor3's solver is suitable for large number of equations (three degrees of freedom (DOF) per node); it is not efficient in solving axisymmetric problems where there are only two DOF per node.

Solids of revolution, or axisymmetric solids, can be modelled using simple two-dimensional sections, where in addition to their "plane" behaviour, the "out-of-plane" behaviour is also considered in the implementation of stiffness matrices. The solvers for two-dimensional programs, such as that implemented in VecTor2 (Vecchio), can be used in the solution of systems of equations for axisymmetric problems, improving cost-effectiveness without losing sight of the three-dimensional behaviour of the solid of

revolution. The current version of program VecTor6 allows for the analysis of axisymmetric solids subjected to axisymmetric loading only, and does not consider large deformations. Program VecTor6 adds to the family of VecTor programs the capability of a straightforward analysis of reinforced concrete structures such as tanks, silos, spherical domes, circular slabs, and circular columns, without requiring a complete three-dimensional analysis.

This Chapter describes the basic characteristics of program VecTor6. Compression field modelling of confined concrete is described including the implementation of the proposed models given in Chapter 3. The library of finite elements developed to date for VecTor6 is also described, with complete closed-form formulations of their corresponding stiffness matrices given in Appendix F. The general finite element formulation along with the flow chart of the analysis scheme is given at the end of this Chapter.

4.2 Compression Field Modelling of Confined Concrete

The set of constitutive material models used in the analysis of confined concrete are described herein. Compression field modelling makes use of formulations derived from the Modified Compression Field Theory (Vecchio and Collins 1986) and of proposed models presented in this thesis, to model concrete solids where confinement and dilatation are crucial to predicting or reproducing the response of concrete. The base curves for concrete in compression and tension, tension stiffening, lateral expansion due to Poisson effects, strength enhancement, strain at peak stress, concrete softening, concrete cracking criterion, and the basic stress-strain curve for steel and FRP composites, are given below in the principal stress (strain) directions.

4.2.1 Concrete in Compression

Concrete in compression is modelled using the pre- and post- peak curves described in Chapter 3, and rewritten here. For the pre-peak curve, the model by Hoshikuma et al. (1996) is used:

$$f_{ci} = E_{ci}\varepsilon_{ci}\left[1+\frac{1}{n}\left(\frac{\varepsilon_{ci}}{\varepsilon_{pi}}\right)^{n-1}\right] \quad \text{Eq. 117}$$

$$n = \frac{E_{ci}.\varepsilon_{pi}}{E_{ci}.\varepsilon_{pi} - f_{pi}} \quad \text{Eq. 118}$$

where i = 1, 2, 3, denotes the principal stress directions, and ε_p and f_p are the strain at peak stress and the peak stress, respectively. For post-peak behaviour, the following proposed curve (see Section 3.4.2.4) is used.

$$f_{ci} = \frac{f_{pi}}{A\left(\frac{\varepsilon_{ci}}{f_{pi}}\right)^2 - B\left(\frac{\varepsilon_{ci}}{f_{pi}}\right)+C+1.0} \quad \text{Eq. 119}$$

where:

$$A = k_d \quad \text{Eq. 120}$$

$$B = 2\frac{A}{E_{\text{sec}}} \quad \text{Eq. 121}$$

$$C = \frac{A}{E_{\text{sec}}^{\ 2}} \quad \text{Eq. 122}$$

$$E_{\text{sec}} = \frac{f_{pi}}{\varepsilon_{pi}} \quad \text{Eq. 123}$$

$$k_d = \frac{1}{4}\left(\frac{f_{pi}}{\varepsilon_{c80i} - \varepsilon_{pi}}\right)^2 \quad \text{Eq. 124}$$

and ε_{c80i} is the strain at 80% of peak stress (See Section 4.2.4.2).

4.2.2 Concrete in Tension

The stress-strain curve for concrete in tension comprises an ascending linear elastic portion up to the tensile strength, f'_{ct}, and a descending portion that accounts for tension stiffening. The tensile strength of concrete f'_{ct}, and the cracking stain ε_{cr}, are obtained from the equations (Yamamoto and Vecchio 2001):

$$f'_{ct} = 0.65 f'^{0.33}_{c} \qquad \textbf{Eq. 125}$$

$$\varepsilon_{cr} = \frac{f'_{ct}}{E_c} \qquad \textbf{Eq. 126}$$

The ascending curve is given by:

$$f_{ci} = E_c \varepsilon_{ci}, \quad \varepsilon_{ci} < \varepsilon_{cr} \qquad \textbf{Eq. 127}$$

The descending curve is the tension stiffening model of Collins and Mitchell (1987)

$$f_{ci} = \frac{f'_{ct}}{1 + \sqrt{500 \varepsilon_{ci}}}, \quad \varepsilon_{ci} > \varepsilon_{cr} \qquad \textbf{Eq. 128}$$

4.2.3 Concrete Dilatation

The Poisson effect or lateral expansion in the principal direction *i*, due to a compressive stress in the principal direction *j*, in a confined element, is given by (see Section 3.2.2):

$$\nu_{ij} = \nu_o + \alpha \frac{\varepsilon_{ci}}{\varepsilon_{pi}^{2.0}} .10^{-3} \qquad \textbf{Eq. 129}$$

$$\alpha = 1.9 + 24.2 \frac{f_{cl}}{f'_c} \qquad \textbf{Eq. 130}$$

where ν_o is the initial Poisson's ratio, and the average lateral pressure, f_{cl}, in a general three-dimensional finite element, is calculated from (compression negative):

$$f_{cli} = -\frac{f_{cj} + f_{ck}}{2}, \quad f_{cli} > 0$$

where f_{cj}, $f_{ck} < 0$, j and k are the principal directions normal to i. The variable Poisson's ratio proposed by Vecchio (1992) is used for elements in non-confined triaxial states (i.e. $f_{cj} > 0$ and/or $f_{ck} > 0$)

$$\nu_{ij} = \nu_o \left[1 + 1.5 \left(\frac{2\varepsilon_{cj}}{\varepsilon_{co}} - 1 \right)^2 \right] \leq 0.5 \qquad \text{Eq. 131}$$

4.2.5 Compression Softening

Softening in the response of concrete in compression due to opening of cracks in the principal tensile direction perpendicular to the major compression stress, is calculated using Vecchio Model A (1992). The reduction factor, β, is given by:

$$\beta = \frac{1}{1 + 0.55 \left[0.35 \left(\frac{-\varepsilon_{c1}}{\varepsilon_{c3}} \right) - 0.280 \right]^{0.80}} \leq 1.0 \qquad \text{Eq. 132}$$

4.2.4 Strength Enhancement, Strain at Peak Stress, and Strain at 80% of Peak Stress

4.2.4.1 Strength Enhancement

The stress at peak, f_{cc}, is calculated from the modified Ottosen criterion described in Chapter 3, Sections 3.3.3.2 to 3.3.3.4, as follows

$$a \frac{J_2}{f'^{\,2}_c} + \lambda \frac{\sqrt{J_2}}{f'_c} + b \frac{I_1}{f'_c} - 1 = 0 \qquad \text{Eq. 133a}$$

$$\lambda = k_1 + k_2 . \cos 3\theta \qquad \text{Eq.133b}$$

where a, k_1, k_2, and b are the parameters of the criterion (See Section 3.3.3.2). The values for the independent parameter, a, are calculated for each confinement level and

concrete strength, are reproduced in Table 19, for the case of a tensile strength equal to $f'_{ct} = 0.65\, f'^{0.33}_{c}$.

Table 19. Proposed values for parameter a

LN	HN	LH	HH
17.10	17.10	17.45	15.06

Value for HN assumed that for LN in corroboration

A procedure similar to that described by Selby and Vecchio (1997) is used to find the largest compressive stress (f_{c3}*) on the failure surface, when the solid is subjected to the principal stresses f_{c1} and f_{c2} in the other directions. The Newton-Raphson method is used to find the root of the modified Ottosen curve (i.e. f_{c3}*), by using a "seed" value for f_{c3}*, called here f_{c3}'

$$f_{c3}' = -\sqrt{f'^{2}_{c} + f_{c1}^{2} + f_{c2}^{2}} \qquad \text{Eq. 134}$$

The value for f_{c3} at step n is calculated from the value encountered in the previous step n-1, using the following expression where F is the modified Ottosen model.

$$f_{c3_n} = f_{c3_{n-1}} - \frac{\dfrac{\partial F(f_{c3_{n-1}})}{\partial f_{c3}}}{F(f_{c3_{n-1}})} \qquad \text{Eq. 135}$$

The process is terminated (i.e. $f_{c3n} = f_{c3}$*) when the difference between the previous and the current values is smaller than 0.00001. The stress on the failure surface is considered the peak stress, i.e. f_{c3}* = f_{cc}. The strength enhancement factor k_{σ}, due to confinement, can be written as:

$$k_{\sigma} = \frac{f_{cc}}{f'_{c}} \geq 1.0 \qquad \text{Eq. 136}$$

The value for the peak stress affected by strength enhancement and concrete softening is calculated as:

$$f_{p} = k_{\sigma}.\beta.f'_{c} \qquad \text{Eq. 137}$$

4.2.4.1 Strain at Peak Stress

The proposed formulation for the strain at peak stress is used in the compression field modelling of confined concrete (See Section 3.3.4):

$$\frac{\varepsilon_{cc}}{\varepsilon_{co}} = 1.0 + \left(24.4 - 0.116 f'_c\right)\frac{f_{cl}}{f'_c} \geq 1.0 \qquad \textbf{Eq. 138}$$

or,

$\varepsilon_{cc} = k_s.\varepsilon_{co}$, with

$$k_s = 1.0 + \left(24.4 - 0.116 f'_c\right)\frac{f_{cl}}{f'_c} \geq 1.0 \qquad \textbf{Eq. 139}$$

The value for the strain at peak stress affected by confinement and softening is calculated as:

$$\varepsilon_p = k_s.\beta.\varepsilon_{co} \qquad \textbf{Eq. 140}$$

4.2.4.2 Strain at 80% of Peak Stress

The proposed formulation for the strain at 80% peak stress is used in the compression field modelling of confined concrete (See Section 3.4.2.2):

$$\frac{\varepsilon_{c80}}{\varepsilon_{co}} = 1.5 + \left(89.5 - 0.6 f'_c\right)\frac{f_{cl}}{f'_c} \geq 1.5 \qquad \textbf{Eq. 141}$$

The value for the strain at 80% of peak stress can be expressed as:

$$\varepsilon_{c80} = k_{s80}\varepsilon_{co} \qquad \textbf{Eq. 142}$$

with

$$k_{s80} = 1.5 + \left(89.5 - 0.6 f'_c\right)\frac{f_{cl}}{f'_c} \geq 1.5 \qquad \textbf{Eq. 143}$$

4.2.6 Cracking Criterion

The Mohr-Coulomb criterion with tension cut-off is used to determine the cracking stress f_{cr}, in triaxial states of stress. Note that the uniaxial tensile strength f'_{ct} is an upper bound on the cracking strength.

$$f_{crf} = \frac{2c.\cos\phi}{1+\sin\phi} \qquad \textbf{Eq. 144}$$

where c is the cohesion and $\phi = 37^{\circ}$ (Vecchio 1992) is the angle of internal friction in concrete.

$$c = f'_c \frac{1-\sin\phi}{2\cos\phi} \qquad \textbf{Eq. 145}$$

$$f_{cr} = f_{crf}\left[1+\frac{f_{c3}}{f'_c}\right] \qquad \textbf{Eq. 146}$$

with:

$f_{cr} \geq 0.20$ [MPa]

$f_{cr} \leq f'_{ct}$

4.2.7 Steel and FRP Composites

4.2.7.1 Steel

A bilinear curve with strain hardening is used to model steel in compression and tension. Steel buckling is not considered, and steel (or FRP) and concrete are perfectly bonded.

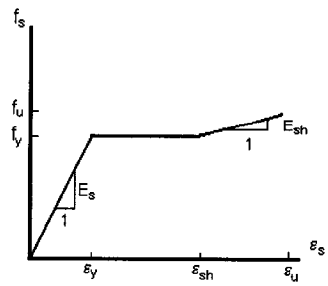

Figure 94. Stress-strain curve for steel.

$$f_s = E\varepsilon_s, \qquad \varepsilon_s \le \varepsilon_y \qquad \textbf{Eq.147a}$$

$$f_s = f_y, \qquad \varepsilon_y \le \varepsilon_s \le \varepsilon_{sh} \qquad \textbf{Eq.147b}$$

$$f_s = f_y + E_{sh}\varepsilon_s, \qquad \varepsilon_{sh} \le \varepsilon_s \le \varepsilon_u \qquad \textbf{Eq. 147c}$$

where E_s is the initial stiffness, f_y is the yield strength, ε_y is the strain at yield, E_{sh} is the strain hardening stiffness, ε_{sh} is the strain at the initiation of strain hardening, and ε_u is the strain at rupture.

4.2.7.2 FRP Composites

FRP fabrics are modelled using a linear elastic stress-strain curve that fails just after reaching the rupture stress f_{ju}. The initial stiffness is E_j, and the strain at rupture is ε_{ju}.

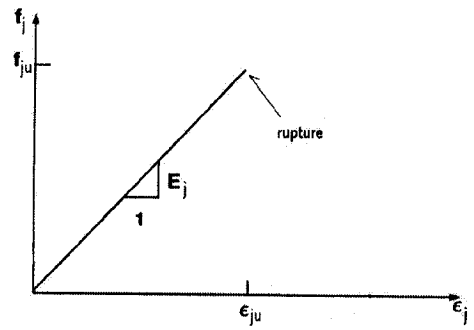

Figure 95. Stress-strain curve for FRP composites.

4.3 Element Library

Three finite elements were implemented into program VecTor6. They include a four-node torus element and a three-node torus element for concrete with or without smeared reinforcement, and a "ring" bar to model steel and FRP composites. A description of each element is presented here, and the stiffness matrices for each element are given in Appendix F. The stiffness matrices of the library of elements

developed and adapted for VecTor6 are closed-form relations that considerably reduce computation times in nonlinear analysis of reinforced concrete.

Each of the elements has two degrees of freedom (DOF) per node. (If the number of nodes of each element is n, then there are 2n DOF per element.) The general three-dimensional material stiffness matrix $\mathbf{D}_{6x6,}$ is represented in cylindrical coordinates (r, z, θ) in Figure 96, where r is the radial direction, z is the direction parallel to the axis of revolution, and θ is the tangential direction (normal to the plane rz). The matrix **D** is given below.

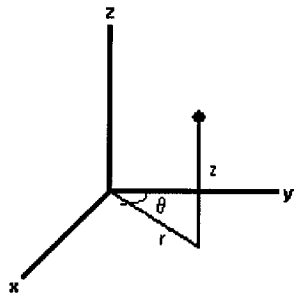

Figure 96. Cylindrical coordinate system.

$$\mathbf{D}_{6x6} = \begin{pmatrix} D_{rr} & D_{rz} & D_{r\theta} & 0 & 0 & 0 \\ D_{rz} & D_{zz} & D_{z\theta} & 0 & 0 & 0 \\ D_{r\theta} & D_{z\theta} & D_{\theta\theta} & 0 & 0 & 0 \\ 0 & 0 & 0 & G_{rz} & 0 & 0 \\ 0 & 0 & 0 & 0 & G_{r\theta} & 0 \\ 0 & 0 & 0 & 0 & 0 & G_{z\theta} \end{pmatrix} \quad \textbf{Eq. 148}$$

Considering only axisymmetric loading, the only possible shear deviation would be in the rz plane, and therefore the values for G_{rq} and $G_{z\theta}$ are necessarily zero. The material matrix can be simplified to a 4 x 4 matrix:

$$\mathbf{D}_{4x4} = \begin{pmatrix} D_{rr} & D_{rz} & D_{r\theta} & 0 \\ D_{rz} & D_{zz} & D_{z\theta} & 0 \\ D_{r\theta} & D_{z\theta} & D_{\theta\theta} & 0 \\ 0 & 0 & 0 & G_{rz} \end{pmatrix} \qquad \text{Eq. 149}$$

The stress and strain vectors, σ and ε, respectively, can be expressed as:

$$\boldsymbol{\varepsilon}^{\mathrm{T}} = \{\varepsilon_r \quad \varepsilon_z \quad \varepsilon_\theta \quad \gamma_{rz}\}_{1x4} \qquad \text{Eq. 150}$$

$$\boldsymbol{\sigma}^{\mathrm{T}} = \{\sigma_r \quad \sigma_z \quad \sigma_\theta \quad \tau_{rz}\}_{1x4} \qquad \text{Eq. 151}$$

$$\boldsymbol{\sigma}_{4x1} = \mathbf{D}_{4x4}\boldsymbol{\varepsilon}_{4x1} \qquad \text{Eq. 152}$$

The strain vector ε is a function of the displacements at the nodes of the finite element.

$$\boldsymbol{\varepsilon}_{4x1} = \mathbf{B}_{4x2n}\boldsymbol{\delta}_{2nx1} \qquad \text{Eq. 153}$$

where **B** is a matrix that is derived from shape functions for the particular element, δ is the displacement vector, and *n* is the number of nodes of the finite element.

The element stiffness matrix **k** is calculated over the volume of the element as:

$$\mathbf{k}_{2nx2n} = \int_V \mathbf{B}^{\mathrm{T}}{}_{2nx4}\mathbf{D}_{4x4}\mathbf{B}_{4x2n}\,dV \qquad dV = 2\pi r.dr.d\theta \qquad \text{Eq. 154}$$

where dV is the infinitesimal volume around the axis of revolution of the element, and *r* is the radius from the axis of revolution to the centroid of the cross section of the element.

The stresses in the radial, tangential and longitudinal directions (i.e. r, θ, and z) are calculated for each finite element at the centroid of the cross section. Each finite element implemented in VecTor 6 is described next.

- *Four-node torus element*

A torus element with a rectangular section is shown in Figure 97. Nodes are numbered counter-clockwise, and the sides of the cross section are parallel to the radial axis and the axis of symmetry, respectively. The dimension in the radial and longitudinal directions are d and a, respectively. The displacements in the plane rz for node k, $u_{r,k}$, and $u_{z,k}$ are represented in Figure 97 along with a rendered view of the element. The stiffness matrix $\mathbf{k}_{8x8}$, is given in Appendix F, Section F.1.

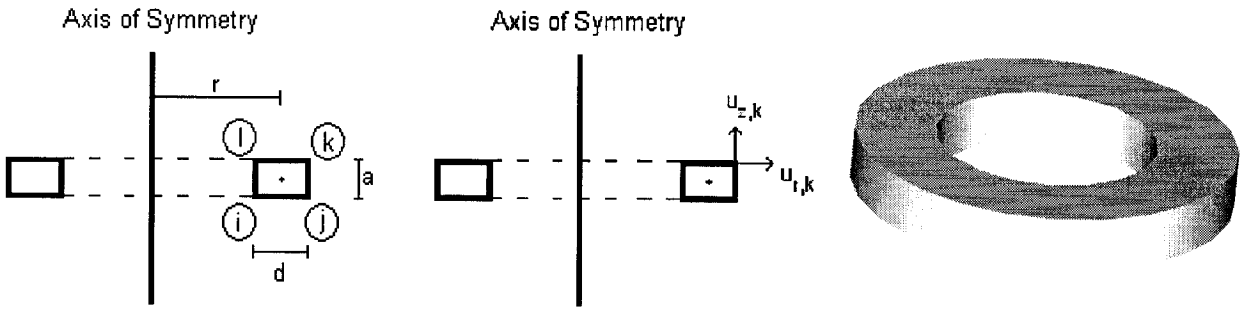

Figure 97. Four-node torus element.

- *Three-node torus element*

This is a constant strain element. The node numbering follows the same scheme as for the four-node element. A sketch of the basic characteristics of the triangular torus is given in Figure 98 . The stiffness matrix $\mathbf{k}_{6x6}$ is given in Appendix F, Section, F.2.

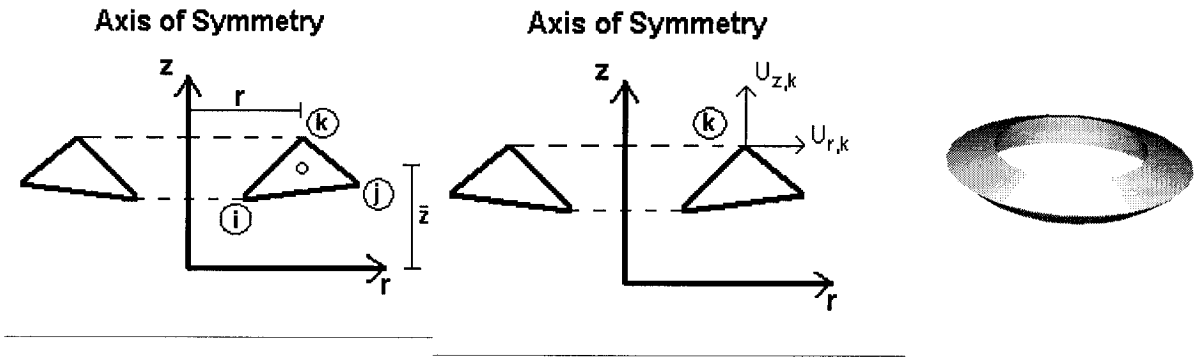

Figure 98. Three-node torus element.

- *Ring Bar*

This is a simple one-node torus that is used to model steel hooks or spirals, or FRP sheets when used to wrap columns in the circumferential direction. It only supports tangential deformation, i.e. along the θ direction, when it expands (or contracts). A sketch is given in Figure 99. The stiffness matrix $\mathbf{k}_{2x2}$ is given in Appendix F, Section F.3.

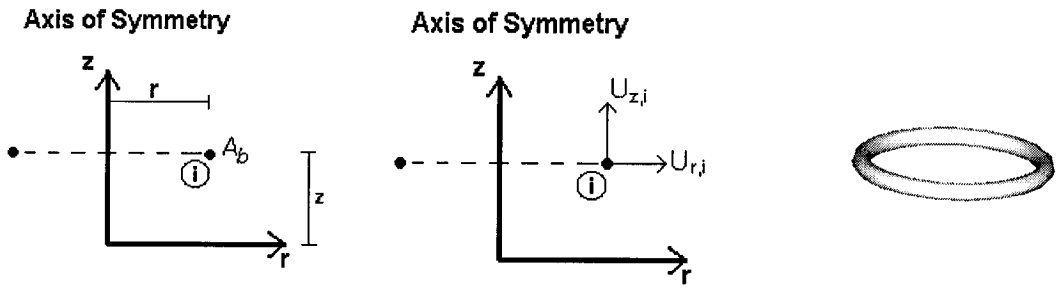

Figure 99. Ring Bar.

4.4 Finite Element Analysis and Flow Chart

The nonlinear elastic analysis procedure employed in VecTor6 follows the same scheme used in all VecTor programs developed at the University of Toronto. A brief summary is given below, and complete details can be found in Selby (1993).

The material stiffness matrix for each finite element is the sum of concrete and steel material matrices in global directions, $\mathbf{D_c}$ and $\mathbf{D_s^i}$, respectively, where *i* represents each steel (or FRP) component.

$$\mathbf{D} = \mathbf{D_c} + \sum_n \mathbf{D_s^i} \qquad \text{Eq. 155}$$

$$\mathbf{D_c} = \mathbf{T_c}^{\mathrm{T}} \mathbf{D_c}' \mathbf{T_c} \qquad \text{Eq. 156}$$

$$\mathbf{D_s^i} = \mathbf{T_s}^{\mathrm{T}} \mathbf{D_s^{i'}} \mathbf{T} \qquad \text{Eq. 157}$$

where $\mathbf{D_c}'$ and $\mathbf{D_s^i}$, are the material matrices in the principal directions, and $\mathbf{T_c}$ and $\mathbf{T_s}$ are the transformation matrices for concrete and steel (or FRP), respectively. The principal material stiffness matrices for concrete and steel are expressed as:

$$\mathbf{D_c}' = \begin{pmatrix} E_{c1} & 0 & 0 & 0 \\ 0 & E_{c2} & 0 & 0 \\ 0 & 0 & E_{c3} & 0 \\ 0 & 0 & 0 & G_c \end{pmatrix} \qquad \text{Eq. 158}$$

$$\mathbf{D_s^{i'}} = \begin{pmatrix} \rho_s E_s & 0 & 0 & 0 \\ 0 & 0 & 0 & 0 \\ 0 & 0 & 0 & 0 \\ 0 & 0 & 0 & 0 \end{pmatrix} \qquad \text{Eq. 159}$$

where E_{ci} and E_s are the secant stiffnesses for concrete and steel, respectively, and ρ_s is the steel ratio. The program VecTor6 calculates the dilatation strains as done in VecTor3 using the concept of prestrains. The concrete dilatation vector ε_{co}' in the principal directions is given by:

$$\boldsymbol{\varepsilon}_{\mathbf{co}}{}^{\mathrm{T}} = \left\{ \varepsilon_{co}{}^{1} \quad \varepsilon_{co}{}^{2} \quad \varepsilon_{co}{}^{3} \right\} \qquad \text{Eq. 160}$$

where

$$\varepsilon_{co}{}^{i} = -\nu_{ij} \frac{f_{cj}}{E_{cj}} - \nu_{ik} \frac{f_{ck}}{E_{ck}} \qquad \text{Eq. 161}$$

and *i*, *j*, and *k* are the principal directions.

Note that v_{ij} is calculated using the proposed formulation in Chapter 3, Section 3.2, and f_{cj} and f_{ck} are computed using the stress-strain curves described in Section 4.2. The transformed concrete dilatations in the global directions are given by:

$$\boldsymbol{\varepsilon}_{co} = \mathbf{T}_c \boldsymbol{\varepsilon}_{co}' \qquad \textbf{Eq. 162}$$

As concrete dilatation varies throughout the loading process, the prestrains due to dilatation are converted to equivalent forces, $\mathbf{F}_{co}$, applied to the finite element at each iteration.

$$\mathbf{F}_{co} = \mathbf{k}_c \boldsymbol{\delta}_{co} \qquad \textbf{Eq. 163}$$

where $\mathbf{k}_c$ is the concrete part of the element stiffness matrix, and δ_{co} is:

$$\boldsymbol{\delta}_{co} = \int_V \boldsymbol{\varepsilon}_{co} dV \qquad \textbf{Eq. 164}$$

These nodal forces are added to the forces externally applied to the structural element at each load step. The secant stiffnesses for the component materials are obtained from stress-strain curves, as shown for concrete in Figure 100, and Eq. 165.

$$E_{ci} = \frac{f_{ci}}{\varepsilon_{ci}} \qquad \textbf{Eq. 165}$$

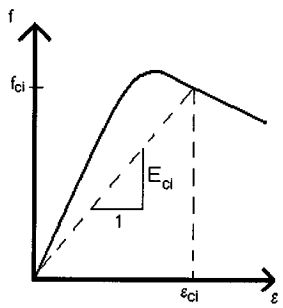

Figure 100. Secant stiffness.

The flow chart in Figure 101 shows the iterative analytical procedure used to calculate the response of a structural element subjected to axisymmetric loading in program VecTor6.

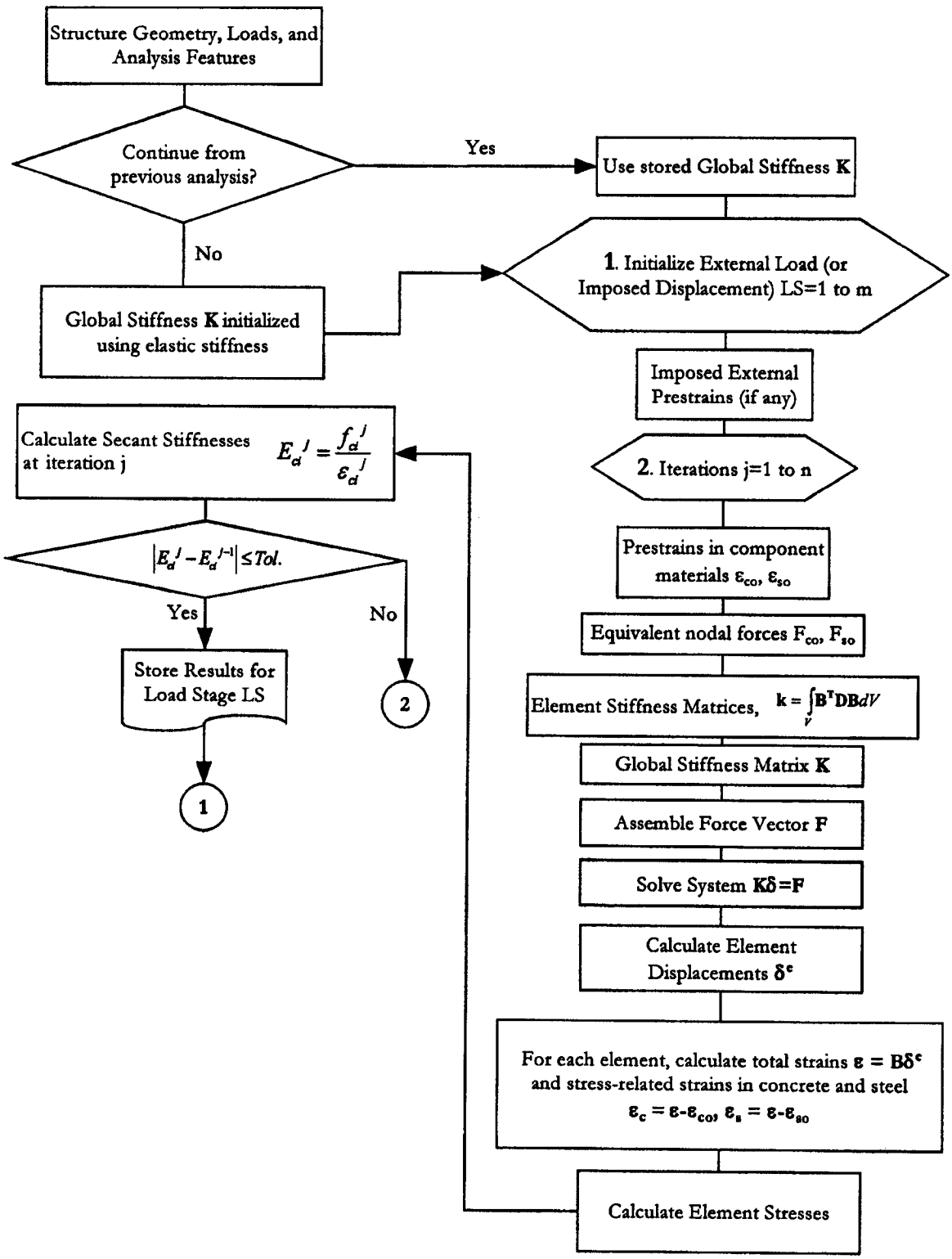

Figure 101. Flow chart for VecTor6.

Chapter 5: Confined Concrete Behaviour and Analysis

5.1 Analytical Comparison of Stress-Strain Curves of Triaxial Tests.

This section examines the stress-strain responses obtained from experiments on concrete cylinders subjected to axial compression and either active lateral pressure or confined with FRP composites. Experimental axial stress-axial strain curves and axial stress-lateral strain curves (if available), are compared with the analytical curves calculated using the proposed models in this thesis. A brief description for each set of specimens is given along with the stress-strain plots.

5.1.1 Candappa, Sanjayan, and Setunge (1999)

The axial stress-axial strain and axial stress-lateral strain curves for 12 of the cylinders tested are shown here. The target strengths of the tests cylinders were 60 MPa, 75 MPa, and 100 MPa, respectively. The cylinders had a diameter of 98 mm and were 200 mm in length. Three sets of four cylinders each, corresponding to the target strengths, were tested in monotonic axial compression and active lateral pressure applied using pressurized oil in a triaxial chamber. The cylinders were subjected to lateral pressures of 0 MPa, 4 MPa, 8 MPa, and 12 MPa, respectively. The peak strength f_{cc}, strain at peak ε_{cc}, and unconfined strain at peak ε_{co}, were obtained from the experimental curves from the paper, as tabulated data were not given by the authors.

Figures 101 to 103 show the axial stress-axial strain and axial stress-lateral strain curves for the 12 specimens (compression positive). The solid lines represent the analytical results, and the curves with markers represent the experimental data. Table 20 shows the main parameters for each curve. Concrete strength and strain at peak

stress are well captured by the proposed models for all types of concrete. The largest underestimation occurred in the calculation of the strengths for the 75 MPa cylinders, which were up to 9% lower than the experimental values. The axial stress-lateral strain curves calculated using the dilatation model follow the general trend of the specimens.

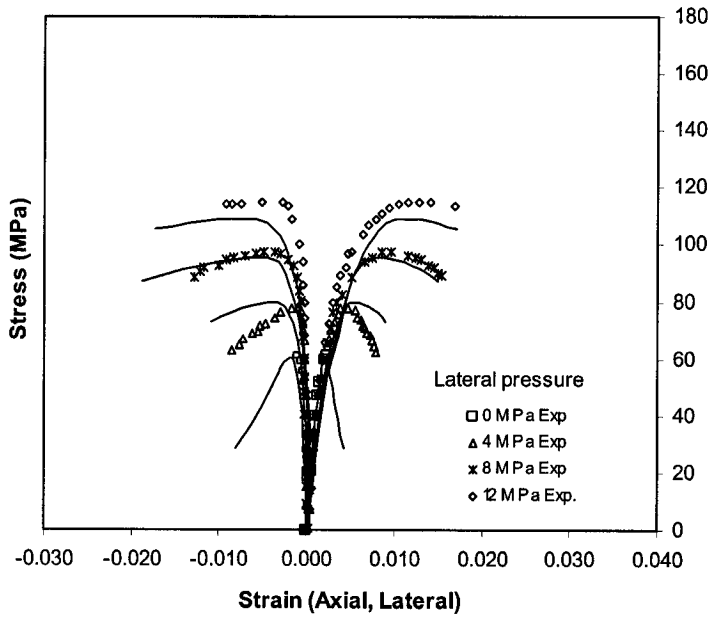

Figure 102. Axial stress–axial strain, and axial stress- lateral strain curves, 60 MPa cylinders, Candappa et al.

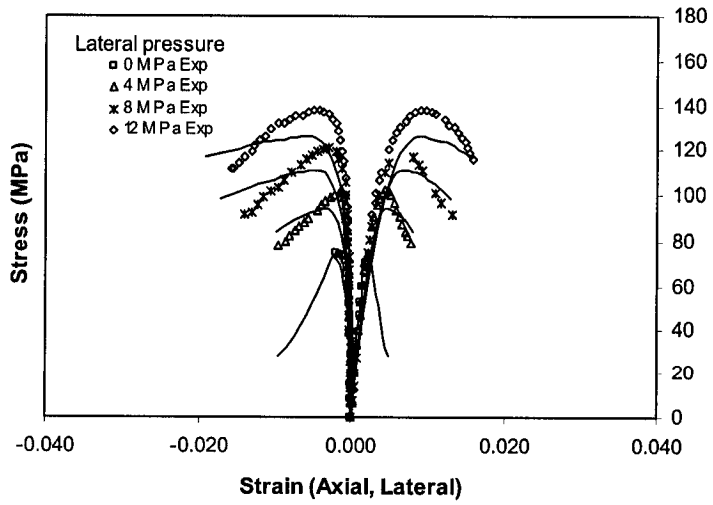

Figure 103. Axial stress–axial strain, and axial stress- lateral strain curves, 75 MPa cylinders, Candappa et al.

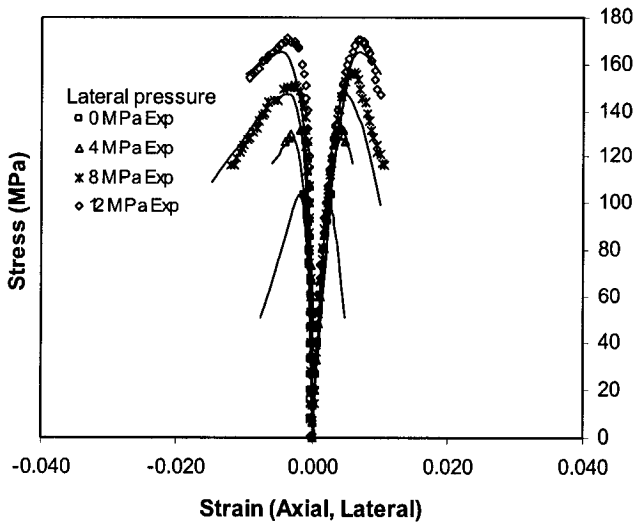

Figure 104. Axial stress–axial strain, and axial stress- lateral strain curves, 100 MPa cylinders, Candappa et al.

Table 20. Experimental and analytical curve parameters of Candappa et al. curves.

		Analytical						Exp.					fcc(an)	ε_{cc}(an)
f'_c	f_{cl}	ε_{co}***	ε_{cc}	ε_{c80}	k_d	f_{cc}	ε_{cl}**	ε_{co}	ε_{cc}	ε_{c80}*	f_{cc}	ε_{cl}**		
[MPa]	[MPa]	[10^{-3}]	[10^{-3}]	[10^{-3}]	[10^{+8}]	[MPa]	[10^{-3}]	[10^{-3}]	[10^{-3}]	[10^{-3}]	[MPa]	[10^{-3}]	fcc(exp)	ε_{cc}(exp)
60	0	2.37	2.37	3.56	6.73	61.5	-1.50	2.37	2.37	3.40	61.5	-1.06	1.00	1.00
	4	2.37	5.04	11.66	0.37	80.2	-3.30	2.37	3.83	8.00	78.1	-1.17	1.03	1.32
	8	2.37	7.71	19.77	0.16	95.5	-5.20	2.37	9.54	21.60	97.5	-4.92	0.98	0.81
	12	2.37	10.37	27.88	0.10	109.0	-7.10	2.37	11.55	111.70	114.8	-2.83	0.95	0.90
75	0	2.44	2.44	3.66	9.17	73.9	-2.40	2.44	2.44	3.50	73.9	-1.97	1.00	1.00
	4	2.44	4.54	9.62	0.86	94.2	-3.80	2.44	4.52	7.50	102.2	-1.52	0.92	1.00
	8	2.44	6.63	15.59	0.38	111.0	-4.80	2.44	8.11	12.80	116.8	-2.89	0.95	0.82
	12	2.44	8.73	21.55	0.24	125.8	-5.90	2.44	9.07	17.60	137.8	-5.01	0.91	0.96
100	0	2.80	2.80	4.20	13.66	103.5	-1.93	2.80	2.80	4.10	103.5	-1.14	1.00	1.00
	4	2.80	4.15	7.17	4.47	127.7	-2.54	2.80	3.91	8.50	132.4	-1.49	0.96	1.06
	8	2.80	5.49	10.13	2.53	147.7	-4.30	2.80	6.09	9.60	156.4	-2.65	0.94	0.90
	12	2.80	6.84	13.10	1.75	165.5	-4.64	2.80	7.11	11.30	170.7	-3.62	0.97	0.96

Notes:

* Estimated from experimental curve

** Lateral strain at peak stress

*** Experimental value

mean	**0.97**	**0.98**
StDev	**0.034**	**0.131**
CV[%]	**3.56**	**13.45**

It should be noted that the specimens can be classified in the low-confined high strength concrete range LH, according to the definitions given in Chapter 3. The experimental strain at unconfined peak stress ε_{co}, was used in the determination of the

stress-strain curves. The value for the initial stiffness E_c was taken from the following expression (See Mitchell and Collins 1997), suitable for high strength concrete:

$$E_c = 3320\sqrt{f'_c} + 6900 \qquad \text{Eq. 166}$$

5.1.2 Xie, Elwi, and MacGregor (1995)

Axial stress-axial strain curves for 19 of the concrete cylinders tested by the authors are shown. As in the previous section, the cylinders were subjected to constant lateral pressure and axial compression. The cylinders had a diameter of 55.5 mm and were 110 mm in length. Concrete strengths were 60 MPa and 92 MPa. The lateral pressure was applied using an oil pump connected to a Hoek triaxial cell. The lateral pressures were 0, 2.3, 5.3, 8.3, 11.3, 14.3, 20.3, 23.3 and 29.3 MPa for the 60 MPa cylinders, and 0, 3.8, 8.3, 12.8, 16.6, 17.3, 21.8, 26.3, 35.5, and 44.5 MPa for the 92 MPa cylinders, respectively. Longitudinal tensile splitting was the failure mode for the specimens with confinement ratios less than 0.15. For high confinement ratios, the failure mode was "highly distributed with little localized damage", according to the researchers. The confinement ratio reached a maximum value of 0.50 and the cylinders shown here can be classified within the LH and HH ranges as defined in Chapter 3.

Figures 104 and 105 show the experimental and analytical axial stress-axial strain curves for the two sets of cylinders. The experimental data was obtained from graphs from the researchers, but not tabulated. Table 21 shows the principal parameters of these curves. The analytical curves were calculated with the proposed models. Lateral strain results were not available.

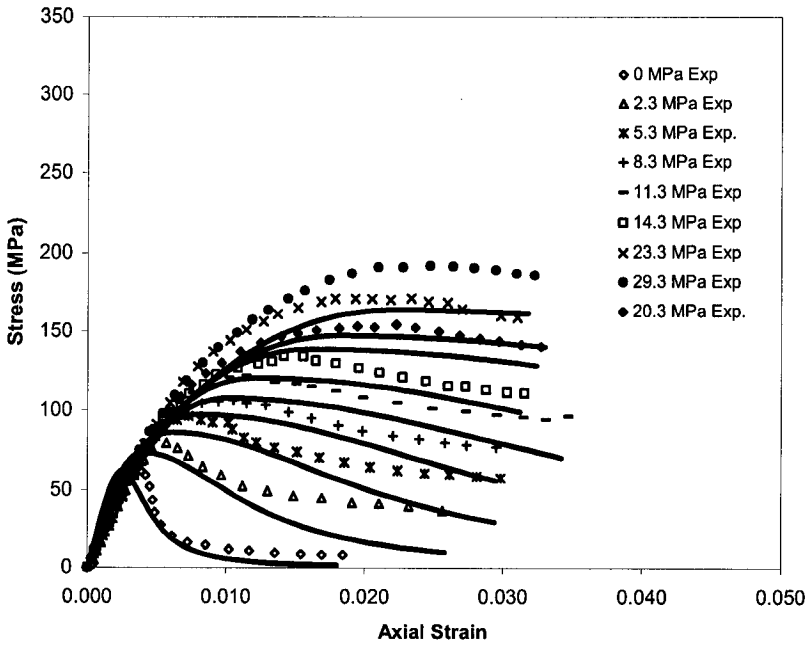

Figure 105. Axial stress–axial strain curves, 60.2 MPa cylinders, Xie et al.

The solid lines in the figures represent the analytical response, and the markers are the experimental curves. The inset shows the lateral pressure applied to each specimen. The analytical axial stress-axial strain behaviour follows that of the experimental results. The analytical strength of the cylinders was underestimated for all values of lateral pressures. This may be explained by the fact that friction of the cylinders against the testing machine at the top and bottom surfaces was not avoided causing additional lateral restraint. It should be noted that the number of tests with high confinement pressures and high strength concrete (HH tests) in which the proposed failure surface was based, was fewer when compared with those used for low confinement ratios, and the proposed model for strength enhancement represents the average of the available tests. This accounts for the need of further testing of high and very high concrete strength cylinders subjected to high confinement pressures.

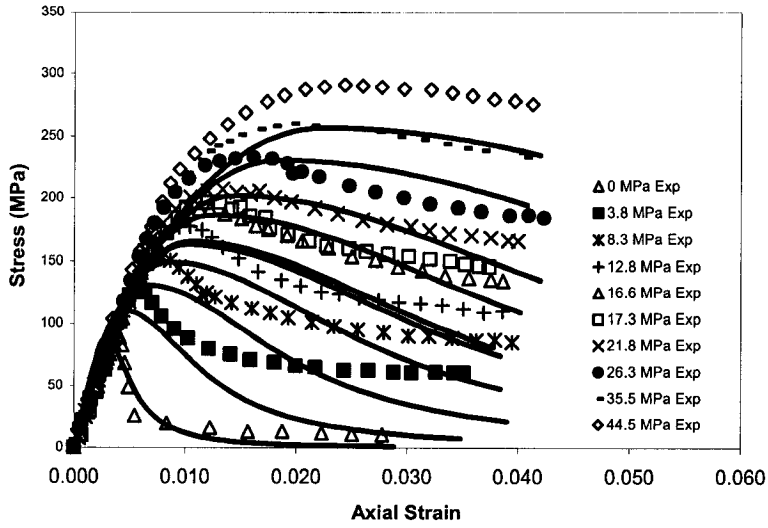

Figure 106. Axial stress–axial strain curves, 92.2 MPa cylinders, Xie et al.

Table 21. Experimental and analytical curve parameters of Xie et al. curves.

		Analytical					Exp.				fcc (anal.)	ε_{cc} (anal.)
f'_c	f_{cl}	ε_{co}**	ε_{cc}	ε_{c80}	k_d	f_{cc}	ε_{co}*	ε_{cc}	ε_{c80}*	f_{cc}	———	———
[MPa]	[MPa]	[10^{-3}]	[10^{-3}]	[10^{-3}]	[10^{+8}]	[MPa]	[10^{-3}]	[10^{-3}]	[10^{-3}]	[MPa]	fcc (exp.)	ε_{cc} (exp.)
60.2	2.30	2.42	4.03	8.57	0.66	73.5	3.00	5.70	8.60	80.6	0.91	0.71
	5.30	2.42	6.14	15.00	0.24	86.2	3.00	7.30	13.40	97.6	0.88	0.84
	8.30	2.42	8.24	21.44	0.14	97.3	3.00	10.50	21.50	107.6	0.90	0.79
	11.30	2.42	10.35	27.88	0.09	107.5	3.00	11.40	29.30	121.6	0.88	0.91
	14.30	2.42	12.46	34.32	0.08	121.7	3.00	14.20	34.50	136.8	0.89	0.88
	20.30	2.42	16.67	47.19	0.05	140.6	3.00	22.30	45.40	156.9	0.90	0.75
	23.30	2.42	18.77	53.63	0.05	149.4	3.00	23.40	44.80	172.1	0.87	0.80
	29.30	2.42	22.98	66.50	0.04	166.1	3.00	24.70	65.90	193.2	0.86	0.93
92.2	3.80	2.80	4.39	8.14	2.16	110.4	3.00	5.80	8.20	129.4	0.85	0.76
	8.30	2.80	6.26	12.82	1.00	131.2	3.00	7.90	12.50	155.6	0.84	0.79
	12.80	2.80	8.14	17.49	0.64	149.3	3.00	10.40	16.50	181.2	0.82	0.78
	16.60	2.80	9.73	21.43	0.49	163.3	3.00	11.20	25.40	199.8	0.82	0.87
	17.30	2.80	10.02	22.16	0.47	165.8	3.00	13.10	26.60	194.3	0.85	0.76
	21.80	2.80	11.90	26.83	0.40	189.4	3.00	13.40	40.60	208.7	0.91	0.89
	26.30	2.80	13.78	31.50	0.33	204.9	3.00	13.10	40.90	234.6	0.87	1.05
	35.50	2.80	17.62	41.05	0.25	234.2	3.00	19.60	57.40	261.1	0.90	0.90
	44.44	2.80	21.35	50.33	0.20	260.8	3.00	24.30	86.00	293.5	0.89	0.88
										mean	**0.87**	**0.84**
										StDev	**0.028**	**0.085**
										CV[%]	**3.25**	**10.11**

Notes:

* Determined from experimental curves, in paper by Xie et al. (1995)

** Calculated

The initial stiffness E_c was calculated using Eq. 166, and the strain at peak unconfined strength ε_{c0} was calculated using the expressions:

$$\varepsilon_{co} = \frac{f'_c}{E_c}\frac{n}{n-1} \qquad \text{Eq. 167a}$$

$$n = 0.8 + \frac{f'_c}{17} \qquad \text{Eq.167b}$$

5.1.3 Attard and Setunge (1996)

High strength concrete cylinders with unconfined concrete strengths ranging from 60 to 130 MPa were tested under low constant lateral pressure and axial compression. The axial stress-axial strain curves of nine of the cylinders published by the authors are reproduced and calculated using the proposed confinement models. The confinement ratios for the cylinder results ranged from 0.04 to 0.13, which place them in the LH range. The 9 cylinders were of concrete strengths of 110, 118, and 120 MPa, divided in groups of three subjected to confining pressures of 5, 10, and 15 MPa, respectively.

These test results form part of the databases used in the formulation of the failure surface, the strain at peak stress, and the strain at 80% of peak stress. Figures 106 to 108 show the experimental (markers) and calculated (solid lines) axial stress-axial strain curves, and Table 22 shows the curve parameters. The experimental data was obtained from the graphs published in the paper.

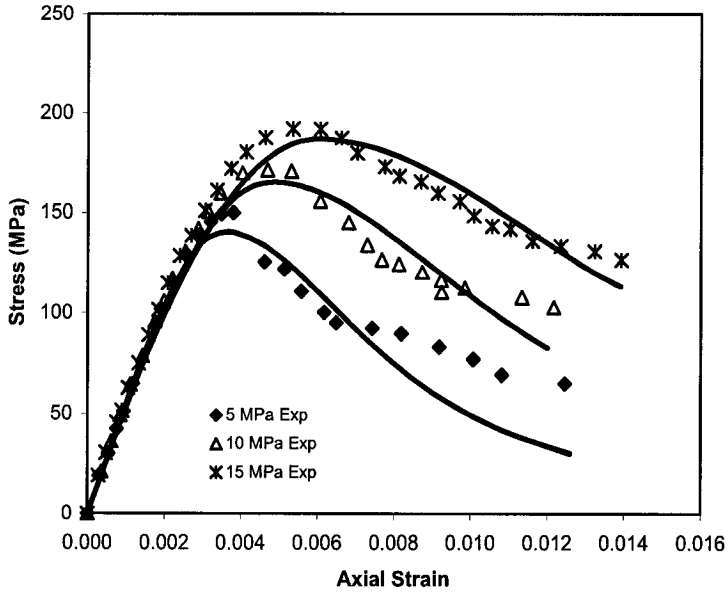

Figure 107. Axial stress–axial strain curves, 110 MPa cylinders, Attard and Setunge.

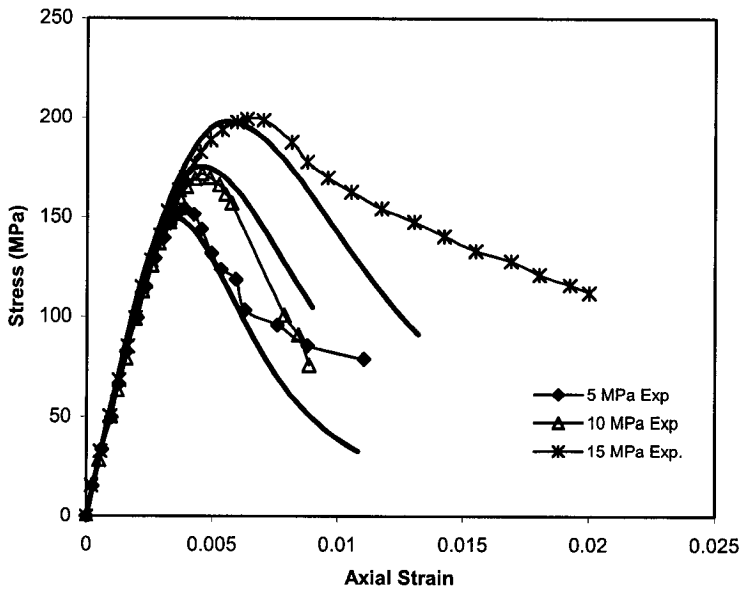

Figure 108. Axial stress–axial strain curves, 118 MPa cylinders, Attard and Setunge.

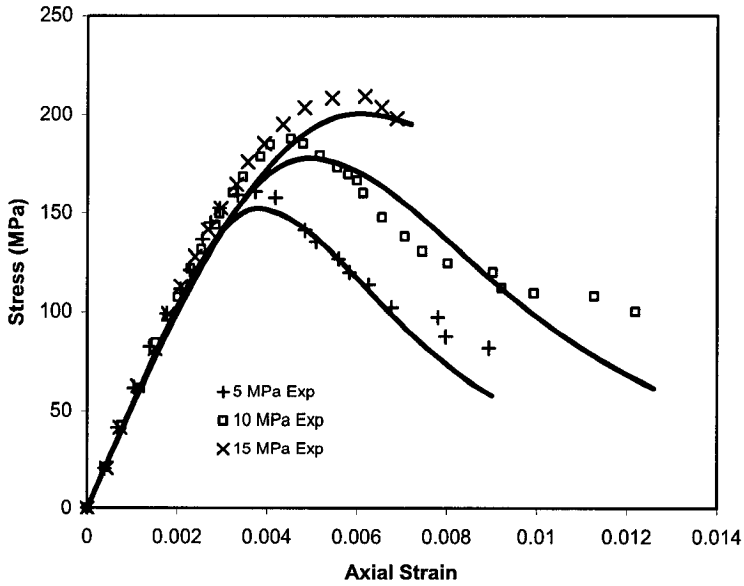

Figure 109. Axial stress–axial strain curves, 120 MPa cylinders, Attard and Setunge.

Table 22. Experimental and analytical curve parameters of Attard-Setunge curves.

		Analytical					Exp.				fcc (anal.)	ε_{cc} (anal.)
f'_c	f_{cl}	ε_{co}**	ε_{cc}	ε_{c80}	k_d	f_{cc}	ε_{co}	ε_{cc}	ε_{c80}*	f_{cc}	———	———
[MPa]	[MPa]	[10^{-3}]	[10^{-3}]	[10^{-3}]	[10^{+8}]	[MPa]	[10^{-3}]	[10^{-3}]	[10^{-3}]	[MPa]	fcc (exp.)	ε_{cc} (exp.)
110	5	2.30	3.52	5.91	8.67	140.5	2.80	3.50	5.20	150.0	0.94	1.01
(cR)***	10	2.30	4.74	8.36	5.20	165.2	2.80	4.40	7.20	175.0	0.94	1.08
	15	2.30	5.96	10.82	3.70	186.9	2.80	6.00	9.80	192.0	0.97	0.99
118	5	2.34	3.41	5.36	14.61	149.7	2.80	3.80	5.40	154.0	0.97	0.90
(aH)***	10	2.34	4.47	7.22	10.67	179.4	2.80	4.90	11.00	173.0	1.04	0.91
	15	2.34	5.54	9.07	7.85	198.0	2.80	6.20	6.50	201.0	0.99	0.89
120	5	2.60	3.74	5.80	13.66	152.0	2.80	4.20	5.50	168.0	0.90	0.89
(bR)***	10	2.60	4.88	7.69	10.01	178.0	2.80	4.80	6.50	187.0	0.95	1.02
	15	2.60	6.02	9.59	7.91	200.7	2.80	5.70	8.80	211.0	0.95	1.06
										mean	**0.96**	**0.97**
										St.Dev	**0.04**	**0.07**
										CV[%]	**3.83**	**7.63**

Notes:

* Estimated from experimental curve

** Calculated

*** Type of Mix (See Attard and Setunge 1996)

The strain ε_{co} was calculated using Eqs.167, and the experimental value for the stiffness was used.

5.1.4 Imran and Pantazopoulou (1996)

The axial stress-axial strain and axial stress–lateral strain curves of the cylinders described in Chapter 3, Section 3.2, used to determine the dilatation model, are compared with their respective analytical counterparts. A detailed description of the cylinders was given in Chapter 3. The cylinders were 55 mm in diameter and 110 mm in length. Concrete strengths at the time of testing were 73.4, 47.4, and 28.6 MPa. The cylinders were divided into three sets according to concrete strength and were tested at constant lateral pressure and increasing axial compression (type **a** tests, as described in the paper). The lateral pressures ratios were 0, 5, 10, 20, 40, 80, and 100 % of the target concrete strengths, which were 65, 43, and 21 MPa, respectively.

As with the previous set of calculations, Table 23 shows the characteristics of the stress-strain curves (lateral strain negative, axial strain positive), and Figures 109 to 111 show the experimental curves (markers) and the calculated curves (thin solid lines). The experimental data was obtained from the researchers. From Table 23, it can be seen that the best strength predictions were found for the 73.4 MPa cylinders, where the calculated to experimental strength ratio was in the range of 0.94 to 1.03. The ratios for 47.4 MPa cylinders ranged between 0.82 and 1.00, and for the low strength concrete of 28.6 MPa, the range was between 0.88 and 1.20. The mean of the analytical to experimental strength ratio and strain at peak stress ratio were 0.99 and 0.80, respectively, with coefficients of variation of 9.0% and 11.3%, respectively.

The 47.4 MPa and 73.4 MPa specimens were classified into the LH and HH categories, and the 28.6 MPa set fell into the LN and HN categories. It was also found

that the analytical pre-peak axial stress-axial strain response was less stiff than the experimental response as the lateral pressure increased and that the lateral deformation trend was well captured by the dilatation model. The strain at unconfined peak strength ε_{co}, was calculated using Eqs.166 and 167 for high strength concrete (i.e. 47.4 MPa and 73.4 MPa tests), and Eq.168 for normal strength concrete (i.e. 28.6 MPa tests).

$$\varepsilon_{co} = \frac{2f'_c}{E_c} \qquad \textbf{Eq. 168a}$$

$$E_c = 5000\sqrt{f'_c} \qquad \textbf{Eq.168b}$$

Table 23. Experimental and analytical curve parameters of Imran-Pantazopoulou curves.

		Analytical						Exp.				f_{cc}(an)	ε_{cc}(an)
f'_c	f_{cl}	ε_{co}*	ε_{cc}	ε_{c80}	k_d	f_{cc}	ε_{cl}**	ε_{co}	ε_{cc}	f_{cc}	ε_{cl}**	———	———
[MPa]	[MPa]	[10^{-3}]	[10^{-3}]	[10^{-3}]	[10^{+8}]	[MPa]	[10^{-3}]	[10^{-3}]	[10^{-3}]	[MPa]	[10^{-3}]	f_{cc}(exp)	ε_{cc}(exp)
28.6	0.00	2.14	2.14	3.21	1.79	28.6	-2.40	2.60	2.60	28.6	-1.84	1.00	0.82
	1.05	2.14	3.80	8.89	0.10	32.5	-3.41	2.60	4.70	33.6	-4.53	0.97	0.81
	2.10	2.14	5.46	14.58	0.04	36.1	-3.60	2.60	6.75	36.4	-6.73	0.99	0.81
	4.20	2.14	8.78	25.94	0.02	42.5	-5.74	2.60	13.85	48.1	-10.06	0.88	0.63
	8.40	2.14	15.42	48.68	0.01	78.4	-9.23	2.60	23.75	65.2	-14.96	1.20	0.65
	14.70	2.14	25.37	82.78	0.01	104.3	-15.53	2.60	34.25	92.3	-21.56	1.13	0.74
	21.00	2.14	35.33	116.88	0.01	126.7	-28.62	2.60	44.60	114.4	-29.21	1.11	0.79
47.4	0.00	2.21	2.21	3.32	4.60	47.4	-2.24	2.80	2.80	47.4	-1.24	1.00	0.79
	2.15	2.21	4.11	9.44	0.28	56.8	-3.14	2.80	4.30	57.7	-3.24	0.98	0.96
	4.30	2.21	6.01	15.56	0.12	64.9	-4.09	2.80	6.90	67.3	-3.4	0.96	0.87
	8.60	2.21	9.81	27.80	0.05	79.2	-6.82	2.80	14.60	83.6	-7.96	0.95	0.67
	17.20	2.21	17.40	52.28	0.02	106.1	-12.20	2.80	25.30	118.1	-14.89	0.90	0.69
	30.10	2.21	28.79	89.01	0.01	138.2	-17.30	2.80	36.00	161.1	-15.12	0.86	0.80
	43.00	2.21	40.19	125.73	0.01	166.9	-23.20	2.80	47.30	204.7	-17.21	0.82	0.85
73.4	0.00	2.58	2.58	3.87	8.09	73.4	-1.64	3.25	3.25	73.4	-1.54	1.00	0.79
	3.20	2.58	4.37	8.98	0.95	90.0	-2.73	3.25	4.95	96.1	-3.05	0.94	0.88
	6.40	2.58	6.16	14.10	0.43	103.9	-3.80	3.25	6.50	108.7	-3.78	0.96	0.95
	12.80	2.58	9.75	24.32	0.19	127.9	-6.70	3.25	10.45	125.6	-5.28	1.02	0.93
	25.60	2.58	16.91	44.78	0.10	173.2	-10.94	3.25	20.25	168.6	-8.62	1.03	0.84
	38.40	2.58	24.08	65.23	0.06	209.1	-15.94	3.25	31.05	204.0	-8.84	1.03	0.78
	51.20	2.58	31.24	85.68	0.05	241.7	-20.94	3.25	40.90	240.5	-29.33	1.01	0.76
											mean	**0.99**	**0.80**
											StDev	**0.09**	**0.09**
											CV[%]	**8.98**	**11.35**

Notes:

* Calculated

** Lateral strain at peak stress

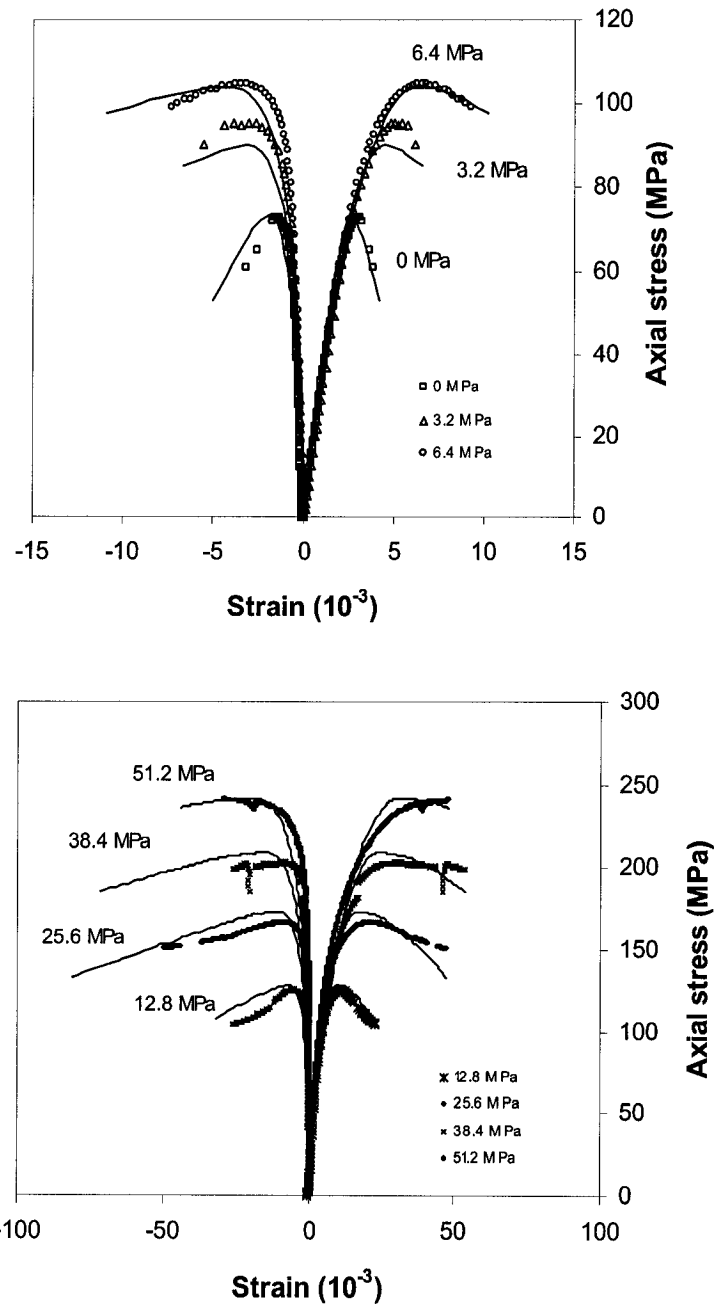

Figure 110. Axial stress–axial strain, and axial stress-lateral strain curves, 73.4 MPa cylinders, Imran and Pantazopoulou.

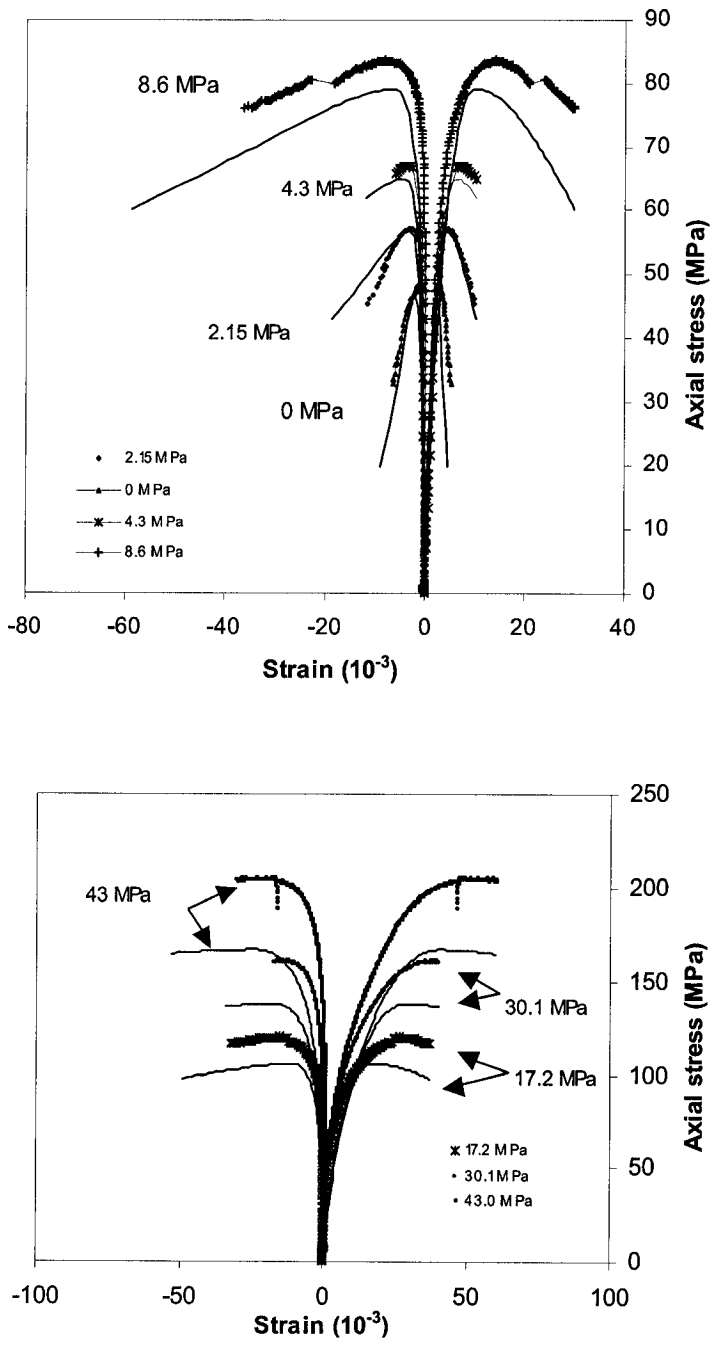

Figure 111. Axial stress–axial strain, and axial stress-lateral strain curves, 47.4 MPa cylinders, Imran and Pantazopoulou.

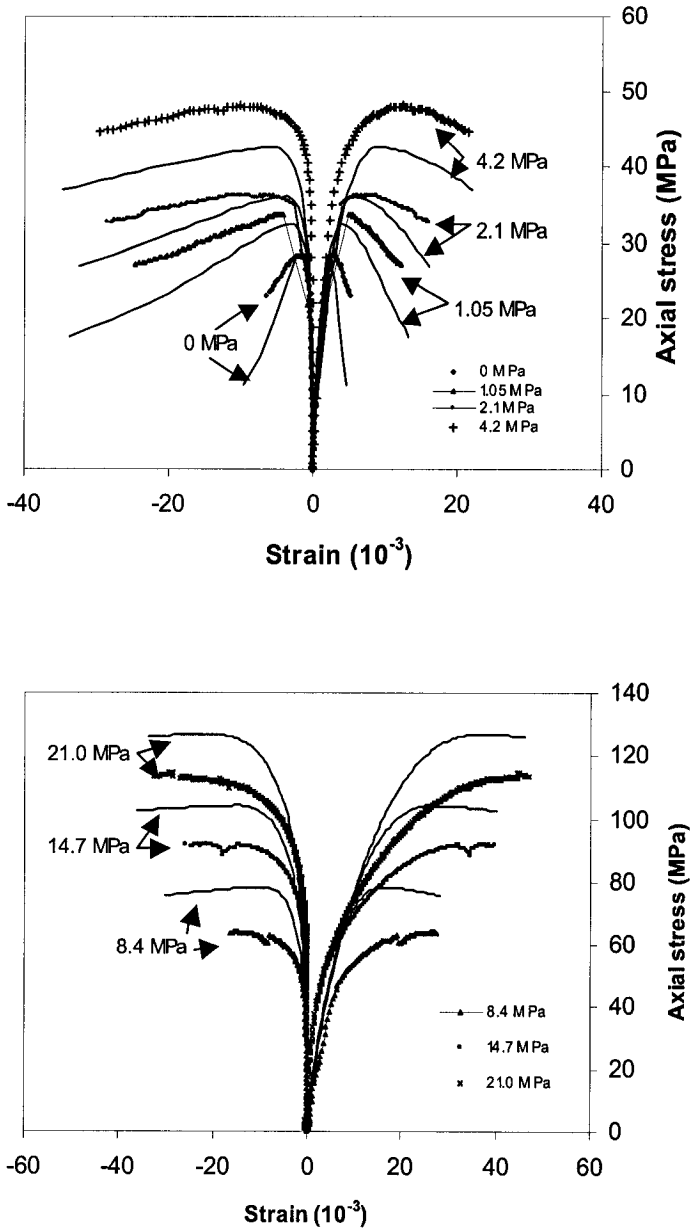

Figure 112. Axial stress–axial strain, and axial stress-lateral strain curves, 28.6 MPa cylinders, Imran and Pantazopoulou.

5.1.4 Karabinis and Rousakis (2002)

This testing program consisted of concrete cylinders with a diameter of 200 mm and a length of 320 mm, wrapped with carbon fibre fabric CFRP (as previously discussed in Chapter 2). The cylinders were wrapped with 1, 2 and 3 layers of fibre. Material properties are given in Table 24. The wraps were oriented perpendicular to the longitudinal axis of the cylinder in such a way that they did not contribute to the axial resistance of the confined specimen and provided only lateral confinement. The properties of concrete are also shown in Table 24. The cylinders were subjected to axial compression.

Table 24. Material properties of Karabinis et al. cylinders

Carbon CFRP	Weight [g/m²]	Thickness [mm]	Ej [MPa]	ε_{ju} [10^{-3}]
	200	0.117	240000	0.0155
Concrete	**f'c [MPa]**	**Ec [MPa]**	**ε_{co} [10^{-3}]**	
Type A	38.5	24500	0.00280	
Type B	35.7	23500	0.00202	

In Table 24, ε_{ju} is the rupture strain of the CFRP, and the thickness is given per layer. Six cylinders, three per type of concrete, representing the confinement of 1, 2, and 3 layers of CFRP, were selected for modelling using program VecTor6. Analyses of these tests serve two purposes: to establish the capacity of the material models to reproduce the incremental lateral pressure due to the confining fabric, and to check the features of the program VecTor6.

The analytical model is depicted in Figure 113. Only one quarter of the cylinder is needed to reproduce the behaviour due to the symmetry of the load and the cylinder. Compression field modelling, as described in Chapter 3, was used to analyze the

specimens. Imposed displacements were applied at the top of the cylinder. The experimental values for the material properties of concrete and CFRP were utilized. Concrete was modelled with 160 four-node torus elements, and the CFRP layers were modelled using ring bars attached to the lateral surface nodes of the torus (perfect bond assumed). The area of the ring bar was equivalent to the tributary area between nodes of the CFRP applied. As axial behaviour is the only feature of these bars, they can reproduce the behaviour expected from the fabric in the lateral direction of the cylinder.

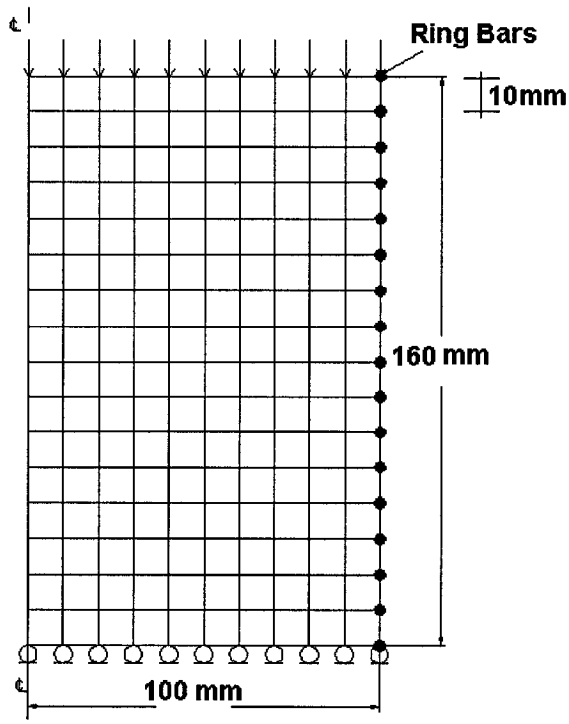

Figure 113. VecTor6 model of Karabinis et al. cylinders

The experimental and analytical axial stress–axial strain curves for Type A cylinders (labelled C1, C7, and C13 in the paper) are shown in Figure 114, and those for Type B cylinders (C4, C12, and C17) are shown in Figure 115. The experimental data was obtained from the researchers.

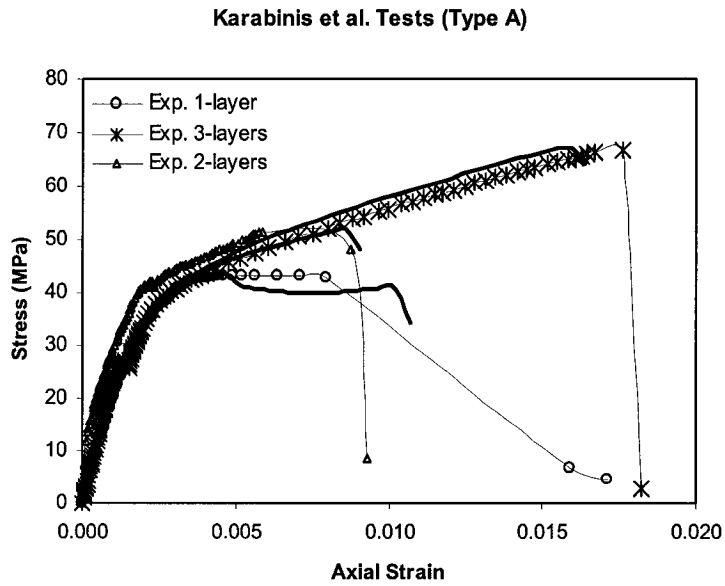

Figure 114. Experimental and analytical stress-strain curves, Type A, Karabinis et al. tests.

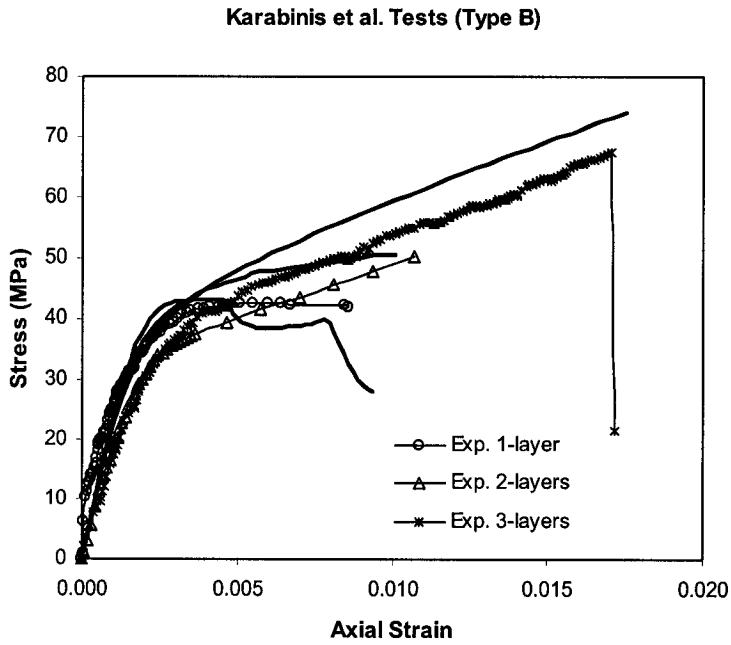

Figure 115. Experimental and analytical stress-strain curves, Type B, Karabinis et al. tests.

In these figures, the solid lines are the analytical estimates, and the lines with markers are the experimental results. The cylinders failed in the tests due to the rupture

of the CFRP fabric at mid-height of the cylinder, a phenomenon that was reproduced by the model. The analytical responses compared well to the experimental responses; the strength and ductility of the FRP-wrapped cylinders were captured correctly by the models. The mode of failure, rupture of the CFRP, was also well captured by the models. The stiffness of the pre-peak response and the trend of increasing strength and ductility with increasing number of CFRP layers were also well modelled. Table 25 shows a comparison of the experimental results published by the authors and those obtained with VecTor6. It should be mentioned that none of these experiments were used in the formulation of the models, and therefore represent a realistic confirmation of the capabilities of the models to reproduce FRP confinement at the material level. Further corroboration will be given in Section 5.2 with structural elements confined with FRP or steel.

Table 25. Comparison of experimental and analytical results, Karabinis et al. tests.

Cylinder		Strength [MPa]	Strength Anal. / Exp.	Strength Gain [%]	Ultimate strain ε_{cu}	ε_{cu} / ε_{co}	ε_{cu} / ε_{co} Anal. / Exp.
Type A							
C1 (1 layer)	Exp.	43.0	1.01	12.0	7.96	2.84	1.28
	Anal.	43.6		13.6	10.20	3.64	
C7 (2 layers)	Exp.	51.5	1.01	34.0	8.77	3.13	0.97
	Anal.	52.0		35.3	8.50	3.04	
C13 (3 layers)	Exp.	67.0	1.00	74.0	17.60	6.29	0.90
	Anal.	67.2		74.5	15.90	5.68	
Type B							
C4 (1 layer)	Exp.	42.5	1.01	19.0	8.59	4.25	0.93
	Anal.	43.1		20.7	7.97	3.95	
C12 (2 layers)	Exp.	50.0	1.01	40.0	10.72	5.31	0.94
	Anal.	50.7		42.0	10.06	4.98	
C17 (3 layers)	Exp.	67.5	1.10	89.0	17.05	8.44	1.03
	Anal.	74.0		107.3	17.50	8.66	
mean			**1.03**				**1.01**
St.Dev.			**0.04**				**0.14**
CV[%]			**3.42**				**14.00**

5.2 Analytical Comparison of Stress-Strain Curves of Column Tests.

This section examines the stress-strain curves obtained from experiments on reinforced concrete columns subjected to axial compression. The columns were confined by FRP composites or steel ties or combinations of both. Cross sections were square or circular, and different arrangements of longitudinal and lateral steel were investigated. The objective of these analyses is to validate the proposed models for confinement at the structural level by using programs VecTor3 and VecTor6. A description of the testing programs, column properties and the experimental results, and comparison with the analytical responses, are presented below. For the analyses, the plain concrete strength was taken as the value given by the researchers.

5.2.1 Demers and Neale (1999)

Repairing of old concrete columns with FRP composites was investigated by testing circular columns in axial compression. The columns were 300 mm in diameter and 1200 mm in length. The variables included in the experimental program were concrete strength, amount of longitudinal steel, amount of lateral steel, steel corrosion and concrete damage. Concrete strengths (f'_c) were 25 MPa and 40 MPa. All columns had 5 bars of longitudinal steel. Corrosion was simulated by reducing by about 5 mm the diameter of the "non-corroded" bars and hoops, while maintaining the other properties constant. Damage was simulated by axially loading the unconfined columns up to the maximum expected "unconfined axial load", and then unloading and wrapping the columns with 3 layers of carbon fibres (CFRP). Hoop spacing was either 150 mm or 300 mm, and the number of CFRP layers was kept constant in all the columns.

Four of the columns tested were analyzed using program VecTor6. The properties for these columns are given in Table 26.

Table 26. Column properties, Demers and Neale tests.

Carbon CFRP*	Thickness (layer) [mm]	E_j [MPa]	ε_{ju} [10^{-3}]
	0.3	84000	0.015
Steel* **	f_y [MPa]	Es [MPa]	
	400	200000	

Column	f'c [MPa]	E_c** [MPa]	ε_{co} [10^{-3}]	d_b [mm]	d_t [mm]	s [mm]	Corrosion Simulated	Damage Loading
U25-1	25	30600	0.0018	11.3	6.4	300	Yes	No
U25-2	25	22300	0.0021	16	11.3	150	No	No
U25-3	25	33800	0.0020	19.5	6.4	150	Yes	No
U25-4	25	25800	0.0021	25.2	11.3	300	No	No

Notes:
*Manufacturer's properties
** From initial load of unconfined columns
***Assumed

In Table 26, E_j is the stiffness of the CFRP, ε_{ju} is the ultimate strain of the CFRP, f_y and E_s are the yield strength and stiffness of the steel (assumed), respectively, d_b and d_t are the diameters of the longitudinal and lateral steel, respectively, and s is the hoop spacing. The experimental data was obtained from the paper.

Half of each column was modelled using a mesh of 400 four-node torus elements. Imposed displacements were applied at the top of the column, and roller-type supports were added at the bottom of the mesh to allow for lateral displacement perpendicular to the loading. As in the case of FRP-confined cylinders, CFRP layers were modelled as ring bars with an area equal to the tributary area of fibre between adjacent nodes. The longitudinal steel was smeared in the axisymmetric elements. A sketch of the mesh is

given in Figure 116 for columns U25-2 and U25-3. The stirrup spacing was modified to 300 mm for columns U25-1 and U25-4, maintaining the same mesh.

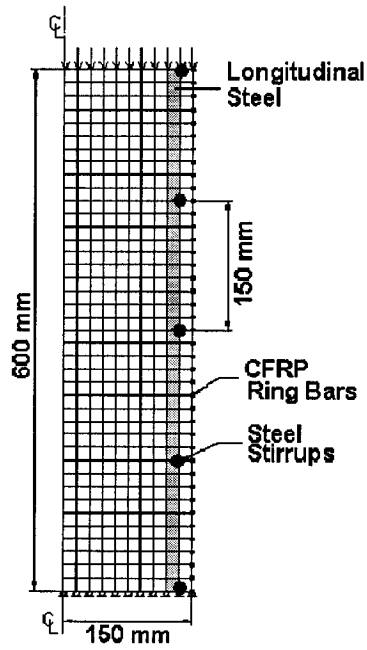

Figure 116. Mesh Details for Demers and Neale Columns.

Compression field modelling (Chapter 4) of this set of columns was carried out using a concrete strength of $0.85f'_c$, to account for size dependency of the plain unconfined concrete strength of a column. The axial stress–axial strain curves for the four columns are presented in Figures 116 to 119, along with the analytical curves obtained with VecTor6 (solid thick lines). A compilation of the results is given in Table 27. The analytical model shows increasing stress with axial strain until failure (rupture of the fabric) for all four columns. The peak strain ε_{cc} occurred at the end of loading in all the analytical curves. The strain ε_{fu} is the measured strain in the FRP at ultimate, which is low when compared to the given rupture strain. This was explained by the researchers due to the non-uniform strain distribution at ultimate and large local strains in the FRP.

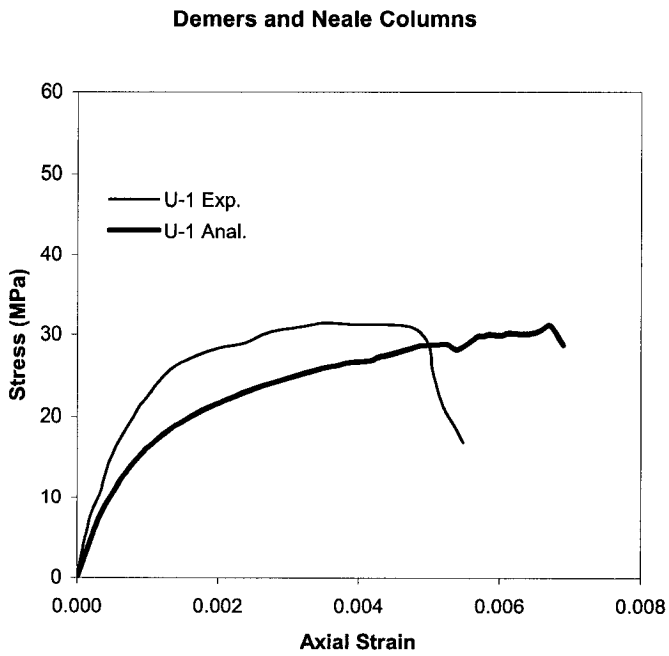

Figure 117. Axial stress–axial strain curve, column U25-1, Demers and Neale.

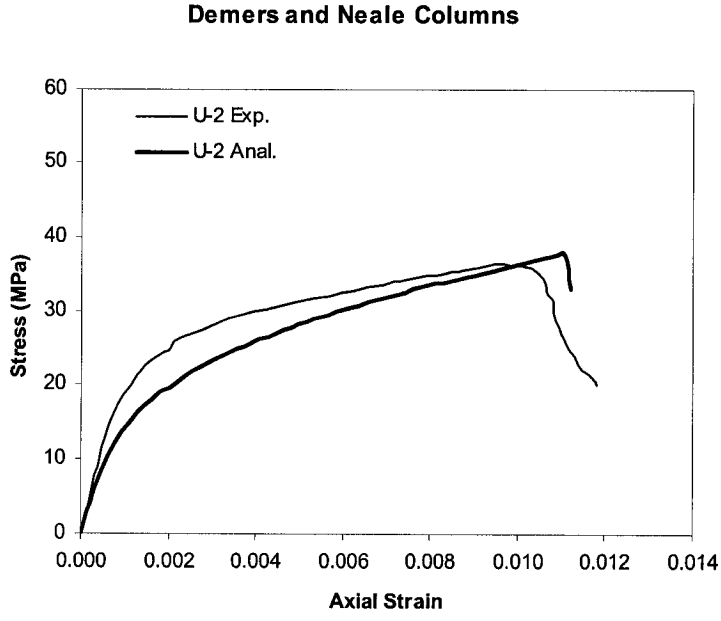

Figure 118. Axial stress–axial strain curve, column U25-2, Demers and Neale.

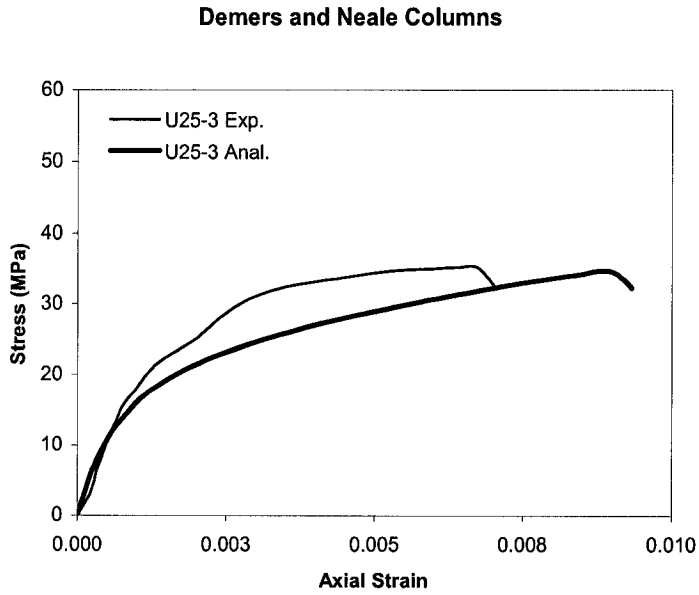

Figure 119. Axial stress–axial strain curve, column U25-3, Demers and Neale.

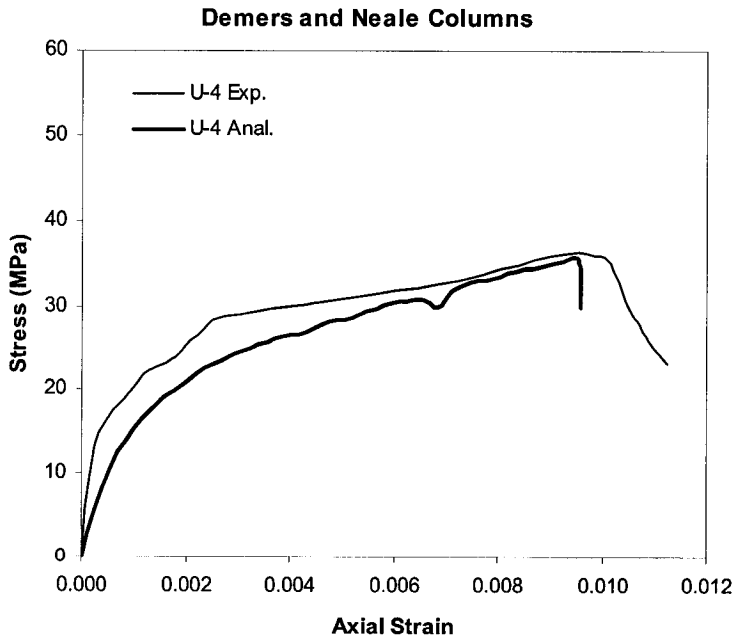

Figure 120. Axial stress–axial strain curve, column U25-4, Demers and Neale.

Table 27. Analytical and experimental results, Demers and Neale columns.

Column		Strength [MPa]	Anal. / Exp.	P_{uc} [kN]	ε_{cc} [10^{-3}]	Anal. / Exp.	ε_{cfu} [10^{-3}]	Anal. / Exp.	ε_{fu} [10^{-3}]
U25-1	Exp.	32.2	0.97	2460	3.80	1.76	4.90	1.37	3.70
	Anal.	31.2		2390	6.70		6.70		
U25-2	Exp.	36.6	1.03	2950	9.90	1.12	10.04	1.11	5.70
	Anal.	37.7		3030	11.10		11.10		
U25-3	Exp.	35.8	0.97	3080	6.60	1.41	6.90	1.35	4.30
	Anal.	34.7		3000	9.30		9.30		
U25-4	Exp.	37.0	0.96	3520	9.80	0.98	9.80	0.98	5.70
	Anal.	35.4		3410	9.60		9.60		
mean			0.98			1.32		1.20	
St.Dev			0.03			0.35		0.19	
CV[%]			3.37			26.27		15.76	

The strength results compare well. However, the analytical responses are somewhat more ductile and less stiff than the experimental responses, except for column U25-4. The stress-strain curves are reasonably traced. The pressure-related dilatation model contributes to the delay in crack propagation in the lateral direction, and to the delay in concrete softening. As in the experimental case, rupture of the FRP causes termination of the load carrying capacity of the columns, a phenomenon well captured by the finite element analysis.

5.2.2 Sheikh and Toklucu (1993)

The effects on confinement of the volumetric ratio of lateral steel, spiral (or hoop) spacing, lateral steel properties and longitudinal steel properties were examined in a series of tests of circular columns subjected to axial compression. The concrete strength was 35 MPa. All columns had 5 bars of longitudinal steel. The properties of the columns analyzed with VecTor6 are given in Table 28.

Table 28. Column properties, Sheikh and Toklucu tests.

Column Label	Section		Longitudinal Reinforcement							
	D [mm]	cover [mm]	d_b [mm]	number bars	ρ_l [%]	f_y [MPa]	E_s [MPa]	ε_y [10^{-3}]	f_u [MPa]	ε_{sh} [10^{-3}]
D14-S10M-P4.4	356	22	25.2	5	2.5	509	198000	2.57	687	12.7
D14-H10M-P3.0	356	22	25.2	5	2.5	509	198000	2.57	687	12.7
D10-S8M-P4.3	254	17	19.5	5	3.0	478	210000	2.28	667	12.4
D10-SD4-P1.6	254	17	19.5	5	3.0	478	210000	2.28	667	12.4
D8-SD5-P3.4	203	13	16.0	5	3.1	484	209000	2.32	646	14.7
D8-SD5-P1.7	203	13	16.0	5	3.1	484	209000	2.32	646	14.7
D8-S3/16-P1.7	203	13	16.0	5	3.1	484	209000	2.32	646	14.7

Column Label	Transverse Reinforcement						Concrete		
	d_b [mm]	ρ_v [%]	s [mm]	f_y [MPa]	ε_y [10^{-3}]	f_u [MPa]	f'_c [MPa]	E_c* [MPa]	ε_{co}* [10^{-3}]
D14-S10M-P4.4	11.3	1.15	112	452	2.26	585	35.9	29960	2.40
D14-H10M-P3.0	11.3	1.69	76	452	2.26	585	35.9	29960	2.40
D10-S8M-P4.3	8.0	0.84	109	607	3.04	682	35.5	29790	2.38
D10-SD4-P1.6	5.7	1.14	41	593	2.97	643	35.5	29790	2.38
D8-SD5-P3.4	6.4	0.86	86	629	3.15	681	34.9	29540	2.36
D8-SD5-P1.7	6.4	1.68	43	629	3.15	681	34.9	29540	2.36
D8-S3/16-P1.7	4.7	0.93	43	620	3.10	689	34.9	29540	2.36

* Calculated

In Table 28, D is the diameter of the circular section, d_b and d_t are the diameters of the longitudinal and lateral steel bars, respectively, ρ_l and ρ_v are the longitudinal and volumetric (transverse) steel ratio, respectively. f_y, f_u, ε_y are the yield strength, the ultimate strength, and strain at yield of the respective steels. E_s is the stiffness of the longitudinal steel, and s is the spiral (or hoop) spacing. The values for the concrete stiffness E_c and the strain at peak unconfined strength ε_{co} were assumed using Eqs. 168 for normal strength concrete. The length of the columns was equal to four times the diameter.

The analytical model for a typical column (D14-H10M-P3.0) is shown in Figure 121. Imposed displacements were applied at the top of the model, and roller-type supports

were added at the bottom of the mesh to allow for lateral displacement perpendicular to the loading. The longitudinal steel was smeared in the axisymmetric elements adjacent to the cover elements, and the spirals (or hoops) were modelled using ring bars. The concrete cover was taken from the outer lateral surface to the centre of the spiral (hoop).

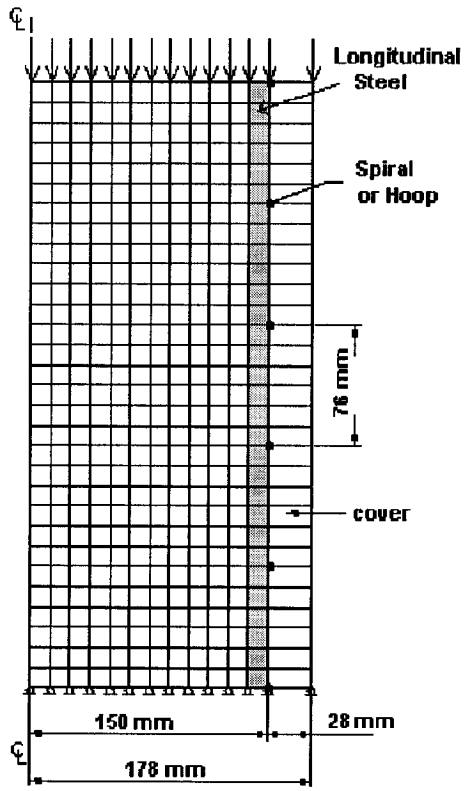

Figure 121. Mesh details for Sheikh and Toklucu column D14-H10M-P3.0.

As in the previous set of columns (Section 5.1) a concrete strength of $0.85f'_c$ was used. The model for concrete dilatation has no upper boundary for the maximum Poisson's ratio and therefore no limit to the possible lateral strains that the analytical column may reach. Due to the fact that concrete cover elements of these columns were not bounded by FRP composites, as was the case with the FRP-wrapped columns, and

the four-node torus element behaviour is limited to small deformations (not full Lagrangian elements), the cover elements were automatically deactivated in VecTor6 once their lateral stiffness decreased to a very small value (between 10 MPa and 1% of the initial stiffness). This allowed for the continuation of imposed axial displacements beyond cover spalling until failure of the concrete core in the post-peak range.

Experimental axial load – axial strain, and axial load – spiral strain curves for the columns are presented in Figures 121 to 127, along with the analytical curves obtained with VecTor6 (solid thick lines). A compilation of the results are given in Table 29. The experimental data was obtained from the researchers.

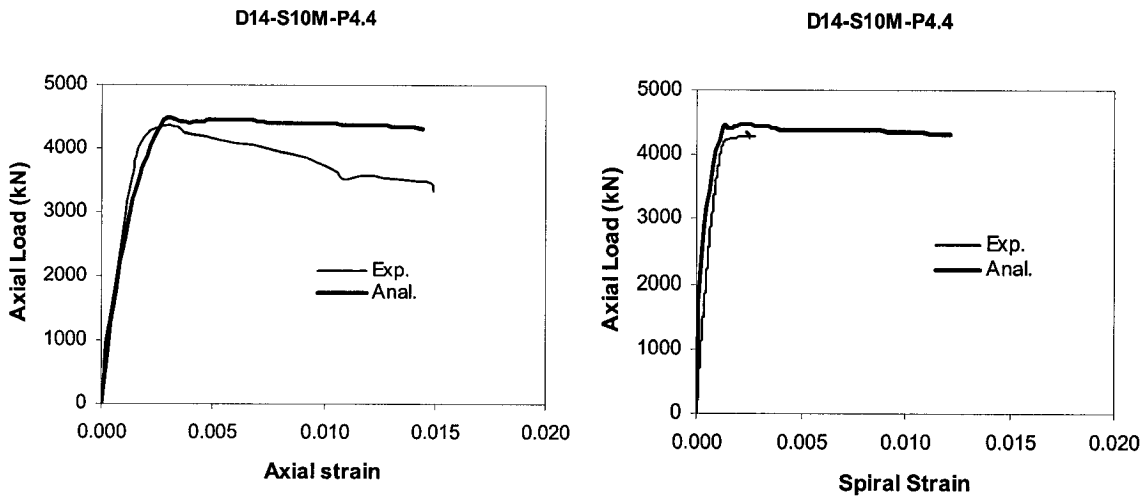

Figure 122. Axial load–axial strain, - spiral strain curves, column D14-S10M-P4.4

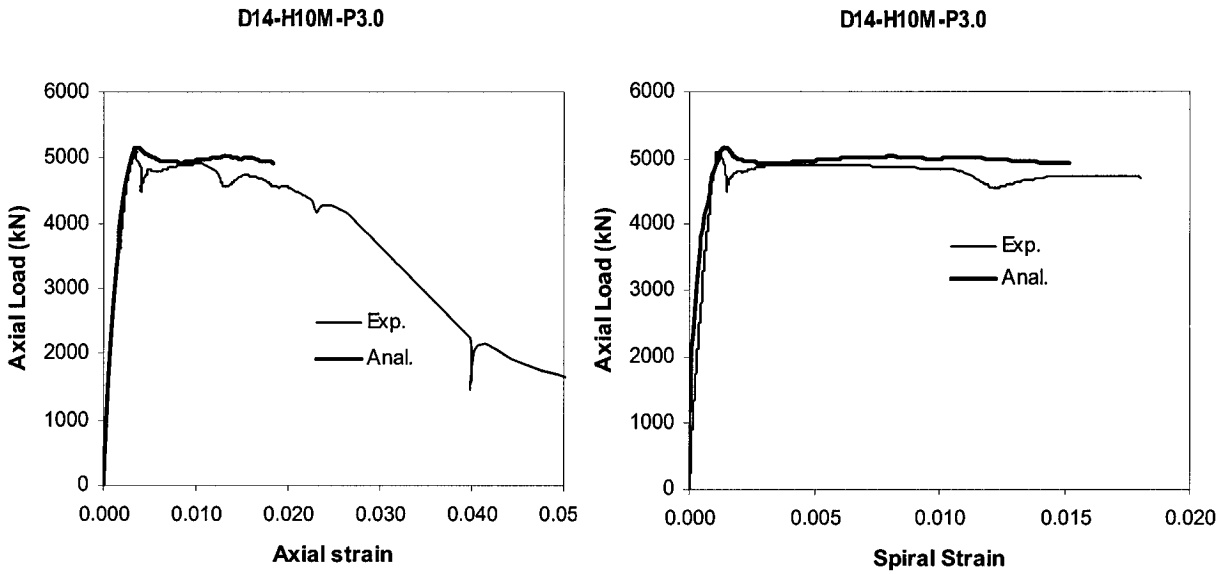

Figure 123. Axial load–axial strain curve, -spiral strain curves, column D14-H10M-P3.0

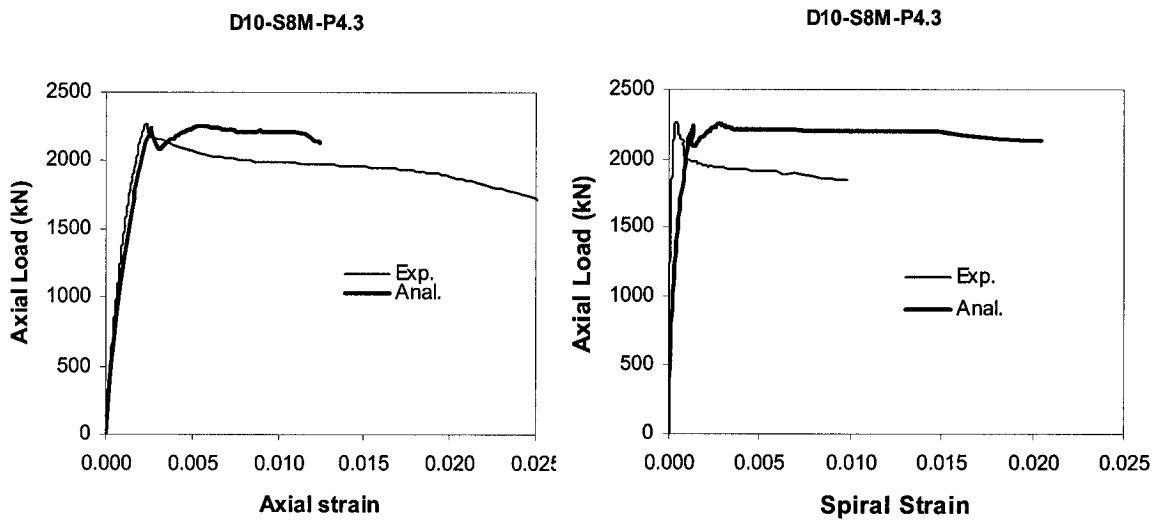

Figure 124. Axial load–axial strain, -spiral strain curves, column D10-S8M-P4.3

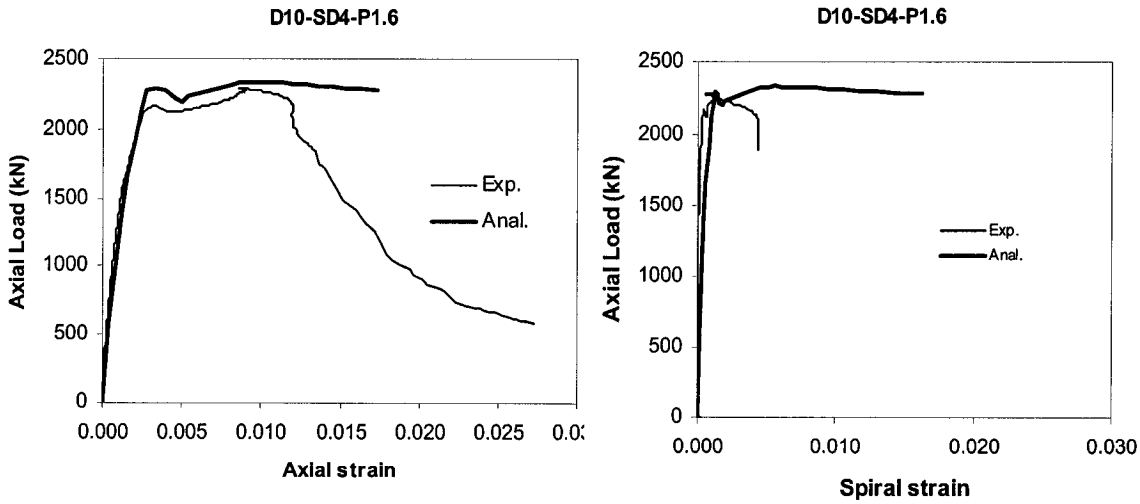

Figure 125. Axial load–axial strain curve, -spiral strain curves, column D10-SD4-P1.6

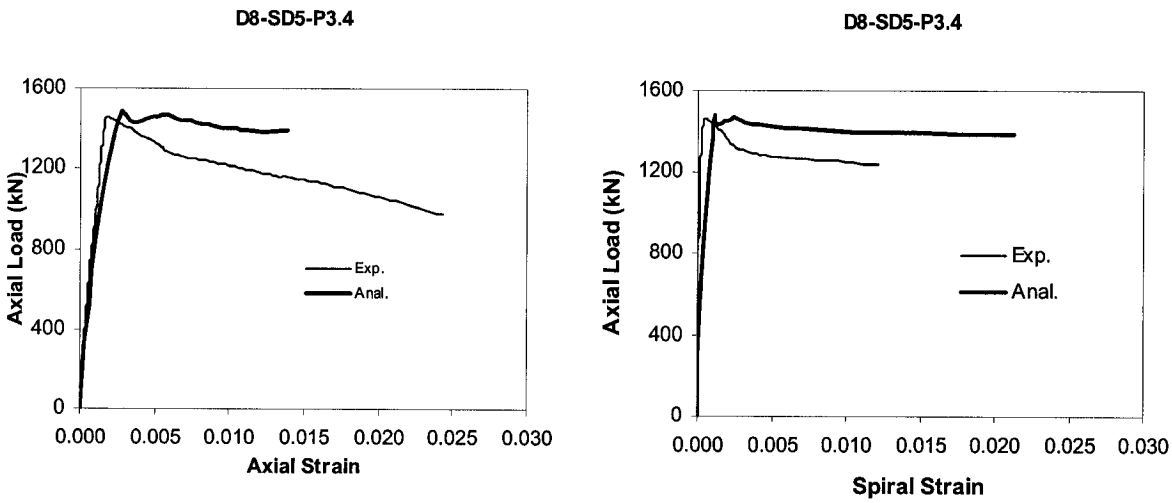

Figure 126. Axial load–axial strain, -spiral strain curves, column D8-SD5-P3.4

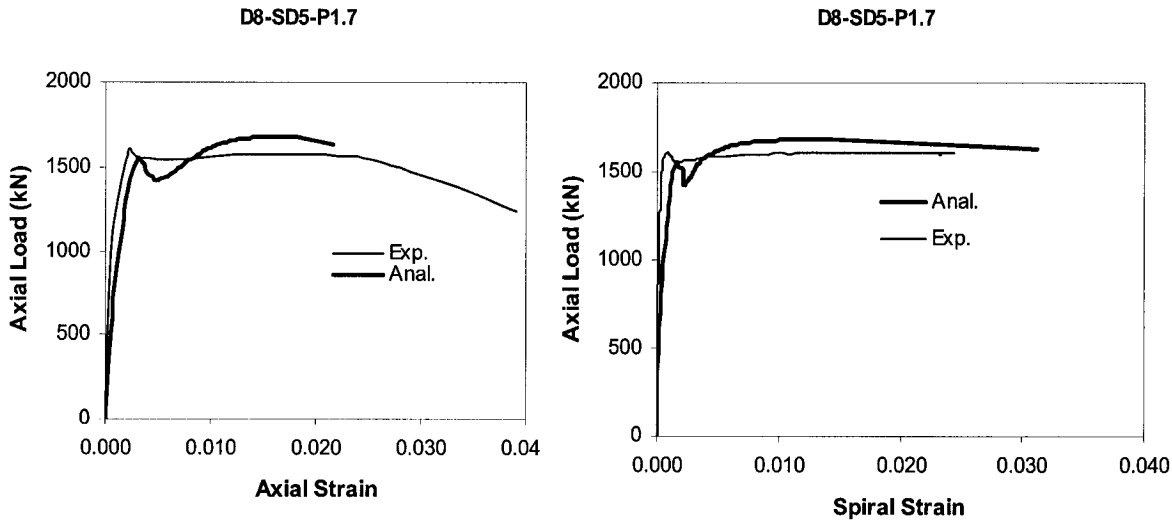

Figure 127. Axial load–axial strain, -spiral strain curves, column D8-SD5-P1.7

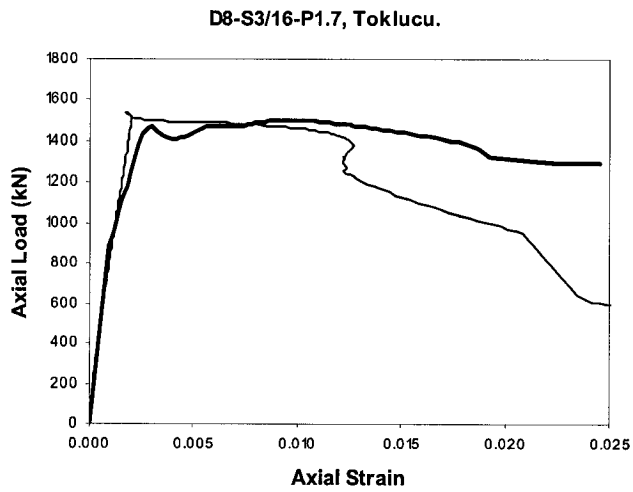

Figure 128. Axial load–axial strain curve, column D8-S3/16-P1.7

Table 29. Analytical and experimental results, Sheikh and Toklucu columns.

Column Label	P_{max}			peak axial strain				axial strain @ spalling		spiral (hoop) stress @ P_{cmax}	
			Anal.	Exp.		Anal.					
	Exp.	Anal.	-------	1st	2nd	1st	2nd	Exp.[a]	Anal.	Exp.	Anal.
	[MPa]	[MPa]	Exp.	[10^{-3}]	[10^{-3}]	[10^{-3}]	[10^{-3}]	[10^{-3}]	[10^{-3}]	[10^{-3}]	[10^{-3}]
D14-S10M-P4.4	4350	4480	1.03	3.50	--	2.95	5.00	2.00	2.30	452	452
D14-H10M-P3.0	5100	5160	1.01	3.60	12.20	3.55	14.90	2.00	2.30	415	396
D10-S8M-P4.3	2270	2260	1.00	2.30	--	2.60	4.80	2.00	2.50	53	273
D10-SD4-P1.6	2290	2330	1.02	3.20	8.80	3.30	9.50	2.00	2.30	575	593
D8-SD5-P3.4	1460	1480	1.01	2.00	--	2.80	5.50	2.00	2.30	101	226
D8-SD5-P1.7	1610	1680	1.04	2.30	12.20	3.10	16.70	2.00	2.30	650	630
D8-S3/16-P1.7	1540	1500	0.97	3.50	--	3.00	9.70	2.00	2.50	400	620
mean			1.01								
StDev.			0.02								
CV[%]			2.23								

[a] Estimated value of starting of cover spalling by Sheikh and Toklucu (1993)

Table 29 describes the maximum load P_{max}, the ratio between the analytical and experimental maximum loads, the analytical and experimental peak strains for the first peak just at the onset of the post-peak curve, the second peak (if any) after cover spalling, the axial strain when the concrete cover started cracking and spalling, and the spiral (hoop) stress measured at the maximum load in the concrete P_{cmax}. These values represent the sequence of events during the loading of each column.

From the results, the experimental maximum load was well captured by the model. The average analytical to experimental P_{max} ratio was 1.01 with a CV of 2.2%, demonstrating the capabilities of the compression field modelling to reproduce the load capacity of these set of columns. The first and second peak strains were also closely respresented. After cover spalling, the analytical models showed some gain in strength and reached a second peak depending on the column configuration (spiral spacing, volumetric ratio). The analytical pre-peak curves followed the initial loading path of the columns very closely, and the post-peak regimes were reasonably traced. The onset of

cover spalling in the models was at an axial strain between 2.30 and 2.50 x 10^{-3}, which was approximately the value for the peak unconfined concrete strain of the specimens, and compared well with the observed spalling. The spiral stress at the maximum concrete load was also well captured. However, the axial load-lateral steel strain curves were somewhat less stiff than the experimental curves, indicating some overestimation of the lateral steel stress at maximum concrete load and in some cases early termination of the axial load-axial stress curve due to failure of the analytical model. Also, buckling of the longitudinal bars is not captured by the program.

Figure 129a shows a longitudinal cut between two spiral (hoop) spacings in a model of a column. This figure illustrates a sketch of a typical distribution of lateral stresses in the concrete core and concrete cover at any load stage, obtained with VecTor6. As can be seen, the confined and unconfined zones are well defined; the confined sectional area decreases from the spiral level to the mid-height between spirals. Figure 129b shows a sketch of the deformed state of a column model at the time of failure.

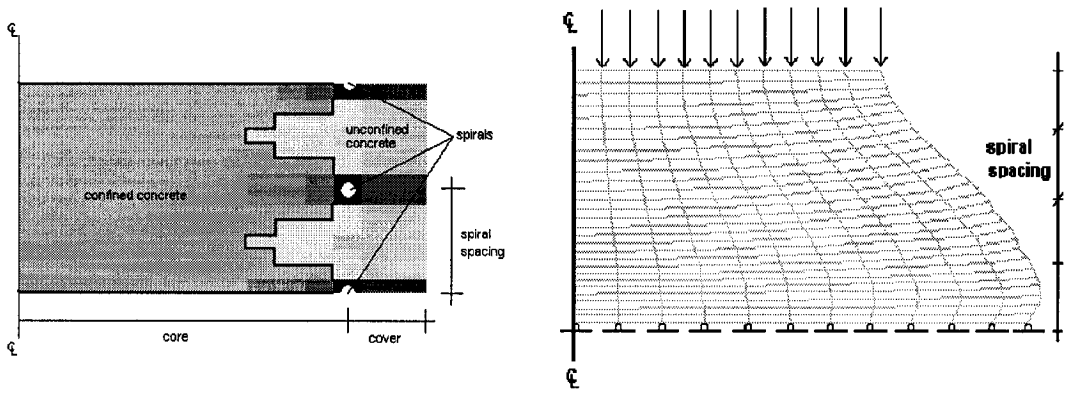

(a) (b)

Figure 129. (a) Sketch of confined and unconfined zones, and (b) Deformed shape of column.

5.2.3 Montgomery and Sheikh (1996)

This investigation was a continuation of the work of Sheikh and Toklucu (1993) on the study of the effects of confinement on concrete columns. The circular columns tested in axial compression had concrete strengths between 70 MPa and 90 MPa. All columns had 5 bars of longitudinal steel. The length of each column was equal to four times its diameter. The properties for the representative columns analyzed with VecTor6 are given in Table 30.

Table 30. Column properties, Montgomery and Sheikh tests.

Column Label	Section		Longitudinal Reinforcement								
	D [mm]	cover [mm]	d_b [mm]	bars	ρ_l [%]	f_y [MPa]	E_s [MPa]	ε_y [10-3]	f_u [MPa]	E_{sh} [MPa]	ε_{sh} [10-3]
H-D25-S11.3-P109	254	17	19.5	5	3.0	474	210220	2.60	650	2890	9
H-D25-S8-P79	254	17	19.5	5	3.0	474	210220	2.60	650	2890	9
H-D20-S6.4-P43	203	13	16.0	5	3.1	482	205230	2.34	643	3160	19

Column Label	Transverse Reinforcement							Concrete		
	d_b [mm]	ρ_v [%]	s [mm]	f_y [MPa]	ε_y [10-3]	f_u [MPa]	ε_{sh} [10-3]	f'_c [MPa]	E_c [MPa]	ε_{co} [10-3]
H-D25-S11.3-P109	11.3	1.67	109	522	2.4	675	19	69.7	39000	2.00
H-D25-S8-P79	8.0	1.13	79	666	4.91	700	4.91	69.7	39000	2.00
H-D20-S6.4-P43	6.4	1.69	43	646	5.24	695	5.24	69.7	39000	2.00

For Table 30, the definitions of the variables are the same as those defined in Section 5.2.2. The analytical model for these columns is similar to that described for Toklucu specimens shown in Figure 121. The concrete strength was set to $0.85f'_c$, and cover elements were automatically deactivated in the program at a lateral stiffness between 10 MPa and 1% of the initial stiffness.

The axial load – axial strain curves for the columns are presented in Figures 129 to 131, along with the analytical curves obtained with VecTor6 (solid thick lines). A

compilation of the results are given in Table 31. The experimental data was obtained from the researchers.

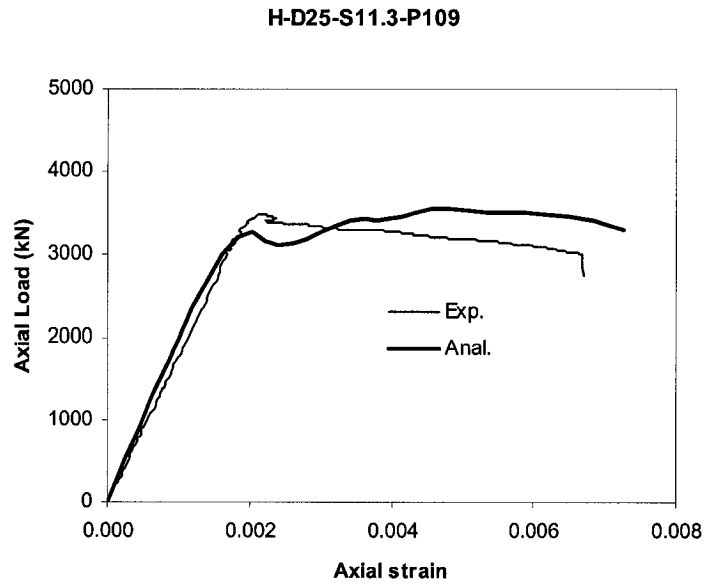

Figure 130. Axial load–axial strain curve, Montgomery and Sheikh column H-D25-S11.3-P109.

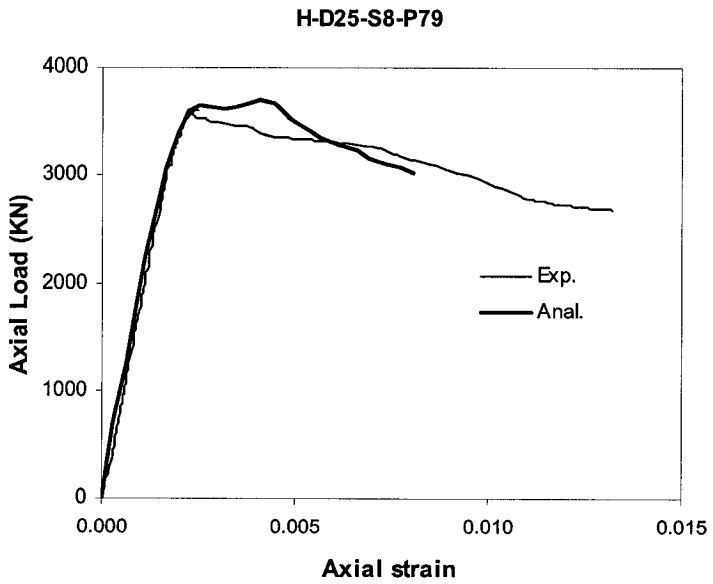

Figure 131. Axial load–axial strain curve, Montgomery and Sheikh column H-D25-S8-P79.

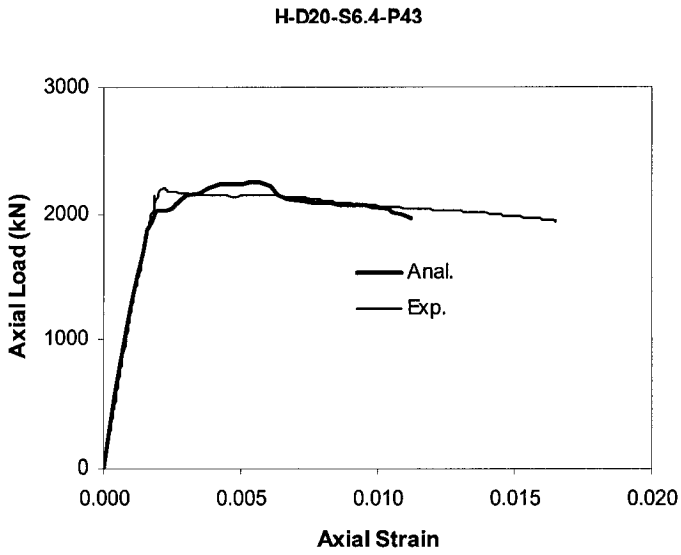

Figure 132. Axial load–axial strain curve, Montgomery and Sheikh column H-D20-S6.4-P43.

Table 31. Analytical and experimental results, Montgomery and Sheikh columns.

Column Label	P_{max}			peak axial strain				axial strain @ spalling		spiral (hoop) stress @ P_{cmax}	
			Anal.	Exp.		Anal.					
	Exp. [MPa]	Anal. [MPa]	------- Exp.	1st [10^{-3}]	2nd [10^{-3}]	1st [10^{-3}]	2nd [10^{-3}]	Exp. [10^{-3}]	Anal. [10^{-3}]	Exp. [10^{-3}]	Anal. [10^{-3}]
H-D25-S11.3-P109	3480	3530	1.01	2.10	--	2.00	4.50	2.20	1.80	522	510
H-D25-S8-P79	3610	3700	1.02	2.40	--	2.50	4.10	2.50	2.50	87	310
H-D20-S6.4-P43	2210	2250	1.02	2.20	--	2.00	5.70	2.10	1.80	88	380
mean			1.02								
St.Dev.			0.005								
CV[%]			0.53								

The structural behaviour of these columns when subjected to concentric axial compression was well-captured by the program, as in the previous cases. The difference in the analytical peak load with respect to that observed during the tests is negligible. The first peak strains compared well with the experimental results, although no second peak strain was observed in the experiments. The initial stiffness is perfectly traced in the models. The onset of cover spalling in the models was at an axial strain

between 1.80 and 2.50 x 10^{-3}, which also coincided approximately with the unconfined concrete strain of the specimens, and compared well with the observed results. The analytical lateral steel stresses at maximum concrete load were larger for two of the columns than those observed, indicating a more rapid development of lateral strains in the analytical models. Modelling of these columns was made to check the capabilities of program VecTor6 and compression field modelling in reproducing the behaviour of confined concrete at the structural level, where several physical parameters influence the behaviour, such as the lateral steel spacing, amount of lateral and longitudinal steel, and material properties.

5.2.4 Sheikh and Uzumeri (1980)

The ability of the proposed models to simulate the behaviour of rectangular columns subjected to axial compression was also checked. The confinement models were implemented in program VecTor3, a general three-dimensional nonlinear finite element program, and used to analyze some of the specimens tested by Sheikh and Uzumeri. The researchers investigated the relationships between different tie and longitudinal steel configurations that included several combinations of tie spacings, longitudinal and lateral steel ratios, and bar arrangements. The failure modes varied from brittle to ductile and the effects of these variables on the behaviour of confined concrete were studied.

The columns analyzed are described in Table 32; concrete strength was between 35 MPa and 40 MPa, tie spacings varied between 0.08*b* and 0.33*b*, where *b* was the size of the column, and the number of longitudinal bars was either 12 or 16. Table 32

follows the same notation as that for the previous columns described in earlier sections. The columns were square (i.e. $b = h$) and were 1955 mm in length. Figure 133 shows a sketch of a typical specimen. Steel plates were added at the top and bottom to avoid premature failure of the columns away from the middle third.

Table 32. Column properties, Sheikh and Uzumeri tests.

Column	Section			Longitudinal Reinforcement								
	b [mm]	h [mm]	cover [mm]	d_b [mm]	bars	ρ_l [%]	f_y [MPa]	E_s [MPa]	ε_y [10-3]	f_u [MPa]	E_{sh} [MPa]	ε_{sh} [10-3]
4C4-12	305	305	17	15.9	16	3.44	407	206700	1.97	635	8268	7.20
4B3-19	305	305	15	19.1	12	3.67	391	196365	1.99	540	6235	7.80
4B4-20	305	305	17	19.1	12	3.67	391	196365	1.99	540	6235	7.80
4D3-22	305	305	15	19.1	12	3.67	391	196365	1.99	540	6235	7.80
4D6-24	305	305	16	19.1	12	3.67	391	196365	1.99	540	6235	7.80

Column	Transverse Reinforcement							Concrete		
	d_b [mm]	ρ_v [%]	s [mm]	f_y [MPa]	ε_y [10-3]	f_u [MPa]	ε_{sh} [10-3]	f'_c [MPa]	E_c [MPa]	ε_{co} [10-3]
4C4-12	3.2	1.52	25.4	634	3.17	760	---	40.8	31930	2.20
4B3-19	7.9	1.80	101.6	480	2.40	500	---	33.4	28900	2.20
4B4-20	4.8	1.70	38.1	480	2.40	540	---	34.7	29430	2.20
4D3-22	7.9	1.60	82.6	480	2.40	500	---	35.5	29780	2.20
4D6-24	6.4	2.30	38.1	480	2.40	510	---	35.8	29930	2.20

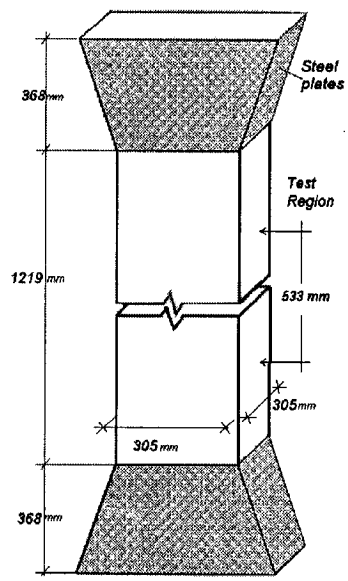

Figure 133. Typical Sheikh and Uzumeri column.

The columns were subjected to monotonic axial compression using displacement-controlled load stages. Axial and tie deformations were measured using LVDTs and strain gauges glued to the steel bars. A detailed description of the testing procedure is given by Sheikh (1978). The experimental data was obtained from the researchers.

The finite element models for the columns consisted of concrete 8-noded regular hexahedral elements and steel truss bars. The longitudinal steel was smeared into the concrete solids and the tie steel was modelled using truss bars. The bar nodes were attached to the solid elements for perfect bond. One-quarter of the cross section of each column was modelled due to the symmetry of the load and the cross section. The tie and longitudinal arrangements analyzed are shown in Figure 134, and sketches of the finite element meshes for each arrangement are shown in Figure 135 along with a typical profile of the column models.

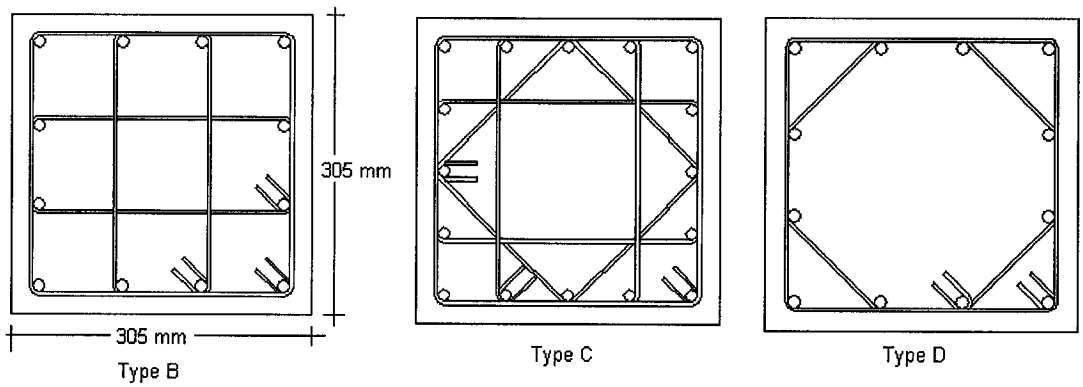

Figure 134. Type Sheikh and Uzumeri tie and longitudinal steel arrangements.

The geometry of the finite element models is given in Table 33, where a "layer" consists of the number of finite elements that makes up the cross section.

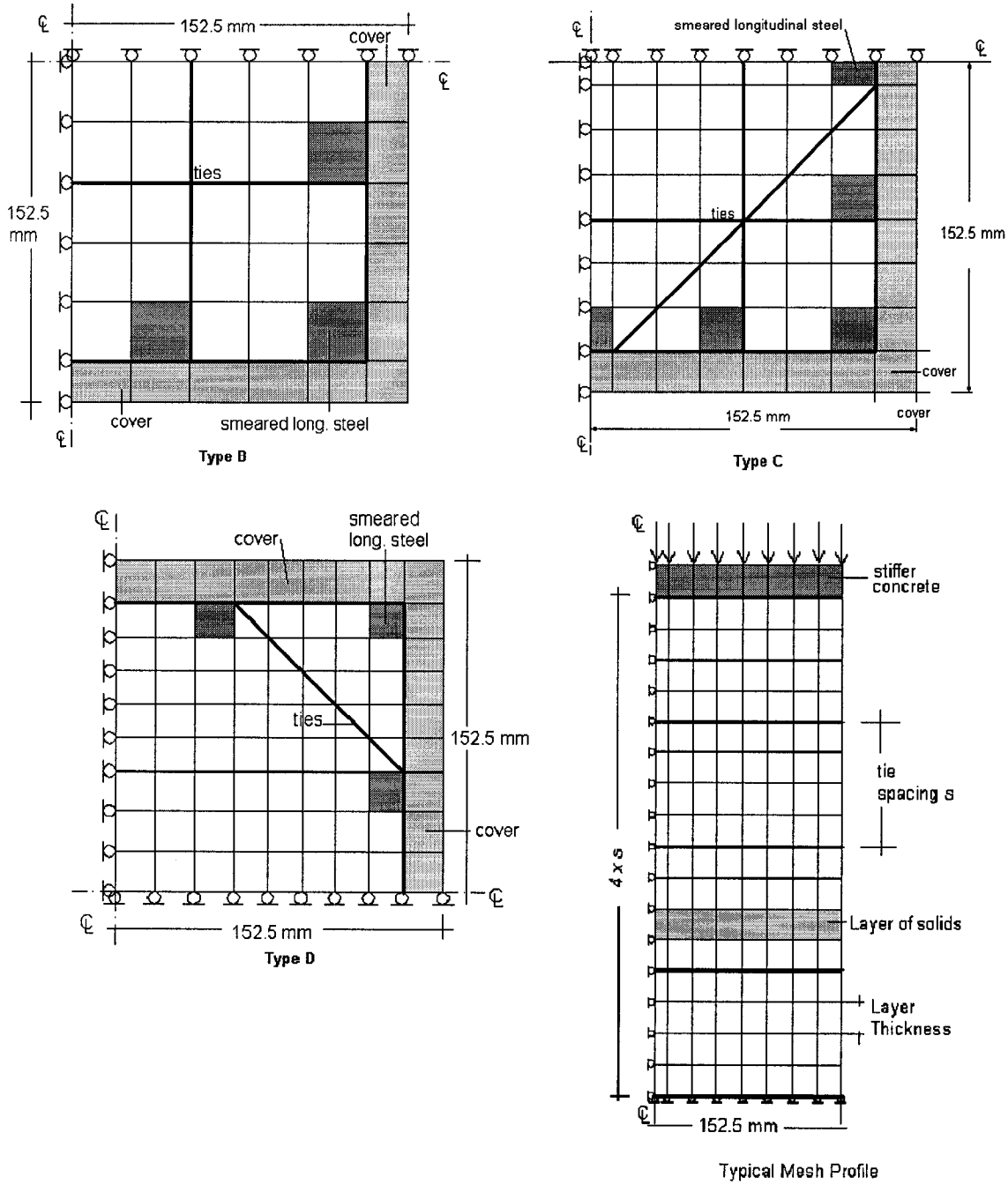

Figure 135. Mesh details for Sheikh and Uzumeri columns.

Imposed displacements were applied at the top layer, which was modelled with stronger concrete to evenly distribute displacements through the cross section.

Table 33. Finite element mesh properties, Sheikh and Uzumeri columns.

Column	Geometry				
	Layers	Layers per tie spacing	Layer Thickness [mm]	8-node solids per layer	Truss Bars per tie setup
4C4-12	17	1	25.40	64	44
4B3-19	17	4	25.40	36	24
4B4-20	17	1	38.10	36	24
4D3-22	26	4	20.65	81	27
4D6-24	18	2	19.05	81	27

As in the previous cases, the unconfined concrete strength of each column was set to $0.85f'_c$, and the cover elements were automatically deactivated in VecTor3 once their lateral stiffness decreased to 1% of the initial stiffness. The axial load–strain curves are plotted in Figures 135 to 139, along with the analytical curves obtained with VecTor3 (solid thick lines). A compilation of the results are given in Table 34.

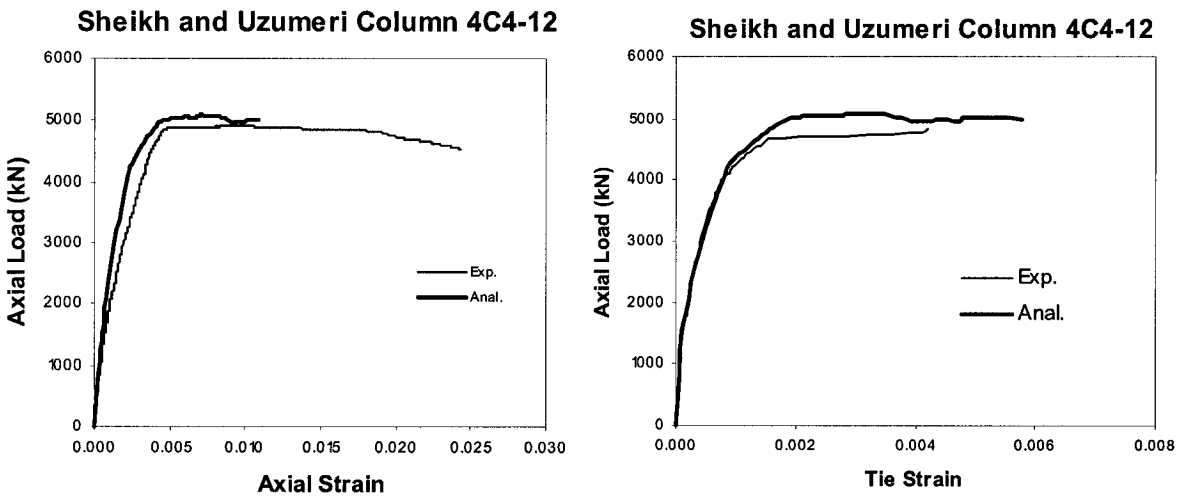

Figure 136. Behaviour of specimen 2C4-12.

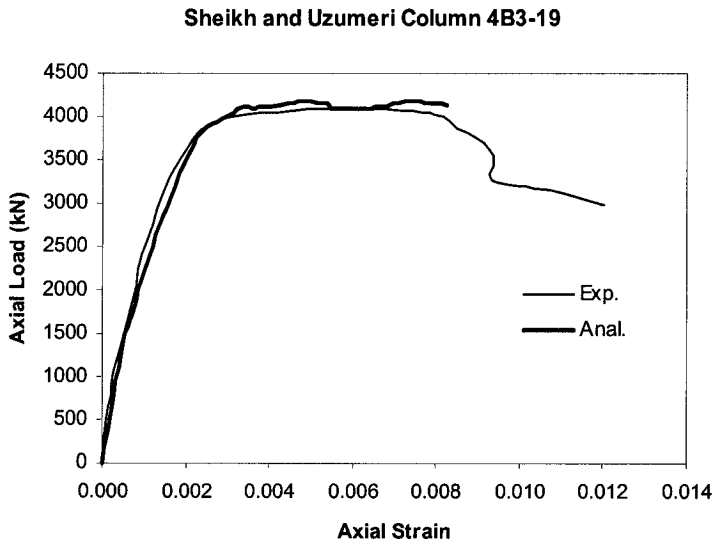

Figure 137. Behaviour of specimen 4B3-19.

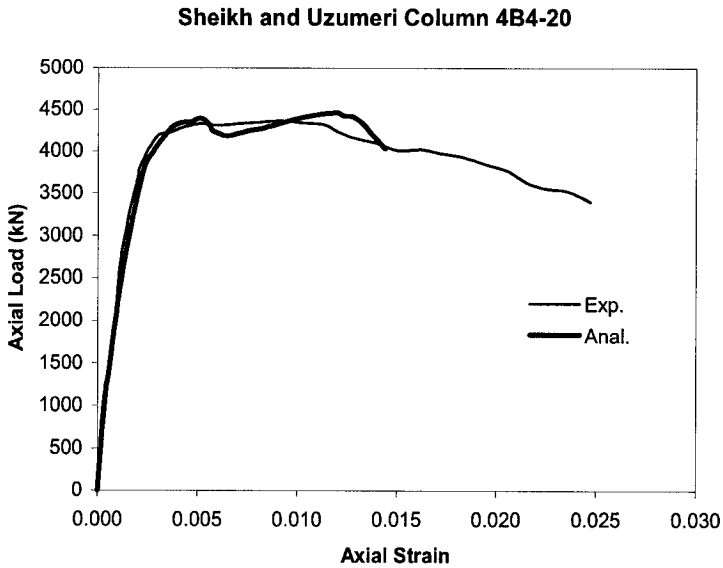

Figure 138. Behaviour of specimen 4B4-20

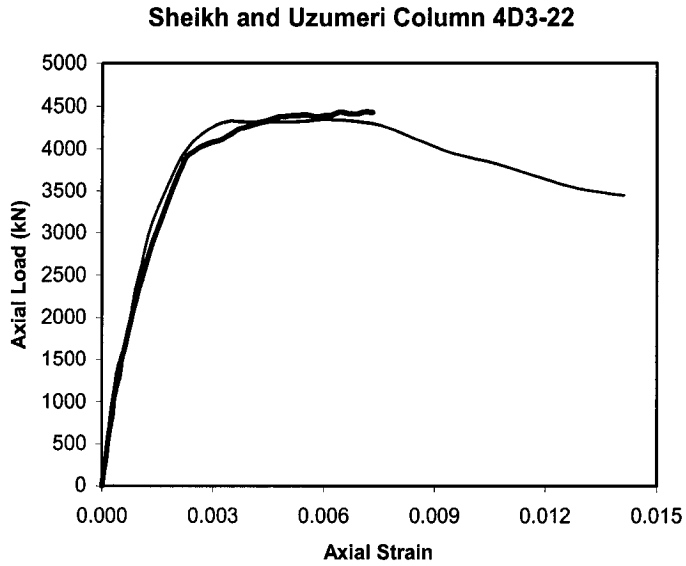

Figure 139. Behaviour of specimen 4D3-22.

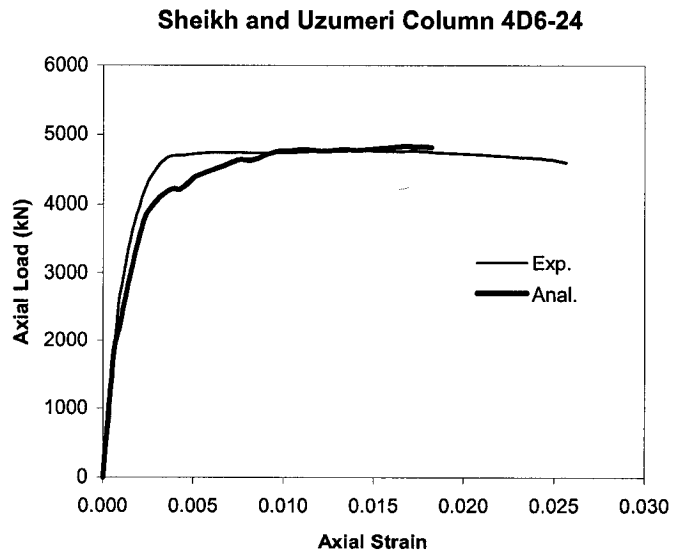

Figure 140. Behaviour of specimen 4D6-24.

Table 34. Analytical and experimental results, Sheikh and Uzumeri columns.

Column	P_{max}		Anal.	peak axial strain				axial strain		tie stress	
				Exp.		Anal.		@ spalling		@ P_{cmax}	
	Exp.	Anal.	-------	1st	2nd	1st	2nd	Exp.	Anal.	Exp.	Anal.
	[MPa]	[MPa]	Exp.	[10^{-3}]	[10^{-3}]]	[10^{-3}]	[10^{-3}]	[10^{-3}]	[10^{-3}]	[10^{-3}]	[10^{-3}]
4C4-12	4915	5094	1.04	5.20	20.50	7.00	--	1.5 to 2.0	2.10	469	582
4B3-19	4092	4168	1.02	6.10	--	7.50	--	1.5 to 2.0	1.40	400	300
4B4-20	4368	4416	1.01	8.00	--	5.10	12.00	1.5 to 2.0	1.80	544	494
4D3-22	4301	4438	1.03	4.10	--	6.50	--	1.5 to 2.0	1.50	386	385
4D6-24	4723	4831	1.02	3.70	17.70	3.90	16.80	1.5 to 2.0	1.70	475	480
mean			1.02								
StDev.			0.010								
CV[%]			1.00								

This set of columns serves to determine the capabilities of the proposed models when used in a general three-dimensional nonlinear finite element program. The several arrangements of column sections and different tie spacings represent a wide spectrum of possible confinement behaviour, from brittle to ductile.

Figure 141 shows in grey scale a distribution of compressive axial stresses in a cross section for one of the type D columns analyzed, at a stage close to failure in the analytical model. The longitudinal steel bars and the stirrups are also plotted over the stress distribution. The unloading (dark grey) of the concrete cover and the concrete adjacent to the longitudinal bars is evident. At this stage, the cover had spalled off and carried no more load, whereas the concrete core was triaxially compressed and reached compressive stress values above the unconfined concrete strength $0.85f'_c$.

Concrete cover began to spall off at axial strains close to the recorded experimental values. Also, the overall average strain in the tie steel at the maximum concrete load compares reasonably well with the experimental data. The pre-peak response was well captured and the maximum analytical to experimental load ratio reached an average of

1.02 with a covariance of 1.0%, indicating that the set of modified compression field models are also able to reproduce the capacity of these square columns. The axial load –tie strain curve for column 2C4-12 is also shown in Figure 136. It can be seen that the analytical post-peak response of the tie strain was overestimated, causing failure of the model prematurely. The analytical axial stress-axial strain post-peak curves trace the experimental axial stress-axial strain curves; however, the analytical models failed at earlier load stages than the specimens. The reason for the early failure of the models may be two-fold. First, the lateral expansion of the concrete elements rose faster than in the experiments causing rapid early increments of the tie strains and premature failure in the post-peak branch. Second, the small-deformation elements implemented in VecTor3 do not properly account for the large deformations seen in the lateral expansion of confined concrete elements. After spalling of the concrete cover (i.e. deactivation of cover elements) the 8-noded elements near the perimeter tie were further exposed to large lateral deformations that caused numerical instability (i.e. geometrical instability in the finite elements) in the program at late load stages.

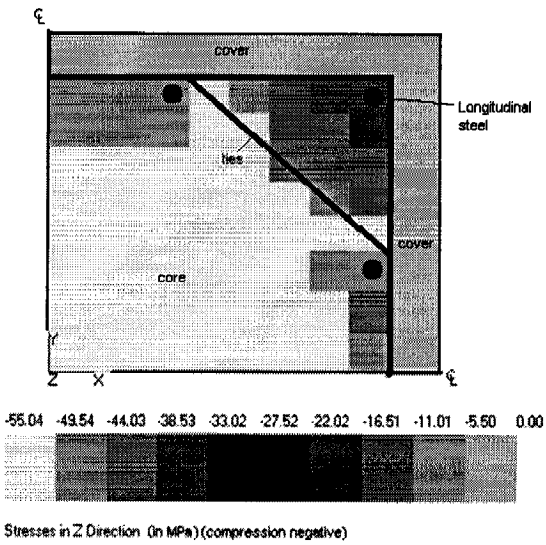

Figure 141. Typical distribution of analytical axial compressive stresses for a type-D column.

5.3 Applications

This section contains the analyses of five circular columns tested in the structural laboratories at the University of Toronto. Four of the columns were cast in fibre reinforced polymer (FRP) shells using one or two layers of carbon fibre or glass fibre; these columns were tested under axial compression. The fifth column was wrapped with FRP fabric and tested under cyclic loading and constant axial load. This set of columns was analyzed using program VecTor6 to obtain the axial stress-axial strain responses for all of the columns. The analytical curve for the axial stress-axial strain of the column subjected to cyclic load was used to model the envelope of moment-curvature response.

The objective of these numerical applications is to evaluate the capacities and limitations of the program and the compression field modelling approach in reproducing the responses of FRP shell-confined columns and columns subjected to axial and flexural loading.

5.3.1 FRP shell-confined columns subjected to axial compression

Two circular columns tested by Cairns (2001) confined with carbon FRP shells, and two circular columns tested by Jaffry and Sheikh (2001) confined with glass FRP shells subjected to monotonic axial compression, were analyzed. The four columns had a diameter of 356 mm and a length of 1524 mm. The average value of the unconfined concrete strength was 33 MPa for Cairns columns and 30 MPa for Jaffry and Sheikh columns, respectively. It should be noted that the strength obtained from standard cylinder tests and the column strength of plain concrete control columns in both test series were approximately the same.

The columns tested were cast into prefabricated fibre mandrels (CFRP or GFRP). The test regions of the columns were created by dividing the length of each column into three regions of equal length and adding glass fibre fabric (GFRP) in the two outer regions. A 0.5 mm layer of vinyl was added to break the bond between the shell and the concrete. Two columns from each researcher were selected for analytical modelling. The columns had one or two layers of FRP and no steel reinforcement. The material properties are given in Table 35.

Table 35. Material properties of Cairns and Jaffry and Sheikh Columns

Shell	F_{ju} [N/mm]	ε_{ju}	
CFRP	835	0.0215	
GFRP	535	0.0237	
Concrete	f'_c [MPa]	E_c [MPa]	ε_{co}
Cairns (2001)	33	30000	0.00180
Jaffry and Sheikh (2001)	30	29300	0.00185

In Table 35, F_{ju} is the ultimate force per unit thickness of the fibre; these values for carbon and glass fibre were the averages from tests on coupons made by the researchers. The strain at ultimate of the FRP is ε_{ju}, and f'_c, E_c, and ε_{co} are the unconfined concrete strength, the initial stiffness of concrete and the strain at peak unconfined stress, respectively.

The analytical modelling for all of the columns followed the same approach as in the previous sections of this Chapter. Four-node torus elements were used to model the concrete, and ring bars were used to model the FRP shell. Note that the thicknesses of the shells were not specifically given in the reports by the researchers, due to the variability of thickness within the fabric. Instead, the strength of the fabric was given as

a force per unit thickness. It was assumed in the analysis that the given strength (in Newtons per millimetre) can be modelled as strength (in MPa) per layer, each layer with a thickness of 1 mm. The area of FRP shell was then distributed among the ring bars accordingly. The stiffness of the shell was calculated as the ratio between the strength (in MPa) and the strain at ultimate ε_{ju}. Imposed displacements at the top of the model were used to calculate the stress-strain response of the columns. The unconfined concrete strength was used in the analytical model as no difference was seen in the strength of plain concrete columns and cylinders.

The analytical axial stress-axial strain curves (heavy solid lines) along with the experimental curves are plotted in Figure 142 for Cairns columns and Figure 143 for Jaffry and Sheikh columns, respectively. The experimental data was obtained from the graphs given in the reports by Cairns (2001) and Jaffry and Sheikh (2001).

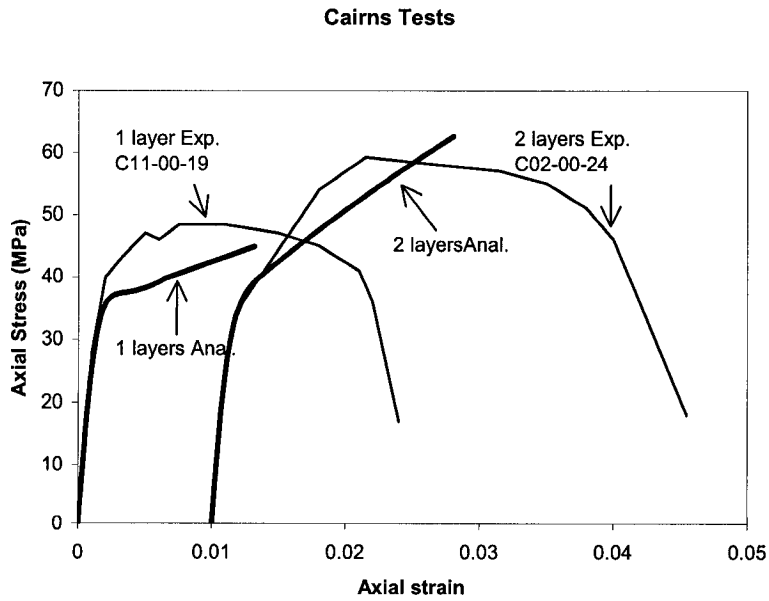

Figure 142. Analytical and experimental stress-strain curves for Cairns columns.

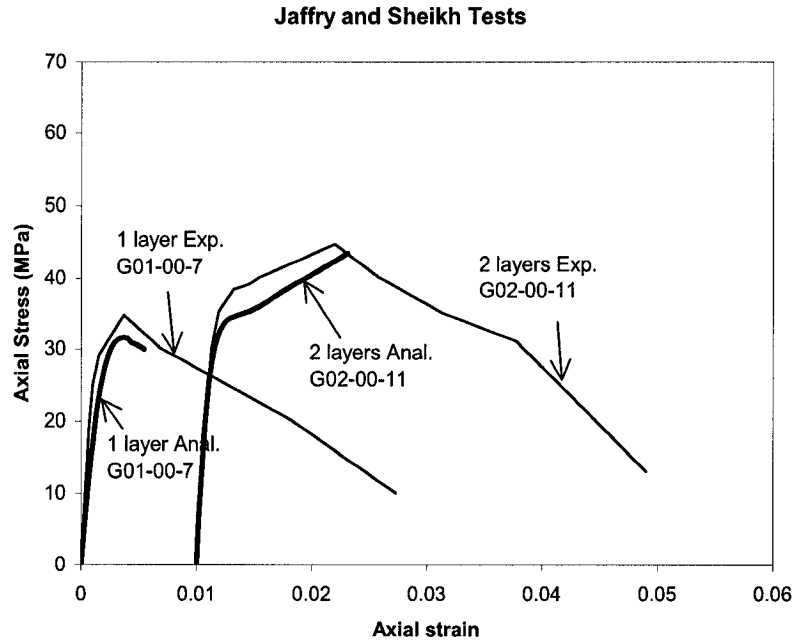

Figure 143. Analytical and experimental stress-strain curves for Jaffry and Sheikh columns.

The labels in these plots correspond to those given by the researchers. The analytical responses are compared to the experimental responses in Table 36. Note that column C11-00-19, tested by Cairns, contained an additional layer of carbon fibre in the longitudinal direction of the column.

Table 36. Analytical and experimental results of Cairns and Jaffry and Sheikh columns.

Column Label		Strength		strain	
		f_{cc} [MPa]	Anal. / Exp.	ε_{cc} [10^{-3}]	Anal. / Exp.
Cairns					
C11-00-19 (1 transverse layer)	Exp.	48.4	0.93	11.50	1.15
(1 longitudinal layer)	Anal.	44.9		13.20	
C02-00-24 (2 transverse layers)	Exp.	59.3	1.05	13.75	1.29
	Anal.	62.3		17.80	
Jaffry and Sheikh					
G01-00-7 (1 transverse layer)	Exp.	34.8	0.91	3.70	1.01
	Anal.	31.6		3.72	
G02-00-11 (2 transverse layers)	Exp.	44.8	0.97	11.99	1.09
	Anal.	43.5		13.10	
mean			**0.96**		**1.14**
St.Dev			**0.06**		**0.12**
CV[%]			**6.53**		**10.70**

From the results, the analytical values for the strength of concrete and the strain at peak strength are reasonably captured by the program. The ascending analytical branches of the stress-strain curves followed those of the experimental responses; the stiffnesses of the columns softened until reaching the peak stress. At this point, the analytical responses showed rupture of the FRP and failure of the column. The analytical response of column G01-00-7 tested by Jaffry and Sheikh with one layer of glass fibre, showed some softening of the concrete after peak stress and then rupture of the FRP. Note that the glass fibre used in these tests had less stiffness than the carbon fibre in a ratio of about 1 to 2.

The experimental response of column C11-00-19 showed vertical rupture of the FRP in the test region at peak stress; one of the lateral strain gauges was mounted in the place where rupture initiated. The readings in this gauge showed a strain at rupture very close to the strain at rupture obtained in the tensile coupon tests of the CFRP. Longitudinal gauges on the surface of the fabric produced readings up to the rupture of the fabric and then failed. Column C22-00-24 showed no sign of distress or visible warning of rupture of the CFRP just before the "violent" failure of the column (see Cairns 2001). It should be mentioned that the researcher reported that the strain readings after peak stress were not dependable.

In the report by Jaffry and Sheikh (2001), it was stated that a moderately ductile response was achieved with columns confined with one layer of GFRP, and specimens confined with two layers of GFRP showed two slopes in the ascending branch of the axial stress-axial strain responses after peak. It was also indicated that little activation (i.e. exertion of lateral pressure on the concrete) of the GFRP shell could have

happened before reaching the peak unconfined stress in the concrete. After this point, and due to the increasing lateral expansion, the fabric exerted high lateral pressure.

Some observations can be made from the experimental and analytical responses. The experimental responses in all of these columns show a kink just after reaching the peak stress, and only a few points in the axial stress-axial strain curve were captured by the data acquisition system. Photographs of these specimens after failure revealed extensive damage in the concrete. After reaching the maximum stress, the behaviour of these specimens could have been the result of progressive rupture of FRP and due to the pieces of concrete holding some strength while remaining in place due to the fabric envelope. This behaviour was not captured by VecTor6. The effects of progressive rupture or delamination of the FRP is not possible to be captured with the current version of VecTor6.

Another assumption in the analysis is the perfect bonding between the fabric and the concrete, which was prevented in the experiments. And the additional layer in the longitudinal direction in column C11-00-14 could have led to an increase in the strength of the column, something that was not modelled with the program. Finally, the use of the unconfined concrete strength in the analysis was based on the reported strength of plain columns. However, the influence of size effect on the behaviour of columns deserves more attention.

5.3.2 FRP confined column subjected to lateral cyclic loading and axial load.

A circular column tested by Sheikh and Yau (2002), confined with two layers of glass fibre and subjected to constant axial compression and lateral cyclic loading, was

examined. The analytical moment-curvature response of the monotonic envelop was compared to that obtained in the test.

The objective of the testing program was to investigate the strengthening of old columns and retrofitting of damaged columns with FRP. Twelve columns with a diameter of 356 mm and length of 1473 mm were tested under two different axial compressive loads and cyclic loading. Column ST-2NT was analyzed and the moment-curvature response was obtained from the axial stress-axial strain concrete curve generated by program VecTor6 using compression field modelling.

The material properties of column ST-2NT are given in Table 37. This column had six 25M (500 mm^2) longitudinal bars, a clear concrete cover of 20 mm, and US#3 (71 mm^2) spirals at 300 mm spacing. The column was wrapped before testing with 2 layers (each 1.25 mm thick) of glass fibre. The column was cast with a reinforced concrete stub at its base with dimensions 762 x 508 x 815 mm. The stub simulated the discontinuity due to beams or footings in a building.

Table 37. Material properties of column ST-2NT.

Shell	F_{ju} [N/mm]	ε_{ju}			
GFRP (1.25 mm layer)	518	0.0197			
Concrete	f'_c [MPa]	E_c* [MPa]	ε_{co}*		
	40.4	28000	0.00210		
	f_y [MPa]	f_u [MPa]	E_s [MPa]	ε_{sh}	ε_u
Longitudinal steel	490	680	196000	0.0115	0.131
Spiral steel	510	785	182000	0.0095	0.0894

* assumed

In Table 37, F_{ju} is the force per 1.25 mm layer of GFRP ε_{ju} is the rupture strain of the fabric, and the properties for concrete and steel follow the same notation throughout this Chapter.

A constant axial load of 1000 kN was applied at the free end of the column, simultaneously with cyclic lateral displacements increasing until failure. A sketch of the column is given in Figure 144.

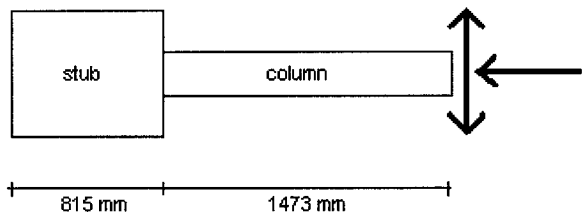

Figure 144. Sketch of column ST-2NT.

The analytical model was similar to those used for the columns in the previous section. Four-node torus elements were used to model the concrete, and ring bars were used to model the GFRP and the spiral steel. The longitudinal reinforcement was smeared in the torus elements.

Program VecTor6 was used to obtain the axial load-axial stress curve for this column considering the steel hoops in the model and assuming that it was subjected to monotonic axial compression until failure, which was caused by rupture of the FRP in the model. Figure 145 shows the total axial load versus axial stress curve, along with the corresponding load taken by the longitudinal steel and the concrete. As in the previous section, the unconfined concrete strength was used in the calculations. The

axial stress-axial strain curve was then obtained from the concrete axial load-axial stress curve, by dividing the concrete load by the net area of concrete of the cross section of the column (total area less the area of longitudinal steel).

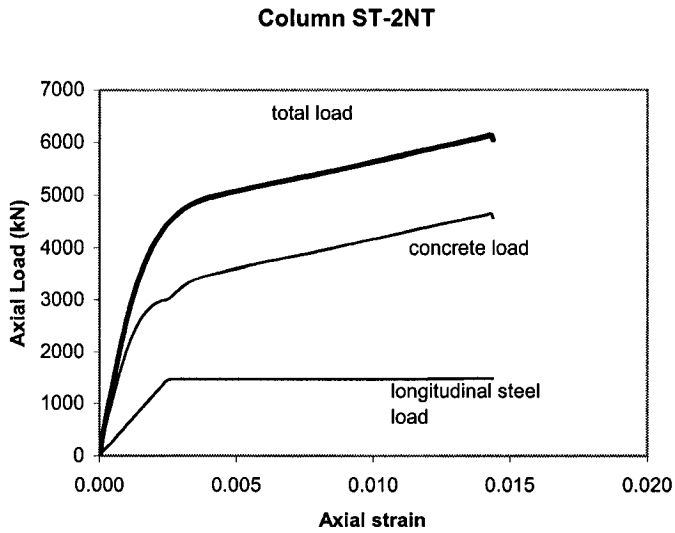

Figure 145. Analytical response of column ST-2NT in monotonic compression.

The axial stress-axial strain curve generated by VecTor6 is shown in Figure 146. The data from this curve was used to calculate and compare the monotonic moment-curvature envelop to that of the actual response of the column under cyclic behaviour.

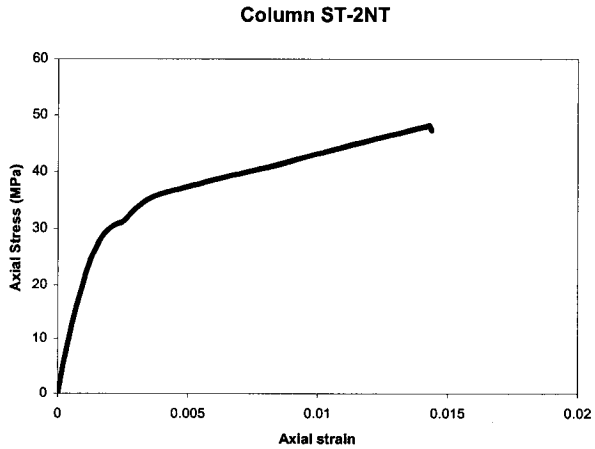

Figure 146. Analytical axial stress-axial strain curve of column ST-2NT

The analytical and experimental moment-curvature responses are shown in Figure 147. It can be seen that the analytical response agrees well with the experimental response. The analytical maximum moment was 255 kN.m and occurred at a curvature of 0.115 x 10^{-6} rad / mm, the experimental maximum average moment was 266 kN.m at a curvature of about 0.080 to 0.100 x 10^{-6} rad / mm.

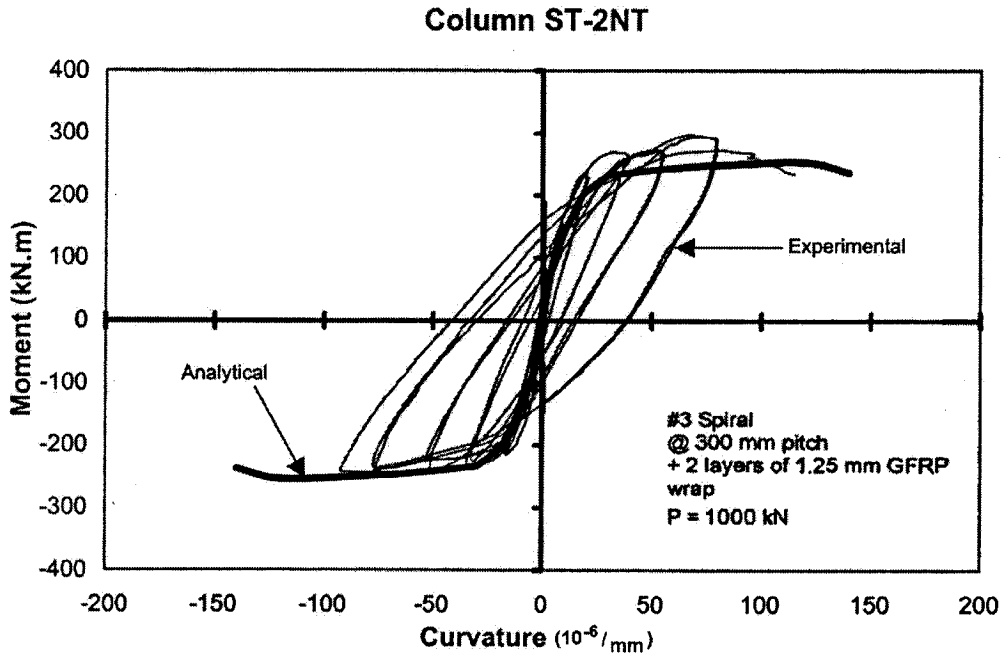

Figure 147. Analytical and experimental moment-curvature responses of column ST-2NT.

The analytical moment-curvature curve of the column with no glass polymer wraps and subjected to the same axial load was also calculated. The calculated response is plotted in Figure 148 and compared with the analytical response for the column with FRP wraps. The confinement effect of the FRP on the ductility and strength enhancement is clearly observed. The sequence of events for the analytical model was: initiation of cracking at a moment of about 55 kN.m, yielding of longitudinal steel at 175 kN.m, peak moment, rupture of FRP, and initiation of concrete crushing at 255

kN.m. The analytical moment-curvature envelope was carried out until the outermost fibres in compression sustained no more load and disintegrated at about 220 kN.m.

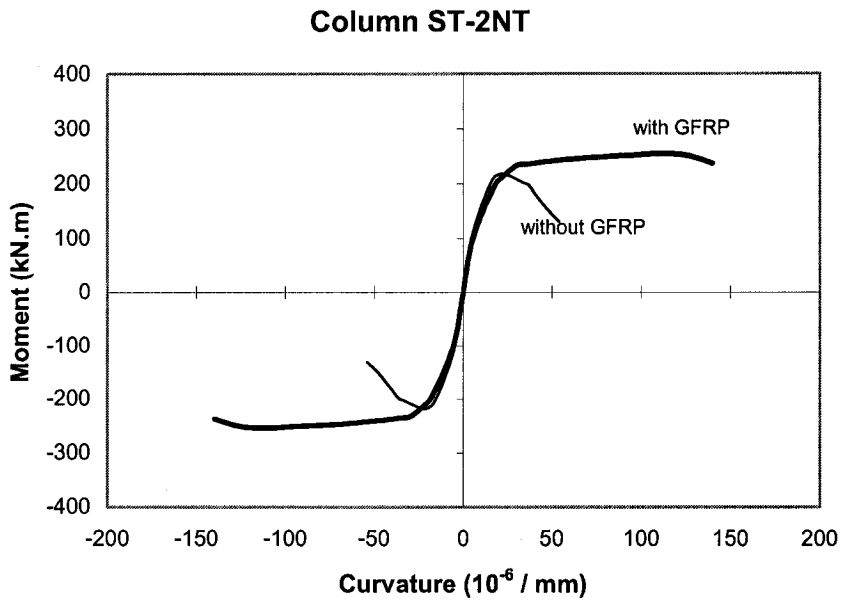

Figure 148. Analytical responses of column ST-2NT with and without GFRP wraps.

5.4 Summary.

The proposed models for concrete strength, compressive stress-strain response of confined concrete, and concrete dilatation were corroborated against several experimental tests. Results of cylinders subjected to active lateral pressure and axial compression, or wrapped with FRP fabric (i.e. subjected to passive lateral pressure) and axial compression, were used in testing the models. Analytical axial stress – axial strain, and axial stress - lateral strain curves for the confined concrete were compared to the experimental curves at the material level.

The confinement models were implemented in the nonlinear finite element programs VecTor6 and VecTor3 to analyze concrete columns subjected to monotonic axial compression. Circular columns confined with hoops or spirals, or hoops and FRP fabric, were modelled using the newly developed program VecTor6 for reinforced concrete solids of revolution. Square columns with different tie and longitudinal steel arrangements were modelled in the general three-dimensional analysis program VecTor3.

The objective was to evaluate the capabilities of the proposed models to reproduce the behaviour of confined concrete at the material and structural level. The analytical and experimental results agreed well, particularly with respect to maximum load capacity.

The confinement models covered a wide range of concrete strengths and confinement levels in the corroborations presented. Response of cylinders with unconfined concrete strengths from 28 MPa to 120 MPa and confinement levels of up to 100%, and response of columns with unconfined concrete strengths ranging from 35 MPa to 70 MPa confined with steel spirals or hoops, or FRP fabric, were well captured. The modelling of circular columns wrapped with FRP by using ring bars in program VecTor6, developed for this work, captured well the stress-strain response and mode of failure of FRP-confined concrete.

Concrete dilatation plays an important role in the response of confined concrete. The model proposed, simple in nature, resembles the observed behaviour of concrete expansion as a function of the confinement level and concrete strength. It is seen that

high strength concrete expands less than normal strength concrete when both are subjected to the same confinement level.

Applications of the confinement models and program VecTor6 were carried out. Circular columns wrapped with glass and carbon fibre shells subjected to axial compression and a column wrapped with glass fibre subjected to axial load and cyclic lateral load were analyzed. The analytical axial stress-axial strain responses agreed well with the experimental results, considering the testing procedures and the limitations of the program. The moment-curvature envelope of the column subjected to cyclic load was traced well, suggesting that the analytical axial stress-axial strain curve used in the calculations of the flexural response corresponded to the observed behaviour.

Chapter 6: Conclusions and Recommendations

6.1 Conclusions

A set of constitutive models for predicting the behaviour of triaxially compressed concrete was developed. A database of concrete cylinders (subjected to active lateral pressure) and reinforced concrete columns was used to formulate models for concrete dilatation, strength gain due to confinement, strain at peak stress, and compressive stress-strain response for concrete.

The model developed for concrete dilatation can be used to determine the secant Poisson's ratio in one direction due to compressive stresses in a plane normal to that direction. It is a function of the concrete strength f'_c, and the pressure exerted normal to the direction of calculation. As the pressure increases, the expansion of concrete decreases. The model also reflects the tendency of high strength concrete to expand less with respect to normal strength concrete under the same loading conditions. The secant Poisson's ratio has no upper boundary, as it may reach values greater than 0.5 due to cracking of concrete.

A four-parameter Ottosen-type model was used to formulate the strength gain in concrete due to confinement. Three of the parameters were calculated as function of the remaining parameter by solving a system of equations with a set of boundary conditions. Four values for the independent parameter were proposed as a function of the confinement ratio (i.e. lateral pressure over concrete strength, f_{cl} / f'_c), and the type of concrete. Two categories of confinement ratios and types of concrete were proposed covering concrete strengths from 20 to 130 MPa and confinement ratios of 0.0 to 1.0.

A simple model for calculating the strain at peak stress was suggested from statistical analysis of a database of concrete cylinders subjected to active lateral pressure and axial compression. The strain at peak was calculated as a function of the concrete strength and the confinement ratio. A similar procedure was used to establish a model for the post-peak strain at 80% of the peak stress, which was used in the determination of the post-peak stress-strain curve. The scatter in the regression analyses of both strains increased as the concrete strength and confinement ratios increases, due to the small number of available data in this range.

The stress-strain curve for concrete in compression accounted for the increase in strength and deformability of confined concrete. The curve proposed by Hoshikuma et al. (1996) was used to model the pre-peak portion of the curve, giving accurate results due to its boundary features. The post-peak curve was a transformation of the *witch of Agnesi* that accounted for the confinement dependency of the post-peak portion. A shape factor was proposed to transform the *witch*, which was then expressed as a function of the strain at peak stress, strain at 80% of peak stress, and the strength of concrete. The proposed curve was able to trace the post-peak behaviour seen in the database of cylinders.

The database used in the determination of the statistical parameters of the models is based on tests done in cylinders subjected to triaxial compression and columns under monotonic axial compression. The principal directions of stresses and strains did not change for any of the specimens included. The models for confinement were developed in the principal directions of the stress and strain tensors, which make them suitable for application in problems where rotation of cracks can occur.

The models were implemented into two in-house nonlinear finite element programs, VecTor3 and VecTor6, for three-dimensional analysis of general reinforced concrete solids and axisymmetric solids of revolution, respectively. The latter was written for this work to model concrete cylinders and reinforced concrete circular columns confined with steel spirals (or hoops) or/and FRP fabrics. Program VecTor6 was based on VecTor3 with a new library of torus-type elements.

Results obtained from axially compressed tests of concrete cylinders subjected to active lateral pressure or wrapped with FRP, circular columns and square columns reinforced with steel spirals, hoops, ties or FRP wraps, were corroborated against the implemented models using both programs. The analytical stress (or axial load) – axial strain, and stress (or load) - lateral strain curves compared well with experimental results, verifying the capabilities of the models and the programs to model the confinement behaviour of a wide range of concretes subjected to a wide spectrum of lateral pressures.

Applications of the confinement models were also given. Circular columns wrapped with glass or carbon fibre shells and subjected to monotonic compression were analyzed. The flexural response of a column wrapped with glass fibre and subjected to constant axial compression and cyclic lateral loading was calculated. The analytical axial stress-axial strain and moment-curvature responses resembled those of the experiments. The agreement of the flexural response, in particular, indicates the capacity of compression field modelling to reproduce complex responses of structural elements subjected to extreme loading.

6.2 Recommendations for Future Work

The newly developed models were used to corroborate the behaviour of concrete confined by several means, using steel or fibre reinforced polymers, or actively confined with pressure applied directly to the concrete surface. There are, however some limitations to the models and the finite element programs that deserve further attention.

- There is a need to widen the database of results from triaxial tests of concrete, especially high and very high strength concrete (i.e. over 75 MPa) tested over a wide range of confinement ratios.

- Measurements of lateral strains should be standardized. The strain gauges that have been used by several researchers (e.g. Imran and Pantazopoulou (1996), Sfer et al (2002)) sensed the general lateral behaviour around the circumference of a cylinder subjected to constant lateral pressure, and not localized damage. However, they had limitations in the maximum strain that could be measured. The use of fibre optics (see references in Li and Ansari 1999) seems to capture strains of up to 7% in an accurate manner.

- Overestimation of concrete expansion may occur when using the proposed dilatation model. The model is based on a relative small number of tests and the scatter (as a function of the coefficient of variation CV) in its application may be considerable. A trend between the confinement level and the concrete strength was found, which should be refined.

- Statistical fitting to determine coefficients of stress-strain based models is always open to improvement as the need for more detailed and accurate models increases.

- The proposed failure surface is a function of a parameter which was fitted to a large set of tests on columns and cylinders using different ranges of confinement levels and concrete strengths. The criterion represents an average value of the strength gain in confined concrete, and its accuracy depends on the sensitivity of the independent parameter to the selected database of tests. In several of the graphs shown for cylinders subjected to constant lateral pressure, the criterion underestimates or overestimates the value of the peak stress. The general coefficient of variance of the results (see Chapter 3) was found to be approximately 13%. An improved prediction of the strength may be found by widening the database of tests and refining the criterion, using more ranges of confinement levels and concrete strengths, particularly for the cases of high confinement of normal and high strength concrete (HN and HH ranges).

- It was found from the literature (e.g. Assa et al. 2001a, 2001b) that it is difficult to estimate the descending branch of the stress-strain curve for confined concrete after a stress of about 80% of the peak stress. Highly confined concrete will show no descending branch et all. The post-peak stress-strain curve proposed was based on these experimental facts and therefore no attempt was made to define a residual stress on the onset of failure in the post-peak regime.

- In the analytical models for the columns, it was assumed that the strength of plain concrete was that given by the researchers in their reports, which accounted for the observed size effect with respect to the strength obtained from standard concrete cylinder tests. All of the circular columns examined had a length to diameter ratio of four, although with different diameters. Size effect, however, was not investigated and may have an influence in the response of slender columns subjected to axial compression, and presumably more influence in the response of slender columns subjected to eccentric load.

- The in-house nonlinear finite element programs VecTor3 and VecTor6 should include elements that account for large deformations. The termination of the numerical analysis at post-peak stages earlier than the experimental curves, in some of the cases shown in Chapter 5, was a combination of overestimation of the dilatation and the use of small-deformation elements in the programs. Full Lagrangian elements can be used to model the large lateral deformations that confined concrete may experience, and second-order effects (i.e. geometrical stability) that are not taken into account in the currently implemented elements in programs VecTor3 and VecTor6.

- The solution technique in programs VecTor3 and VecTor6 is based on load or imposed displacement stepwise iterations, whereby the secant stiffness matrices of the component materials are updated at every load stage. This method provides a stable solution as the secant stiffness is always positive. Load-increment solution

methods such the arc-length method are not implemented in the family of VecTor programs.

- It was seen that the analytical load-deformation responses produced by VecTor6 were not affected when the number of elements in the analytical model was increased by a factor of about two and the aspect ratio of the elements was kept relatively constant. It is important, however, to note that the elements derived for VecTor3 and VecTor6 have strains and stresses calculated at the centroid of their cross sections, which implies that very coarse meshes yield poor results.

- Implementation of unsymmetrical features in the element library of VecTor6 is required to account for unsymmetrical loading.

- Implementation of mechanisms to determine buckling of bars in VecTor3 and VecTor6 is recommended. It has been seen in test of columns that buckling of bars may occur just after rupture of the lateral reinforcement (in well-confined columns) or before (in poor-confined columns). Buckling may also affect the cyclic response of structural elements. In general, the buckling of bars is not represented in the current versions of programs VecTor3 and VecTor6.

References

ACI-318 Committee. *ACI Building Code,* 2002, Farmington Hills, MI, USA. 443 p.

Ansari, F., and Li, Q. (1998). "High-strength concrete subjected to triaxial compression." *ACI Mat. J.,* 95(6), 747-755.

Ansari, A., and Li, Q. (1999). "Mechanics of damage and constitutive relationships for high-strength concrete in triaxial compression." *J. of Eng. Mech., ASCE,* 125(1), 1-9.

Assa, B., Nishiyama, M., and Watanabe, F. (2001a). "New approach for modeling confined concrete. I: Circular columns." *J. Struct. Eng.,* 127(7), 743-750.

Assa, B., Nishiyama, M., and Watanabe, F. (2001b). "New approach for modeling confined concrete. II: Rectangular columns." *J. Struct. Eng.,* 127(7), 751-757.

Attard, M.M., and Setunge, S. (1996). "Stress-strain relationship of confined and unconfined concrete." *ACI Mat. J.,* 93(5), 432-442.

Barros, M.H.F. (2001). "Elasto-plastic modeling of confined concrete elements following MC90 equations." *Eng. Struct.,* 23, 311-318.

Cairns, S.W. (2001). "Circular concrete columns externally reinforced with pre-fabricated carbon polymer shells." M.A.Sc. Thesis, University of Toronto, Canada. 233p.

Candappa, D.P., Setunge, S., and Sanjayan, J.G. (1999). "Stress versus strain relationship of high strength concrete under high lateral confinement." *Cem. Conc. Res.*, 29, 1977-1982.

Candappa, D.C., Sanjayan, J.G., and Setunge, S. (2001). "Complete triaxial stress-strain curves of high-strength concrete." *J. of Mat. Civ. Eng., ASCE*, 13(3), 209-215.

Chen, W.F. (1982). *Plasticity in Reinforced Concrete,* 1st Ed., McGraw-Hill, USA. 474 p.

Cleason, C. (1999). "Finite element analysis of confined concrete columns. " *Report to the Div. Conc. Struct.*, Chalmers University of Technology. Göteborg, Sweden. 20 p.

Collins, M.P., and Mitchell, D. (1997). *Prestressed Concrete Structures,* 1st Ed, Response Publications, Toronto and Montreal, Canada. 766 p.

Demers, M., and Neale, K.W. (1999). "Confinement of reinforced concrete columns with fibre-reinforced composite sheets – an experimental study." *Can. J. Civ. Eng.*, Vol.26, 226-241.

Gardner, N.J. (1969). "Triaxial behavior of concrete." *ACI J.,* Paper No. 66-15, 136-146.

Ghazi, M., Attard, M.M., and Foster, S.J. (2002). "Modelling triaxial compression using the Microplane formulation for low confinement." *Comp. & Struct.,* 80, 919-934.

Hoshikuma, J., Kazuhiko, K., Kazuhiko, N., and Taylor, A.W. (1996). "A model for confinement effect on stress-strain relation of reinforced concrete columns for seismic

design." *Proc., 11th World Conf. Earthquake Eng.,* Elsevier Science, London, UK, No. 825.

Imran, I., and Pantazopoulou, S.J. (1996). "Experimental study of plain concrete under triaxial stress." *ACI Mat. J.,* 93(6), 589-601.

Jaffry, S.A., and Sheikh, S.A. (2001). "Concrete filled glass fibre reinforced polymer (GFRP) shells under concentric compression" Research Report SJ-01-01, Dept. Civ. Eng., Univ. of Toronto, Canada. 202 p.

Karabinis, A.I., and Rousakis, T.C. (2002). "Concrete confined by FRP material: A plasticity approach." *Eng. Struct.,* 24, 923-932.

Kent, D.C.; and Park, R., (1971). "Flexural Members with Confined Concrete" *J. Struc. Div. ASCE*, 97(ST7), 1969-1990.

Kupfer, H., Hilsdorf, H.K., and Rusch, H. (1969). "Behavior of concrete under biaxial stresses." *ACI J.,* Paper No. 66-52, 656-666.

Kwon, M., and Spacone, E. (2002). "Three-dimensional finite element analyses of reinforced concrete columns." *Comp. & Struct.,* 80, 199-212.

Lam, L., and Teng, J.G. (2002). "Strength models for fiber-reinforced plastic-confined concrete." *J. Struct. Eng., ASCE*, 128(5), 612-623.

Lee, Y-H., Willam, K., and Kang, H-D. (1997). "Experimental observations of concrete behavior under uniaxial compression." *CEAE-Dept. Univ.Colorado,* Boulder, CO, 11 p.

Liu, J., and Foster, S.J. (1998). "Finite-element model for confined concrete columns." *J. Struct. Eng. ASCE* , 124(9), 1011-1017.

Liu, J., and Foster, S.J. (2000). "A three-dimensional finite element model for confined concrete structures." *Comp.& Struct.*, 77, 441- 451.

Mander, J.B., Priestley, M.J.N., and Park, R. (1988). "Observed stress-strain behavior of confined concrete.: *J. Struct. Eng.,* 114(8), 1827-1849.

Mirmiran, A., Zagers, K., and Yuan, W. (2000). "Nonlinear finite element modeling of concrete confined by fiber composites." *Fin. Elem. Anal. Des.,* 35, 79-96.

Montgomery, D.L., and Sheikh, S.A. (1996). "Behavior of spirally reinforced high strength concrete columns." Research Report, Dept. Civ. Eng., Univ. of Toronto, Toronto, Canada. 271 p.

Montoya, E., Vecchio, F.J., and Sheikh, S.A. (2001). "Compression field modeling of confined concrete." *Struct. Eng. and Mech.,* 12(3), 231-248.

Pessiki, S., Graybeal, B., and Mudlock, M. (2001). "Proposed design of high-strength spiral reinforcement in compression members." *ACI Struct. J.,* 98(6), 799-810.

Pivonka, P., Lackner, R., and Mang, H. (2000). "Numerical analyses of concrete subjected to triaxial compressive loading." *European Congress on Comp. Methods in Applied Mech.,* ECCOMAS 2000, Barcelona, 26 p.

Purba, B.K., and Mufti, A.A. (1999). "Investigation of the behaviour of circular concrete columns reinforced with carbon fiber reinforced polymer (CFRP) jackets." *Can. J. Civ. Eng.*, 26, 590-596.

Razvi, S., and Saatcioglu, M. (1999). "Confinement model for high-strength concrete." *J. Struct. Eng.,* 125(3), 281-289.

Richart, F.E., Brandtzaeg, A., and Brown, R.L. (1928). "A study of the failure of concrete under combined compressive stresses." *Univ. of Illinois Bulletin* 185. 105 p.

Rochette, P., and Labossiere, P. (2000). "Axial testing of rectangular column models confined with composites." *J. Comp. Constr., ASCE*, 4(3), 129-136.

Saatcioglu, M., and Razvi, S.R. (1992). "Strength and ductility of confined concrete." *J. Struct. Eng.,* 118(6), 1590-1607.

Sankarasubramanian, G., and Rajasekaran, S. (1996). "Constitutive modeling of concrete using a new failure criterion." *Comp. & Struct.,* 58(5), 1003-1014.

Selby, R.G., and Vecchio, F.J. (1993). "Three-dimensional analysis of reinforced concrete solids." Research Report, Dept. Civ. Eng., Univ. of Toronto, Canada.

Selby, R.G., and Vecchio, F.J. (1997). "A constitutive model for analysis of reinforced concrete solids." *Can. J. Civ. Eng.*, 24, 460-470.

Sfer, D., Carol, I., Gettu, R., and Etse, G. (2002). "Study of the behavior of concrete under triaxial compression." *J. Eng. Mech.,* 128(2), 156-163.

Sheikh, S.A. (1978). "Effectiveness of rectangular ties as confinement steel in reinforced concrete columns". PhD Thesis, University of Toronto, Canada. 256 p.

Sheikh, S.A., and Uzumeri, S.M. (1980). "Strength and ductility of tied concrete columns." *J. Struct. Div.,* 106(sT5), 1079-1112.

Spoelstra, M.R., and Monti, G. (1999). "FRP-confined concrete model." *J. Comp. for Constr, ASCE*; 3(3), 143-150.

Sheikh, S.A., and Toklucu, M. T. (1993). "Reinforced concrete columns confined by circular spiral and hoops". *ACI Structural J.*, 90(5), 542-553.

Sheikh, S.A., and Yau, G. (2002). "Seismic behavior of concrete columns confined with steel and fibre-reinforced polymers." *ACI Structural J.*, 99(1), SP-S08.

Tuma, J. (1987). *Engineering Mathematics Handbook,* 3rd Ed., McGraw-Hill, USA. 498p.

Vecchio, F.J. (1992). "Finite element model of concrete expansion and confinement." *J. Struct. Eng., ASCE,* 118(9), 2390-2406.

Vecchio, F.J., and Collins, M.P. (1986). "The modified compression field theory for reinforced concrete solids subjected to shear." *J. Amer. Conc. Inst.,* 83(2), 219-231.

Vintzileou E.; and Malliri P. (1999). "An empirical model for predicting the mechanical properties of confined concrete." *Conc. Res.*, 51(5), 353-364.

Xiao, Y, and Wu, H. (2000). "Compressive behaviour of concrete confined by carbon fiber composite jackets." *J. of Mat. Civ. Eng., ASCE*, 12(2), 139-146.

Xie, J., Elwi, A.E., and MacGregor, J.G. (1995). "Mechanical properties of three high-strength concretes containing silica fume." *ACI Mat. J.,* 92(2), 135-145.

Yamamoto, T, and Vecchio, F.J. (2001). "Analysis of reinforced concrete shells for transverse shear and torsion." *ACI Struct. J.*, 98(2), 191-200.

Yip, W.K. (1998). "Generic form of stress-strain equations for concrete." *Cem.& Conc. Res.*, 28(1), 33-39.

Zienkiewicks, O.C., and Taylor, R.L. (2000). *The Finite Element Method,* 5th Ed., Butterworth-Heinemann, UK. 663 p.

Appendix A: Column Behaviour at Peak Strength

A.1 Column Details

The following tables show the description of all the columns utilized in the comparison of analytical and experimental strength of confined concrete in Chapter 3, Section 3.3.1.

The notation for the tables is as follows:

b_c: centre-to-centre dimension of the square section between perimeter hoops

ϕ_c: centre-to-centre diameter of circular section between spirals (circular ties)

s: tie (spiral) spacing

d_b: diameter of confining steel

f_y: yield stress of confining steel

f_s: steel stress at maximum confining pressure

f'_c: unconfined concrete strength

f_{cc}: peak strength

f_{cl}: maximum lateral pressure

Table 38. Sheikh and Uzumeri columns (square)

Column Label	Section				Concrete			
	s	d_b	f_y	f_s	f'_c	f_{cc}	f_{cl}	f_{cl}/f'_c
	[mm]	[mm]	[MPa]	[MPa]	[MPa]	[MPa]	[MPa]	[%]
2A1-1	57.2	4.8	400	455	37.5	37.6	1.84	4.9
2A1H-2	57.2	4.8	262	255	37.0	39.6	1.03	2.8
4C1-3	50.8	3.2	520	489	36.4	37.4	2.15	5.9
4C1H-4	50.8	3.2	290	282	36.7	37.4	1.24	3.4
4C6-5	38.1	4.8	400	500	34.9	48.7	6.59	18.9
4C6H-6	38.1	4.8	262	255	34.3	44.6	3.36	9.8
4A3-7	76.2	7.9	470	475	40.9	44.5	3.91	9.6
4A4-8	28.7	4.8	496	420	40.8	47.2	3.39	8.3
4A5-9	76.2	9.5	303	345	40.5	42.4	4.10	10.1
4A6-10	35.1	6.4	400	455	40.7	45.3	5.33	13.1
4C3-11	95.3	6.4	400	358	40.7	43.9	3.36	8.3
4C4-12	25.4	3.2	634	469	40.8	50.6	4.12	10.1
4A1-13	57.2	4.8	496	475	31.3	34.6	1.92	6.1
2A5-14	76.2	9.5	400	427	31.5	36.9	5.08	16.1
2A6-15	35.1	6.4	427	413	31.7	39.6	4.84	15.3
2C1-16	50.8	3.2	580	589	32.5	37.6	2.59	8.0
2C5-17	101.6	7.9	480	348	32.9	38.0	4.66	14.2
4B3-19	101.6	7.9	480	400	33.4	40.6	4.37	13.1
4B4-20	38.1	4.8	480	544	34.7	44.8	5.72	16.5
4D3-22	82.6	7.9	480	386	35.5	43.4	3.46	9.8
4D4-23	28.7	4.8	480	531	35.8	46.9	4.93	13.8
4D6-24	38.1	6.4	480	475	35.8	49.6	5.92	16.5

b_c = 267 mm

Table 39. Sheikh and Toklucu columns (circular)

Column Label	Section					Concrete			
	b_c or ϕ_c [mm]	s [mm]	d_b [mm]	f_y [MPa]	f_s [MPa]	f'_c [MPa]	f_{cc} [MPa]	f_{cl} [MPa]	f_{cl}/f'_c [%]
D14-S10M-P2.2	300.7	56.0	11.3	452	574	35.9	51.9	6.84	19.0
D14-S10M-P3.0	300.7	76.0	11.3	452	536	35.9	48.6	4.70	13.1
D14-S10M-P4.4	300.7	112.0	11.3	452	452	35.9	41.4	2.69	7.5
D14-S10M-P6.0	300.7	152.0	11.3	452	77	35.9	42.9	0.34	0.9
D14-S8M-P2.2	304.0	56.0	8.0	607	607	35.9	44.6	3.58	10.0
D14-S8M-P3.0	304.0	76.0	8.0	607	185	35.9	47.8	0.80	2.2
D14-S8M-P4.4	304.0	112.0	8.0	607	157	35.9	46.7	0.46	1.3
D14-SD4-P2.2	306.3	56.0	5.7	593	257	35.9	46.0	0.76	2.1
D14-H10M-P3.0	300.7	76.0	11.3	452	415	35.9	49.1	3.64	10.1
D10-S10M-P3.1	208.7	79.0	11.3	452	509	35.5	42.9	6.19	17.4
D10-S10M-P4.3	208.7	109.0	11.3	452	90	35.5	39.0	0.79	2.2
D10-S8M-P1.6	212.0	41.0	8.0	607	607	35.5	49.8	7.02	19.8
D10-S8M-P2.1	212.0	53.0	8.0	607	607	35.5	46.5	5.43	15.3
D10-S8M-P3.1	212.0	79.0	8.0	607	580	35.5	43.9	3.48	9.8
D10-S8M-P4.3	212.0	109.0	8.0	607	53	35.5	36.4	0.23	0.6
D10-SD5-2.7	213.6	69.0	6.4	629	---	35.5	---	---	---
D10-SD4-P1.6	214.3	41.0	5.7	593	575	35.5	41.3	3.34	9.4
D10-SD4-P2.1	214.3	53.0	5.7	593	262	35.5	41.0	1.18	3.3
D10-H8M-P2.1	212.0	53.0	8.0	607	607	35.5	48.0	5.43	15.3
D8-8M-P2.5	169.0	64.0	8.0	607	607	34.9	46.1	5.64	16.2
D8-SD5-P2.5	170.6	64.0	6.4	629	625	34.9	40.4	3.68	10.6
D8-SD5-P2.5	170.6	64.0	6.4	629	630	34.9	38.9	3.71	10.6
D8-SD5-P3.4	170.6	86.0	6.4	629	477	34.9	35.8	2.09	6.0
D8-SD5-P1.7	170.6	43.0	6.4	629	660	34.9	46.0	5.79	16.6
D8-SD5-P1.7	170.6	43.0	6.4	629	650	34.9	44.9	5.70	16.3
D8-SD5-P1.7	170.6	43.0	6.4	629	660	34.9	45.9	5.79	16.6
D8-S3/16-P1.7	172.3	43.0	4.7	620	400	34.9	40.6	1.87	5.4
D8-HD5-P2.5	170.6	64.0	6.4	629	629	34.9	42.0	3.71	10.6

Table 40. Montgomery and Sheikh columns (circular)

Column Label	Section					Concrete			
	b_c or ϕ_c [mm]	s [mm]	d_b [mm]	f_y [MPa]	f_s [MPa]	f'_c [MPa]	f_{cc} [MPa]	f_{cl} [MPa]	f_{cl}/f'_c [%]
H-D25-S11.3-P41	208.7	41.0	11.3	522	580	69.7	93.0	13.60	19.5
H-D25-S11.3-P53	208.7	53.0	11.3	522	314	69.7	86.5	5.69	8.2
H-D25-S11.3-P79	208.7	79.0	11.3	522	487	69.7	91.2	5.92	8.5
H-D25-S11.3-P109	208.7	109.0	11.3	522	522	69.7	75.2	4.60	6.6
H-D25-S8-P41	212.0	41.0	8.0	666	700	69.7	76.4	8.10	11.6
H-D25-S8-P53	212.0	53.0	8.0	666	632	69.7	75.8	5.65	8.1
H-D25-S8-P79	212.0	79.0	8.0	666	87	69.7	78.2	0.52	0.7
H-D25-S5.7-P41	214.3	41.0	5.7	583	245	69.7	87.7	1.42	2.0
H-D20-S11.3-P64	165.7	64.0	11.3	522	522	69.7	85.9	9.87	14.2
H-D20-S9.5-P43	167.5	43.0	9.5	508	508	69.7	83.5	10.00	14.3
H-D20-S9.5-P64	167.5	64.0	9.5	508	393	69.7	77.0	5.20	7.5
H-D20-S9.5-P86	167.5	86.0	9.5	508	371	69.7	74.1	3.65	5.2
H-D20-S6.4-P43	170.6	43.0	6.4	646	88	69.7	72.3	0.77	1.1
VH-D20-S11.3-P43	165.7	43.0	11.3	522	522	89.8	104.6	14.69	16.4
VH-D20-S8-P43	169.0	43.0	8.0	666	658	89.8	91.6	9.10	10.1

Table 41. Pessiki et al. (circular)

Column Label	Section					Concrete			
	b_c or ϕ_c [mm]	s [mm]	d_b [mm]	f_y [MPa]	f_s [MPa]	f'_c [MPa]	f_{cc} [MPa]	f_{cl} [MPa]	f_{cl}/f'_c [%]
24-A	610.0	48.0	8.9	524	483	58.6	82.5	2.07	3.5
24-B	610.0	64.0	8.9	703	655	58.6	79.4	2.09	3.6
24-C	610.0	38.0	8.9	752	586	58.6	77.0	3.15	5.4
24-D	610.0	44.0	8.9	765	586	58.6	71.6	2.72	4.6
14-A	356.0	44.0	8.9	524	552	58.6	113.5	4.38	7.5
14-B	356.0	60.0	8.9	703	655	58.6	108.1	3.82	6.5
14-C	356.0	35.0	8.9	752	793	58.6	105.7	7.92	13.5
14-D	356.0	38.0	8.9	765	862	58.6	103.9	7.93	13.5
14-A'	356.0	41.0	9.1	524	545	52.1	105.4	4.65	8.9
14-C'	356.0	28.0	9.1	752	745	52.1	105.9	9.39	18.0
14-D'	356.0	29.0	9.1	765	758	52.1	112.8	11.05	21.2
14-E'	356.0	44.0	9.1	1345	1131	52.1	94.1	10.63	20.4
14-F'	356.0	62.0	10.9	1276	1110	52.1	95.4	7.38	14.2

Table 42. Razvi and Saatcioglu (circular)

Column Label	Section					Concrete			
	b_c or ϕ_c [mm]	s [mm]	d_b [mm]	f_y [MPa]	f_s [MPa]	f'_c [MPa]	f_{cc} [MPa]	f_{cl} [MPa]	f_{cl}/f'_c [%]
CC-1	223.7	135.0	6.3	660	660	51.0	59.9	1.36	2.7
CC-2	218.7	135.0	11.3	400	400	51.0	62.3	2.72	5.3
CC-3	223.7	70.0	6.3	660	660	51.0	68.4	2.63	5.2
CC-4	223.7	70.0	6.3	660	660	51.0	67.4	2.63	5.2
CC-8	223.7	70.0	6.3	660	660	105.4	122.9	2.63	2.5
CC-9	218.7	135.0	11.3	400	400	105.4	134.7	2.72	2.6
CC-10	218.7	60.0	11.3	400	400	105.4	135.3	6.11	5.8
CC-11	223.7	60.0	6.3	660	660	105.4	124.8	3.07	2.9
CC-12	222.5	60.0	7.5	1000	818	105.4	127.7	5.41	5.1
CC-14	222.5	60.0	7.5	1000	851	78.2	102.5	5.63	7.2
CC-15	218.7	60.0	11.3	400	400	78.2	105.2	6.11	7.8
CC-16	222.5	100.0	7.5	1000	796	78.2	95.1	3.16	4.0
CC-19	218.7	100.0	11.3	400	400	78.2	94.6	3.67	4.7
CC-20	223.7	100.0	6.3	660	660	78.2	88.4	1.84	2.4
CC-21	223.7	70.0	6.3	660	660	78.2	93.4	2.63	3.4
CC-22	218.7	135.0	11.3	400	400	78.2	89.3	2.72	3.5

Table 43. Razvi and Saatcioglu (square)

Column Label	Section					Concrete			
	b_c or ϕ_c [mm]	s [mm]	d_b [mm]	f_y [MPa]	f_s [MPa]	f'_c [MPa]	f_{cc} [MPa]	f_{cl} [MPa]	f_{cl}/f'_c [%]
CS-1	218.7	55.0	11.3	400	400	105.4	120.8	6.67	6.3
CS-2	223.5	55.0	6.5	570	570	105.4	121.6	6.15	5.8
CS-3	223.5	55.0	6.5	570	570	105.4	129.1	6.15	5.8
CS-4	222.5	55.0	7.5	1000	787	105.4	123.4	8.53	8.1
CS-5	222.5	120.0	7.5	1000	729	105.4	122.5	4.83	4.6
CS-6	223.5	85.0	6.5	400	400	105.4	115.7	2.10	2.0
CS-7	223.5	120.0	6.5	400	400	105.4	115.0	1.98	1.9
CS-8	218.7	85.0	11.3	400	400	105.4	117.8	6.47	6.1
CS-9	218.7	120.0	11.3	400	400	105.4	134.2	6.11	5.8
CS-11	218.7	40.0	11.3	400	400	68.9	93.9	9.17	13.3
CS-12	218.7	55.0	11.3	400	400	68.9	82.1	6.67	9.7
CS-13	223.5	55.0	6.5	570	570	78.2	85.9	6.15	7.9
CS-14	223.5	55.0	6.5	570	570	68.9	94.3	6.15	8.9
CS-15	222.5	55.0	7.5	1000	831	68.9	95.5	9.00	13.1
CS-16	222.5	85.0	7.5	1000	814	68.9	95.2	7.60	11.0
CS-17	223.5	85.0	6.5	400	400	68.9	75.2	2.10	3.0
CS-18	223.5	85.0	6.5	400	400	78.2	76.4	2.79	3.6
CS-19	218.7	85.0	11.3	400	400	78.2	104.2	6.47	8.3
CS-20	218.7	85.0	11.3	400	400	51.0	106.3	8.63	16.9
CS-22	222.5	85.0	7.5	1000	795	51.0	68.0	5.57	10.9
CS-23	222.5	120.0	7.5	1000	792	51.0	71.3	5.24	10.3
CS-24	218.7	85.0	11.3	400	400	51.0	72.6	6.47	12.7
CS-25	218.7	120.0	11.3	400	400	51.0	69.7	6.11	12.0
CS-26	223.5	55.0	6.5	570	570	51.0	76.7	6.15	12.1

Table 44. Nagashima et al. (1992) (square)*

Column Label	Section					Concrete			
	b_c or ϕ_c [mm]	s [mm]	d_b [mm]	f_y [MPa]	f_s [MPa]	f'_c [MPa]	f_{cc} [MPa]	f_{cl} [MPa]	f_{cl}/f'_c [%]
HH08LA	199.9	55.0	5.1	1387	767	98.8	122.8	7.13	7.2
HH10LA	199.9	45.0	5.1	1387	795	98.8	122.5	8.71	8.8
HH13LA	199.9	35.0	5.1	1387	835	98.8	131.5	11.20	11.3
HH15LA	198.6	45.0	6.4	1368	840	98.8	127.0	13.33	13.5
HH20LA	198.6	35.0	6.4	1368	884	100.4	148.2	17.14	17.1
HL06LA	200.0	45.0	5.0	807	794	100.4	118.2	7.03	7.0
HL08LA	200.0	35.0	5.0	807	807	100.4	133.2	9.04	9.0
LL05LA	200.0	55.0	5.0	807	807	51.3	68.9	5.58	10.9
LL08LA	200.0	35.0	5.0	807	807	51.3	79.4	9.04	17.6
LH08LA	199.9	55.0	5.1	1387	829	51.3	70.9	6.92	13.5
LH13LA	199.9	35.0	5.1	1387	917	51.3	85.7	11.20	21.8
HH13MA	199.9	35.0	5.1	1387	833	100.4	131.8	11.20	11.2
HH13HA	199.9	35.0	5.1	1387	833	100.4	129.2	11.20	11.2
LL08MA	200.0	35.0	5.0	807	807	51.3	79.6	9.04	17.6
LL08HA	200.0	35.0	5.0	807	807	51.3	78.0	9.04	17.6
LH15LA	198.6	45.0	6.4	1368	920	52.4	88.7	13.33	25.4
HH13LB	199.9	27.0	5.1	1387	860	100.4	131.7	12.39	12.3
HH13LD	199.9	25.0	5.1	1387	849	100.4	128.2	13.38	13.3
LL08LB	200.0	27.0	5.0	807	807	52.4	82.4	9.99	19.1
LL08LD	200.0	25.0	5.0	807	807	52.4	77.3	10.79	20.6
HH13MSA	199.9	35.0	5.1	1387	833	100.4	129.7	11.20	11.2
HH13HSA	199.9	35.0	5.1	1387	833	100.4	134.8	11.20	11.2
LL08MSA	200.0	35.0	5.0	807	807	52.4	79.0	9.04	17.3
LL08HSZ	200.0	35.0	5.0	807	807	52.4	80.5	9.04	17.3

* See paper by Razvi and Saatcioglu (1999)

Table 45. Nagashima et al. (1993) (square)*

Column Label	Section					Concrete			
	b_c or ϕ_c [mm]	s [mm]	d_b [mm]	f_y [MPa]	f_s [MPa]	f'_c [MPa]	f_{cc} [MPa]	f_{cl} [MPa]	f_{cl}/f'_c [%]
1	214.0	31.0	6.0	813	813	92.4	145.0	14.67	15.9
2	214.0	31.0	6.0	813	813	92.4	137.0	14.67	15.9
3	214.0	31.0	6.0	813	813	92.4	145.0	14.67	15.9
4	214.0	45.0	6.0	813	813	92.4	122.0	10.11	10.9
5	214.0	60.0	6.0	813	799	92.4	120.0	7.58	8.2
6	214.0	60.0	6.0	813	799	92.4	110.0	7.58	8.2
7	214.0	60.0	6.0	813	799	92.4	120.0	7.58	8.2
8	214.0	31.0	4.0	840	818	92.4	120.0	6.68	7.2
9	214.0	31.0	6.0	462	462	96.2	134.0	8.34	8.7
10	214.0	31.0	6.0	462	462	96.2	133.0	8.34	8.7
11	214.0	45.0	6.0	462	462	96.2	117.0	5.75	6.0
12	214.0	60.0	6.0	462	462	96.2	115.0	4.31	4.5
13	214.0	60.0	6.0	462	462	96.2	115.0	4.31	4.5
14	216.0	31.0	4.0	481	481	96.2	115.0	3.83	4.0

* See paper by Razvi and Saatcioglu (1999)

Table 46. Li (circular)*

Column Label	Section					Concrete			
	b_c or ϕ_c [mm]	s [mm]	d_b [mm]	f_y [MPa]	f_s [MPa]	f'_c [MPa]	f_{cc} [MPa]	f_{cl} [MPa]	f_{cl}/f'_c [%]
3A	204.0	20.0	6.0	445	445	63.0	93.0	6.17	9.8
6A	204.0	35.0	6.0	445	445	63.0	78.0	3.52	5.6
9A	204.0	50.0	6.0	445	445	63.0	74.7	2.47	3.9
12A	204.0	65.0	6.0	445	445	63.0	70.6	1.90	3.0
3B	204.0	20.0	6.0	445	445	72.3	108.8	6.17	8.5
6B	204.0	35.0	6.0	445	445	72.3	92.7	3.52	4.9
9B	204.0	50.0	6.0	445	445	72.3	85.0	2.47	3.4
12B	204.0	65.0	6.0	445	445	72.3	73.8	1.90	2.6
2HB	203.6	20.0	6.4	1318	1039	52.0	126.0	16.42	31.6
4HB1	203.6	35.0	6.4	1318	948	52.0	87.5	8.56	16.5
6HB	203.6	50.0	6.4	1318	897	52.0	68.5	5.67	10.9
2HC1	203.6	20.0	6.4	1318	962	82.5	146.0	15.21	18.4
4HC	203.6	35.0	6.4	1318	884	82.5	106.8	7.98	9.7
6HC	203.6	50.0	6.4	1318	841	82.5	92.3	5.31	6.4

* See paper by Razvi and Saatcioglu (1999)

A.2 Analytical and Experimental Strengths for Column Database

The analytical strengths calculated from the available models are plotted against the experimental strengths in the following graphs for each of the models considered in Chapter 3, Section 3.3.1.

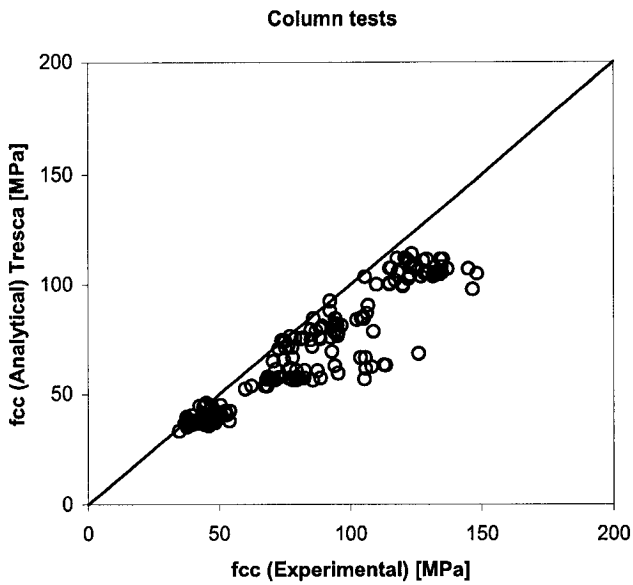

Figure 149. Analytical to experimental strength, Tresca model.

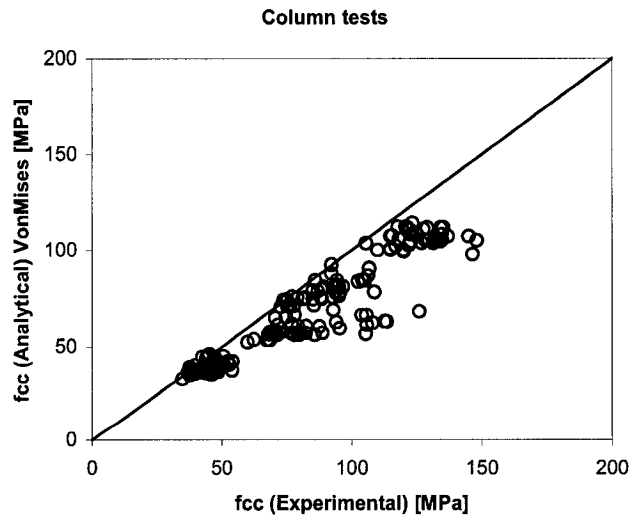

Figure 150. Analytical to experimental strength, Von Mises model.

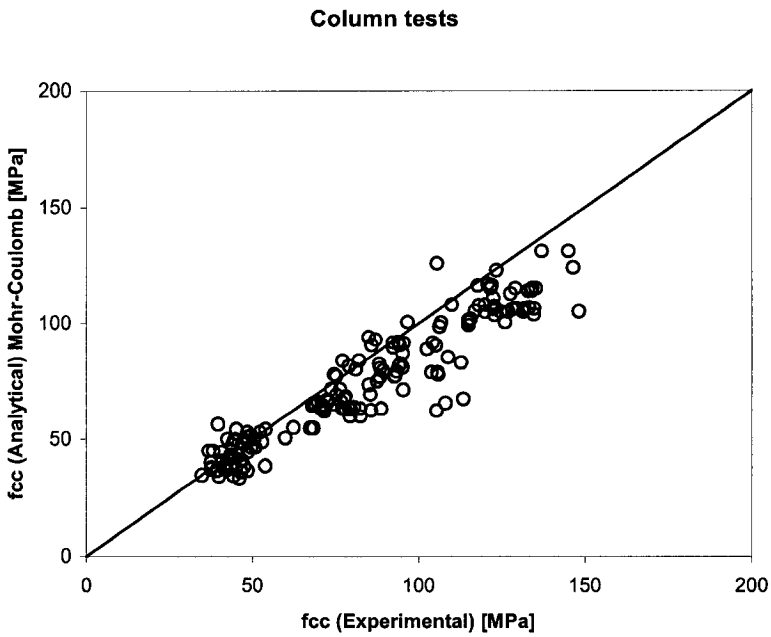

Figure 151. Analytical to experimental strength, Mohr-Coulomb model.

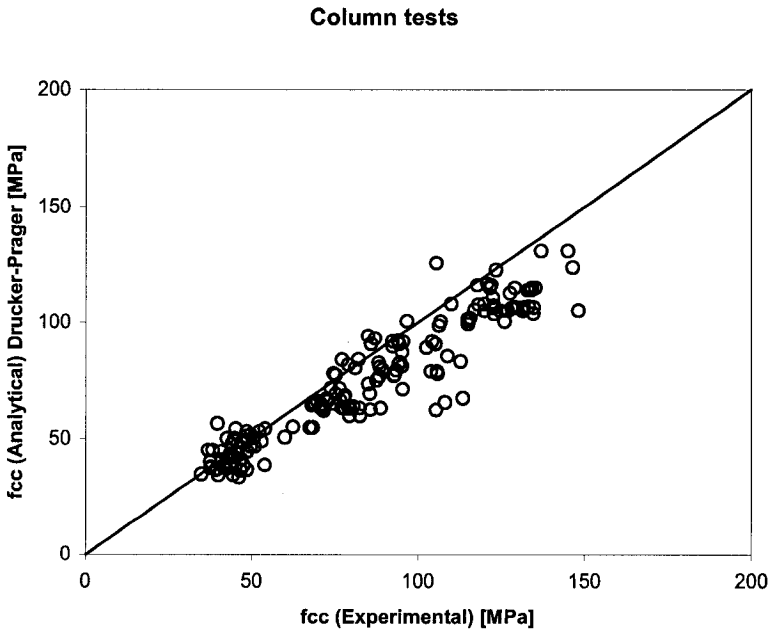

Figure 152. Analytical to experimental strength, Drucker-Prager model.

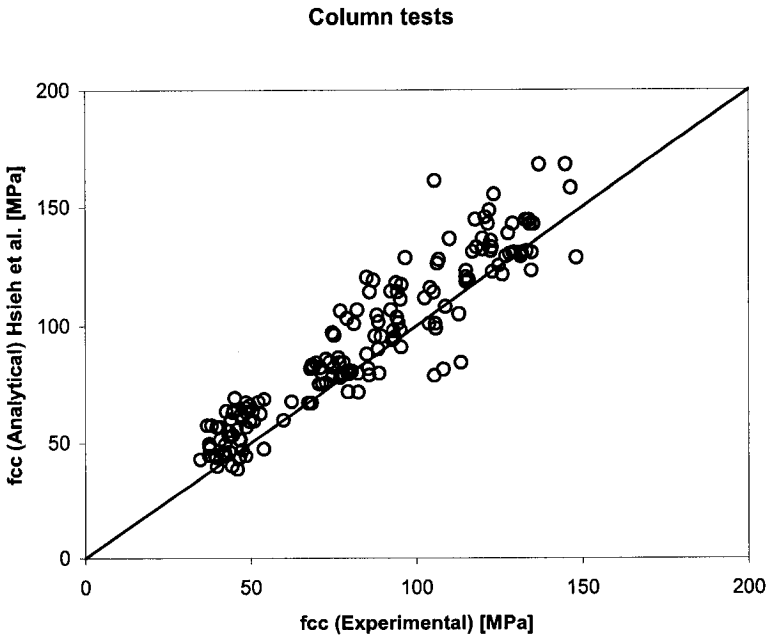

Figure 153. Analytical to experimental strength, Hsieh et al. model.

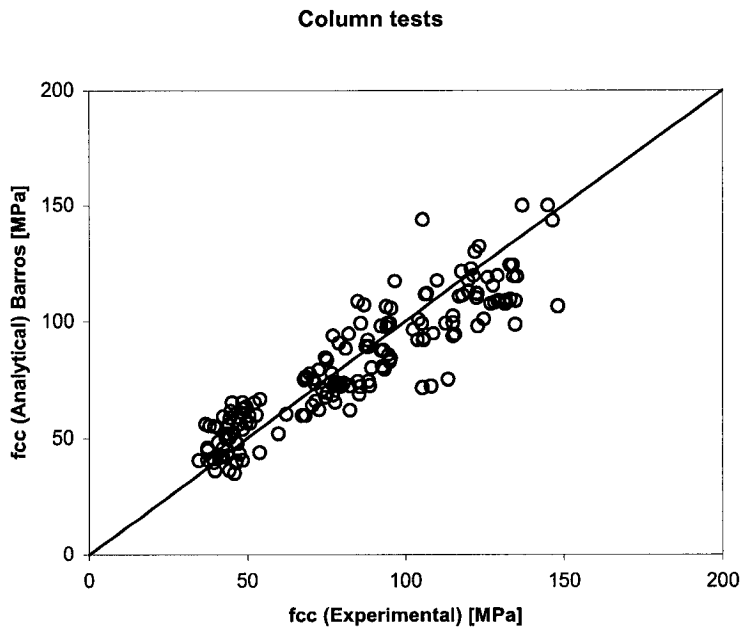

Figure 154. Analytical to experimental strength, Barros model.

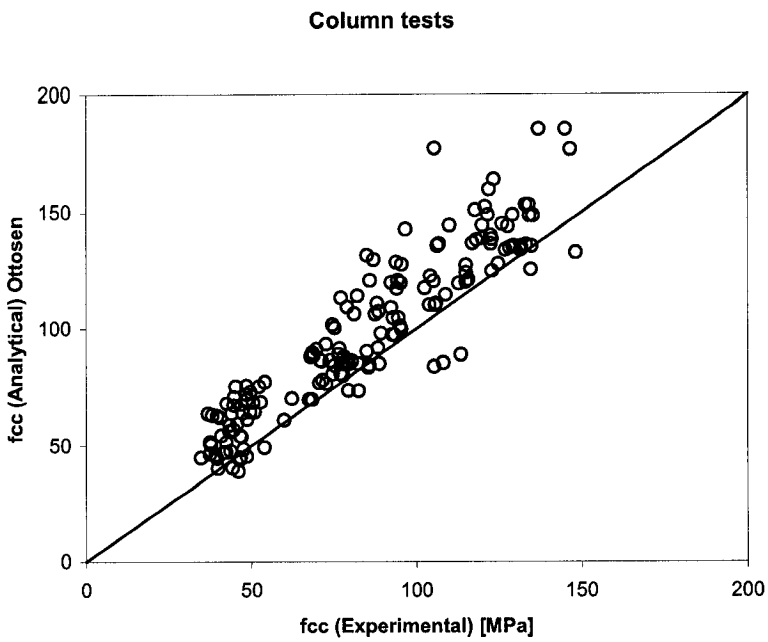

Figure 155. Analytical to experimental strength, Ottosen model.

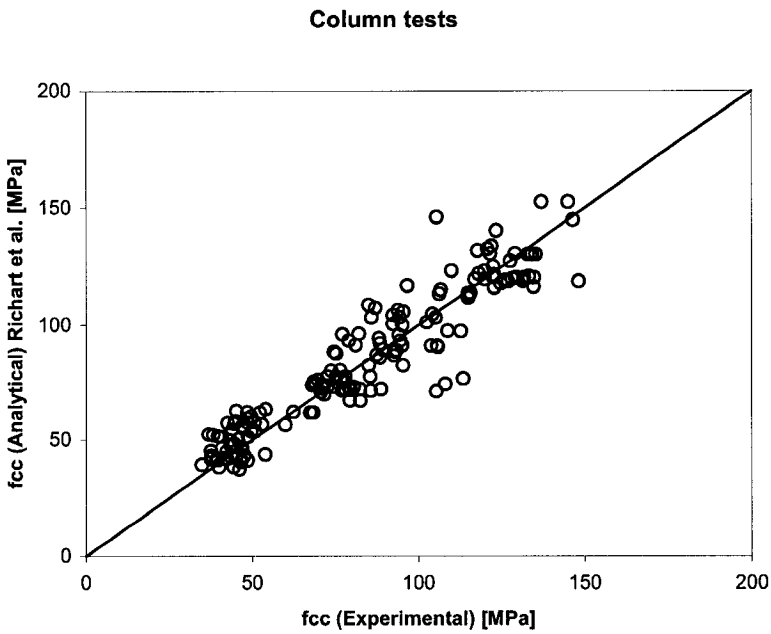

Figure 156. Analytical to experimental strength, Richart et al. model.

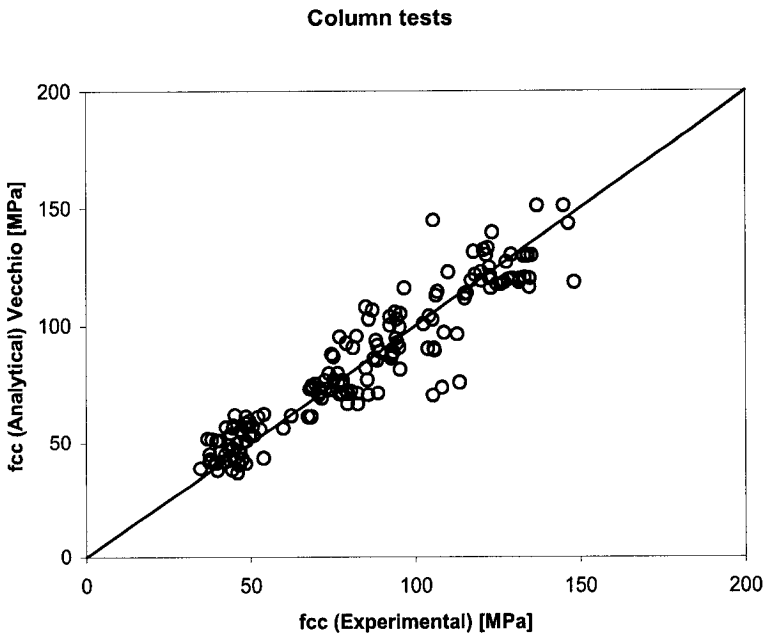

Figure 157. Analytical to experimental strength, Vecchio model.

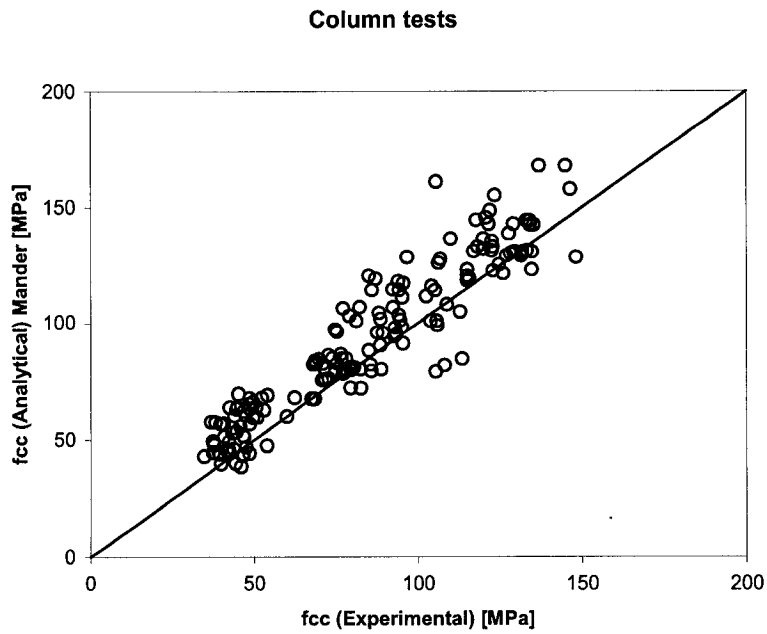

Figure 158. Analytical to experimental strength, Mander model.

Appendix B: Cylinder Behaviour at Peak Strength

B.1 Cylinder Details

The following tables describe all cylinders utilized in the comparison of analytical and experimental strength of confined concrete in Chapter 3, Section 3.3.2.

The notation for the tables is as follows:

f'_c: unconfined concrete strength

f_{cc}: peak strength

f_{cl}: maximum lateral pressure

Table 47. Hurlbut specimens

Concrete			
f'_c [MPa]	f_{cc} [MPa]	f_{cl} [MPa]	f_{cl}/f'_c [%]
22.1	25.8	0.69	3.1
22.1	32.9	3.44	15.6
22.1	51.0	6.89	31.2
22.1	77.9	13.79	62.5

Table 48. Gardner specimens

Concrete			
f'_c [MPa]	f_{cc} [MPa]	f_{cl} [MPa]	f_{cl}/f'_c [%]
27.6	72.4	8.62	31.2
27.6	117.9	17.24	62.5
27.6	144.8	25.86	93.7

Table 49. Li and Ansari specimens

Concrete			
f'_c [MPa]	f_{cc} [MPa]	f_{cl} [MPa]	f_{cl}/f'_c [%]
47.8	71.0	8.30	17.36
47.8	97.6	16.60	34.73
47.8	116.3	24.80	51.88
47.8	128.3	33.20	69.46
47.8	148.5	51.40	107.53
75.7	125.3	13.80	18.23
75.7	151.6	27.60	36.46
75.7	179.9	41.40	54.69
75.7	203.2	55.20	72.92
75.7	218.2	69.00	91.15
106.0	184.8	20.70	19.53
106.0	223.7	41.40	39.06
106.0	274.5	62.10	58.58
106.0	302.4	82.80	78.11

Table 50. Richart et al. specimens

Concrete			
f'_c [MPa]	f_{cc} [MPa]	f_{cl} [MPa]	f_{cl}/f'_c [%]
17.8	23.6	1.24	7.0
17.8	36.1	3.79	21.4
17.8	44.4	5.38	30.3
17.8	52.1	7.52	42.3
17.8	61.6	10.41	58.6
17.8	74.5	13.86	78.1
17.8	98.3	20.76	116.9
17.8	121.9	28.21	158.8
25.2	46.7	3.79	15.0
25.2	59.4	7.52	29.8
25.2	83.8	13.86	54.9
25.2	132.1	28.21	111.7
7.2	27.7	3.79	52.4
7.2	43.2	7.52	103.8
7.2	70.2	13.86	191.4
7.2	120.3	28.21	389.5

Table 51. Attard and Setunge specimens

Concrete			
f'_c [MPa]	f_{cc} [MPa]	f_{cl} [MPa]	f_{cl}/f'_c [%]
120.0	125.0	0.50	0.4
120.0	128.0	1.00	0.8
120.0	165.0	5.00	4.2
120.0	192.0	10.00	8.3
120.0	220.0	15.00	12.5
120.0	234.0	20.00	16.7
120.0	168.0	5.00	4.2
120.0	187.0	10.00	8.3
120.0	211.0	15.00	12.5
110.0	150.0	5.00	4.5
110.0	175.0	10.00	9.1
110.0	192.0	15.00	13.6
110.0	153.0	5.00	4.5
110.0	164.0	10.00	9.1
110.0	185.0	15.00	13.6
100.0	106.0	1.00	1.0
100.0	121.0	5.00	5.0
100.0	144.0	10.00	10.0
100.0	165.0	15.00	15.0
100.0	127.0	5.00	5.0
100.0	153.0	10.00	10.0
100.0	169.0	15.00	15.0
132.0	180.0	5.00	3.8
132.0	200.0	10.00	7.6
132.0	222.0	15.00	11.4
126.0	162.0	5.00	4.0
126.0	186.0	10.00	7.9
126.0	211.0	15.00	11.9
118.0	154.0	5.00	4.2
118.0	173.0	10.00	8.5
118.0	201.0	15.00	12.7
96.0	119.0	5.00	5.2
96.0	147.0	10.00	10.4
96.0	157.0	15.00	15.6
60.0	67.0	1.00	1.7
60.0	98.0	5.00	8.3
60.0	122.0	10.00	16.7
60.0	145.0	15.00	25.0

Table 52. Imran and Pantazopoulou specimens

Concrete			
f'_c [MPa]	f_{cc} [MPa]	f_{cl} [MPa]	f_{cl}/f'_c [%]
73.4	96.1	3.20	4.4
73.4	108.7	6.40	8.7
73.4	125.6	12.80	17.4
73.4	168.6	25.60	34.9
73.4	203.9	38.40	52.3
73.4	240.5	51.20	69.8
47.4	57.6	2.15	4.5
47.4	67.3	4.30	9.0
47.4	83.6	8.60	18.0
47.4	118.1	17.20	36.3
47.4	161.1	30.10	63.5
47.4	204.7	43.00	90.7
28.6	33.6	1.05	3.7
28.6	26.37	2.10	7.3
28.6	48.1	4.20	14.7
28.6	65.2	8.40	29.4
28.6	92.3	14.70	51.4
28.6	114.5	21.00	73.4

Table 53. Xie, Elwi and McGregor specimens

Concrete			
f'_c [MPa]	f_{cc} [MPa]	f_{cl} [MPa]	f_{cl}/f'_c [%]
60.2	80.6	2.29	3.8
60.2	97.6	5.30	8.8
60.2	107.6	8.31	13.8
60.2	156.9	20.29	33.7
60.2	193.2	29.32	48.7
60.2	172.1	23.30	38.7
60.2	121.6	11.32	18.8
60.2	136.8	14.33	23.8
60.2	58.4	0.84	1.4
92.2	129.4	3.78	4.1
92.2	155.6	8.30	9.0
92.2	181.2	12.82	13.9
92.2	194.3	17.33	18.8
92.2	208.7	21.85	23.7
92.2	234.6	26.28	28.5
92.2	199.8	16.50	17.9
92.2	261.1	35.50	38.5
92.2	293.5	44.44	48.2
119.0	172.3	6.07	5.1
119.0	212.2	12.02	10.1
119.0	225.9	17.97	15.1
119.0	251.0	24.04	20.2
119.0	261.8	29.99	25.2
119.0	281.0	36.06	30.3
119.0	316.3	47.96	40.3
119.0	367.4	59.98	50.4

B.2 Analytical and Experimental Strengths for Cylinder Database

The strengths calculated from the available models are plotted against the experimental strengths in the following graphs for each of the models considered in Chapter 3, Section 3.3.2. The Tresca and Von Mises models produced similar results and are not plotted separately. Similarly, results from Mohr-Coulomb and Drucker-Prager models, being equal, are plotted in the same figure.

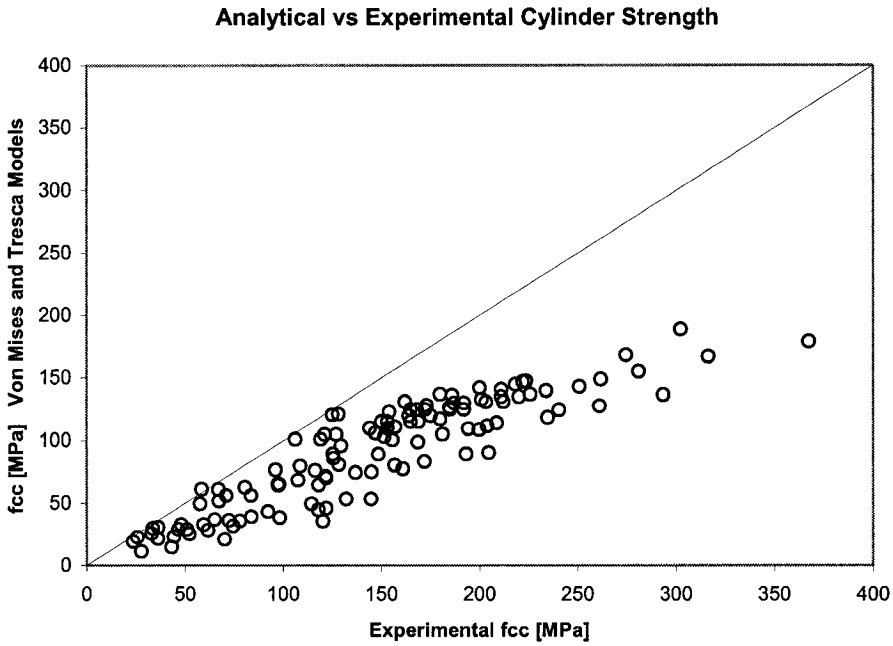

Figure 159. Analytical to experimental strength, Tresca and Von Mises model.

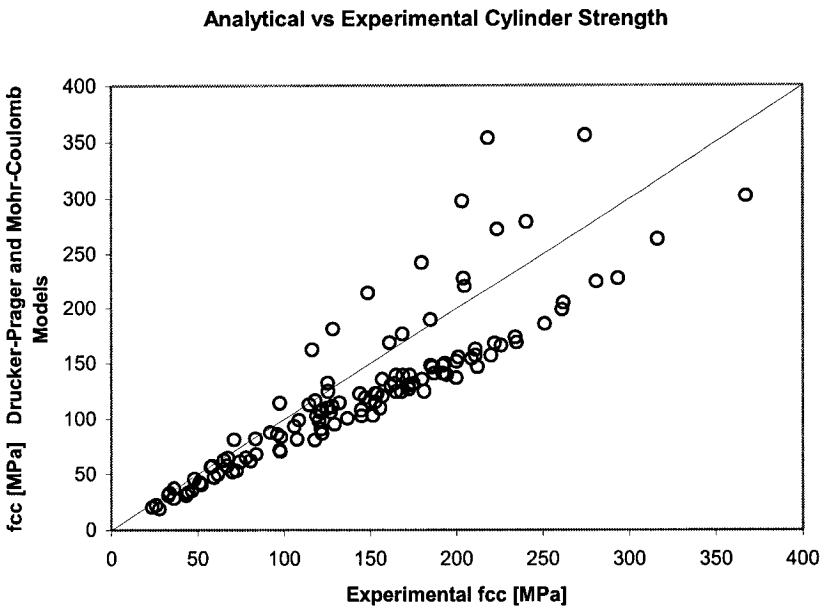

Figure 160. Analytical to experimental strength, Drucker-Prager and Mohr-Coulomb models.

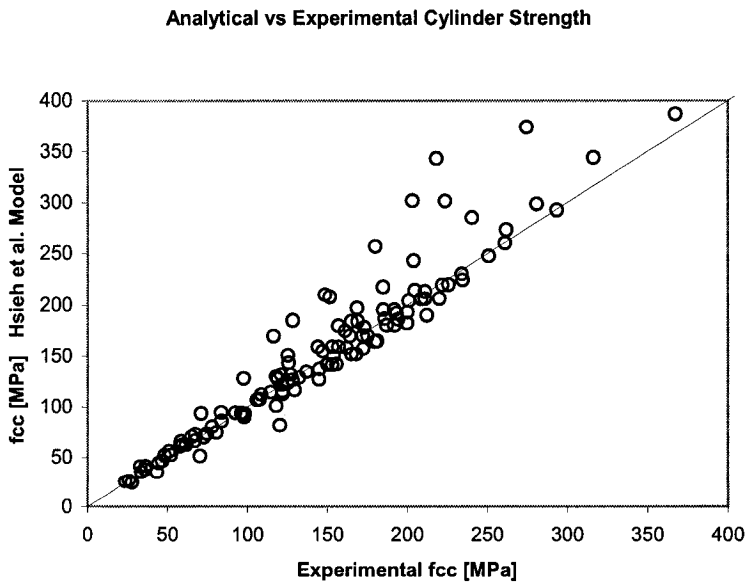

Figure 161. Analytical to experimental strength, Hsieh et al. model.

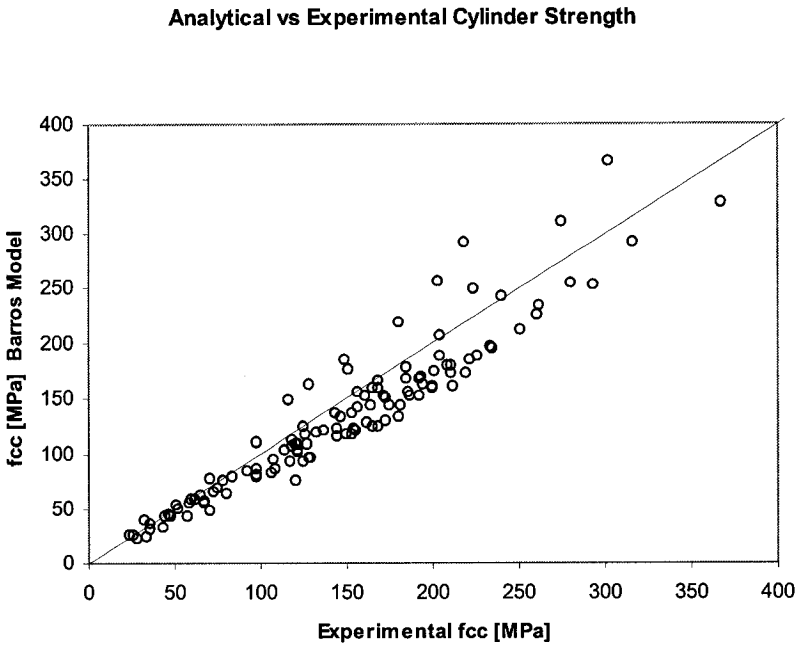

Figure 162. Analytical to experimental strength, Barros model.

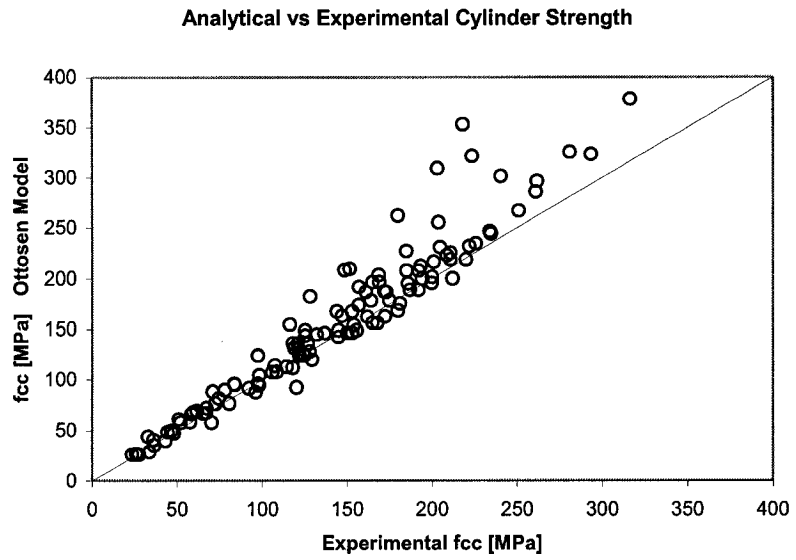

Figure 163. Analytical to experimental strength, Ottosen model.

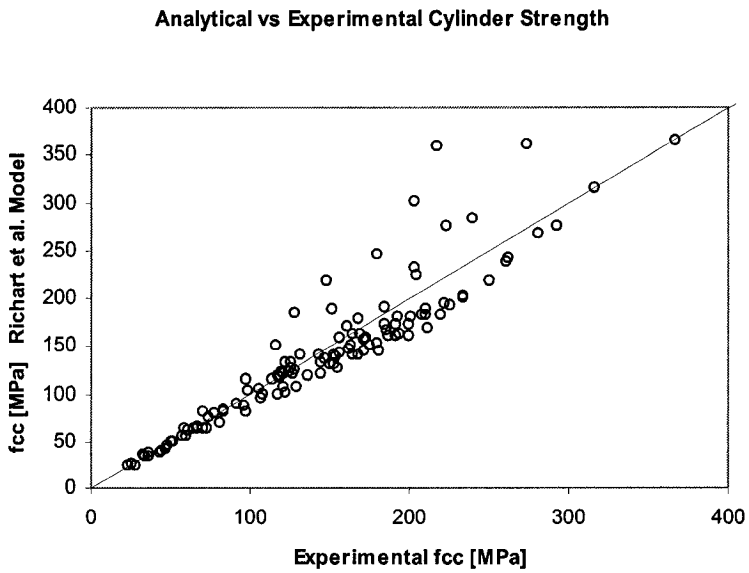

Figure 164. Analytical to experimental strength, Richart et al. model.

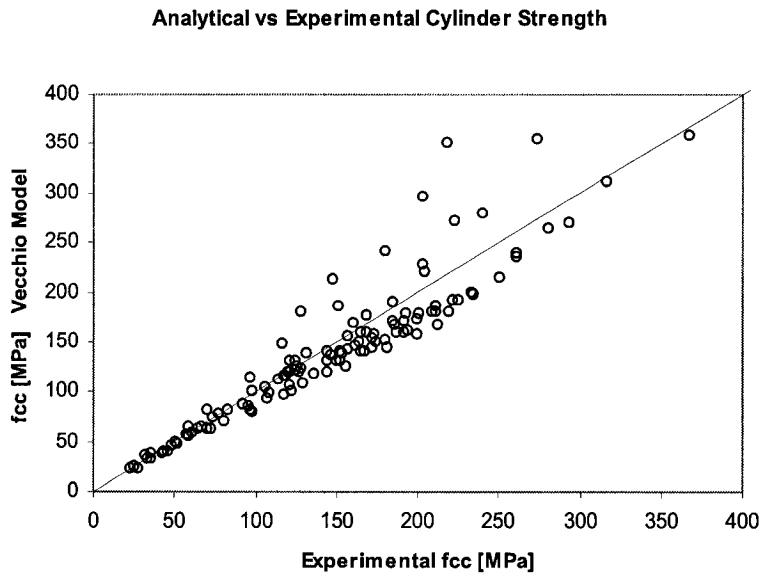

Figure 165. Analytical to experimental Strength, Vecchio model.

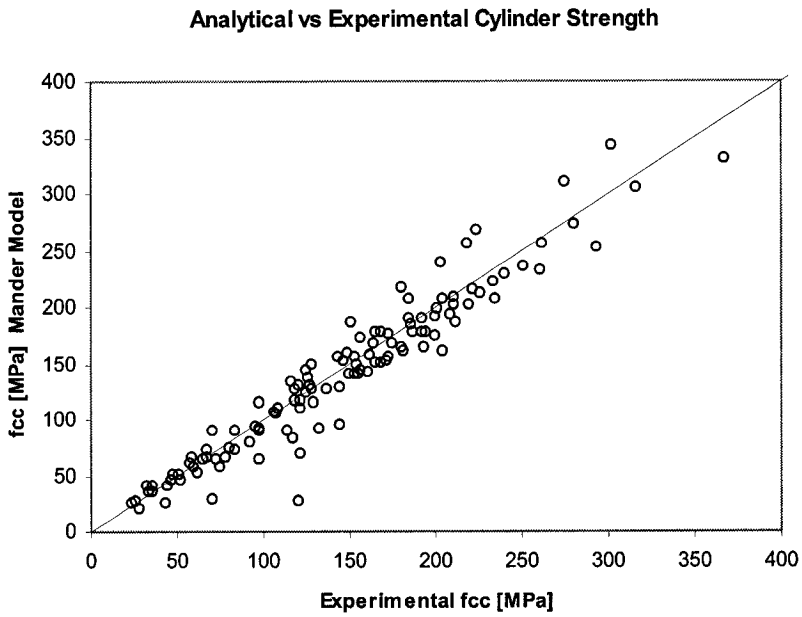

Figure 166. Analytical to experimental Strength, Mander model.

Appendix C: Determination of Parameter *a* for Ottosen Model

C.1 Reinforced Concrete Columns

The experimental results for the columns listed in Appendix A were used to calculate the parameter a for the Ottosen model, as discussed in Chapter 3, Section 3.3.3.3. The triaxial stress results were plotted in the Haigh-Westergaard coordinate system (ξ, ρ); where:

$$\xi = \frac{I_1}{\sqrt{3}} \qquad \textbf{Eq. 169a}$$

$$\rho = \sqrt{2J_2} \qquad \textbf{Eq.169b}$$

The pair of coordinates for each column was normalized with respect to the unconfined concrete strength f'c, i.e. (ξ/f'_c, ρ/f'_c), and the columns were divided into four categories: LN, HN, LH, and HH, as described in Chapter 3, Section 3.3.3.1.

The list for the columns in each category is given in Tables 52 to 54 (there are no HN values in the database), along with the normalized Haigh-Westergaard coordinates. The Ottosen failure surface was fitted to the experimental values in the following manner:

The Ottosen failure surface is given by:

$$a\frac{J_2}{f'^{\,2}_c} + \lambda\frac{\sqrt{J_2}}{f'_c} + b\frac{I_1}{f'_c} - 1 = 0 \qquad \textbf{Eq. 170}$$

The stress invariant I_1 can be calculated in terms of the parameter a and the experimental value for J_2; as:

$$I_1 = \frac{f'_c}{b(a)}\left[1 - a\frac{J_2}{f'^{\,2}_c} - \lambda(a)\frac{\sqrt{J_2}}{f'_c}\right] \qquad \textbf{Eq. 171}$$

where:

$$b = \frac{1}{9}a\left[\frac{f_{bc} - f_{ct}}{f'_c}\right] + \frac{1}{3}\left[\frac{f'_c}{f_{ct}} - \frac{f'_c}{f_{bc}}\right] \quad \text{Eq. 172}$$

$$\lambda(a) = k_1(a) + k_2(a).\cos 3\theta \quad \text{Eq. 173}$$

and

$$k_1 = \frac{\sqrt{3}}{2}\left\{1 + \frac{f'_c}{f_{ct}} - \frac{1}{3}a\left[1 + \frac{f_{ct}}{f'_c}\right]\right\} \quad \text{Eq. 174}$$

$$k_2 = \frac{\sqrt{3}}{2}\left\{\frac{f'_c}{f_{ct}} - 1 - 2b - \frac{1}{3}a\left[\frac{f_{ct}}{f'_c} - 1\right]\right\} \quad \text{Eq. 175}$$

For triaxial tests that produce points along the compressive meridian, as is the case with both the columns and the concrete cylinders ($0 > f_{c1} = f_{c2} > f_{c3}$):

$$\cos 3\theta = -1$$

Therefore:

$$\lambda = k_1 - k_2$$

The analytical value for the parameter a was obtained by minimizing the square of the difference between the analytical and the experimental values for the invariant I_1. The minimum *error* thus obtained represented the best fit to the experimental values for the triaxial tests in the compression meridian. The *error* was calculated as:

$$error = \min \sum \left(I_{1anal.} - I_{1exp.}\right)^2 \quad \text{Eq. 176}$$

The values calculated for *a* for each of the categories are

Table 54. Values for parameter *a* from column specimens

LN	HN	LH	HH
17.10	----	17.45	----

Using $f_{ct} = 0.65 f_c^{0.33}$

The category HH was not considered, as the database had only 3 column specimens in that category. Also, no specimens were reported for category HN.

Table 55. Low confinement, normal strength concrete (LN).

Researcher	Column Label	Experimental		Proposed Model	
		ξ / f'_c	ρ / f'_c	ξ / f'_c	ρ / f'_c
Sheikh & Uzumeri	2A1-1	0.63	0.78	0.74	0.93
	2A1H-2	0.65	0.85	0.67	0.88
	4C1-3	0.66	0.79	0.77	0.95
	4C1H-4	0.63	0.81	0.69	0.90
	4C6-5	1.02	0.98	1.15	1.16
	4C6H-6	0.86	0.98	0.89	1.02
	4A1-13	0.71	0.86	0.78	0.95
	2A5-14	0.86	0.82	1.07	1.12
	2A6-15	0.90	0.90	1.05	1.11
	2C1-16	0.76	0.88	0.84	0.99
	2C5-17	0.83	0.83	1.02	1.09
	4B3-19	0.85	0.89	0.99	1.08
	4B4-20	0.94	0.92	1.09	1.13
	4D3-22	0.82	0.92	0.89	1.02
	4D4-23	0.91	0.96	1.01	1.09
	4D6-24	0.99	1.00	1.08	1.13
Toklucu	D14-S10M-P2.2	1.04	1.05	1.12	1.15
	D14-S10M-P3.0	0.96	1.06	0.96	1.06
	D14-S10M-P4.4	0.83	1.00	0.82	0.98
	D14-S10M-P6.0	0.75	0.91	0.78	0.95
	D14-S8M-P2.2	0.85	0.96	0.89	1.02
	D14-S8M-P3.0	0.84	1.01	0.81	0.97
	D14-S8M-P4.4	0.82	1.04	0.74	0.93
	D14-SD4-P2.2	0.78	1.03	0.68	0.89
	D14-H10M-P3.0	0.93	1.18	0.75	0.93
	D10-S10M-P3.1	0.98	0.98	1.08	1.13
	D10-S10M-P4.3	0.73	0.92	0.73	0.92
	D10-S8M-P1.6	1.10	1.09	1.16	1.17
	D10-S8M-P2.1	0.83	1.08	0.71	0.91
	D10-S8M-P3.1	0.80	1.04	0.70	0.90
	D10-S8M-P4.3	0.67	0.90	0.64	0.86
	D10-SD4-P1.6	0.77	0.97	0.74	0.93
	D10-SD4-P2.1	0.74	1.00	0.64	0.86
	D10-H8M-P2.1	1.03	1.10	1.03	1.10
	D8-SD5-P2.5	0.76	0.95	0.74	0.93
	D8-SD5-P2.5	0.77	0.89	0.84	0.99
	D8-SD5-P3.4	0.70	0.88	0.73	0.92
	D8-SD5-P1.7	0.97	1.06	0.99	1.08
	D8-SD5-P1.7	0.99	1.01	1.06	1.12
	D8-SD5-P1.7	0.94	1.04	0.94	1.05
	D8-S3/16-P1.7	0.82	0.94	0.87	1.01
	D8-HD5-P2.5	0.78	1.06	0.63	0.86

Table 56. Low confinement, high strength concrete (LH).

Researcher	Column Label	Experimental		Proposed Model	
		ξ / f'_c	ρ / f'_c	ξ / f'_c	ρ / f'_c
Sheikh & Uzumeri	4A3-7	0.74	0.81	0.96	1.12
	4A4-8	0.77	0.88	0.91	1.09
	4A5-9	0.72	0.77	0.98	1.14
	4A6-10	0.79	0.80	1.08	1.21
	4C3-11	0.72	0.82	0.91	1.09
	4C4-12	0.83	0.93	0.98	1.14
Montgomery	H-D25-S11.3-P41	0.99	1.00	1.20	1.29
	H-D25-S11.3-P53	0.82	0.97	0.90	1.08
	H-D25-S11.3-P79	0.83	0.96	0.92	1.10
	H-D25-S11.3-P109	0.70	0.83	0.84	1.03
	H-D25-S8-P41	0.76	0.89	0.89	1.07
	H-D25-S8-P53	0.75	0.86	0.91	1.09
	H-D25-S8-P79	0.67	0.89	0.67	0.89
	H-D25-S5.7-P41	0.74	0.98	0.70	0.92
	H-D20-S11.3-P64	0.87	0.91	1.09	1.21
	H-D20-S9.5-P43	0.86	0.88	1.10	1.22
	H-D20-S9.5-P64	0.74	0.83	0.94	1.11
	H-D20-S9.5-P86	0.69	0.82	0.85	1.04
	H-D20-S6.4-P43	0.62	0.84	0.64	0.87
	VH-D20-S11.3-P43	0.85	0.83	1.15	1.26
	VH-D20-S8-P43	0.63	0.82	0.70	0.93
Pessiki et al.	24-A	0.85	1.12	0.73	0.95
	24-B	0.82	1.08	0.73	0.95
	24-C	0.82	1.03	0.80	1.00
	24-D	0.76	0.96	0.77	0.98
	14-A	1.20	1.52	0.88	1.07
	14-B	1.14	1.45	0.85	1.04
	14-C	1.20	1.36	1.10	1.22
	14-D	1.18	1.34	1.10	1.22
	14-A'	1.27	1.58	0.99	1.19
	14-C'	1.38	1.51	1.34	1.45
	14-F'	1.22	1.38	1.21	1.36
Razvi & Saatcliouglu (Circular)	CC-1	0.71	0.94	0.69	0.92
	CC-2	0.77	0.95	0.80	1.00
	CC-3	0.83	1.05	0.80	1.00
	CC-4	0.82	1.04	0.80	1.00
	CC-8	0.70	0.93	0.69	0.91
	CC-9	0.77	1.02	0.69	0.91
	CC-10	0.81	1.00	0.82	1.02
	CC-11	0.72	0.94	0.71	0.93
	CC-12	0.76	0.95	0.79	1.00
	CC-14	0.84	1.01	0.87	1.06
	CC-15	0.87	1.03	0.90	1.07
	CC-16	0.75	0.96	0.75	0.96
	CC-19	0.75	0.95	0.78	0.98
	CC-20	0.68	0.90	0.68	0.91
	CC-21	0.73	0.95	0.72	0.94
	CC-22	0.70	0.90	0.73	0.94

Table 56. Cont'd

Researcher	Column Label	Experimental		Proposed Model	
		ξ / f'_c	ρ / f'_c	ξ / f'_c	ρ / f'_c
Razvi & Saatcliouglu (Square)	CS-1	0.73	0.88	0.84	1.03
	CS-2	0.73	0.89	0.82	1.02
	CS-3	0.77	0.95	0.82	1.02
	CS-4	0.77	0.89	0.91	1.08
	CS-5	0.72	0.91	0.77	0.98
	CS-6	0.66	0.88	0.67	0.89
	CS-7	0.65	0.88	0.66	0.89
	CS-8	0.72	0.86	0.83	1.03
	CS-9	0.80	0.99	0.82	1.02
	CS-11	0.94	1.00	1.09	1.21
	CS-12	0.80	0.89	0.96	1.12
	CS-13	0.73	0.83	0.90	1.08
	CS-14	0.79	0.92	0.90	1.08
	CS-15	0.95	1.03	1.08	1.21
	CS-16	0.93	1.04	1.01	1.16
	CS-17	0.67	0.87	0.71	0.93
	CS-18	0.69	0.87	0.75	0.96
	CS-19	0.86	1.02	0.91	1.09
	CS-20	0.91	1.02	1.01	1.16
	CS-22	0.90	1.00	1.01	1.16
	CS-23	0.93	1.06	0.98	1.14
	CS-24	0.97	1.06	1.07	1.20
	CS-25	0.93	1.02	1.04	1.18
	CS-26	1.01	1.13	1.05	1.18
Nagashima et al. (1992)	HH08LA	0.78	0.97	0.81	1.01
	HH10LA	0.78	0.97	0.80	1.00
	HH13LA	0.83	1.05	0.79	0.99
	HH15LA	0.80	1.01	0.79	0.99
	HH20LA	0.90	1.17	0.77	0.98
	HL06LA	0.74	0.92	0.80	1.00
	HL08LA	0.82	1.04	0.79	0.99
	LL05LA	0.90	1.01	1.01	1.16
	LL08LA	1.01	1.18	0.97	1.13
	LH08LA	0.92	1.04	1.01	1.16
	LH13LA	1.07	1.29	0.96	1.12
	HH13MA	0.81	1.03	0.78	0.99
	HH13HA	0.80	1.01	0.78	0.99
	LL08MA	1.01	1.19	0.97	1.13
	LL08HA	0.99	1.16	0.97	1.13
	LH15LA	1.08	1.31	0.94	1.11
	HH13LB	0.81	1.03	0.78	0.98
	HH13LD	0.79	1.00	0.78	0.99
	LL08LB	1.01	1.21	0.94	1.11
	LL08LD	0.96	1.13	0.94	1.11
	HH13MSA	0.80	1.01	0.78	0.99
	HH13HSA	0.83	1.06	0.78	0.99
	LL08MSA	0.98	1.15	0.96	1.12
	LL08HSA	1.00	1.18	0.96	1.12

Table 56. Cont'd

Researcher	Column Label	Experimental ξ / f'_c	Experimental ρ / f'_c	Proposed Model ξ / f'_c	Proposed Model ρ / f'_c
Nagashima et al. (1993)	1	1.09	1.15	1.17	1.27
	2	1.04	1.08	1.17	1.27
	3	1.09	1.15	1.17	1.27
	4	0.89	0.99	1.01	1.16
	5	0.84	0.99	0.91	1.09
	6	0.78	0.91	0.91	1.09
	7	0.84	0.99	0.91	1.09
	8	0.83	1.00	0.87	1.06
	9	0.90	1.07	0.93	1.10
	10	0.90	1.06	0.93	1.10
	11	0.77	0.94	0.83	1.02
	12	0.74	0.94	0.77	0.98
	13	0.74	0.94	0.80	1.02
	14	0.74	0.94	0.75	0.96
Li	3A	0.97	1.13	0.97	1.13
	6A	0.78	0.97	0.81	1.01
	9A	0.73	0.94	0.75	0.96
	12A	0.68	0.89	0.71	0.93
	3B	0.97	1.16	0.92	1.09
	6B	0.80	1.01	0.78	0.99
	9B	0.72	0.93	0.73	0.94
	12B	0.62	0.81	0.69	0.92
	4HB1	1.16	1.24	1.19	1.28
	6HB	0.89	0.99	1.01	1.16
	2HC1	1.24	1.30	1.26	1.32
	4HC	0.86	0.98	0.96	1.12
	6HC	0.72	0.86	0.84	1.04

Table 57. High confinement, high strength concrete (HH).

Researcher	Column Label	Experimental $\xi / f'c$	Experimental $\rho / f'c$	Proposed Model $\xi / f'c$	Proposed Model $\rho / f'c$
Pessiki et al.	14-D'	1.49	1.59	1.30	1.32
	14-E'	1.28	1.31	1.28	1.31
Li	2HB	1.76	1.72	1.60	1.49

Parameter *a* not calculated for HH columns.

C.2 Concrete Cylinders

The experimental results in the normalized Haigh-Westergaard coordinate system for the concrete cylinders described in Appendix B are given in Tables 55 to 58.

Table 58. Low confinement, normal strength concrete (LN).

Researcher	fcl [MPa]	Experimental ξ / f'c	Experimental ρ / f'c	Proposed Model ξ / f'c	Proposed Model ρ / f'c
Hurlbut	0.69	0.71	0.93	0.72	0.95
	3.44	1.04	1.09	1.21	1.33
Richart	1.24	0.85	1.03	0.89	1.08
	3.79	1.24	1.39	1.19	1.32
Imran &	1.05	0.72	0.93	0.70	0.90
Pantazopoulou	2.1	0.82	0.98	0.81	0.97
	4.2	1.14	1.25	1.03	1.09

Table 59. High confinement, normal strength concrete (HN).

Researcher	fcl [MPa]	Experimental ξ / f'c	Experimental ρ / f'c	Proposed Model ξ / f'c	Proposed Model ρ / f'c
Hurlbut	6.89	1.69	1.63	1.85	1.85
	13.79	2.76	2.37	2.84	2.49
Gardner	8.62	1.88	1.89	1.85	1.85
	17.24	3.19	2.98	2.84	2.48
	25.86	4.11	3.52	3.73	2.99
Richart	3.79	1.42	1.49	1.50	1.60
et al.	5.38	1.79	1.79	1.82	1.83
	7.52	2.18	2.05	2.22	2.10
	10.41	2.68	2.35	2.72	2.41
	13.86	3.32	2.79	3.29	2.74
	20.76	4.55	3.57	4.36	3.31
	28.21	5.80	4.31	5.46	3.83
	7.52	1.70	1.68	1.80	1.81
	13.86	2.55	2.26	2.61	2.34
	28.21	4.31	3.36	4.23	3.24
	3.79	**2.82**	2.70	2.53	2.30
	7.52	**4.64**	4.02	4.01	3.13
	13.86	**7.81**	6.35	6.27	4.18
	28.21	**14.09**	10.38	10.93	5.91
Imran &	8.4	1.65	1.62	1.92	2.00
Pantazopoulou	14.7	2.45	2.21	2.70	2.56
	21	3.16	2.67	2.95	2.38

Note: Highlighted values not considered in calculation of parameter *a*. (f'_c < 10 MPa).

Table 60. Low confinement, high strength concrete (LH).

Researcher	f_{cl} [MPa]	Experimental ξ / f'_c	Experimental ρ / f'_c	Proposed Model ξ / f'_c	Proposed Model ρ / f'_c
Li & Ansari	7.38	1.18	1.24	1.15	1.20
	12.77	1.26	1.33	1.24	1.30
	20.06	1.26	1.31	1.30	1.35
Attard & Setunge	0.50	0.61	0.85	0.60	0.84
	1.00	0.63	0.86	0.62	0.86
	5.00	0.84	1.09	0.79	1.02
	10.00	1.02	1.24	0.97	1.17
	15.00	1.20	1.39	1.14	1.30
	20.00	1.32	1.46	1.29	1.42
	5.00	0.86	1.11	0.79	1.02
	10.00	1.00	1.20	0.97	1.17
	15.00	1.16	1.33	1.14	1.30
	5.00	0.84	1.08	0.81	1.03
	10.00	1.02	1.22	1.00	1.20
	15.00	1.17	1.31	1.18	1.34
	5.00	0.86	1.10	0.81	1.03
	10.00	0.97	1.14	1.00	1.20
	15.00	1.13	1.26	1.18	1.34
	1.00	0.62	0.86	0.63	0.87
	5.00	0.76	0.95	0.83	1.05
	10.00	0.95	1.09	1.04	1.23
	15.00	1.13	1.22	1.23	1.38
	5.00	0.79	1.00	0.83	1.05
	10.00	1.00	1.17	1.04	1.23
	15.00	1.15	1.26	1.23	1.38
	5.00	0.83	1.08	0.77	1.00
	10.00	0.96	1.18	0.94	1.15
	15.00	1.10	1.28	1.09	1.27
	5.00	0.79	1.02	0.78	1.01
	10.00	0.94	1.14	0.96	1.16
	15.00	1.10	1.27	1.12	1.29
	5.00	0.80	1.03	0.79	1.02
	10.00	0.94	1.13	0.98	1.18
	15.00	1.13	1.29	1.15	1.31
	5.00	0.78	0.97	0.84	1.06
	10.00	1.00	1.17	1.06	1.24
	15.00	1.12	1.21	1.26	1.39
	1.00	0.66	0.90	0.67	0.90
	5.00	1.04	1.27	0.97	1.17
	10.00	1.37	1.52	1.29	1.42

Table 60. Cont'd

Researcher	fcl	Experimental		Proposed Model	
	[MPa]	ξ / f'c	ρ / f'c	ξ / f'c	ρ / f'c
Imran &	3.20	0.81	1.03	0.76	0.97
Pantazopoulou	6.4	0.96	1.14	0.92	1.09
	12.8	1.19	1.26	1.21	1.28
	2.15	0.75	0.96	0.74	0.94
	4.3	0.92	1.09	0.90	1.04
	8.6	1.23	1.29	1.17	1.22
Xie,Elwi &	2.29	0.82	1.06	0.77	1.00
McGregor	5.30	1.04	1.25	0.99	1.19
	8.31	1.19	1.35	1.19	1.34
	11.32	1.38	1.50	1.37	1.48
	0.84	0.58	0.78	0.65	0.89
	3.78	0.86	1.11	0.79	1.01
	8.30	1.08	1.30	1.00	1.20
	12.82	1.29	1.49	1.19	1.34
	17.33	1.43	1.57	1.37	1.48
	16.50	1.46	1.62	1.34	1.45
	6.07	0.89	1.14	0.83	1.05
	12.02	1.15	1.37	1.05	1.23
	17.97	1.27	1.43	1.24	1.38

Table 61. High confinement, high strength concrete (HH).

Researcher	f_{cl} [MPa]	Experimental ξ / f'_c	Experimental ρ / f'_c	Proposed Model ξ / f'_c	Proposed Model ρ / f'_c
Li & Ansari	16.6	1.58	1.39	1.67	1.51
	24.8	2.01	1.56	2.13	1.73
	33.1	2.35	1.63	2.56	1.93
	41.4	2.80	1.83	2.99	2.10
	27.6	1.58	1.34	1.82	1.68
	41.4	2.00	1.49	2.18	1.75
	55.2	2.39	1.60	2.80	2.17
	69.0	2.72	1.61	3.26	2.38
	41.4	1.67	1.40	1.98	1.85
	62.1	2.17	1.64	2.54	2.15
	82.8	2.55	1.69	3.06	2.42
Attard & Setunge	15.00	1.68	1.77	1.44	1.42
Imran & Pantazopoulou	25.6	1.73	1.59	1.77	1.64
	38.4	2.21	1.84	2.25	1.90
	51.2	2.70	2.11	2.71	2.12
	17.2	1.86	1.74	1.71	1.53
	30.1	2.70	2.26	2.42	1.86
	43	3.54	2.79	3.08	2.13
Xie,Elwi & McGregor	20.3	1.89	1.85	1.69	1.56
	29.3	2.42	2.22	2.10	1.78
	23.3	2.10	2.02	1.83	1.64
	14.3	1.59	1.66	1.40	1.40
	21.9	1.58	1.66	1.48	1.51
	26.3	1.80	1.85	1.63	1.60
	35.5	2.08	2.00	1.93	1.78
	44.4	2.39	2.21	2.20	1.94
	24.0	1.45	1.56	1.41	1.50
	30.0	1.56	1.59	1.58	1.62
	36.1	1.71	1.68	1.74	1.73
	48.0	2.00	1.84	2.05	1.92
	60.0	2.36	2.11	2.35	2.09

The values for *a* in each category of confinement level and concrete strength are given in Table 62.

Table 62. Values for parameter *a* from cylinder specimens.

LN	HN	LH	HH
2.73	2.41	12.04	15.06

Using $f_{ct} = 0.65 f_c^{0.33}$

C.3 Final values for Parameter *a*

The number of specimens utilized in the statistical fitting for parameter a for each category of confinement level and concrete strength is given in Table 63.

Table 63. Number of specimens per confinement category.

	LN	HN	LH	HH
Columns	42	----	123	----
Cylinders	7	18	59	31

In the case of high confinement, the available data came from tests of cylinders, as explained in Chapter 3, Section 3.3.3.1. Reinforced concrete columns subjected to passive confinement reach values of lateral pressure smaller than 20 % of f'_c. Low confinement of normal and high strength concrete (LN and LH categories) is best represented in this database by the column specimens, which greatly exceed in number those of cylinder specimens in the same categories. The final proposed values for the parameter a are given in Table 64 when the tensile strength of concrete is calculated using $f'_{ct} = 0.65 f'^{0.33}_c$. For low confinement, the values obtained from column tests best represent the confined behaviour, whereas for high confinement, which was not typical of column behaviour, the values obtained from triaxial tests best represent the material behaviour.

Table 64. Final proposed values for parameter *a*.

LN	HN	LH	HH
17.10	2.41	17.45	15.06

These values are used in the prediction of concrete strengths of the experimental database, and for comparisons with other available models. Further corroborations are made in Chapters 3 and 5.

In addition to Table 64, Table 65 shows the values for the parameter a when the tensile strength f'_{ct} is calculated using different formulations. The procedure described in this section was applied to obtain these values. No differences were found in the computation of the analytical strength values for the columns and cylinders in the database when using the various tensile strength formulations, as the procedure utilized to estimate a reaches the best fit to the experimental results and the analytical values of invariant I_1 are similar to those obtained when using $f'_{ct} = 0.65f'^{0.33}_{c}$.

Table 65. Parameter a for various formulations of tensile strength f'_{ct}

f'_{ct}	LN	HN	LH	HH
$0.33f'^{0.5}_{c}$	18.72	2.94	10.62	13.91
$0.60f'^{0.5}_{c}$	8.07	1.10	4.63	6.67
$0.10f'_{c}$	8.14	1.59	1.98	3.57

The biaxial strength f_{cb} was calculated using $f_{cb} = 1.16f'_{c}$

C.4 Analytical to Experimental Strength for Columns with Proposed Model

Figures 159 to 167 show the ratio of analytical to experimental strength ratio versus the average lateral pressure f_{cl}, obtained using the proposed Ottosen-type model for each group of columns described in Chapter 3, Section 3.3.1. The concrete strength f'_c was used in the calculations.

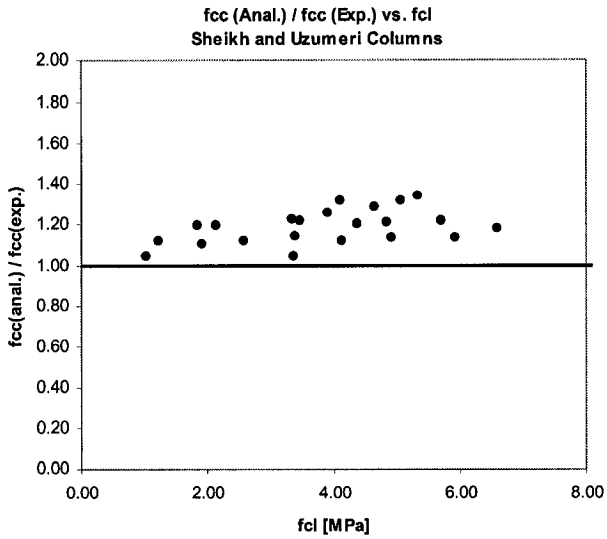

Figure 167. Analytical to experimental results, Sheikh and Uzumeri columns, proposed model.

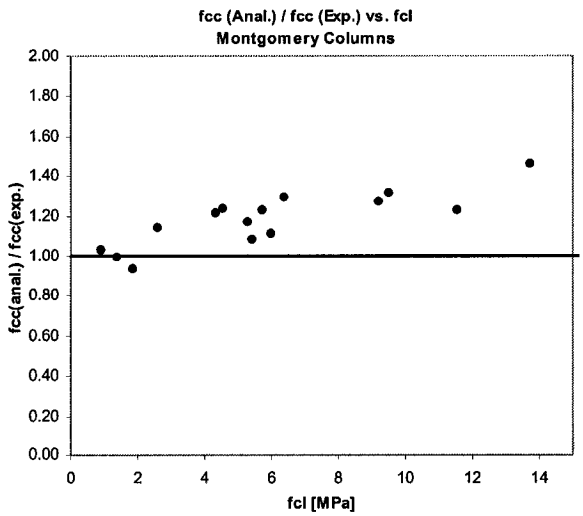

Figure 168. Analytical to experimental results, Montgomery and Sheikh columns, proposed model.

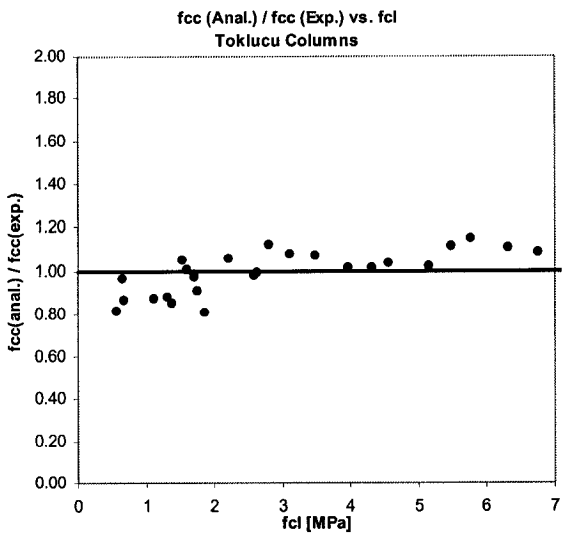

Figure 169. Analytical to experimental results, Sheikh and Toklucu columns, proposed model.

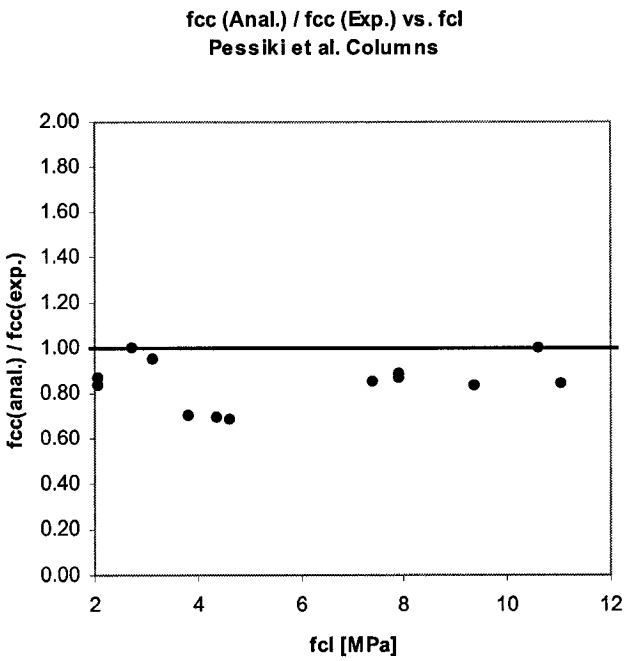

Figure 170. Analytical to experimental results, Pessiki et al. columns, proposed model.

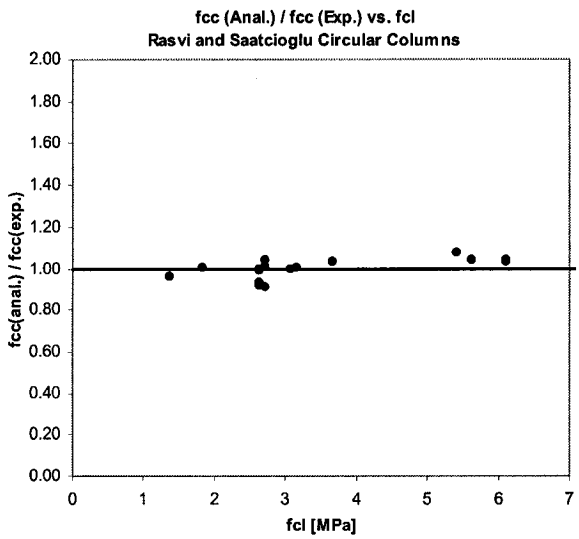

Figure 171. Analytical to experimental results, Razvi and Saatcioglu circular columns, proposed model.

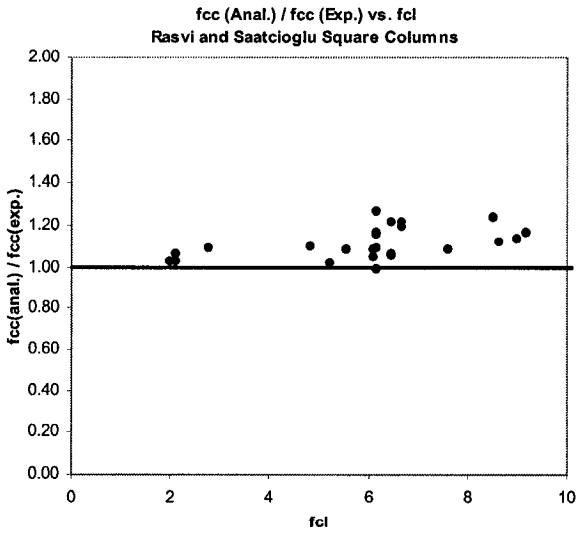

Figure 172. Analytical to experimental results, Razvi and Saatcioglu square columns, proposed model.

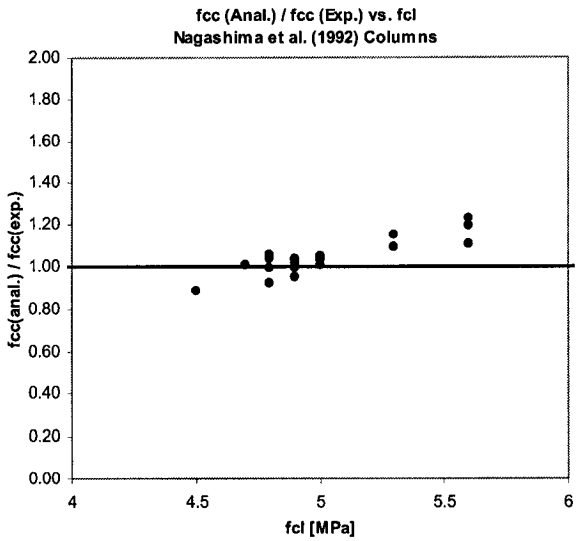

Figure 173. Analytical to experimental results, Nagashima et al. (1992) columns, proposed model.

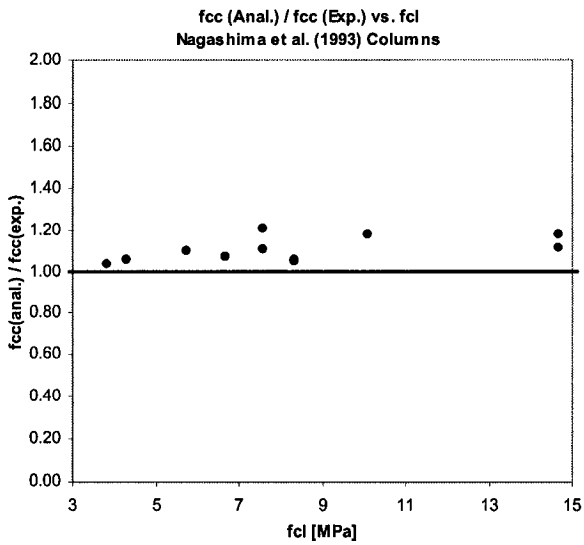

Figure 174. Analytical to experimental results, Nagashima et al. (1993) columns, proposed model.

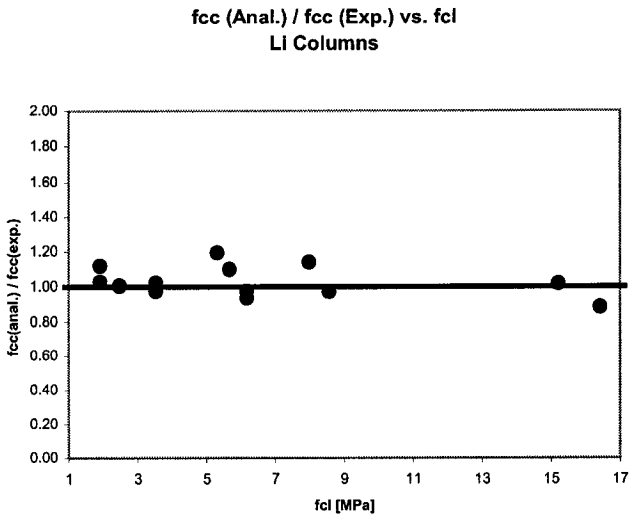

Figure 175. Analytical to experimental results, Li columns, proposed model.

C.5 Analytical to Experimental Strength for Cylinders with Proposed Model

Figures 168 to 174 describe the ratio of analytical to experimental strength versus the average lateral pressure f_{cl} obtained using the new proposed Ottosen-type model, for each group of cylinders described in Chapter 3, Section 3.3.2.

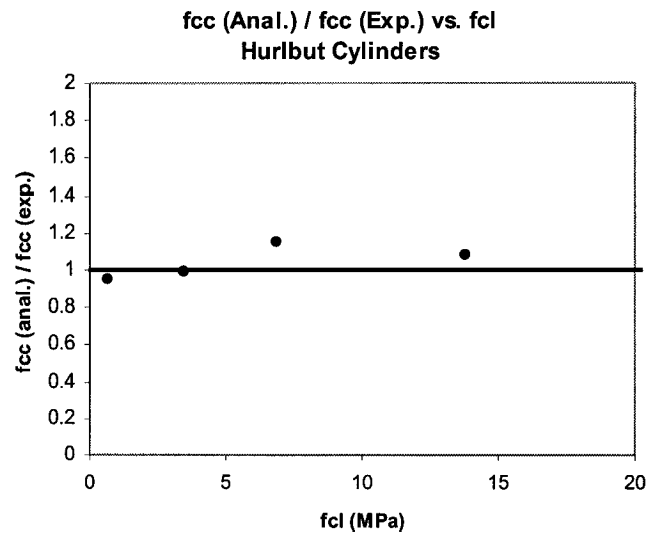

Figure 176. Analytical to experimental results, Hurlbut cylinders, proposed model.

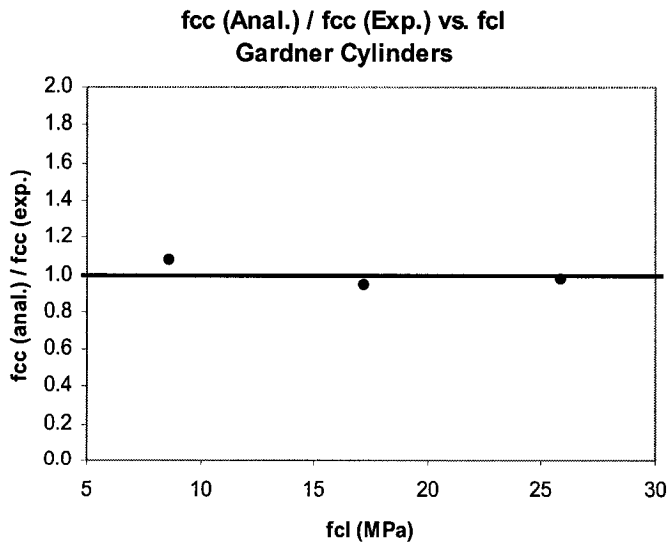

Figure 177. Analytical to experimental results, Gardner cylinders, proposed model.

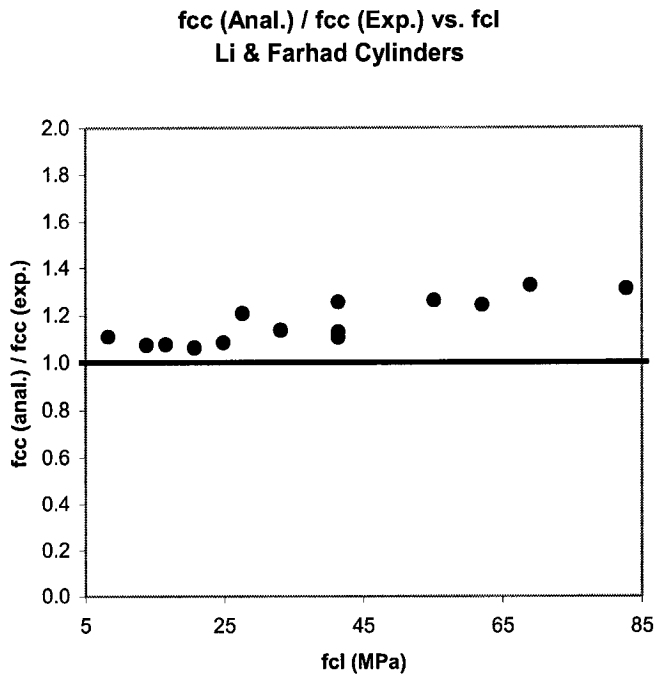

Figure 178. Analytical to experimental results, Li and Ansari cylinders, proposed model.

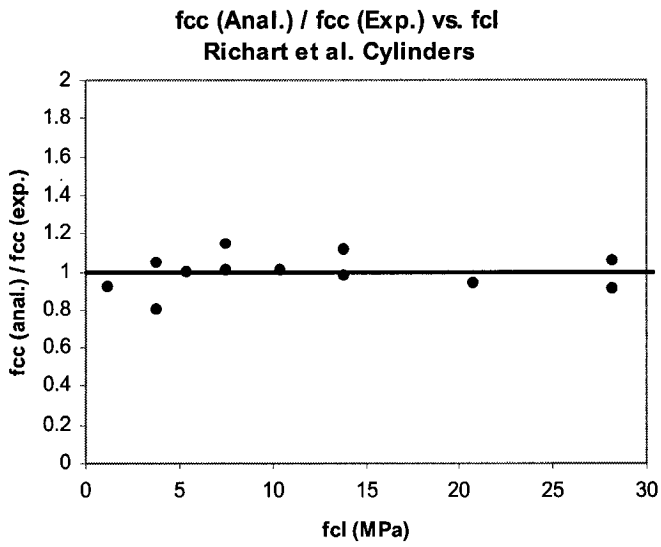

Figure 179. Analytical to experimental results, Richart et al. cylinders, proposed model.

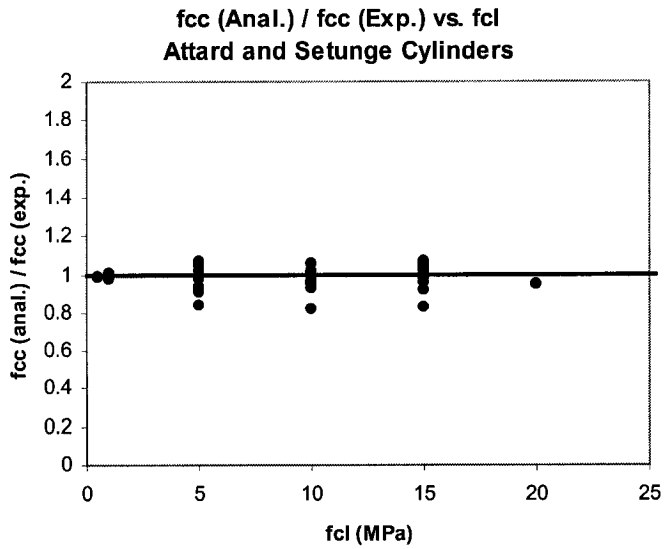

Figure 180. Analytical to experimental results, Attard and Setunge cylinders, proposed model.

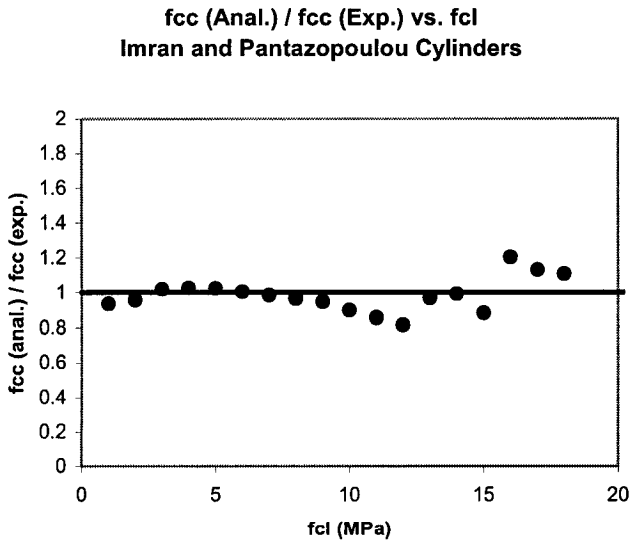

Figure 181. Analytical to experimental results, Imran and Pantazopoulou cylinders, proposed model.

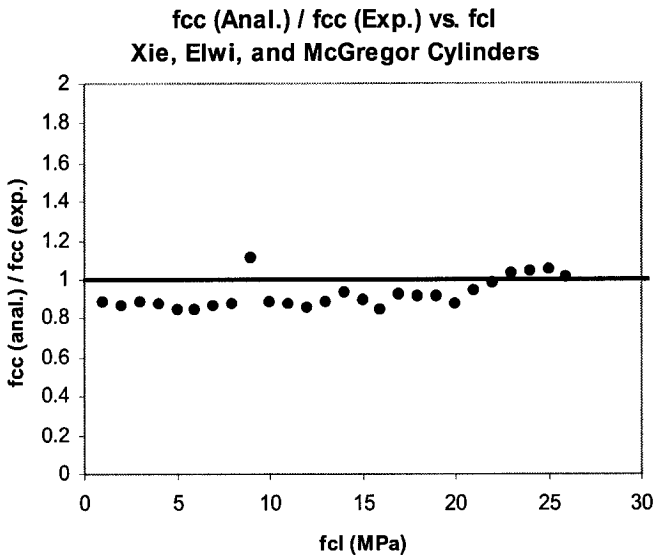

Figure 182. Analytical to experimental results Xie, Elwi and McGregor cylinders, proposed model.

Appendix D: Determination of Strain at Peak Stress, ε_{cc}.

D.1 Experimental Data

The triaxial tests used in the formulation for calculating the strain at peak stress, ε_{cc}, is given in the following Tables, where ε_{co} is the strain at peak stress f'_c in unconfined concrete.

Table 66. Li and Ansari tests.

Concrete		ε_{co}	ε_{cc}	$\frac{\varepsilon_{cc}}{\varepsilon_{co}}$	ε_{cc}
f'c	fcl/f'c		(exp.)		(anal.).
[MPa]	[%]	$[10^{-3}]$	$[10^{-3}]$		$[10^{-3}]$
47.8	17.36	2.0	13.5	6.7	8.6
47.8	34.73	2.0	15.7	7.8	15.2
47.8	51.88	2.0	20.5	10.2	21.8
47.8	69.46	2.0	24.2	12.0	28.4
47.8	107.53	2.0	29.5	14.6	35.1
75.7	18.23	2.0	8.0	3.9	7.8
75.7	36.46	2.0	12.6	6.2	13.6
75.7	54.69	2.0	20.4	10.1	19.4
75.7	72.92	2.0	30.2	14.9	25.1
75.7	91.15	2.0	38.7	19.1	30.9
106.0	19.53	1.9	8.9	4.6	6.5
106.0	39.06	1.9	10.6	5.5	11.1
106.0	58.58	1.9	19.3	10.0	15.7
106.0	78.11	1.9	21.0	10.8	20.3

Table 67. Imran and Pantazopoulou tests.

Concrete		ε_{co}	ε_{cc}	$\frac{\varepsilon_{cc}}{\varepsilon_{co}}$	ε_{cc}
f'c	fcl/f'c		(exp.)		(anal.).
[MPa]	[%]	$[10^{-3}]$	$[10^{-3}]$		$[10^{-3}]$
73.4	4.4	3.25	4.95	1.5	5.5
73.4	8.7	3.25	6.50	2.0	7.8
73.4	17.4	3.25	10.45	3.2	12.3
73.4	34.9	3.25	20.25	6.2	21.3
73.4	52.3	3.25	31.05	9.6	30.3
73.4	69.8	3.25	40.90	12.6	39.4
47.4	4.5	2.80	4.30	1.5	5.2
47.4	9.1	2.80	6.90	2.5	7.6
47.4	18.1	2.80	14.60	5.2	12.4
47.4	36.3	2.80	25.30	9.0	22.0
47.4	63.5	2.80	36.00	12.9	36.5
47.4	90.7	2.80	47.30	16.9	50.9
28.6	3.7	2.60	4.70	1.8	4.6
28.6	7.3	2.60	6.75	2.6	6.6
28.6	14.7	2.60	13.85	5.3	10.7
28.6	29.4	2.60	23.75	9.1	18.7
28.6	51.4	2.60	34.25	13.2	30.8
28.6	73.4	2.60	44.60	17.2	42.9

Table 68. Attard and Setunge tests.

Concrete f'c [MPa]	Concrete fcl/f'c [%]	ε_{co} [10^{-3}]	ε_{cc} (exp.) [10^{-3}]	ε_{cc} / ε_{co}	ε_{cc} (anal.) [10^{-3}]
120.0	0.4	3.0	2.6	0.9	3.1
120.0	0.8	3.0	2.9	1.0	3.3
120.0	4.2	3.0	3.8	1.3	4.3
120.0	8.3	3.0	5.3	1.8	5.6
120.0	12.5	3.0	6.0	2.0	6.9
120.0	16.7	3.0	8.0	2.7	8.3
120.0	4.2	2.8	4.2	1.5	4.0
120.0	8.3	2.8	4.8	1.7	5.3
120.0	12.5	2.8	5.7	2.0	6.5
110.0	4.5	2.8	3.5	1.3	4.3
110.0	9.1	2.8	4.4	1.6	5.8
110.0	13.6	2.8	6.0	2.1	7.3
110.0	4.5	2.8	4.1	1.5	4.3
110.0	9.1	2.8	5.5	2.0	5.8
110.0	13.6	2.8	5.9	2.1	7.3
100.0	1.0	2.7	3.1	1.1	3.0
100.0	5.0	2.7	3.6	1.3	4.4
100.0	10.0	2.7	4.7	1.7	6.2
100.0	15.0	2.7	5.8	2.1	7.9
100.0	5.0	2.6	3.9	1.5	4.3
100.0	10.0	2.6	5.2	2.0	5.9
100.0	15.0	2.6	7.5	2.9	7.6
132.0	3.8	3.4	5.0	1.5	4.6
132.0	7.6	3.4	5.8	1.7	5.8
132.0	11.4	3.4	7.8	2.3	6.9
126.0	4.0	3.4	5.0	1.5	4.7
126.0	7.9	3.4	7.1	2.1	6.1
126.0	11.9	3.4	8.9	2.6	7.4
118.0	4.2	2.8	3.8	1.4	4.1
118.0	8.5	2.8	4.9	1.8	5.4
118.0	12.7	2.8	6.2	2.2	6.6
96.0	5.2	2.8	3.7	1.3	4.7
96.0	10.4	2.8	5.2	1.9	6.7
96.0	15.6	2.8	5.3	1.9	8.6
60.0	1.7	2.1	2.7	1.3	2.7
60.0	8.3	2.1	4.8	2.3	5.2
60.0	16.7	2.1	7.6	3.6	8.2
60.0	25.0	2.1	9.9	4.7	11.3

D.2 Normalized Strain at Peak Stress versus Confinement Level

The strain at peak stress, ε_{cc}, was normalized with respect to the strain at unconfined peak strength, ε_{co}, and plotted against the confinement level f_{cl} / f'_c. Each set of tests (per researcher) was divided into groups according to concrete strength f'_c. The trend lines for each group are also plotted in the figures.

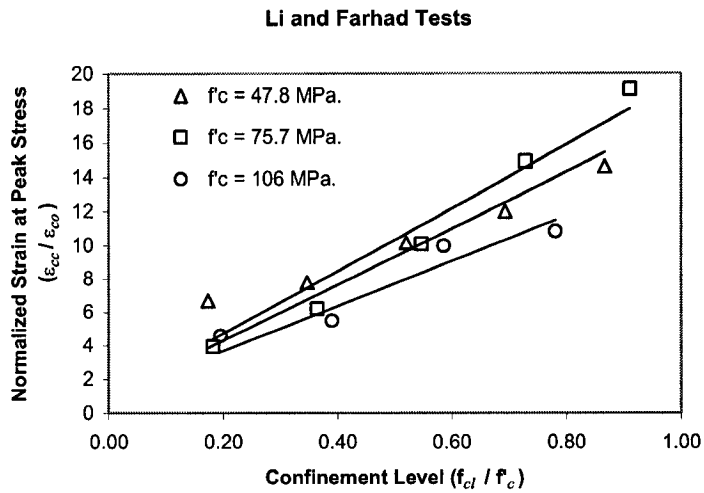

Figure 183. Normalized strain at peak stress versus confinement level, Li and Ansari tests.

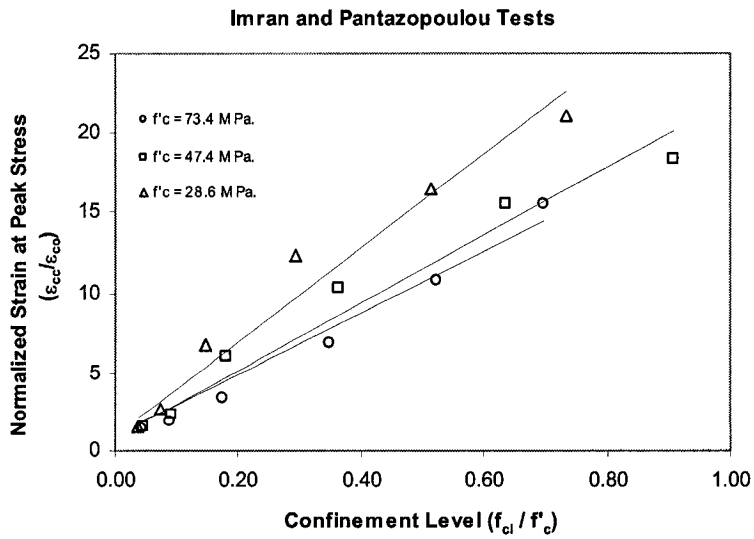

Figure 184. Normalized strain at peak stress versus confinement Level, Imran and Pantazopoulou tests.

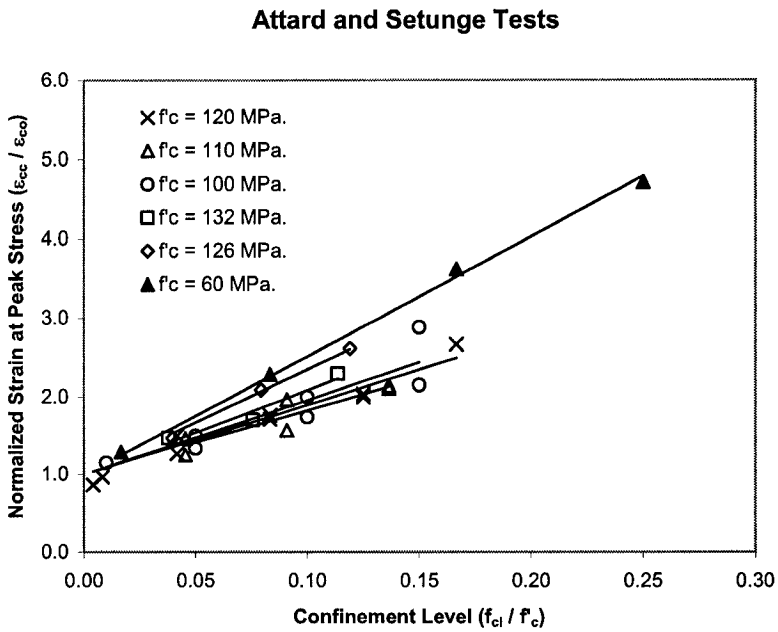

Figure 185. Normalized strain at peak stress versus confinement level, Attard and Setunge tests.

Appendix E: Determination of Strain at 80% of Peak Stress, ε_{c80}.

E.1 Experimental Data

The triaxial tests used in calculating the strain at 80 % of the peak stress, ε_{c80}, are given in the following Tables, where ε_{co} is the strain at peak unconfined stress f'_c.

Table 69. Li and Ansari tests.

Concrete		ε_{co}	ε_{c80} (exp.)	$\frac{\varepsilon_{c80}}{\varepsilon_{co}}$	ε_{c80} (anal.).
f'_c [MPa]	f_{cl}/f'_c [%]	[10^{-3}]	[10^{-3}]		[10^{-3}]
47.8	0.0	2.02	4.1	2.0	3.0
47.8	17.3	2.02	22.4	11.1	24.3
47.8	34.7	2.02	39.6	19.6	45.6
47.8	52.0	2.02	48.5	24.0	66.9
47.8	69.3	2.02	75.3	37.3	88.2
47.8	86.7	2.02	78.2	38.7	109.5
75.7	0.0	2.03	2.4	1.2	3.0
75.7	18.2	2.03	19.3	9.5	19.3
75.7	36.4	2.03	25.9	12.8	35.7
75.7	54.7	2.03	74.7	36.8	52.0
75.7	72.9	2.03	103.0	50.7	68.3
106	0.0	1.94	2.2	1.1	2.9
106	19.5	1.94	15.2	7.8	12.7
106	39.0	1.94	21.9	11.3	22.5
106	58.6	1.94	41.9	21.6	32.3
106	78.1	1.94	48.4	24.9	42.1

Table 70. Attard and Setunge tests.

Concrete		ε_{co}	ε_{c80} (exp.)	$\frac{\varepsilon_{c80}}{\varepsilon_{co}}$	ε_{c80} (anal.).
f'_c [MPa]	f_{cl}/f'_c [%]	[10^{-3}]	[10^{-3}]		[10^{-3}]
110	5.0	2.9	5.2	1.8	7.8
110	9.0	2.9	7.2	2.5	10.5
110	14.0	2.9	9.8	3.4	13.9
120	4.0	3.2	5.5	1.7	7.0
120	8.0	3.2	6.5	2.0	9.3
120	13.0	3.2	8.8	2.8	12.1
132	4.0	4	7.2	1.8	7.6
132	8.0	4	9.6	2.4	9.3
132	11.0	4	11.2	2.8	10.5

Table 71. Candappa et al. tests.

Concrete		ε_{co}	ε_{c80} (exp.)	$\frac{\varepsilon_{c80}}{\varepsilon_{co}}$	ε_{c80} (anal.).
f'_c [MPa]	f_{cl}/f'_c [%]	[10^{-3}]	[10^{-3}]		[10^{-3}]
40	0	2.56	3.7	1.4	3.8
40	10	2.56	22.9	9.0	20.6
40	20	2.56	34.4	13.5	37.4
40	30	2.56	64.8	25.4	54.1
60	0	2.37	3.4	1.4	3.6
60	7	2.37	8.0	3.4	12.4
60	13	2.37	21.6	9.1	20.0
75	0	2.44	3.5	1.4	3.7
75	5	2.44	7.5	3.1	9.1
75	10	2.44	12.8	5.2	14.5
75	16	2.44	17.6	7.2	21.0
100	0	2.8	4.1	1.5	4.2
100	4	2.8	8.5	3.0	7.5
100	8	2.8	9.6	3.4	10.8
100	12	2.8	11.3	4.0	14.1

Table 72. Xie et al. tests.

Concrete		ε_{co}	ε_{c80} (exp.)	$\frac{\varepsilon_{c80}}{\varepsilon_{co}}$	ε_{c80} (anal.).
f'_c [MPa]	f_{cl}/f'_c [%]	[10^{-3}]	[10^{-3}]		[10^{-3}]
119	0.0	4.2	4.8	1.1	6.1
119	7.0	4.2	8.6	2.1	10.2
119	13.0	4.2	13.4	3.2	14.3
119	19.0	4.2	21.5	5.1	19.1
119	26.0	4.2	29.3	7.0	23.2
119	33.0	4.2	34.5	8.2	27.3
119	39.0	4.2	45.4	10.8	31.5
119	52.0	4.2	44.8	10.7	40.4
119	65.0	4.2	65.9	15.7	48.6
92.2	0.0	4.1	4.5	1.1	5.9
92.2	4.0	4.1	8.2	2.0	11.7
92.2	9.0	4.1	12.5	3.0	18.9
92.2	14.0	4.1	16.5	4.0	26.2
92.2	19.0	4.1	25.4	6.2	33.4
92.2	19.0	4.1	26.6	6.5	33.4
92.2	24.0	4.1	40.6	9.9	42.1
92.2	29.0	4.1	40.9	10.0	49.3
92.2	39.0	4.1	57.4	14.0	63.7
92.2	48.0	4.1	86.0	21.0	78.2

E.2 Normalized Strain at 80% of Peak Stress versus Confinement Level

The strain at 80% of peak stress, ε_{c80}, was normalized with respect to the strain at peak for unconfined concrete, ε_{co}, and plotted against the confinement level f_{cl} / f'_c. Each set of tests (per researcher) was divided into groups according to unconfined concrete strength f'_c. The trend lines for each group are also plotted in the figures.

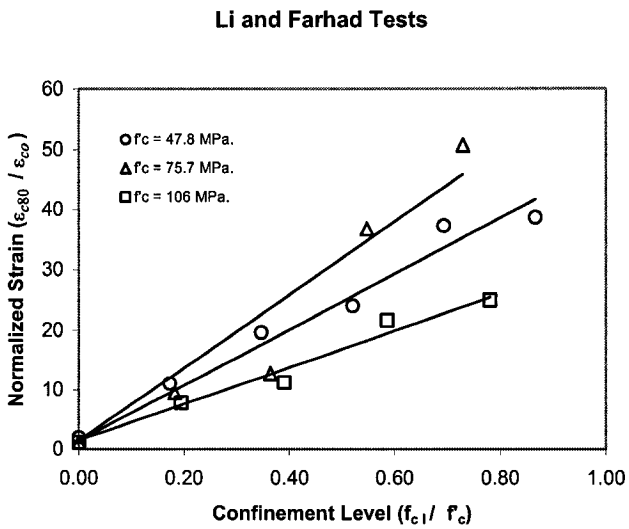

Figure 186. Normalized strain at 80% peak stress versus confinement level, Li and Ansari tests.

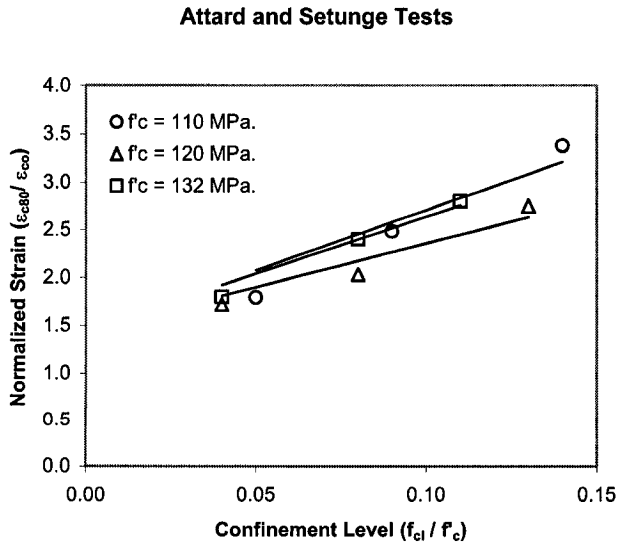

Figure 187. Normalized strain at 80% peak stress versus confinement level, Attard and Setunge tests.

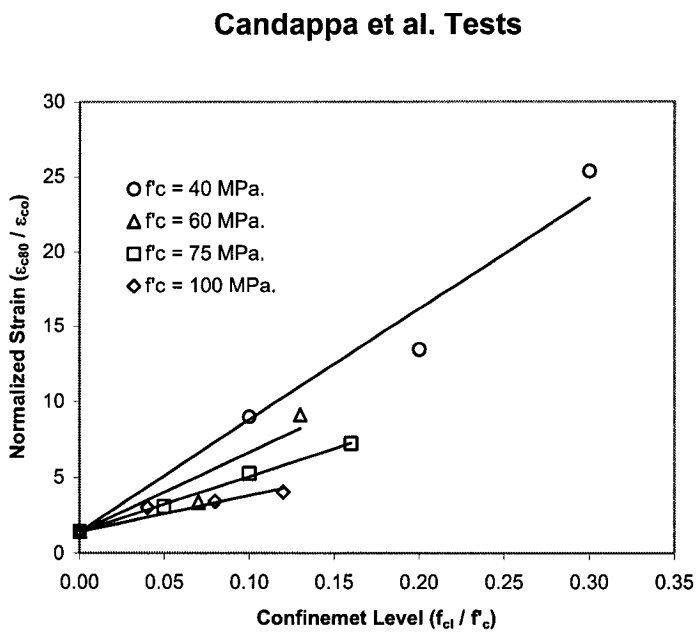

Figure 188. Normalized strain at 80% peak stress versus confinement level, Candappa et al. tests.

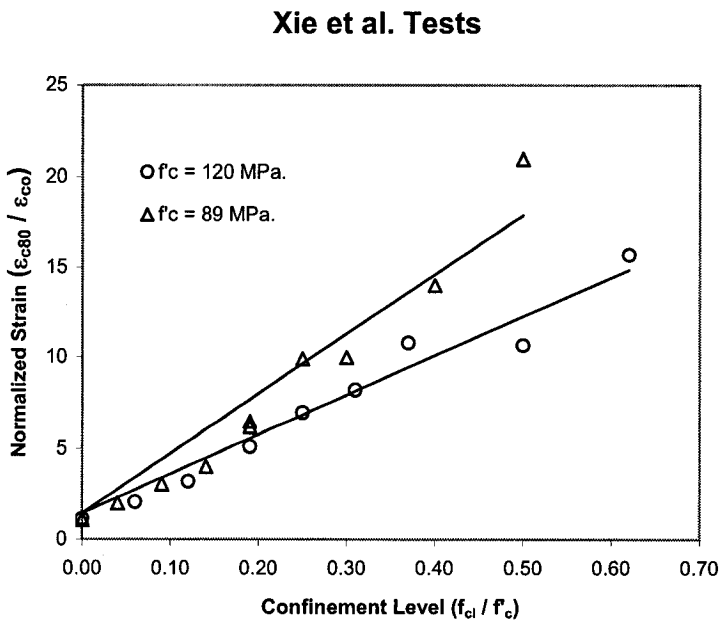

Figure 189. Normalized strain at 80% peak stress versus confinement level, Candappa et al. tests.

Appendix F: Stiffness Matrices for Torus Elements

F.1 Four-node Torus Element

The following are the stiffness matrix coefficients for the four-node torus described in Chapter 4, Section 4.3. The stiffness matrix is 8 x 8.

$$k(1,1) = a^2 \frac{D_{rr}}{3} - \frac{a^2 d}{r}\frac{D_{r\theta}}{3} + \left(\frac{ad}{r}\right)^2 \frac{D_{\theta\theta}}{9} + d^2 \frac{G_{rz}}{3}$$

$$k(1,2) = ad\frac{(D_{rz} + G_{rz})}{4} - \frac{ad^2}{r}\frac{D_{z\theta}}{6}$$

$$k(1,3) = d^2 \frac{G_{rz}}{6} - a^2 \frac{D_{rr}}{3} + \left(\frac{ad}{r}\right)^2 \frac{D_{\theta\theta}}{18}$$

$$k(1,4) = ad\frac{(D_{rz} - G_{rz})}{4} - \frac{ad^2}{r}\frac{D_{z\theta}}{12}$$

$$k(1,5) = -a^2 \frac{D_{rr}}{6} + \left(\frac{ad}{r}\right)^2 \frac{D_{\theta\theta}}{36} - d^2 \frac{G_{rz}}{6}$$

$$k(1,6) = -ad\frac{(D_{rz} + G_{rz})}{4} - \frac{ad^2}{r}\frac{D_{r\theta}}{12}$$

$$k(1,7) = a^2 \frac{D_{rr}}{6} - \frac{a^2 d}{r}\frac{D_{r\theta}}{6} + \left(\frac{ad}{r}\right)^2 \frac{D_{\theta\theta}}{18} - d^2 \frac{G_{rz}}{3}$$

$$k(1,8) = ad\frac{(G_{rz} - D_{rz})}{4} + \frac{ad^2}{r}\frac{D_{z\theta}}{6}$$

$$k(2,2) = d^2 \frac{D_{zz}}{3} + a^2 \frac{G_{rz}}{3}$$

$$k(2,3) = ad\frac{(G_{rz} - D_{rz})}{4} - \frac{ad^2}{r}\frac{D_{z\theta}}{12}$$

$$k(2,4) = d^2 \frac{D_{zz}}{6} - a^2 \frac{G_{rz}}{3}$$

$$k(2,5) = -ad\frac{(G_{rz} + D_{rz})}{4} - \frac{ad^2}{r}\frac{D_{z\theta}}{12}$$

$$k(2,6) = -\frac{1}{2}k(2,2)$$

$$k(2,7) = -k(1,8)$$

$$k(2,8) = -d^2\frac{D_{zz}}{3} + a^2\frac{G_{rz}}{6}$$

$$k(3,3) = a^2\frac{D_{rr}}{3} + \frac{a^2 d}{r}\frac{D_{r\theta}}{3} + \left(\frac{ad}{r}\right)^2\frac{D_{\theta\theta}}{9} + d^2\frac{G_{rz}}{3}$$

$$k(3,4) = -ad\frac{\left(G_{rz} + D_{rz}\right)}{4} - \frac{ad^2}{r}\frac{D_{z\theta}}{6}$$

$$k(3,5) = a^2\frac{D_{rr}}{6} + \frac{a^2 d}{r}\frac{D_{r\theta}}{6} + \left(\frac{ad}{r}\right)^2\frac{D_{\theta\theta}}{18} - d^2\frac{G_{rz}}{3}$$

$$k(3,6) = ad\frac{\left(D_{rz} - G_{rz}\right)}{4} + \frac{ad^2}{r}\frac{D_{z\theta}}{6}$$

$$k(3,7) = -a^2\frac{D_{rr}}{6} + \left(\frac{ad}{r}\right)^2\frac{D_{\theta\theta}}{36} - d^2\frac{G_{rz}}{6}$$

$$k(3,8) = -k(2,5)$$

$$k(4,4) = k(2,2)$$

$$k(4,5) = -k(3,6)$$

$$k(4,6) = k(2,8)$$

$$k(4,7) = ad\frac{\left(G_{rz} + D_{rz}\right)}{4} - \frac{ad^2}{r}\frac{D_{z\theta}}{12}$$

$$k(4,8) = k(2,6)$$

$$k(5,5) = k(3,3)$$

$$k(5,6) = -k(3,4)$$

$$k(5,7) = k(1,3)$$

$$k(5,8) = -k(2,3)$$

$$k(6,6) = k(4,4)$$

$$k(6,7) = -k(1,4)$$

$$k(6,8) = k(2,4)$$

$$k(7,7) = k(1,1)$$

$$k(7,8) = -k(1,2)$$

$$k(8,8) = k(4,4)$$

The matrix is symmetric; all the coefficients above must be multiplied by the factor:

$$\frac{2\pi r}{ad}$$

where :

r: radius of the centroid of the section to the axis of revolution

a: is the height of the section, and

d: is the width of the section along the radial axis, as shown in Figure 190.

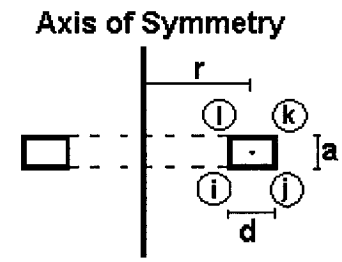

Figure 190. Four-node torus element, numbering.

F.2 Three-node Torus Element

The following are the stiffness matrix coefficients for the three-node torus described in Chapter 4, Section 4.3. The stiffness matrix is 6 x 6 (adapted from Zienkiewicz and Taylor 2002)

$$k(1,1) = B_i^2 D_{rr} + \frac{A_i B_i}{r} D_{r\theta} + B_i^2 D_{r\theta} + \frac{B_i G_i}{r}\tilde{z} + B_i C_i D_{r\theta} + C_i^2 D_{\theta\theta} + G_i^2 G_{rz}$$

$$k(1,2) = B_i G_i D_{rz} + \frac{A_i G_i}{r} D_{z\theta} + B_i G_i D_{z\theta} + \frac{G_i^2}{r} D_{z\theta}\tilde{z} + B_i G_i G_{rz}$$

$$k(1,3) = B_i B_j D_{rr} + \frac{A_i B_j}{r} D_{r\theta} + B_i B_j D_{r\theta} + \frac{B_j G_i}{r} D_{r\theta}\tilde{z} + B_i C_j D_{r\theta} + C_i C_j D_{\theta\theta} + G_i G_j G_{rz}$$

$$k(1,4) = B_i G_j D_{rz} + \frac{A_i G_j}{r} D_{z\theta} + B_i G_j D_{z\theta} + \frac{G_i G_j}{r} D_{z\theta}\tilde{z} + B_j G_i G_{rz}$$

$$k(1,5) = B_i B_k D_{rr} + \frac{A_i B_k}{r} D_{r\theta} + B_i B_k D_{r\theta} + \frac{B_k G_i}{r} D_{r\theta}\tilde{z} + B_i C_k D_{r\theta} + C_i C_k D_{\theta\theta} + G_i G_k G_{rz}$$

$$k(1,6) = B_i G_k D_{rz} + \frac{A_i G_k}{r} D_{z\theta} + B_i G_k D_{z\theta} + \frac{G_i G_k}{r} D_{z\theta}\tilde{z} + B_k G_i G_{rz}$$

$$k(2,2) = G_i^2 D_{zz} + B_i^2 G_{rz}$$

$$k(2,3) = B_j G_i D_{rz} + C_j G_i D_{z\theta} + B_i C_j G_{rz}$$

$$k(2,4) = G_i G_j D_{zz} + B_i B_j G_{rz}$$

$$k(2,5) = B_k G_i D_{rz} + C_k G_i D_{z\theta} + B_i G_k G_{rz}$$

$$k(2,6) = G_i G_k D_{zz} + B_i B_k G_{rz}$$

$$k(3,3) = B_j^2 D_{rr} + \frac{A_j B_j}{r} D_{r\theta} + B_j^2 D_{r\theta} + \frac{B_j G_j}{r} D_{r\theta}\tilde{z} + B_j C_j D_{r\theta} + C_j^2 D_{\theta\theta} + G_j^2 G_{rz}$$

$$k(3,4) = B_j G_j D_{rz} + \frac{A_j G_j}{r} D_{z\theta} + B_j G_j D_{z\theta} + \frac{G_j^2}{r} D_{z\theta}\tilde{z} + B_j G_j G_{rz}$$

$$k(3,5) = B_j B_k D_{rr} + \frac{A_j B_k}{r} D_{r\theta} + B_j B_k D_{r\theta} + \frac{B_k G_j}{r} D_{r\theta}\tilde{z} + B_j C_k D_{r\theta} + C_j C_k D_{\theta\theta} + G_j G_k G_{rz}$$

$$k(3,6) = B_j G_k D_{rz} + \frac{A_j G_k}{r} D_{z\theta} + B_j G_k D_{z\theta} + \frac{G_j G_k}{r} D_{z\theta}\tilde{z} + B_k G_j G_{rz}$$

$$k(4,4) = G_j{}^2 D_{zz} + B_j{}^2 G_{rz}$$

$$k(4,5) = B_k G_j D_{rz} + C_k G_j D_{z\theta} + B_j G_k G_{rz}$$

$$k(4,6) = G_j G_k D_{zz} + B_j B_k G_{rz}$$

$$k(5,5) = B_k{}^2 D_{rr} + \frac{A_k B_k}{r} D_{r\theta} + B_k{}^2 D_{r\theta} + \frac{B_k G_k}{r} D_{r\theta}\tilde{z} + B_k C_k D_{r\theta} + C_k{}^2 D_{\theta\theta} + G_k{}^2 G_{rz}$$

$$k(5,6) = B_k G_k D_{rz} + \frac{A_k G_k}{r} D_{z\theta} + B_k G_k D_{z\theta} + \frac{G_k{}^2}{r} D_{z\theta}\tilde{z} + B_k G_k G_{rz}$$

$$k(6,6) = G_k{}^2 D_{zz} + B_k{}^2 G_{rz}$$

where, according to Figure 191:

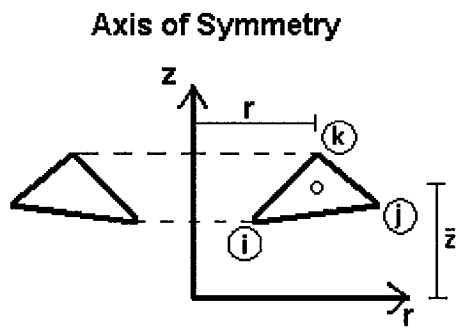

Figure 191. Three-node torus element, numbering.

The triangle *ijk* is in the plane rz. The coordinates of the centroid of the triangle are given by:

$$\tilde{z} = \frac{z_i + z_j + z_k}{3}$$

$$r = \frac{r_i + r_j + r_k}{3}$$

The coordinates of the nodes *i*, *j*, and *k* are given by:

Node *i* (r_1,z_1,θ), node *j* (r_2,z_2,θ), and node *k* (r_3,z_3,θ), and

$$A_i = r_2 z_3 - z_2 r_3$$

$$B_i = z_2 - z_3$$

$$G_i = r_3 - r_2$$

$$A_j = r_3 z_1 - z_3 r_1$$

$$B_j = z_3 - z_1$$

$$G_j = r_1 - r_3$$

$$A_k = r_1 z_2 - z_1 r_2$$

$$B_k = z_1 - z_2$$

$$G_k = r_2 - r_1$$

$$C_m = \frac{A_m}{r} + B_m + G_m \frac{\tilde{z}}{r}, \quad m = i, j, k$$

The matrix is symmetric; all the matrix coefficients must be multiplied by the factor:

$$\frac{\pi r}{2A}$$

where

$$A = \frac{z_1(r_2 - r_3) + z_2(r_3 - r_1) + z_3(r_1 - r_2)}{2}$$

is the cross sectional area of the 3-noded torus element.

F.3 Ring Bar

The following are the stiffness matrix coefficients for the ring bar described in Chapter 4, Section 4.3. The stiffness matrix is 2 x 2.

$$k(1,1) = 2\pi A_b \frac{D_{\theta\theta}}{r}$$

$$k(1,2) = k(2,1) = k(2,2) = 0$$

where A_b is the cross sectional area of the ring bar, and r is the radius of the ring bar with respect to the axis of revolution, as shown in Figure 192.

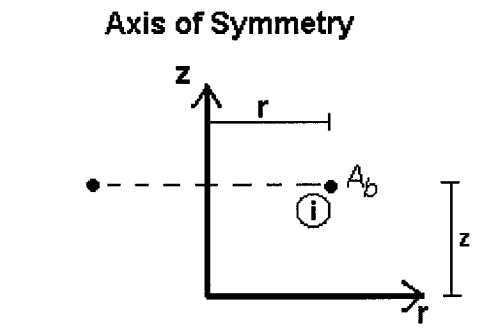

Figure 192. Ring bar, numbering.

Appendix G: Notation.

a, b, k_1, k_2: Ottosen surface parameters.

B: matrix that is derived from shape functions for a finite element.

D : diameter of a circular column section.

D : material stiffness matrix.

d_b : diameter of longitudinal steel in columns.

$\mathbf{D_c}$: material stiffness matrix for concrete

$\mathbf{D_s}$: material stiffness matrix for steel (or FRP fabric).

d_t : diameter of lateral steel in columns.

E_c : initial stiffness of the concrete compressive stress-strain curve.

E_{ci} : actual secant stiffness of concrete in the principal direction *i*.

E_j, : initial stiffness of stress-strain curve for FRP fabric.

E_s: initial stiffness of the stress-strain curve for steel.

E_{sec} : secant stiffness at peak stress of concrete.

E_{sh} : strain hardening stiffness of steel.

f'_c : unconfined concrete strength.

f'_{ct} : tensile strength of concrete.

f_{bc} : biaxial strength of concrete.

f_c : actual stress in concrete.

$f_{c1} \geq f_{c2} \geq f_{c3}$: principal concrete stresses.

f_{cc} : confined concrete strength.

f_{ci} : average lateral pressure in concrete normal to the principal direction *i*.

f_{ci} : stress in a finite concrete in the principal direction *i*.

f_{cl} / f'_c: ratio of lateral pressure to unconfined concrete strength f_{cl} / f'_c

f_{cl} : lateral pressure exerted in a concrete element.

$\mathbf{F_{co}}$: equivalent force vector.

f_{cr} : cracking stress of concrete.

f_{ju}. : rupture stress of FRP fabric.

f_p : peak stress (considering the effects of softening and confinement).

f_y : steel yield strength.

I_1 : stress invariant.

J_2 : stress invariant.

J_3 : stress invariant.

k : element stiffness matrix.

k_d : shape factor of the post-peak confined concrete curve.

k_σ: strength enhancement factor.

n : number of nodes of a finite element.

P_{cmax} : maximum concrete axial load in columns.

P_{max} : maximum axial load in columns.

r : radius from the axis of revolution to the centroid of the cross section of an axisymmetric element.

s : spacing of lateral steel in columns.

$\mathbf{T_c}$: transformation matrix for concrete.

$\mathbf{T_s}$: transformation matrix for steel (or FRP).

w/c: water/cement ratio.

α : regression parameter for concrete dilatation model.

β : softening factor for concrete in compression.

δ: displacement vector.

δ_{co} : equivalent displacement vector.

ε_c / ε_{cc}: axial strain ratio in concrete.

ε_c: axial strain in concrete.

ε_{c80} : compressive strain in concrete at 80% of peak stress.

ε_{cc}: strain at peak stress in concrete.

ε_{ci} : strain in a finite concrete solid in the principal direction *i*

ε_{cl} : lateral strain in concrete.

ε_{co} : unconfined peak compressive strain in concrete.

ε_{co}': concrete dilatation vector.

ε_{cr} : concrete cracking strain.

ε_{ju} : strain at rupture of FRP fabric.

ε_p : strain at peak stress (considering the effects of softening and confinement).

ε_{sh} : strain at the initiation of strain hardening in steel.

ε_u : strain of steel at rupture.

ε_y :strain in steel at yield.

ε : strain vector.

ν : secant Poisson's ratio.

ν_{ij} : Poisson effect or lateral expansion in the principal direction *i*, due to a compressive stress in the principal direction *j*.

ν_o: initial Poisson's ratio.

ρ_l :longitudinal steel ratio (columns).

ρ_v :volumetric (transverse) steel ratio (columns).

σ : stress vector.

ξ, ρ : Haigh-Westergaard coordinates.